INTERFACIAL AND MECHANICAL PROPERTIES OF CARBON NANOTUBES: A FORCE SPECTROSCOPY STUDY

A Dissertation
Presented to
The Academic Faculty

by

Mark Andrew Poggi

In Partial Fulfillment
Of the Requirements for the Degree
Doctor of Philosophy in the
School of Chemistry and Biochemistry

Georgia Institute of Technology
September 2004

INTERFACIAL AND MECHANICAL PROPERTIES OF CARBON NANOTUBES:
A FORCE SPECTROSCOPY STUDY

Approved by:

Dr. Lawrence A. Bottomley, Advisor

Dr. F. Levent Degertekin

Dr. Jiri Janata

Dr. Boris Mizaikoff

Dr. Thomas M. Orlando

Dr. Robert L. Whetten

Date Approved: September 10, 2004

DEDICATION

To my mom and dad, who never discouraged creative thought and bent over backwards to make growing up fun for me and my brothers and sisters. I hope they realize that they are the most giving and loving individuals I have ever known.

To my brothers and sisters (David, April, Sarah and Nathan). For always making me laugh. Everything we do together is always an adventure, whether we're building a room, eating dinner, or driving to Las Vegas… (lets not re-live that) something unique is bound to occur.

Finally to my wife (and best friend) Meredith, whom made all of the work presented herein possible. Saying "Thank You" isn't enough for all of the time she's spent listening and talking with me about my work. Your strength has given me the strength to make it through what seemed to be impossible. I'm the luckiest guy "on the planet" to have been able to share this experience with you. I love you Mer.

Let the fun begin!

ACKNOWLEDGMENTS

I would like to sincerely thank my Advisor Professor Lawrence A. Bottomley for helping mold me into the scientist that I've always wanted to become and for his tireless efforts to ensure that I posses the highest level of understanding and never letting me reach that "invisible bar".

I would like to thank my doctoral committee for guiding my scientific growth. I would like to thank Andrew McFarland, for numerous helpful discussions regarding cantilever beam mechanics and for performing the FEA simulations. Brent Nelson for providing several stimulating discussions pertaining to AFM. Jeffrey Boyles for writing the data acquisition code for some of the force spectroscopy experiments. I would like to thank both Dr. Peter Lillehei of NASA Langley and Professor F. Levent Degertekin of Mechanical Engineering for helping in broadening my understanding of some of the fundamental physics in AFM. Jean Jarvaise of Veeco Metrology for assistance with modifying our AFM and several helpful discussions. Gary Spinner of the MiRC clean room for his tireless efforts to ensure that instrumentation in the cleanroom ran smoothly and his open-mindedness towards trying new processes.

I would like to thank NASA Langley through the Graduate Student Research Program, the American Chemical Society Division of Analytical Chemistry and the National Science Foundation through the Student Teacher Enhancement Partnership for providing financial support.

TABLE OF CONTENTS

LIST OF TABLES

LIST OF FIGURES

LIST OF SYMBOLS AND ABBREVIATIONS

A_{DC}	DC amplitude
ATP	adenosine triphosphate
atm	atmospheres
AFM	atomic force microscopy
$<A^2>$	mean square beam amplitude
BMH	Blackman-Harris window
CVD	chemical vapor deposition
CESR	conduction electron spin resonance
CFM	chemical force microscopy
°C	degrees Celsius
DNA	deoxyribonucleic acid
DSA	dynamic signal analyzer
E	elastic modulus
ESR	electron spin resonance
EDTA	ethylenediaminetetraacetic acid
FFT	fast Fourier transform
FET	field-effect transistor
FEA	finite element analysis
FIB	focused-ion beam
f_O	resonant frequency
GHz	Gigahertz

GPa	Gigapascal
Hz	hertz
HOPG	highly oriented pyrollitic graphite
IR	infrared radiation
IC	integrated circuit
IFM	interfacial force microscope
I	ionization potential
I	moment of inertia
k_{eff}	effective spring stiffness
k	spring constant
l	cantilever beam length
LFM	lateral force microscopy
lbs	pounds
m_{eff}	effective mass
MHz	Megahertz
MPa	Megapascal
m	meter
μm	micrometer
MPFS	multi parameter force spectroscopy
MWNT	multiwalled carbon nanotube
m_{NT}	nanotube mass
η	hardness
NTA	N-nitrilo-triacetic acid

NASA	National Aeronautics and Space Administration
nm	nanometer
nN	nanonewton
NSOM	near-field scanning optical microscopy
N	Newton
ρ	density
Pa	pascal
PNA	peptidenucleic acid
PSD	position sensitive detector
PSD	power spectral density
pN	piconewton
PEVK	proline-glutamate-valine-lysine
Q	quality
r.m.s.	root-mean-square
σ_p	Hammett substituent constant
SAM	self-assembled monolayers
SECM	scanning electrochemical microscopy
SEM	scanning electron microscope
SFM	scanning force microscopy
SPM	scanning probe microscopy
STM	scanning tunneling microscopy
STS	scanning tunneling spectroscopy
SAM	signal access module

SWNT	single walled carbon nanotube
t	cantilever beam thickness
TPD	temperature programmed desorption spectroscopy
TSG	template stripped gold
™	trademark
TEM	transmission electron microscope
TDFM	transverse dynamic force microscope
UHV	ultra high vacuum
USB	universal system bus
V	volts
V_{PP}	peak-to-peak voltage
w	cantilever beam width

SUMMARY

Polymer composites with applications in space are a high priority for the National Aeronautics and Space Administration (NASA). Thus, next generation polymer composites that utilize the high-impact properties of carbon nanotubes are desired.

Atomic Force Microscopy (AFM) is a tool that has been integral in the characterization of materials on the nanoscale. The mechanical response of single molecules can be observed and characterized. The efforts of this research were to characterize the polymer/nanotube interface so that scientists may have a clearer understanding of how molecules interact with the nanotube as well as the mechanical response of the nanotube. As a result, a new force spectroscopic tool was developed (Multi Parameter Force Spectroscopy). This probing approach has been critical in facilitating the understanding of how carbon nanotubes respond on the nanoscale.

Ultimately, this research has led to a clearer understanding of the chemistry between single molecules and carbon nanotubes. Also, this research has led to a force spectroscopic approach that should be extremely helpful in characterizing the mechanical response of a myriad of nanoscale objects, thus making nanoscale devices a reality.

CHAPTER 1

REVIEW OF ATOMIC FORCE MICROSCOPY

History of Scanning Probe Microscopy

Scanning Probe Microscopy (SPM) is a family of related techniques that provide information about atomic scale structure and processes. The first of these to be developed was the Scanning Tunneling Microscope (STM) by Gerd Binning and Heinrich Rohrer at IBM Zurich in 1981 [1,2]. They were awarded the Nobel Prize in Physics in 1986 for their invention. In 1986 Binnig, Calvin Quate, and Christopher Gerber invented another scanning probe instrument called the Atomic Force Microscope (AFM) [3].

These powerful techniques and others have been rapidly adopted by the scientific community and applied in numerous fields ranging from biology to materials science. The number of publications and patents in the SPM field has increased exponentially over the last twenty years [4]. In 1984 there were 16 publications utilizing scanning probe microscopy, whereas in 2003 there were over 10,000. Since the conception of the STM and the AFM, a plethora of other scanning probe techniques have been devised that have helped scientists understand chemical and physical phenomena that occur on the nano-scale.

Fundamentals of Atomic Force Microscopy

AFM is a surface analysis tool that is capable of achieving sub-angstrom resolution of the topological features of a surface [5]. The operation of the AFM is similar to that of a profilometer, which tracks the vertical movement of a stylus as it travels over a surface. The AFM can be viewed as a nanoscale profilometer that can yield a topographical map of the underlying surface.

AFM operates in the following manner: a cantilever beam with a micro-machined tip on the end is brought into close proximity with the surface of a sample. The sample is rastered below the cantilever beam. Sample topography and forces exerted between the tip and the sample cause upward or downward deflections of the cantilever. Movement of the cantilever beam is typically tracked by illuminating the reflective back-side of the cantilever with a laser and monitoring the movement of the reflected spot on a position-sensitive detector (PSD) [6]. The voltage output from the detector is proportional to the position of the movement of the laser spot on the face of the detector. These voltage changes are sent to a control module, which converts the voltage level into a distance. An image is computed by correlating the output voltage from the PSD with the X and Y coordinates of the sample. A schematic of the AFM is provided in Figure 1.1. This scheme is the simplest and most commonly used in commercial instruments. A variation of this scheme involves scanning the tip over the sample surface to allow analysis of larger samples.

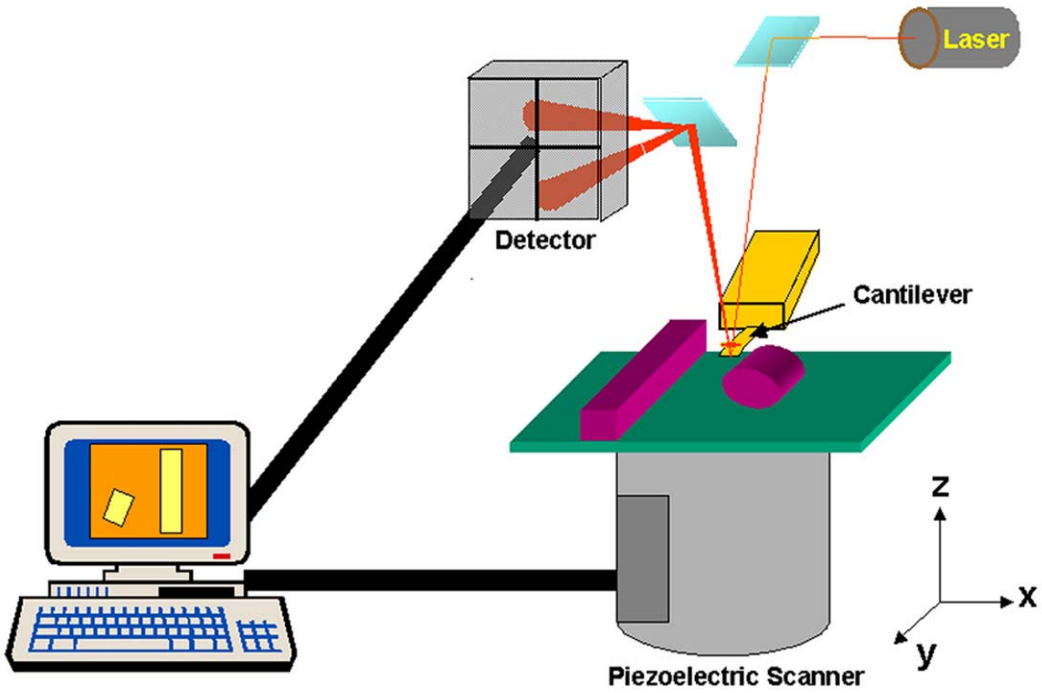

Figure 1.1. Schematic of the typical components that make up an atomic force microscope.

Instrument Components

There are several integral components in an AFM. Some of the most pivotal components are: vibration isolation units, piezoelectric scanners, cantilever probes, and detectors.

Vibration Isolation

Rigidity is important because all SPM techniques require minimization of all sources of electrical and mechanical noise [7]. Typically, electrical wires in the microscope are fully shielded and all mechanical components are held tightly in place. The entire microscope is mounted on a vibration isolation apparatus. Vibration isolation units can range from simple homemade units such as a concrete block hanging from bungee-cords (~$100) to vibration isolation tables that have pneumatically suspended tabletops (> $2,500). If these types of noise are not controlled or reduced, visualizing atomic-scale features is impossible.

Piezoelectric Scanners

Piezoelectrics are materials whose dimensions deform in response to an applied electric field. Application of precisely controlled voltages to a piezoelectric produce extremely precise movements. The geometry of piezoelectric positioning devices used in AFM includes bars, bimorphs or tubes; tubular scanners are the most commonly used. They operate at a high resonant frequency, enabling high scan rates. Piezoelectric scanners exhibit both linear and nonlinear responses to an applied voltage (Figure 1.2). As a result, careful scanner calibration is required. Thermal isolation of the piezoelectric

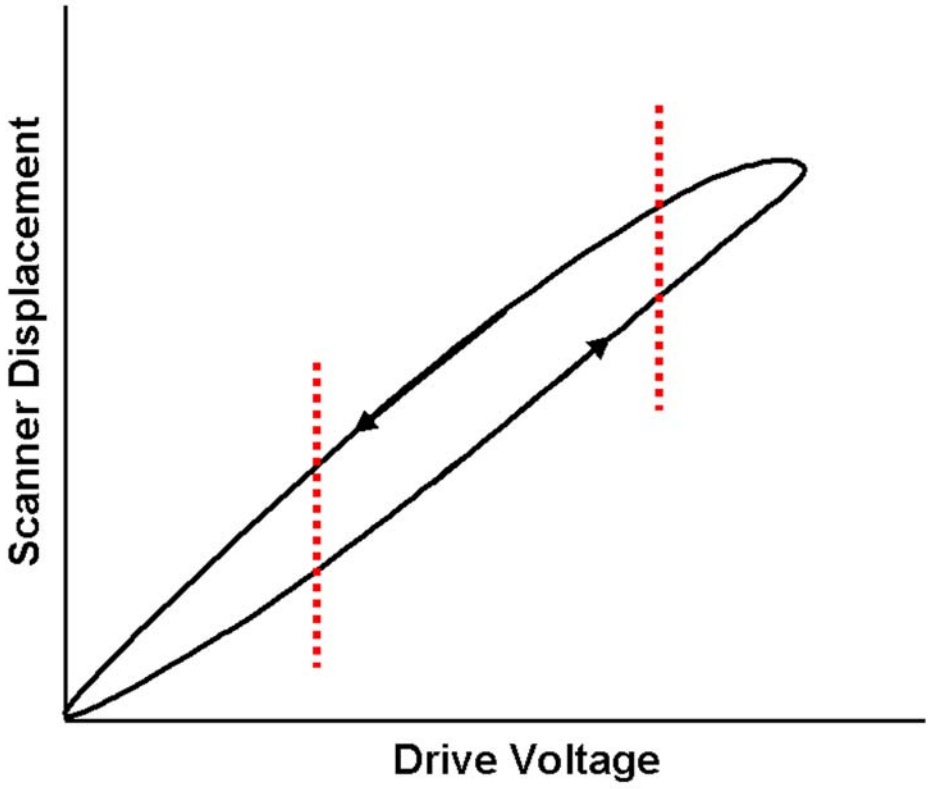

Figure 1.2. Plot of the response of a typical piezoelectric scanner to an applied voltage. The area of the response curve that is between the dashed lines is the area of linear response.

elements is necessary because their dimensions are also sensitive to temperature fluctuations [6].

Scanner calibration is typically performed using a standard surface having image features comparable in size to experimental sample features. For example, one would not want to calibrate the movement of a scanner using a grating that has 20 μm spacings and then attempt to image a sample that has feature sizes below 1 μm. It is recommended that a piezoelectric be calibrated versus a large-scale grating (> 10 μm line spacing) and versus a smaller scale grating (< 1 μm line spacing) to correct for the nonlinearities in scanner movement. Gratings are typically used as calibration standards. They are created using micromachining techniques [8] and then characterized using other surface profiling techniques.

The sample can be mounted directly onto the scanner and rastered underneath the cantilever tip, or the cantilever can be mounted to a scanner tube and rastered over a sample fixed below it. The former case is advantageous in imaging larger samples and increases the speed of imaging [9].

Samples for analysis are mounted onto a specimen disk that can be magnetically held onto the piezoelectric scanner. Double-sided tape is typically used when imaging samples in air and leads to very little movement of the sample on the specimen disk. Double-sided tape typically does not work well when imaging in liquid environments.

More permanent adhesives are required (such as glue or two-part epoxies), with careful consideration of the chemical inertness and potential out-gassing of the adhesive.

Cantilevers

Cantilevers are commercially produced from silicon and silicon nitride using microfabrication processes similar to those employed in integrated circuit manufacture. Cantilevers are often coated with metal on the topside to enhance laser reflection. There are two primary geometries of AFM cantilevers; triangular and rectangular (Figure 1.3). Rectangular cantilevers are susceptible to torsional bending during contact mode imaging whereas, triangular cantilevers have been designed to reduce the lateral forces exerted on the cantilever.

Important cantilever specifications are their dimensions, flexibility, and resonance characteristics (resonance frequency and quality factor). The fundamental resonance frequency of the cantilever should be high in order to avoid interference from building vibrations and acoustic noise. Thermal noise from the cantilever can limit the sensitivity of the AFM and should be minimized by using shorter length cantilevers. A shorter length cantilever also provides greater angular displacement of the laser resulting in greater resolution.

Cantilever tip shape and dimensions are critical to the quality of the AFM image. The overall tip geometry is often square pyramidal resulting from an etching process. The aspect ratio (height to width ratio) of the tip is important for imaging rough samples in

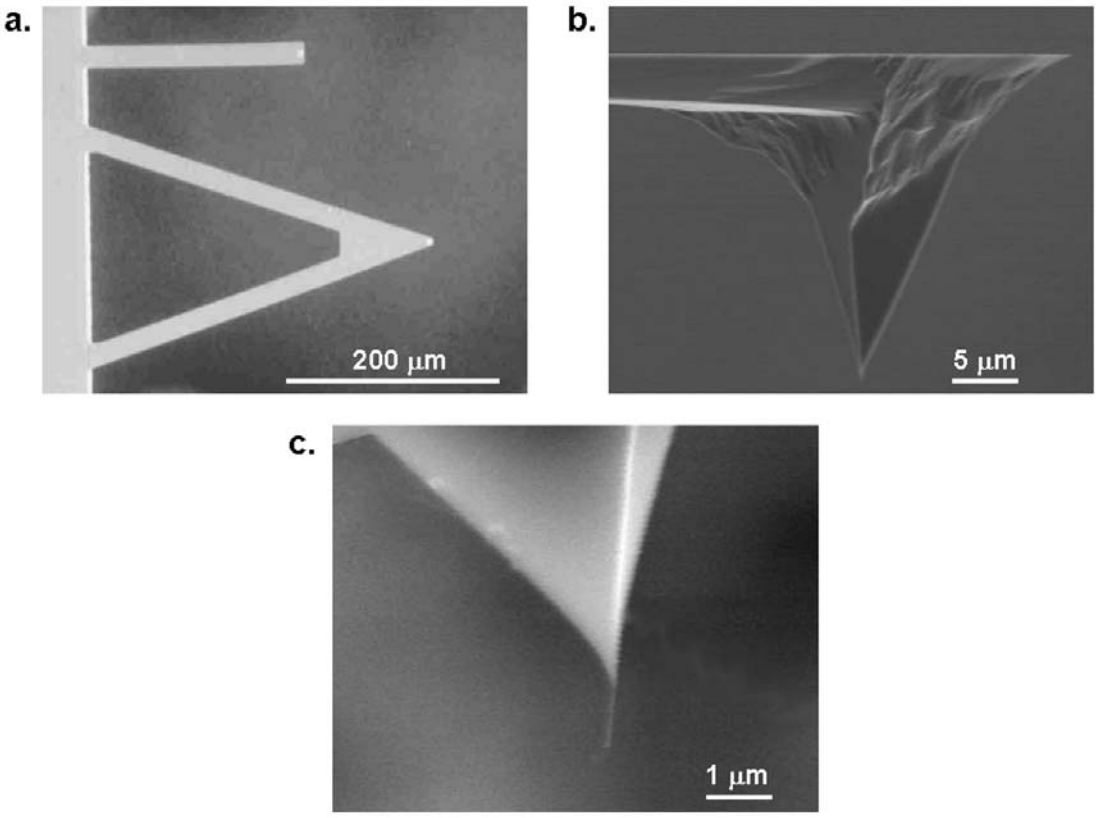

Figure 1.3. Scanning electron micrographs of cantilever probes that are typically used in AFM. (a) a rectangular cantilever (top) and a triangular cantilever (bottom). (b) Zoomed image of the microfabricated tip located at the end of the cantilever probe. (c) Image of a single walled carbon nanotube on the end of a cantilever tip (Probe fabricated by Nanodevices).

order to fully contact recesses. Tip sharpness, or the radius of curvature at the apex, is one of the key elements in achieving high-resolution images. Both tip contamination (eg. polymer stuck on the tip) or general wear (mechanical rounding) can drastically reduce image resolution. Recently, carbon nanotubes have become popular tips because of their high aspect ratio, small radius of curvature, and durability (Figure 1.3c). Tips are often functionalized in order to study tip to sample interactions or to conduct chemically sensitive measurements. Arrays of parallel cantilevers have been developed for use in sensor applications, data storage, and increasing scan sizes and imaging speed. A more in-depth explanation of cantilever probe fabrication and the cantilever beam's mechanical properties will be described in Chapter 3.

Detectors

The original AFM used a STM to sense the movement of the cantilever in response to interactions with the sample. In most commercial AFM instruments, optical detectors have supplanted this type of electrical detector. The most widely used detection system uses laser beam reflection off the end of the cantilever onto a position sensitive detector (PSD). A change in the angle of the cantilever moves the spot on the detector, producing a change in the voltage output. Early on in AFM, two-segment photodiodes were used (Figure 1.4a). Transducers were used that compared the light intensity on the top segment versus that on the bottom segment and convert this into an output voltage of the photodiode to the voltage level on the bottom face of the photodiode. This type of PSD only allows for tracking the vertical movement of the laser spot (i.e. vertical movement of the cantilever). Surface scientists later realized that the twisting motion that the cantilever

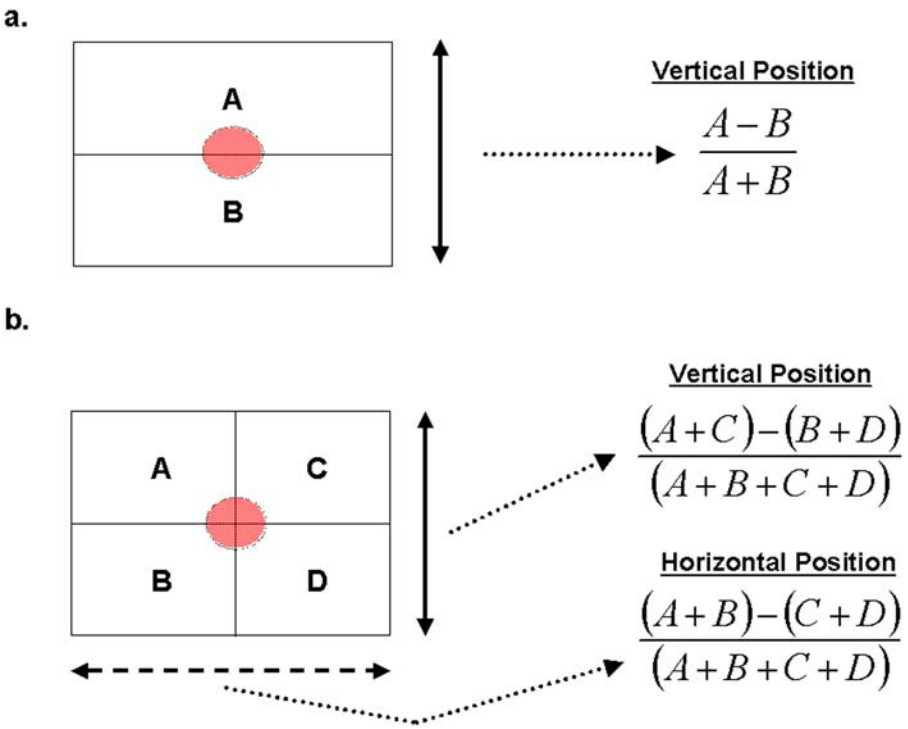

Figure 1.4. Schematic of a two segment (a) and a four segment (b) photodiode device used to monitor cantilever deflection and torsion. Cantilever deflection (and torsion) is determined by the ratio of voltages on each segment of the detector, as defined in the equations given to the right of each schematic.

experiences when imaging could reveal useful information regarding friction between the tip and the sample (Lateral Force Microscopy, see below). To facilitate this, a quad-photodiode was used (Figure 1.4b). The quadrant-photodiode is capable of measuring vertical cantilever deflection (quadrants A and C vs. quadrants B and D) as well as cantilever torsion (quadrants A and B vs. quadrants C and D).

Integration of a detector onto the cantilever (i.e. strain gauge) has also been accomplished using the piezoresistive properties of silica. As the cantilever beam bends, the electrical resistance of the beam changes. Thus, by monitoring the fluctuations of an electrical current passing through the cantilever, one can interpret cantilever bending. This eliminates the laser and the position sensitive detector. This integrated approach is beneficial for imaging samples that are light sensitive. The idea of integrating a detector on the cantilever has also led to the development of a cantilever that is piezoelectrically actuated (thus eliminating the bulky piezo scanner).

Imaging Modes

The atomic force microscope can be operated in several modes (contact, torsional, force modulation, intermittent contact, non-contact and force volume). Each imaging mode can provide a plethora of information regarding the chemical and physical nature of a surface. [10]. Several other imaging modes have been developed over the years but the following modes of operation are still the most widely used [11,12].

Contact Mode

In this mode, the probe tip is maintained in contact with the sample surface. The image can be acquired under four different imaging methods: deflection, height, friction, and force modulation. In the deflection method, the image is a map of cantilever bending as a function of position and is acquired under variable vertical loading forces. To image under constant applied force, the height method uses a closed-loop feedback system to raise or lower the sample (or tip) to maintain a fixed cantilever deflection. The user optimizes feedback system performance by adjustment of the proportional and integral gains. Proportional gain sets the magnitude whereas integral gain sets the temporal response of corrective action to return the cantilever to its reference position. If the gains are too high, feedback oscillations produce image artifacts. If the gains are too low, resolution is poor due to slow response of the feedback loop.

Force Curves

Force curves are used to correlate vertical movement of the scanner with cantilever deflection. An "ideal" force curve is depicted in Figure 1.5a. Force curves are obtained by disabling the scanner movement in the x and y directions and extending and retracting the scanner in the z-direction. As the tip approaches the sample, no cantilever bending is observed until the gap between the tip and the sample is extremely small (typically < 1 nm). At this point, attractive van der Waals interactions between the tip and the substrate will pull the cantilever downward [13,14]. Once in contact, raising the sample produces an upward bend in the cantilever. On the downward movement of the scanner, the cantilever gradually returns to its original position. Eventually the scanner is retracted far

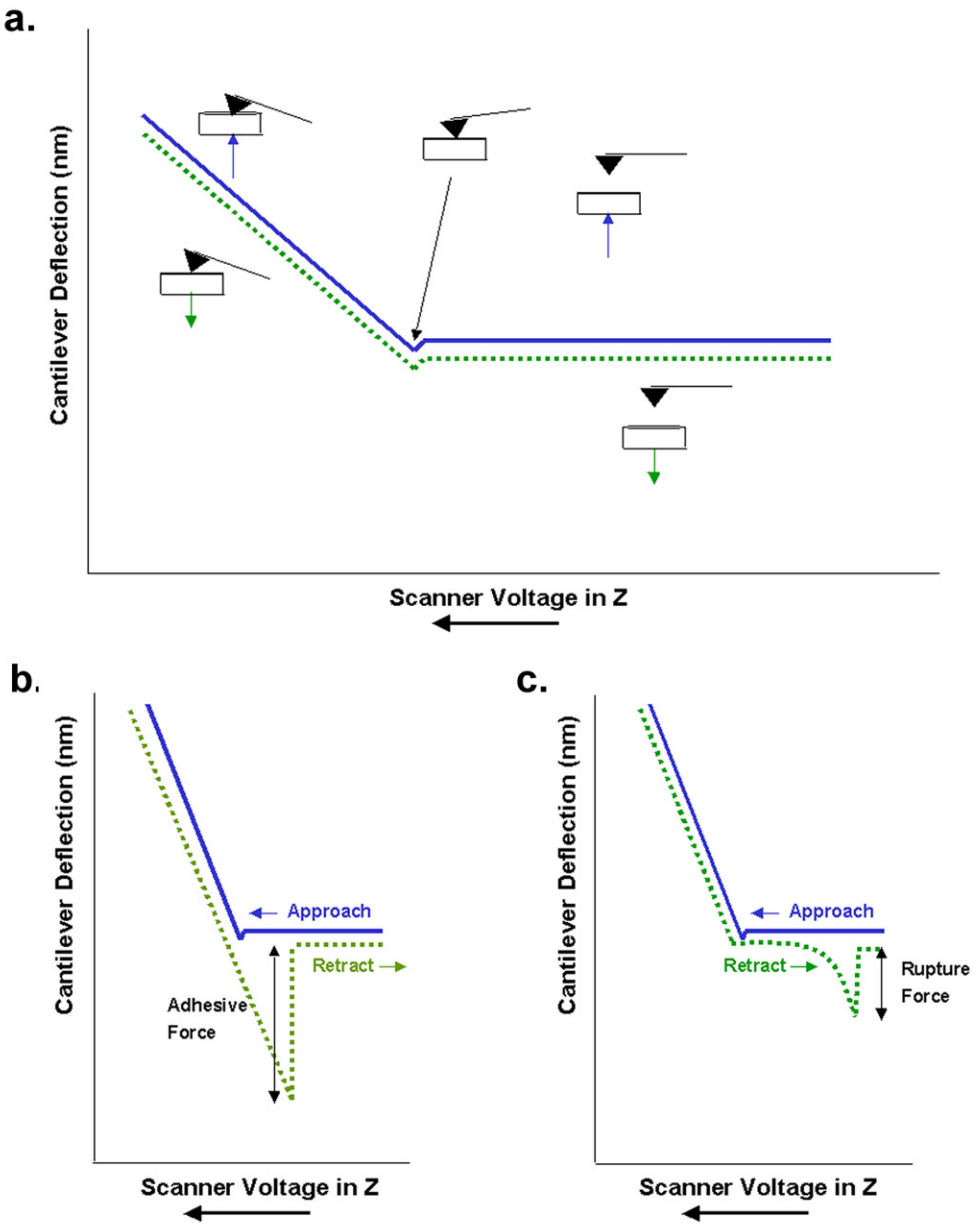

Figure 1.5. Force curves depicting different motions of the cantilever beam. The blue line represents the cantilever's position during the approach of the scanner towards the cantilever. The green line represents the cantilever's position during the retraction of the scanner away from the cantilever. (a) Ideal force curve where no interfacial adhesion is present between the cantilever tip and the underlying surface. (b) Typical force curve where adhesion is present between the cantilever tip and the substrate (c) Single molecule force curve that is typically observed when pulling on a molecule that is affixed between the cantilever tip and the surface.

enough away from the cantilever until the tip and the surface are separated in space. In the presence of attractive or adhesive forces, downward deflection of the cantilever (past the beam's static position) may be observed. When the restoring force of the cantilever exceeds these forces, the tip releases from the substrate surface and the cantilever returns to its original position (Figure 1.5b). The magnitude of the mechanical load that is vertically imposed on the beam is computed by multiplying the total vertical deflection of the beam times the stiffness of the cantilever. The magnitude of the attractive or adhesive force is calculated by multiplying the downward deflection of the cantilever times its spring constant. When a sample is stored at room conditions, hydration layers (water layers) are present on virtually every type of sample surface. The thin hydration layers can bring the tip into contact with the surface. Regardless of a sample's hydrophobicity a nanometer-scale water layer will be present. Water layers can be reduced by storing samples in a dessicator, imaging in a dry environment (for example a N_2 enclosed AFM) or working under ultra high vacuum conditions (UHV) [6].

Force curves enable calibration of cantilever deflection and commensurate movement of the laser spot on the PSD. This is accomplished by fitting a line to the portion of the force curve where the scanner is pushing up on the cantilever beam. The units of the sensitivity parameter are: change in voltage across the PSD (volts) / change in voltage being applied to the scanner (volts). This parameter is also used to determine the spring constant of the cantilever beam (see Chapter 3).

A third type of force curve is depicted in Figure 1.5c. When contact of the tip to a long molecule on the surface occurs, mechanically induced elongation and unfolding results from downward movement of the scanner. This mechanically induced unfolding yields a more gradual deflection of the cantilever with respect to the movement of the scanner away from the beam. With knowledge of the stiffness of the cantilever, researchers have attempted to interpret the forces required to unfold biomolecules and polymers.

Torsional Mode

This mode of AFM requires a quadrant photodiode was implemented into AFMs. This mode measures the local variations of friction that may exist between the cantilever tip and the substrate. Lateral forces on the tip cause torsional bending (twisting) of the cantilever that is detected by horizontal movement of the laser spot on the detector. This is also referred to as Friction Force Microscopy. For example, this can be used to interpret the "stickiness" of a sample (hydrophilicity or hydrophobicity). Figure 1.6 is an example of a typical topographical image with a corresponding friction map. Areas that are lighter in the friction image depict areas on the surface where the cantilever experienced a high degree of drag.

Force Modulation Imaging

Force modulation is a contact imaging method that enables simultaneous measurement of the topology and compliance of the substrate. In force modulation, a piezoelectric actuator oscillates the cantilever chip. The tip is positioned above the substrate so that during its oscillation, the tip slightly indents the substrate. The amplitude of the

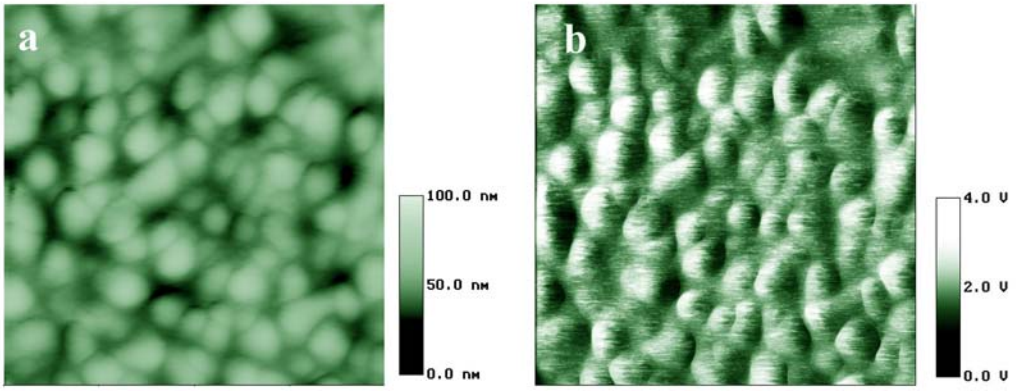

Figure 1.6. Contact mode AFM of the surface of a TiO_2 thin film. (a) Topographical image of a 1 μm × 1μm domain. (b) Corresponding friction map of the same region. (Reproduction from Roberson and Poggi et al. [15])

cantilever's oscillation is monitored as the tip is rastered across the surface. Compliant areas on the sample will produce larger cantilever deflections compared to more rigid areas. This is an invaluable method for characterizing the mechanical and topological properties of composite materials on the nanoscale.

Intermittent Contact Mode

Intermittent contact or TappingMode™ oscillates the cantilever at its resonance frequency or one of the higher vibrational modes [16]. To operate in intermittent contact mode, the cantilever chip is mounted into a holder that mechanically oscillates the entire cantilever chip (via a piezoelectric that is fused to the cantilever chip holder). Surface topology is measured with the height method while maintaining constant dampening of cantilever oscillation rather than cantilever measuring beam deflection as is done in contact mode. Cantilever oscillation amplitude dampening is maintained at a fixed value using a closed-loop feedback system to raise or lower the sample (or tip).

Increasing or decreasing the drive voltage being sent to the piezoelectric in the chip holder can modulate the oscillation amplitude of the cantilever. The major advantages of intermittent contact mode imaging are reduced vertical loads, lateral forces, and adhesive interactions between the tip and the substrate. This mode enables imaging of soft samples or molecules that are not strongly attached to the surface. Low drive amplitude is desired to minimize impact on soft molecules; however the drive amplitude must be sufficient to overcome attractive capillary forces. This problem can be resolved by

imaging under fluid. Imaging under fluid also provides the opportunity to examine interactions between the substrate and molecules in the liquid environment.

Oscillation Amplitude Curves

Oscillation amplitude curves are similar to the force curves. They are acquired by moving the scanner in the z-direction and monitoring the corresponding change in oscillation amplitude of the cantilever (at a specified drive frequency). A typical oscillation amplitude curve and corresponding deflection curve (force curve) acquired with a silicon cantilever beam is shown in Figure 1.7. During the extension of the scanner towards the cantilever, the oscillation amplitude of the beam remains unchanged until the tip begins to gets close to the sample. When the van der Waals forces pull the tip into contact with the substrate, a gradual drop in the oscillation amplitude is observed. The oscillation amplitude of the cantilever "bottoms out" or remains at a constant negative value while the tip is "pinned" on the surface. Then as the scanner retracts from the surface, and the adhesive interaction between the tip and the surface is exceeded, the cantilever's oscillation amplitude is almost instantaneously restored (far right portion of Figure 1.7b). The "ringing" that is observed near the far right of the oscillation amplitude curve is a result of the cantilever snapping off of the surface and then returning to its fundamental resonance. Oscillation amplitude curves are important observables that allow microscopists to more precisely position the cantilever in ultra-close proximity with the underlying surface while minimizing tip damage.

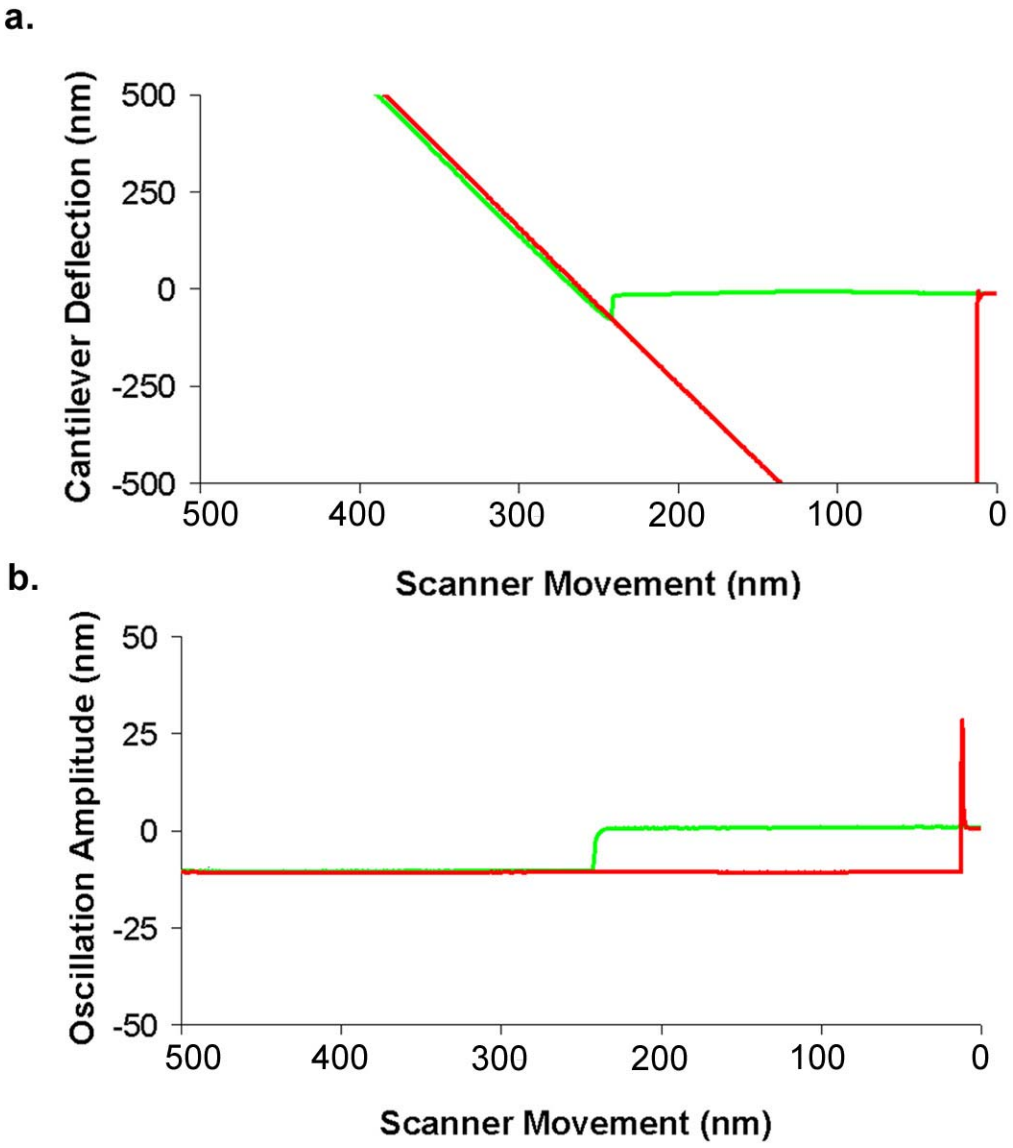

Figure 1.7. (a) Force Curve acquired using a Veeco FESP Probe and a clean gold substrate (the green line represents the cantilever's position during the approach of the scanner towards the cantilever, while the red line represents the cantilever's position during the retraction of the scanner away from the cantilever. (b) Corresponding oscillation amplitude curve while the cantilever is driven at 67kHz.

Phase Imaging

Phase imaging is an extension of intermittent contact mode that enables measurement of surface properties such as adhesion, friction, and elasticity. Phase imaging detects the phase shift of the cantilever oscillation, which is related to the surface rigidity. Phase shifts above 90º are due to attractive interactions, whereas phase shifts below 90º are due to repulsive interactions. Phase imaging has become the workhorse tool for analyzing the elasticity of composite materials. For topologically homogeneous surfaces, more elastic domains are readily distinguished from less elastic regions in the phase image. Figure 1.8 depicts a Tapping Mode™ topographical and phase image of a colloidal hydrogel particles deposited on a glass microscope slide.

Noncontact Mode

Noncontact mode (or Dynamic Force) imaging relies on longer-range molecular forces to obtain surface topology [17]. The cantilever is either artificially oscillated at its resonance frequency by a piezoactuator (as in intermittent contact mode) or thermally driven. The surface topography is measured by monitoring the shifts in cantilever resonant frequency. The cantilever's resonance will shift depending upon tip/sample interactions. For example, if the cantilever/substrate separation decreases, the cantilever's resonance becomes dampened due to the sample being at a slightly different temperature than that of the cantilever. Specialized expertise in controlling the placement of the tip above the sample is required to avoid image artifacts.

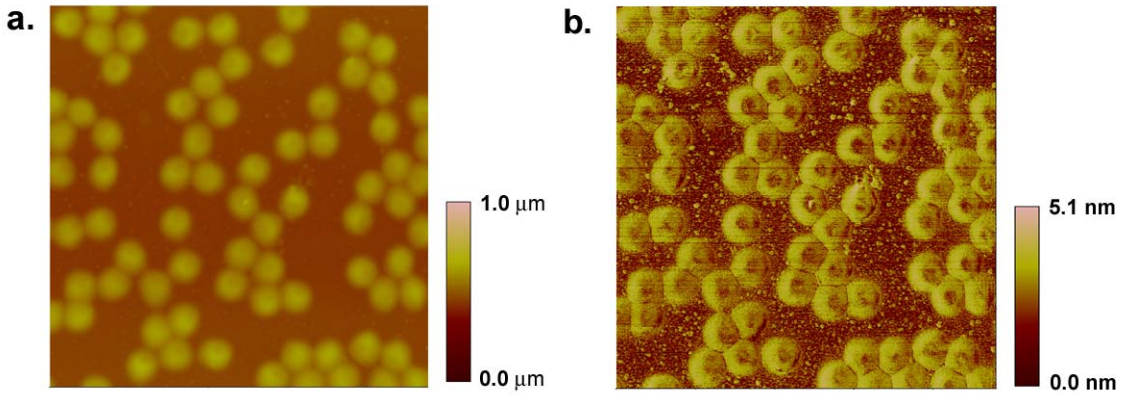

Figure 1.8. Topographical (a) and Phase (b) images of spherical hydrogels on glass acquired simultaneously over a 12 μm × 12μm domain.

Force Volume Imaging

Force volume imaging is an extension of contact mode AFM. A sample is translated underneath the cantilever in the x, y and z direction via the piezo-scanner. As the sample moves in x and y, a topographical image of the underlying sample is generated (Figure 1.9). For every incremental movement in x and y, a corresponding z-movement (extension and retraction of the scanner) is executed for each pixel in the topographical image. During z-movement of the sample, the piezoelectric scanner extends "up" moving the sample closer to the cantilever. Once the sample touches the cantilever, the scanner is extended "up" only to a point that exerts a predefined load on the cantilever. Once the cantilever deflects a certain amount (by monitoring the position of the laser spot on the PSD), the scanner will begin to retract the sample from the cantilever "down". The z-movement of the sample yields a force curve (as discussed previously).

The maximum vertical loading of the sample can be controlled by reversing the scanner movement when the deflection reaches a predetermined value (i.e. trigger threshold). The downward deflection of the cantilever at each location above the sample can provide "maps" of areas of large adhesion (cantilever pulled down a large distance) or small areas of small adhesion (cantilever pulled down a large distance). Force volume imaging can reconstruct surface topology (Figure 1.10a) and also measure cantilever displacement at each topographical pixel (Figure 1.10b and c). If one were interested in the actual forces that the cantilever experiences at each point in the force volume image, by multiplying stiffness of the cantilever times the deflection of the beam the adhesive force present between the cantilever tip and the substrate can be elucidated (as discussed in Chapter 5).

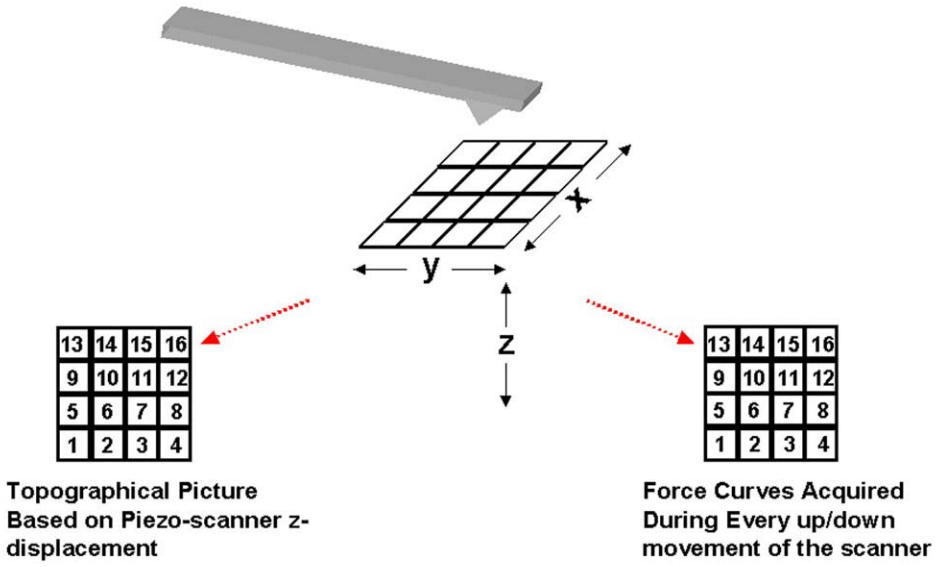

Figure 1.9. Schematic of the movement of a sample during Force Volume imaging. At each topographical pixel in the image a corresponding movement in the z-direction is made (i.e. a force curve)

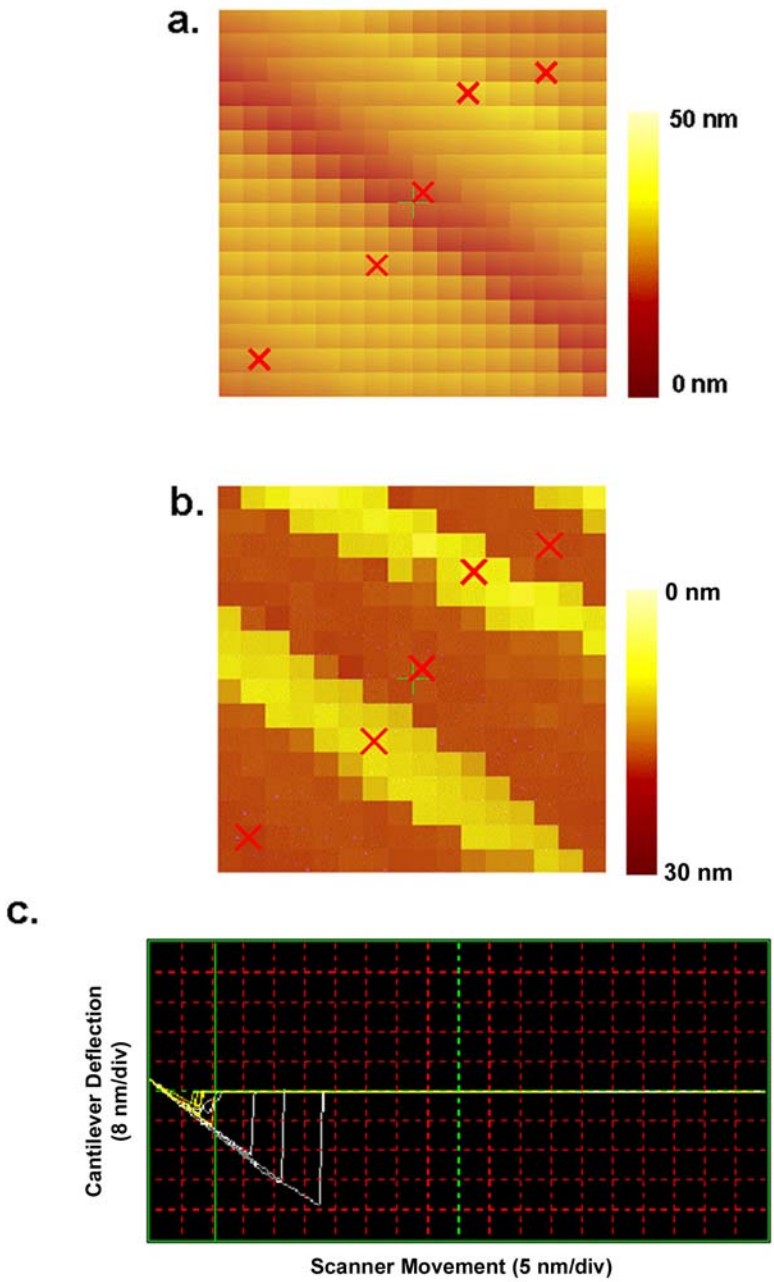

Figure 1.10. (a) Topographical image acquired in Force Volume mode. (b) Force Volume image, where each pixel represents an individual force curve. The contrast in this image is related to the maximum deflection of the cantilever. Force curves that have a small pull down distance are light while force curves that have a large pull down distance are dark (c) Individual force curves that were acquired at each location that is marked with an "X". The yellow line represents the cantilever's position during the approach of the substrate towards the cantilever, while the white line represents the cantilever's position during the retraction of the scanner away from the cantilever.

Force volume imaging is not only used to characterize the adhesion across a surface but can also be used in single molecule mechanical testing experiments. This mode of operation facilitates the interrogation of a large area of a surface, thus large sampling domains can be investigated. As a result this approach in single molecule mechanical testing can aid in locating regions where molecules of interest are located.

In summary, the atomic force microscope is an analytical tool that can yield extremely valuable information regarding chemical and physical phenomena that can and does occurring on the nanoscale. To obtain reliable information with the AFM, one needs to be knowledgeable of its fundamental components, operating principles and equipment. In many instances AFM provides information unobtainable with any other technique. This is why almost every major university in the United States and abroad have one or more scientists who are actively using and or improving this invaluable instrument.

CHAPTER 2

REVIEW OF SCANNING PROBE MICROSCOPY

Scientists across the globe are inventing new scanning probe techniques, improving instrumentation, and developing theories to guide experimentalists and finding new applications of scanning probe microscopy. During the course of my dissertation research, I have co-authored two in-depth review articles focusing on the recent advances in SPM. In preparing these reviews, over 25,000 abstracts pertaining to SPM were reviewed (spanning the years 2000 to 2004). Over 3,000 papers were read and summarized to properly convey the scientific findings in the reviews.

The purpose of this chapter is to highlight innovations and applications of SPM that pertain to the topic of this dissertation. The text that follows are excerpts from the two articles published in Analytical Chemistry [9,18]. Permission to use and elaborate upon these important advancements has been granted by the American Chemical Society, 2004.

Advanced Theoretical Modeling

Hofer et al. [19] presented a thorough review of theoretical models that have been used to interpret SPM data. Balantekin et al. have devised a model the can elucidate the amount of power that is dissipated into a sample during tapping-mode^{TM} AFM [20]. This model facilitates in the determination of the dampening constant of a sample and could potentially be used to quantify dampening phenomena in composite systems. Boisgard et

al. have presented a short overview covering two models that evaluate the loss of energy when a cantilever tip is oscillated in close proximity of a surface [21]. Rodriguez et al. have provided a thorough interpretation of an AFM when operated under active quality factor control [22]. Their theoretical treatment demonstrates that when using Q-control (the resonant characteristics of the cantilever), the force exerted on the substrate is minimized. Su et al. [23] have correlated residual tip speed before impacting with a surface and the associated tip wear for relatively hard samples. They have shown that a lower setpoint is not harmful and actually leads to higher resolution images. Stark et al. have presented dynamic experiments where the contact force during a typical tapping mode™ experiment is determined [24]. They've shown that under normal imaging condition, the contact force exceeds 200nN. Lee and co-workers [16] used nonlinear dynamical systems theory to analyze the oscillatory properties of a cantilever when used in dynamic force microscopy. They brought better understanding of the sudden global changes that occur in the interaction potential at certain gap widths that cause the tip to irregularly tap the sample. Hoffmann has presented simulations of driving a cantilever off-resonance when performing noncontact-atomic force microscopy [25] which facilitates a more general route to the reconstruction of the surface force gradients.

Couturier et al. have provided a complete analysis of the behavior of a noncontact atomic force microscope (NC-AFM) [26]. They present numerical models for the stability of the cantilever tip when it oscillates close to the sample. Chang and Chu have derived a closed-form expression for the oscillatory behavior of cantilevers with complicated cross-sections [27].

Hardware Improvements/New Techniques

Detectors

Schaffer et al. [28] have implemented a new detector for SFM. The optical power from the beam is distributed across a photodetector array, splitting it into multiple channels. An adjustable gain factor is dynamically set to weigh the contribution from each channel. A factor of five improvement in signal to noise ratio over the conventional segmented detector was obtained. Schaffer has designed an array detector that combines a higher sensitivity and a larger dynamic range (in the z-direction) than conventional 2-segment photodiode detectors [29]. This detector is less susceptible to nonlinearities during force measurements. Onaran and colleagues [30] utilized radiation pressure generated by a focused acoustic beam to implement tapping mode and elasticity imaging by AFM. Their method enables efficient excitation and spatial mapping of both higher-order flexural and torsional modes of AFM cantilevers in liquids.

Cantilever Arrays

Progress in cantilever arrays has been critically evaluated by Vettiger and co-workers.26 Recent emphasis has focused on reducing the size and increasing the number of actuators in the array. Cantilever arrays have been proposed as an alternative high-density data-storage device. King and co-workers[31] continued their evaluation of a resistively heated cantilever as a thermomechanical data storage device. Their technique uses the cantilever to write/read/erase/rewrite bits of data into a thin polymer layer on a silicon surface. Heat conduction governs the ultimate writing and reading capabilities of the

device. They measured and simulated transient thermal and electrical behavior in a resistively heated cantilever and concluded that reduction in cantilever dimensions and tip height should improve the speed and sensitivity of the writing step.

Chow et al. [32] has improved upon previous cantilever arrays by incorporating through-wafer interconnects enabling more complicated and compact arrays to be fabricated. Integration of the cantilevers, tips, and interconnects enabled operation of a high dimension probe array over large areas. Despont et al. [33] set out to improve the data reading and writing characteristics of cantilever arrays. They fabricated a 32 x 32 cantilever array with integrated Schottky diodes in series with each cantilever. This led to a large reduction in cross talk between actuators. Cross and co-workers[34] have carried out theoretical and experimental treatments on the reading/writing capabilities of polymer indentations carried out with a thermomechanically actuated SFM.

In addition to their application in data storage, cantilever arrays facilitate faster imaging over large substrate domains. Sulchek and co-workers[35] created an instrument with parallel readout from an array of five cantilevers using an interferometric detection scheme. Each cantilever contained a phase sensitive diffraction grating consisting of a reference and movable set of interdigitated fingers. As a force is applied to the tip, the movable set is displaced and the intensity of the diffracted orders is altered. The order intensity from each cantilever is measured with a custom array of silicon photodiodes with integrated complementary metal–oxide–semiconductor amplifiers. Their interdigital method for cantilever array readout is scalable, provides angstrom resolution, and is

potentially simpler to implement than other methods. Akiyama et al. [36] has successfully used a 2 x 1 array of active and self-detecting cantilevers to acquire two images taken in parallel. The cantilevers possess an integrated deflection sensor based on a stress sensing metal-oxide-semiconductor transistor and amplifiers for signal readout. The number of electrical interconnects were significantly reduced by routing electric signals directly on the chip. Constant height mode, tapping mode and force mode images were obtained with this array.

Enhanced Image Acquisition

Another focus involved increasing scanning speed. Sulchek and co-workers[37] have achieved high-speed SFM imaging in solution. Their technique used a ZnO self-actuating cantilever and achieved an imaging bandwidth 100 times faster than typical SFMs. Ando et al. [38] designed a SFM capable of obtaining 100 x 100 pixel images of biological media within 80ms. The apparatus consisted of a newly designed sample scanning system free of resonant vibrations up to 60kHz and short, flexible cantilevers with high resonance frequencies. Images detailing the movement of myosin on mica under buffer solution were acquired with this instrument. Several groups have investigated improvements in apparent cantilever Q factor using acoustic, radiation pressure, and magnetic actuation to improve force sensitivity. [39-41] Methods for improving Q factors have immediate application in imaging, dynamic force spectroscopy measurements, and microcantilevers-based sensors. [42,43]

Sulchek et al. critically examined ways to increase the scan speeds of both contact and intermittent contact imaging [44]. Current limitations on scan speeds can be eliminated by integration of a faster feedback actuator as well as active control of the dynamics of the cantilever. Akiyama et al. [45] devised a fast driving technique that utilizes a tuned filter that boosts the servo signal in proportion to its frequency. An imaging bandwidth of 5 kHz was achieved; images were acquired in constant force mode at tip velocities up to 0.62 mm/s. Stark et al. [46] have improved tapping mode imaging by driving cantilever resonance at one frequency and monitoring deflection at a harmonic of this frequency. The result is significant enhancement in image contrast.

Zahl and co-workers have created software that can be used to control many different types of SPMs and process images [47]. The software is extremely flexible and can be used to control many of the different modes in SPM. The software package is available at no cost to users. Trawick and co-workers used a polynomial mapping method to correct for piezoelectric-induced artifacts in SPM images [48]. This correction scheme can reduce the effects of distortion in an AFM image from 5% of the scan width to a single pixel. Kindt et al. [49] developed a real time method for eliminating the drift component associated with AFM images. Their method incorporates automatic changes in the setpoint to maintain a set difference in the relative feature richness of two traces taken with slightly offset setpoints.

Arnold et al. [50] presented a new approach for studying friction and stick-slip phenomena analyzing the torsional resonance of the cantilever. Pfeiffer and coworkers

[51] proved that lateral forces can be measured even when the tip is not in contact with the surface. Alcarez and co-workers measured and modeled the viscous drag that a cantilever experiences when in close proximity with a surface [52]. Correction of the drag artifact could lead to an improvement in the scan speed in contact mode imaging of soft samples in liquid and to an increase in the pulling speed range in force spectroscopy measurements. Two groups have examined the cross-talk that occurs during the acquisition of topographical and friction data in AFM [53,54] and presented methods for detection and correction of this artifact.

Nishino and co-workers[55] developed a tensile loading stage that facilitated the observation of polymer films under stress. Strain was determined from measurements of the changes in distance between image features on a polyethylene terephthalate film surface as a function of tensile load. Strain was evaluated both parallel and perpendicular to the tensile load direction. The microscopic stress–strain relationship determined by SFM coincided with that determined in a conventional macroscopic mode suggesting that deformation of the film is an affine process. Buh and Kopanski [56] have looked at the effect of illumination from the laser of an optical-beam-deflection AFM on a semiconductor sample with a scanning capacitance probe connected in parallel. Significant differences in the capacitance-voltage characteristics were observed and attributed to light spillage over the edges of and transmission through the cantilever. The creation of automated instruments that can acquire images without human involvement was a focus for research on improving SPM instrumentation. For example, Akiyama and co-workers[57] have built a stand-alone instrument for conducting soil and dust analyses on Mars. Their instrument is capable of self-engaging the cantilever on a substrate and

frequency modulation measurements. Barth and co-workers[58] described an array-based SFM designed for imaging interplanetary particles onboard the ESA-Midas/Rosetta space mission vehicle.

New Imaging Techniques

Krotil et al. [59] have created a new scanning force technique in which a low-frequency vertical modulation is combined with a second high-frequency lateral modulation as the tip translates across the surface of the substrate. This enables topographical mapping of the surface simultaneously with quantitative mapping of adhesive, static, and dynamic frictional forces. [60] Similarly, Syed Asif and co-workers[61] have designed a hybrid nanoindenting instrument that combines a depth-sensing nanoindenter with scanning-probe imaging capabilities. This instrument is capable of measuring the damping coefficient and loss modulus of a substrate while generating a topographical picture of the regions with different mechanical properties.

Takano et al. [62] have shown that electric force microscopy (EFM) can be used to map compositional differences in organic monolayers buried under a thick polymeric film. A mixed underlayer comprised of methyl and hydroxyl terminated alkanethiols was patterned onto a gold surface using microcontact printing. EFM imaging exhibits sufficient contrast to function as a mapping methodology for buried functional groups.

Anderson has integrated vibrational spectroscopy with an SFM. [63,64] In the first report, a cantilever was used to spatially enhance a Raman signal via surface enhanced Raman

scattering. In the second report, Anderson used the cantilever as an IR detector and a surface separation device for spectroscopic analyses of substrates. These combined vibrational spectroscopy/probe microscopy approaches enable acquisition of high content spectra that identifies the chemical composition of image features.

With advances in device miniaturization, it is becoming increasingly difficult to test their electrical properties, especially resistance. The probes commonly used in SFM-based electrical characterizations are either silicon probes with conductive coatings or silicon probes with integrated tips. [65] Scanning spreading resistance microscopy (SSRM) is a technique commonly used for characterizing semiconductor devices. Hantschel and co-workers [66] designed diamond-tipped probes integrated onto a silicon cantilever. This probe increases the dynamic range of SSRM by an order of magnitude. Boggild and co-workers [67] fabricated a nanoscale four-point probe device for high spatial resolution conductivity measurements on surfaces and thin films.

Scanning thermal microscopy maps spatial variations in temperature, thermal conductivity, or thermal diffusivity on a surface. Recent efforts have focused on improving spatial resolution and probe response time through reduction in probe geometry. [68-70] Li and co-workers[71] fabricated thermal probes in which a thin thermocouple wire is imbedded in a polyimide cantilever. They found that the thermal sensitivity of polymeric probes could be up to ten times greater than silicon-based probes of similar dimension.

Wold, [72] Cui, [73] and their colleagues have independently shown that conducting probe-SFM is a reliable method for fundamental studies of electron transfer through small numbers of molecules. The junction resistance of alkanethiol molecules increased exponentially with chain length and decreased with increasing load. Conducting probe-SFM measurements open opportunities for exploring electron transfer as a function of molecular deformation. Topinka and co-workers[74] have successfully imaged electron flow from two quantum point contacts. The electron flow is imaged by scanning a negatively charged, conductive SFM tip above the surface of the device while measuring the position dependant conductance.

Burns has presented a unique technique where AFM is coupled in real time with submicron confocal fluorescence imaging [75]. Hu and co-workers have combined tapping-mode atomic force microscopy and fluorescence lifetime imaging microscopy [76]. They have demonstrated that spatially mapping the change in fluorescence lifetime and intensity is a promising approach to spectroscopic imaging at the length scales obtainable with AFM. Noy and Huser [77] integrated an AFM into a scanning confocal optical microscope enabling simultaneous acquisition of optical and topographical images of surfaces.

Fukushima et al. [78] developed an AFM that mounts in an SEM with easy sample change, optical alignment, and sample positioning capabilities. The viewing angle of the SEM was designed so that the apex of the AFM tip could be observed for most samples. Browne et al. have designed a scanning transmission X-ray microscope (STXM) for use

with synchrotron radiation allowing simultaneous X-ray imaging and topological probing of a surface [79]. This technique could provide a plethora of information regarding radiation damage to surfaces or samples, and dynamic processes like specimen corrosion. Bondarenko et al. [80] have developed a scanning magnetic microscope (SMM) that does not induce appreciable applied forces or magnetic excitations on specimens. This microscope is intended to measure weak magnetic field distributions near the surface at micron and sub-micron scales.

Dubreuil et al. [81] have used an AFM to directly image the air/water interface. Phase and topography images revealed information about the layering of Langmuir-Blodgett films. Several groups have employed in situ AFM to characterize adsorbates on the active surface of acoustic resonators [82-84]. This combined technique facilitates correlation of mass changes with topology.

Force Spectroscopy

Biological Samples

Force spectroscopy has matured in the past few years from an experimental technique practiced by a select few to one widely used by the SPM community. The specialized equipment for force spectroscopy is now commercially available from multiple vendors. The issues of force calibration and force sensitivity have been addressed by manufactures allowing for greater confidence in the analyses. Reduction in cantilever dimensions has allowed for the measurement of smaller and smaller forces. This, coupled with a redesign of the optics, has facilitated force measurements in the sub-attonewton range at

millikelvin temperatures. [85] For researchers working under more temperate conditions, low pN forces are now routinely measured. Advances in cantilever design are continuing to push the limits of force detection.

Numerous reviews pertaining to all aspects of force spectroscopy have been published during the past two years. Hugel et al. [86] has thoroughly reviewed the recent progress of SFM-based single molecule mechanical testing emphasizing recent refinements of existing polymer theories and their applicability to interpretation of SFM-based single molecule mechanical measurements. Zlatanova et al. [87] reviewed instrumental aspects of SFM force measurements. Bustamante and co-workers have reviewed the methods currently used in single-molecule mechanical testing of proteins, nucleic acids, protein-DNA complexes and chromatin. [88] The review by Carrion-Vazquez and co-workers[89] focused on protein folding/unfolding. Clausen-Schaumann et al. have highlighted recent progress in single-molecule force spectroscopy and commented on the prospects of force spectroscopy in characterizing molecular motors. [90]

Automated or semi-automated methods of force curve analysis are a continuing area of investigation. Baumgartner et al. [91] developed algorithms for the analysis of force distance curves whereas Gergely et al. [92] developed algorithms detecting rupture points along a force-distance curve. Todd and co-workers[93] have generalized the flexural beam theory for SFM cantilevers to include tip interactions that are present in the snap-to-contact region. They have extended their theory to the analysis of continuous force-separation curves. [94] Vinogradova and co-workers[95] have theoretically evaluated the

possibility of carrying out force measurements (mechanical tests) at much higher speeds than are currently practiced. This has led to the development of a number of models that can be used to estimate the deflection caused by viscous drag on a cantilever in various experiments.

The predominance of the work published in force spectroscopy is shifting from model proteins (e.g. titin) to more complex biologically relevant materials. Thompson et al. [96] examined the self-healing mechanism of bone. They found that bone contains sacrificial bonds that both protect and dissipate energy. The recovery of toughness in these pulling experiments paralleled that of titin and nacre, which have been shown to unfold or extend in a similar manner. Binding of multivalent Ca2+ and phosphate ions to sites on collagen molecules forming "sacrificial bonds" in bone were postulated to account for the observed recovery. Bone that had been soaked in Na+ did not show recovery in either tension or compression and served as a control in support of this postulate.

Individual bacteriorhodopsin molecules were first extracted from a membrane and then pulled to determine the unfolding pathways of the protein. Oesterhelt et al. [97] first imaged a native purple membrane to locate the bacteriorhodopsin molecules and then pushed the tip into the protein with ~1 nN of force. This was sufficient to extract the protein from the membrane and leave a vacancy where the protein once was. Subsequent force spectroscopy measurements on the protein revealed that the anchoring forces for the individual helices of the bacteriorhodopsin molecule ranged between 100 and 200 pN.

Specific attachment of terminal ends allowed for the resolution of unfolding pathways for individual helices.

Oberhauser et al. [98] designed a controlled load apparatus for single molecule mechanical testing that mimics mechanical testing on bulk samples. Their apparatus operates in a manner that directly probes the mechanical stability of elastic proteins. Mitsui et al. [99] designed a method for performing dynamic measurements as well as quasi-static measurements. During the force extension experiment, a sinusoidal excitation is applied to the molecule in the same manner as with macroscopic viscoelastic measurements for bulk polymers. This is important for mechanical studies on polymers and proteins that have a viscoelastic response since these properties can only be measured dynamically. With their approach, differences between random-coil polymers and proteins with high order structures can be deduced.

Li et al. [100-102] investigated "mechanical phenotypes," point mutations within the immunoglobulin molecule generated by protein engineering. They demonstrated a previously unrecognized class of phenotypes that may be common in cell adhesion and muscle proteins. Using protein engineering, Li and coworkers assembled new proteins from three identical repeats of I27-PEVK and showed that the unfolding of tandem modules follows the mechanical stability of the module. This finding enabled the use of the I27 module as a marker for the boundaries of the PEVK segment. With this marker, they were able to determine the persistence and contour lengths of the individual PEVK

molecules. Similar protein engineering techniques were used to examine the unfolding of spectrin. [103]

Clausen-Schaumann et al. examined the kinetics of force-induced melting and reannealing as well as the influence of ionic strength, temperature, and sequence on the mechanical properties of double stranded DNA (ds DNA). [104] They showed that when dsDNA is overstretched, it begins to melt into single strands that can recombine upon relaxation.

Green and Lee[105] have built on their development of tip arrays and tipless cantilevers for force spectroscopy by extending the technique to patterned tip arrays and patterned cantilevers. They use microcontact printing techniques to carefully functionalize a cantilever with both –OH and –CH3 functionality. They pattern the tip array in a similar manner and measure the contact forces. Their approach can be extended to probe intermolecular force information on large libraries of molecules.

Lo et al. [106] and Yuan et al. [107] have independently analyzed dynamic force spectra of biotin-streptavidin interactions over a range of loading rates. Both observed linear relationships between the unbinding force and the log of the loading rate. Two linear regimes in the dynamic force spectrum were observed, indicating that multiple energy barriers exist in the mechanical detachment of biotin from streptavidin.

Hugel et al. [108] investigated the response of single polyvinylamine chains of various line charge densities via single molecule force spectroscopy. They showed that the electrostatic contribution to polyelectrolyte elasticity diminishes under high mechanical stress. The detachment force of single polyvinylamine chains from the silicon oxide surface was a function of the polymer charge density and electrolyte concentration.

Krautbauer and coworkers[109] used single molecule force spectroscopy to characterize DNA-small molecule interactions. Binding of cisplatin and ethidium bromide to duplex DNA produced marked changes in its mechanical properties. Lioubashevski et al. [110] measured hybridization forces between PNA and DNA and detected single-base mismatches. The adhesion force between double-stranded PNA/PNA molecules was 1.8 times larger than double-stranded DNA/PNA. Cocco et al. [111] developed models for the mechanical unzipping of DNA under the conditions used in typical force spectroscopy experiments.

Schmitt and colleagues[112] presented a universal anchor system for high-affinity ligand-receptor systems based on N-nitrilo-triacetic acid (NTA) binding to His-tags. This binding pair requires the presence of a divalent cation. Thus, the molecular interaction can be blocked by addition of EDTA. Mechanical separation of this binding pair in the presence of various cations requires between 22 and 58 pN of force.

Marszalek et al. [113] used single molecule force spectroscopy to identify the components in mixtures of polysaccharides. Using the elasticity of the various

polysaccharides as a fingerprint, the force spectra obtained were related to the conformation of the pyranose ring and the type of glycosidic linkages. Their approach allows for the identification of individual polysaccharide molecules.

To measure the driving forces present during cell division, Matzke et al. [114] probed the stiffening of the cortex of adherent cultured cells along a single scan-line during their division. It was discovered via force mapping that cortical stiffening occurs over the equatorial region of the cell about 160 s before any furrow appears and that stiffening markedly increases as the furrow starts.

Oyama and co-workers[115] have analyzed the adhesion properties of cyclodextrins (CyDs) with various guest materials immobilized on a substrate. There was an observed change in the intermolecular interaction between cyclodextrins (CyDs) with guest materials as was detected via changes in the adhesive force. The adhesive force varied with each separate guest material.

Bowen and co-workers[116] measured the adhesion properties of single Aspergillus niger spores on mica substrates with SFM. A single spore was immobilized on the apex of the tip. The spore's adhesive characteristics depended upon environmental factors such as ionic strength and pH. Specific interactions between appendages and protrusions on the spore surface were postulated to play an important role in adhesion. Bowen et al. [117] used a similar technique to characterize the adhesive properties of metabolically active Saccharomyces cerevisiae cells at a hydrophilic mica surface. Dufrene et al. [118] have

used chemically modified probe tips (hydrophilic/hydrophobic) to characterize the adhesive properties of Phanerochaete chrysosporium spores. van der Aa and co-workers[119] have used force spectroscopy and microscopy to distinguish between dormant and germinating spores. Dormant spores exhibited no surface adhesion while the germinating spores exhibited adhesion forces up to 5.4 N/m. Adhesive interactions were attributed to the stretching of polysaccharides on the cell surface.

Dufrene et al. [120] correlated the adhesion of microbial cells with type of organism, physiological state and environmental conditions. Chen et al. [121] investigated ligand-receptor binding forces for receptors on the surface of fibroblast cells. Lee and co-workers[122] reported two-dimensional force mapping of human platelets adsorbed on a glass substrate under physiological buffer. Their results provide insight into the mechanism of platelet adhesion and aggregation, which play an integral part in hemostasis and thrombosis. Grandbois and co-workers[123] characterized a mixed layer of type A and O red blood cells based on the adhesive strength of a specific receptor-ligand pair. Adhesion maps afforded discrimination of these blood cell types.

Fiorini et al. [124] reported the first direct measurements of competitive binding interactions between an active enzyme (shikimate kinase) immobilized upon the tip and two ligands, one immobilized on the substrate (ATP mimic) and the second in free solution (Shikimic acid). Adhesion experiments were carried out in a competitive scheme with a blunt tip to maximize the number of interactions per rupture event. This technique shows great promise for creating a force spectroscopy-based screening method for enzyme inhibition.

The potential role of SPM in high-resolution epitope mapping of ligand-receptor binding was also evaluated. Kada and co-workers[125] probed the antigenic binding site of a ryanodine receptor in its physiological environment via force spectroscopic measurements and lateral force mapping. LFM images afforded localization of binding sites with nanometer resolution. Varying the loading rate in force spectroscopy experiments revealed a logarithmic dependence of the unbinding forces between the antibody-functionalized probe and the ryanodine receptor that ranged from 42-73 pN. The authors noted that highly oriented immobilized proteins are required for epitope mapping. Harada and co-workers[126] have investigated control of molecular orientation for mechanical testing of antibody-antigen binding using orientationally specific and random antibody immobilization schemes. Adhesion forces between horse spleen ferritin and the antiferritin Fab fragment of IgG for molecularly oriented molecules greatly exceeded those for randomly oriented molecules.

Chemical and Polymer Applications

Humphris et al. have presented a new force spectroscopic technique called transverse dynamic force microscope (TDFM) [127]. This approach allows one to monitor shifts in the cantilever drive frequency, phase and amplitude during a single pulling event. Lim and co-workers used sample modulation force spectroscopy to study the effects of tip roughness and geometry in the AFM measurements of solvation [128]. The sample-modulation response curves allow one to make a direct measurement of the interaction stiffness (force gradient) as a function of tip-sample distance, and this technique is

capable of measuring both repulsive and attractive solvation potentials in a single approach.

Kappl et al. [129] have presented a thorough review of colloidal probe force spectroscopic measurements. Zhang et al. has written a comprehensive review covering many of the force spectroscopic techniques that have been used to probe the local mechanical properties of polymers [130]. Akhremitchev et al. present a thorough review of the use of scanning probe microscopy in characterizing the function and aging of textured, minimally adhesive polymer surfaces [131]. Chen and co-workers have claimed to be the first to successfully measure the lateral Casimir force [132]. A full understanding of the Casimir force could play a large part in applying/utilizing this force in micro-scale devices.

Kudera et al. used single molecule force spectroscopy to investigate the mechanical properties of individual bis-terpyridine ruthenium(II) complexes [133]. Marszalek et al. observed the chair-boat transitions of a single polysaccharide molecule using force spectroscopy (183). Zapotoczny and co-workers measured the rupture forces of individual β-cyclodextrin (β-CD)-ferrocene host-guest complexes in an aqueous medium [134]. The observed rupture force for the host-guest conjugate was 55 ± 10 pN. Tivanski et al. have measured both conduction and adhesion forces simultaneously of a polythiophene [135].

During chemical force microscopy measurements between self-assembled layers of methoxy-tri(ethylene glycol) and methyl-terminated alkanethiols, Dicke et al. have shown that water is crucial for the stability of the surface charge that is associated with organic films and acts as a template for hydroxyl adsorption [136]. Zepeda et al. [137] have determined the energy barriers of alternative interfaces at variable temperatures. This exhaustive endeavor reveals an important role of solvation in many of the systems probed using chemical force microscopy.

Green has reviewed the recent progresses of using a new inverted AFM technique [138], which can carry out combinatorial atomic force microscopy [139]. Connell et al. used adhesion mapping to locate nanometer-scale oil droplets existing on a polystyrene surface [140]. Force curve mapping was used to gently probe the surface of the fluid droplets, and through automated analysis of the force curves, the true topography and microscopic contact angle of the droplets were determined. Eaton and co-workers utilized topographic imaging, adhesion force mapping, and indentation mapping to investigate the surface of an elastomeric filled silicone coating. Topographic observations revealed randomly distributed protruding features, which lead to a source of error when assessing the nanoscale stiction [141]. The source of peak broadening in the adhesion force histograms acquired in typical chemical force microscopy experiments was further characterized by Sato and co-workers on homogenous and non-homogeneous surfaces [142]. Akabori and co-workers have monitored the mechanical properties of a polystyrene film using lateral force microcopy while the film was subjected to a temperature ramp [143]. The authors were able to observe a thinning induced relaxation process, called surface β-relaxation.

Bliznyuk et al. investigated the surface glass transition temperature of several molecular weight films of polystyrene by studying the hysteresis in the loading-unloading cycles of force-distance curves [144]. Harmon and co-workers have measured the change in elastic modulus of hydrogel films as the films were gradually heated past their transition point [145]. They also performed the inverse of the previous experiment where a hydrogel sphere was affixed to the cantilever tip and its compressibility measured during its phase transition. Hodges has presented a very thorough review of AFM-based mechanical testing of polymer films in liquid environments [146].

Bunker et al. used an interfacial force microscope (IFM) to study the surface chemistry changes that occur during the photoactivated opening and closing of rings in tethered spiropyran monolayers [147]. This study demonstrated the ability of the IFM to probe differences in surface polarity, providing insight into the impact of surface charge on electrokinetic flow in microfluidic systems. Houston et al. reviewed the use of the IFM to characterize the adhesion, friction, and mechanical properties of self-assembled systems on gold surfaces [148]. Hugel et al. performed force spectroscopic measurements on a polymer composed of bistable photosensitive azobenzenes [149]. The polymers were exposed to ultraviolet light that induced lengthening and contraction of individual polymers through photo-induced switching the azo groups between their trans and cis configurations. The polymer was found to contract against an external force acting along the polymer backbone, thus delivering mechanical work.

Rabe and co-workers used atomic force acoustic microscopy [150] and monitored the amplitude and phase of the cantilever vibration as well as the shift of the cantilever resonance frequencies to interpret the local tip-sample contact stiffness and used this information to generate elastic maps of a surface. Benmouna and co-workers [151] have developed a unique imaging mode that is capable of measuring the thermal resonance of the cantilever as it travels above a latex surface. This approach provides topologically defined "maps" of the cantilever's resonance as it travels above a substrate. They have also used a similar setup to during themonitor the mechanical pulling of acrylic fibers [152].

Force Spectroscopy Theoretical Advances

In an effort to model the interaction of a solid colloidal probe with an incompressible liquid drop, Bardos presented a very rigorous theoretical interpretation [153]. His models avoid the pitfalls of both perturbation theory and of purely numerical solutions to the Young-Laplace equation. Bedrov et al. has performed molecular dynamics simulations of the mechanical pulling of poly(ethylene oxide) (PEO) chains in water and n-tridecane to elucidate the mechanism(s) of elastic response of the amphiphilic PEO chain in hydrophilic and hydrophobic environments [154]. The simulations quantitatively match AFM-based single molecule mechanical tests. Biesheuvel et al. has derived models describing the electrostatic repulsion between similar surfaces with ionizable surface groups interacting across aqueous solutions [155]. Butt et al. has theoretically treated the jump to contact point of a cantilever tip through a thin polymer film [156]. They have derived a relationship between the force dependence of the activation energy of the point

of initial snap down and the approaching velocity of the tip. Fraxedas and co-workers have presented a new model based on an equivalent spring constant that takes into account the changes in in-plane interactions during nanoindentation [157]. Their model correlates well with experimental data from nanoindentation of several crystalline surfaces. Patrick et al. [158] have used molecular dynamics simulations to provide a detailed description of the adhesive interactions that are probed in chemical force microscopy experiments. Their models take into account atomic-scale motions and distributions of forces. Dean et al. have developed molecular-level models for characterizing electrostatic interactions between polyelectrolyte brushes when explored using chemical force microscopy [159]. The relevance of these models to the modeling of native cartilage is discussed in detail. Dudko and co-workers have described a new model which predicts a distribution of forces, the mean rupture force and the variance during single molecule pulling experiments [160]. The mean rupture force follows a (InV)2/3 dependence on the pulling velocity, V, which differs from earlier predictions and have shown that at low pulling velocities a rebinding process can occur which can delay the rupture of the molecule and lead to a bimodal distribution of the observed rupture forces. Leng et al. [161] used a hybrid molecular dynamics simulation to investigate adhesion and friction in chemical force microcopy experiments. The hybrid simulation method allows one to simulate force-distance curves (or adhesion) and friction loops (or friction) in the CFM on the experimental time scale for the first time. Friedsam et al. have performed Monte Carlo simulations that demonstrate the severe impact that variable polymer spacer lengths can have on the mean rupture force that is observed during single molecule mechanical tests [162].

An exciting new and evolving application of AFM involves the manipulation of matter on the atomic scale. The AFM tip can be used to place, move, or react chemical moieties at specific locations on a surface. This can be achieved by frictional wear, controlled surface oxidation, and/or deliberate material transport between two surfaces. Material transport is unrestricted; atoms, molecules, or even cells can be attached to the AFM tip and transferred to the opposing surface at a desired location. In addition, thermal patterning of substrates can be achieved by contacting a heated cantilever tip with the surface. Potential applications include preparation of ultra-high density data storage devices, nanoscale sensors, and molecular machines.

In summary, scanning probe microscopy has revolutionized our understanding of chemical phenomena on the nanoscale. New applications of this important nanotechnological tool will make possible the manipulation of matter on the atomic scale and enable the construction of new materials and devices for the benefit of mankind.

CHAPTER 3

CANTILEVER FABRICATION AND CALIBRATION

Background

The original cantilever probe used by Binnig and Quate was a diamond tip that was fastened to a piece of gold foil [3]. Now, cantilevers are commercially available with ultra-sharp tips (typically a radius of curvature of around 5-10 nm) [9]. Most AFM cantilevers are fabricated from silicon, silicon dioxide and silicon nitride using silicon micromachining techniques. More recently polymeric cantilevers have been designed that could significantly decrease the cost of the cantilever probes [163,164]. Several methods have been reported regarding the fabrication of cantilevers with carbon nanotubes mounted on the apex of the silicon probe. These cantilevers provide extremely robust tips that are capable of reproducibly resolving ultra-small features. In the beginning of this chapter, a literature review of the methods of fabrication and calibration are presented, followed by an improved calibration method.

Fabrication

Recent progress has been reported in the fabrication and use of ultra-small cantilevers. Chand et al. [165] have fabricated gold cantilevers with integrated silicon tips that were 13-40 μm long. The shortest of these resonated at 0.5 MHz with a Q-factor of 100. Residual stress in the gold was relieved using rapid thermal annealing and thereby reducing the extent of cantilever bending. Hosaka and coworkers[166] fabricated cantilevers that were 7-20mm long having a maximum resonant frequency of 6.6 MHz.

They reported acquisition of images at scanning rates four orders of magnitude faster than normal scanning rates.

Yang and co-workers[167] fabricated ultrathin cantilevers from SIMOX wafers. These cantilevers are theoretically capable of detecting forces as small as 1.4 x 10-16 N in the first resonance mode. Even smaller minimum detectable forces are achievable when using higher resonance modes. McCarthy and colleagues[168] have demonstrated the utility of focused-ion beam (FIB) milling in creating thin cantilevers (below 1μm).

Fabricating cantilevers that possess integrated instrumentation on chip will significantly reduce the size of equipment required for scanning probe experiments. Heisig and co-workers [169] have designed a GaAs cantilever probe with an integrated vertical cavity surface emitting laser above the cantilever tip. This integrated design simplified the optical components of the SFM. Lee et al. [170] designed a single cantilever probe consisting of a small torsional resonator incorporated onto the end of the cantilever for improved force detection/actuation. The cantilever's fundamental resonance frequency was 49 KHz. The resonator was coated with a thin film of Pt-Cr and driven with an external magnetic field at 3 MHz. This approach reduced the minimum detectable force by two orders of magnitude relative to a conventional cantilever and substantially improved the signal to noise ratio necessary for ultrafast scanning. Kawakatsu and co-workers [171] have designed uniquely shaped probes that resonate in the gigahertz range. The oscillator has a tetrahedral or conical tip between 100-1000 nm in diameter supported by an elastic neck.

Hybrid scanning force and near-field scanning optical microscopy (NSOM) probes provide optical and topographical information about the underlying substrate. Dual functioning probes have been made by various micro-machining methods. [172,173] Recent emphasis has been placed on devising methods that create smaller and more reproducible aperture geometries. Focused-ion beam (FIB) milling is a high precision technique that can be used to create unique and reproducible silicon structures. Although a FIB milling tool is expensive and possesses low sample throughput, it is currently the best way to fabricate hybrid probes. Lehrer et al. [174] utilized FIB milling to create a reproducible aperture of less than 50 nm at the tip of a conventional SFM cantilever.

Significant advances in the design and application of microcantilever probes have been reported. Manning and coworkers fabricated piezoelectric tapping mode cantilevers that have an integrated oscillation drive mechanism on the cantilever [175]. Miyahara et al. reported a piezoelectric cantilever capable of simultaneous deflection sensing, cantilever oscillation and feedback actuation in non-contact mode AFM imaging [176]. Rogers and co-workers have fabricated piezoelectric probes capable of imaging in fluid [177]. Brook et al. created a unique piezoresistive probe that can carry out both topological and magnetic imaging [178]. This probe enables scanning Hall probe imaging of nonconducting or unconnected magnetic samples.

Grow et al. presented a simpler method for fabricating silicon nitride cantilevers with oxidation-sharpened tips. The height of the tip is taller than commercially available

nitride tips and is especially useful for imaging fragile samples that possess large topological relief [179].

Bale and Palmer have fabricated tip arrays that are suitable for parallel STM imaging applications [180]. Chow and co-workers [181] have addressed approach alignment and density issues associated with operating two-dimensional scanning probe arrays. They reported the fabrication and characterization of two-dimensional micromachined silicon cantilever arrays with integrated through-wafer electrical interconnects. With these arrays, a substrate domain as large as 3.8 mm x 0.45 mm can be imaged.

Several reports of probes specifically designed for the acquisition of optical information about substrates appeared. For example, Aigouy and co-workers attached a fluorescent, rare-earth-doped fluoride glass particle to the end of an AFM tip [182]. When this probe was scanned over the surface of a nanostructured sample illuminated by a laser beam, the intensity of fluorescence from the particle is then recorded as a function of the position. This method enabled them to map the location of pinhole defects in opaque films. Crozier et al. [183] fabricated a silicon nitride solid immersion lens onto a cantilever beam. This probe was used for scanning optical microscopy and was capable of achieving optical resolution l/(2n) where n is the refractive index of the nitride lens.

Lee, Ding and Bard [184,185] reported the first successful simultaneous topographic and optical imaging of a living unicellular organism using a novel probe tip. The tip, consisting of an optical fiber core, a gold ring, and an insulator, served as an

ultramicroelectrode for scanning electrochemical microscopy (SECM) and as a light source for optical microscopy when coupled to a laser. Images were acquired in either constant force or constant current mode. Improved lateral resolution for both optical imaging and SECM imaging was achieved in using a constant current while maintaining a fixed distance between the tip and the sample. This technique enables simultaneous electrochemical, optical, and structural information about interfaces.

Hughes and co-workers created nanoscale cantilevers composed of zinc oxide [186]. Extremely small forces could be measured using cantilevers of this size once a means for force/deflection transduction is realized. Similarly, chromium nanocantilevers were fabricated and mechanically tested with an AFM probe [187].

Lee and co-workers [188] fabricated a novel probe for integrated AFM-mass spectrometry. The cantilever acts as the force sensor for topological imaging and the tip acts as a sampler for chemical analysis by time-of-flight mass spectrometry. As the tip in contact with the sample scans across the surface, chemical compounds from the surface adhere to it. At a desired location, the tip is raised via the integrated piezoelectric actuator into a position near an extraction electrode. Application of a potential pulse between the tip and the extraction electrode results in ionization and acceleration of the tip-adherent chemicals into the time-of-flight mass analyzer. The mass spectrum provides identification of the tip-adherent molecule(s).

Polymeric Cantilevers

Experimentally induced tip-crash generally requires manual replacement of the cantilever probe. Genolet and co-workers [189] have designed multiple, single-lever probes arranged in a cassette format. The cassette consists of a one-dimensional array of photoplastic cantilevers with integrated tips. The first cantilever is used for imaging while the others are available if the first one becomes degraded. A worn-out cantilever can be replaced with a fresh one by only small positional adjustments and without any changes in the operating conditions.

Genolet et al. [190] produced a hybrid probe that consists of a micromachined polymeric tip with an aperture at the apex that is attached to an optical fiber. This probe takes advantage of the reproducibility of batch fabrication processes for micromachined tips and the well-characterized light guiding characteristics of optical fibers. Extremely small probes have been fabricated without any post processing steps. Topographical and optical imaging with the probe demonstrates the great potential of the photoplastic probe for NSOM applications.

Recently McFarland et al. devised a simple fabrication scheme for the creation of polystyrene cantilever using a solvent-casting approach [191].

Nanotube-tipped Cantilevers

Carbon nanotubes have the potential to be ideal SPM probes due to their unique properties including small diameter, high aspect ratio, large Young's modulus and

mechanical robustness. The nanotubes can also be chemically functionalized leading to advanced chemical and biological mapping studies. The use of nanotubes as probes for SPM has gained momentum in the last three years. Hafner et al., [192] pioneers in the field of using carbon nanotubes as SFM probes, wrote an excellent review of their use in structural and functional imaging. This review covers the topics of the fabrication, structural and mechanical properties, characterization of the tip, resolution, applications, functional imaging and force spectroscopy.

Nanotube tips can be fabricated in a variety of ways. Cheung et al. [193] have grown single-walled nanotubes (SWNTs) directly on the tip via a surface growth chemical vapor deposition method. The tips can also be used in SWNT lithography where SWNTs are patterned on a substrate by peeling them off an SFM tip. Other fabrication techniques include picking up vertically aligned SWNT from a silicon surface[194] and using an arc discharge to transfer multi-walled nanotubes (MWNTs) to the SFM tip. [195]

Nanotube probes are mechanically robust, maintain their lateral resolution and are readily functionalized.13, [192,196,197] Akita et al. [198] have fabricated a nanotweezers consisting of MWNT ~2.5 mm long separated by 780 nm. A DC voltage applied to two electrodes causes the nanotubes to be electrostatically attracted to each other, closing the nanotweezers. Nanotube tips are sharp yet "gentle," providing images of biomolecules and bio-assemblies with resolution comparable to cryogenic electron microscopy. Some of the biological systems examined include: RecA-DNA, [199] mono- and polynucleosomes,21 IgG, [200] IgM, [192] GroES, [200] and amyloid-b fibrils.13

Woolley et al.23 developed a method for multiplexed detection of polymorphic sites and direct determination of haplotypes in DNA fragments. With this technique it is possible to detect single nucleotide polymorphisms in sequences up to 10,000 bases.

Several methods were reported for fabricating nanotube-tipped AFM probes [201-203]. Nishino et al. [204] immobilized carbon nanotubes onto a gold-coated STM tip. Images acquired with these showed increased spatial resolution and afforded chemical discrimination of oxygen functionality present on the substrate surface. Snow and co-workers examined the factors that influence topological imaging with carbon nanotube-tipped probes [205].

Calibration Methods

Current Approaches

Atomic force microscopy (AFM) has become an invaluable metrological tool for science and technology enabling researchers to characterize surface topology on the nanometer scale and visualize the orientation and spatial distribution of molecules adsorbed to surfaces. [19] AFM also has been used to measure the mechanical properties of single molecules, molecular ensembles, and surface structures as well as adhesive interactions between chemically modified tips and a substrate. Knowledge of cantilever beam stiffness (spring constant) is required for proper interpretation of images acquired under constant force and for extracting the mechanical properties of samples from force curve data.

Several methods for determining cantilever beam stiffness have been presented, each with advantages and limitations. [206] Cleveland's method involves measurement of the resonance of the beam before and after loading it with a known mass. [207] Although highly accurate, this method is tedious, time consuming and can lead to damage of the cantilever tip. Gibson and Watson, as well as Tortonese and Kirk have developed a "beam on beam" approach, where the cantilever is brought into contact with a calibrated standard cantilever beam. [208,209] The accuracy of this straightforward method is limited by the certainty to which the reference beam stiffness is known, the positioning of the tip onto the end of the reference beam, and the calibration of the photodiode sensitivity and scanner vertical movement. A third method involves measurement of the dimensions of the beam and calculation of its stiffness assuming a known density and Young's modulus using the following equation for a rectangular cantilever with a rectangular cross section

$$k = \frac{Ewt^3}{4l^3} \qquad \text{Equation 3.1}$$

where k is the spring constant, E is the Young's modulus of the beam and w, l, and t are the beam width, length, and thickness, respectively. The simplicity of this method serves as the basis for its widespread popularity. A fourth method (referred to as Sader's method) involves measurement of the thermal resonance spectrum of the cantilever and fitting a simple harmonic oscillator model to it. [210-212] The thermally driven resonance of a cantilever can be acquired by mounting a cantilever in an AFM, aligning the laser spot on a sebmented photodiode and then monitoring the fluctuations of the light on the detector (Figure 3.1). Using a dynamic signal analyzer, the voltage signal from the

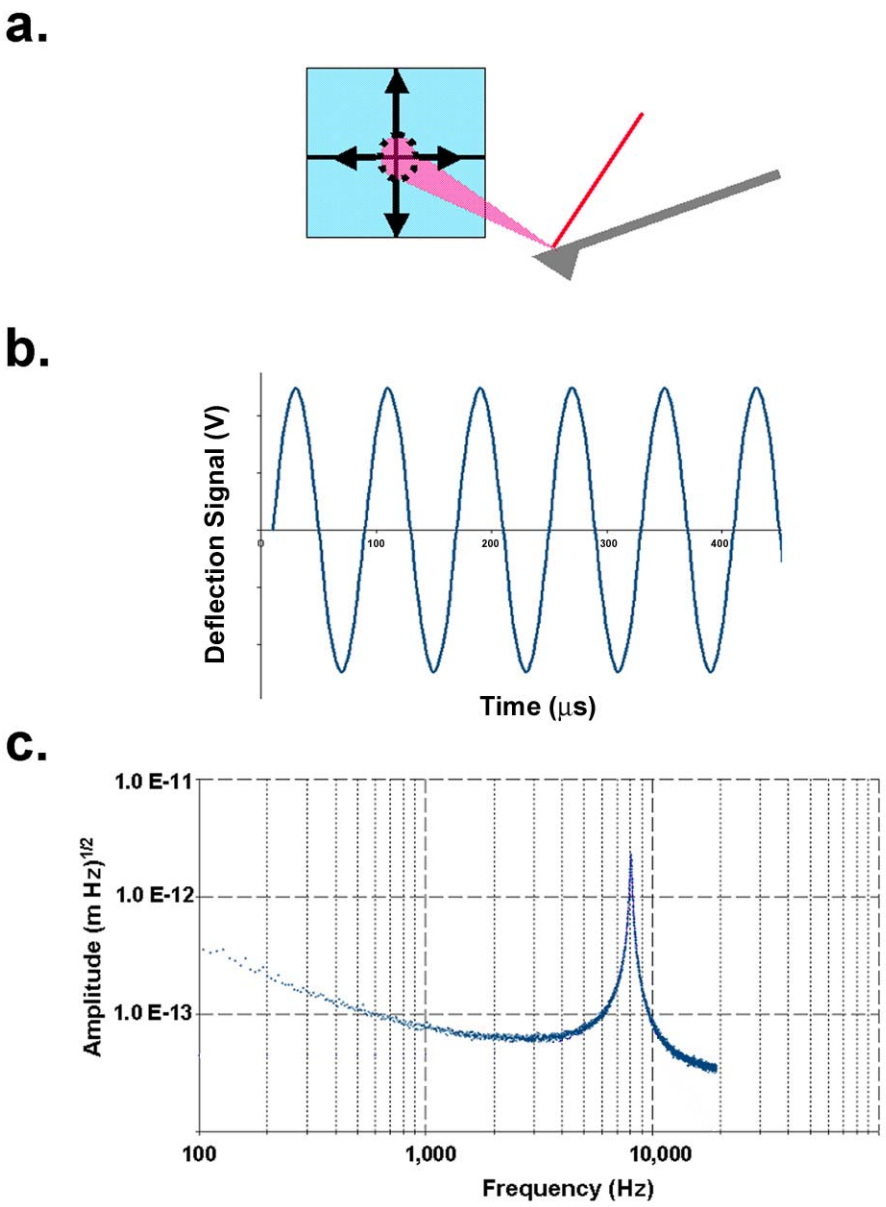

Figure 3.1. (a) Schematic of laser light reflecting off of a cantilever and onto a position sensitive detector. (b) Schematic depicting the variance of the voltage signal coming off of the detector as a function of time from a cantilever under thermal oscillation. (c) Raw power spectral density plot (blue) of a silicon cantilever oscillating in air.

PSD is passed through a fast Fourier transform (FFT). The transform yields the resonant spectra of the cantilever, where the cantilever has a defined resonance, amplitude and quality of oscillation (peak sharpness). Sader's method can be used to approximate the beam stiffness using the following equation:

$$k = 0.1906 * \rho_f * w^2 * l * Q_f * \Gamma_i\left(f_f\right) {f_f}^2 \qquad \text{Equation 3.2}$$

where ρ_f is the density of the fluid, w is the width of the cantilever, l is the length of the cantilever, Q_f is the quality factor in fluid, $\Gamma_i(f_f)$ is imaginary component of the hydrodynamic function and f_f is the primary resonant mode of the cantilever in fluid.

A fifth method (initially devised by Hutter and Bechoefer [213] and then refined for higher vibration modes by Butt and Jaschke [214] models the energy dissipation of a cantilever resonating freely in space. This model fits a Lorentzian to the power spectrum of the cantilever beam's vibrational energy. The refined version of this fit, takes into account the higher vibrational modes of the beam (Figure 3.2). The amplitude of the beams oscillation is determined via the following equation:

$$A(f) = C_0 + \frac{C_1}{f^{C_2}} + A_{DC} f_0^2 \left[\left(f_0^2 - f^2\right)^2 + \frac{f_0^2 f^2}{Q^2} \right]^{-\frac{1}{2}} \qquad \text{Equation 3.3}$$

where C_0, C_1, and C_2 are constants, A_{DC} is the DC amplitude, and Q is the beam and quality. This models a constant (white) noise floor, a second term to model so-called one-over-f (1/f) noise, and a simple harmonic oscillator (SHO) term. Then, the mean-square displacement of the beam is calculated:

$$\left\langle A^2 \right\rangle = \int \left[A(f)\right]^2 df \qquad \text{Equation 3.4}$$

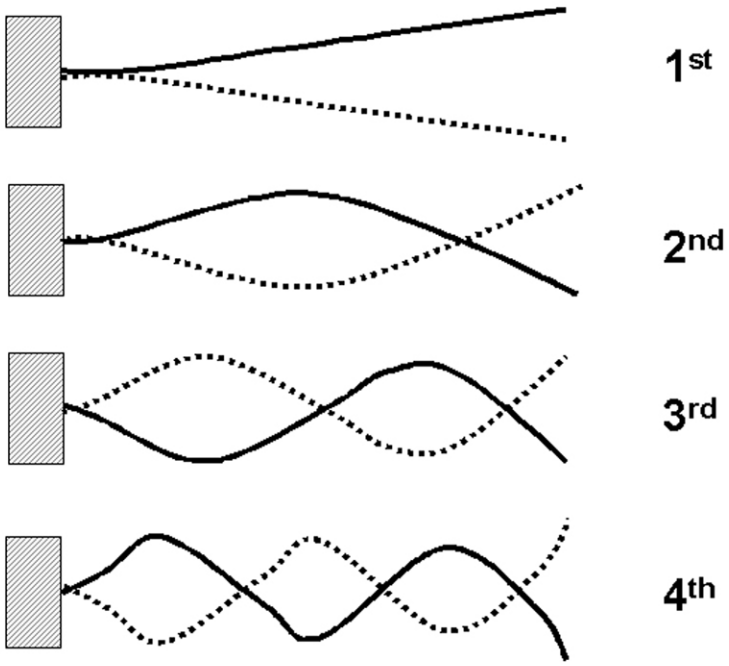

Figure 3.2. The first four vertical oscillation modes of a cantilever beam

Finally, the stiffness of the beams can be determined via equation 3.5:

$$k = \frac{k_B T}{\frac{3}{4}\left\langle A^{*2} \right\rangle} \qquad \text{Equation 3.5}$$

where k_b is the Boltzmann's constant and T is the temperature (in Kelvin). This method requires that a calibrated load be exerted on the cantilever beam (typically carried out by using the calibrated piezo-scanner) [213]. Both of these methods provide estimates of the spring constant, k, and quality factor, Q, of the beam. The theoretical foundation of several of the previously discussed methods assumes a cantilever beam with a rectangular cross section. Burnham and co-workers have commented on the advantage and disadvantages of many of these methods. [206]

New methods for determining cantilever spring constants under fluid have been developed. Maeda and co-workers [215] presented a semi-empirical relationship between the deflection of a cantilever under a point load and the same cantilever under laminar flow. This relationship enables in situ determinations of cantilever force constants and demonstrates that the hydrodynamic contribution to cantilever deflection is linear with speed, independent of tip size and position, and scale invariant. Craig and co-workers [216] have extended this work to include attachment of colloidal particles on the tip. Degertekin et al. [41] have devised a novel method to actuate AFM cantilevers in fluids via focused acoustic waves. This technique can be used to measure the spring constant and resonance frequency of various AFM probes. The frequency response is determined by the bandwidth of an acoustic transducer/Fresnel lens system.

Cain and co-workers [217] developed a method of force calibration for a lateral force microscope. By using spheres of different radii, the effects of contact stiffness can be isolated and an absolute force calibration achieved in terms of measured beam deflections. The method does not rely on any particular model of contact mechanics and extends the capability of lateral force microscopy (LFM) to quantify frictional forces between arbitrary materials.

Improved Stiffness Calculation

High-resolution imaging applications require tips with a small radius of curvature. AFM probe manufacturers now use dynamic micromachining techniques after the beam and the tip have been lithographically defined and etched to produce high aspect ratio tips. The dynamic etch process modifies the shape of both the tip and the cantilever. Dynamic etching of a rectangular beam produces a cantilever with a trapezoidal cross section; [218,219] triangular-shaped cantilevers are similarly effected. [179] Since several of the methods delineated above assume uniform cross-sections, significant error results when using these to determine the spring constant of the cantilever with a sharpened tip (e.g., FESP probes from Veeco Metrology, Golden probes from NT-MDT, and most of the rectangular probes from MikroMasch) [163,164,220]. A straightforward method to determine the spring constant of the beam based on knowledge of the true geometry of the cantilever and its measured resonance has been devised.

The following portion of this chapter involves the use of a modified cantilever calibration approach. The results of this work address some of the shortcomings of many of the

calibration techniques that were previously mentioned. The stiffness calibration reported here is also used in several of the experiments reported in Chapters 6 and 7.

Experimental

Cantilevers fabricated from single crystal <100> silicon wafers were obtained from NanoDevices and Veeco Probes. The geometry of cantilevers with sharpened tips was determined by scanning electron microscopy. Cantilever chips were mounted onto standard aluminum specimen mounts (Ted Pella) pretreated with a small amount of Aquadag colloidal graphite (Ted Pella). Images were acquired with a Hitachi Model S-800 scanning electron microscope (SEM). Distances measured in the SEM were accurate to within ±10%. A Nanoscope IIIa scanning probe microscope (Veeco Metrology) in "Extended Mode" equipped with a signal access module (SAM) and a SR785 Dynamic Signal Analyzer (Stanford Research Systems) were used to monitor/acquire the thermally driven power spectrum of the cantilever beams natural motion.

Results and Discussion

Figure 3.3 presents a set of images acquired on a FESP cantilever probe and is typical of those obtained on all probes examined. Clearly visible in these images is the trapezoidal cross section of the beam. Ten different beams from two different manufacturers and five different fabrication batches were examined. Careful inspection of the images and cantilever dimensions reveals a high degree of uniformity among cantilevers from different manufactures and fabrication batches. The average ratio of the bottom face to

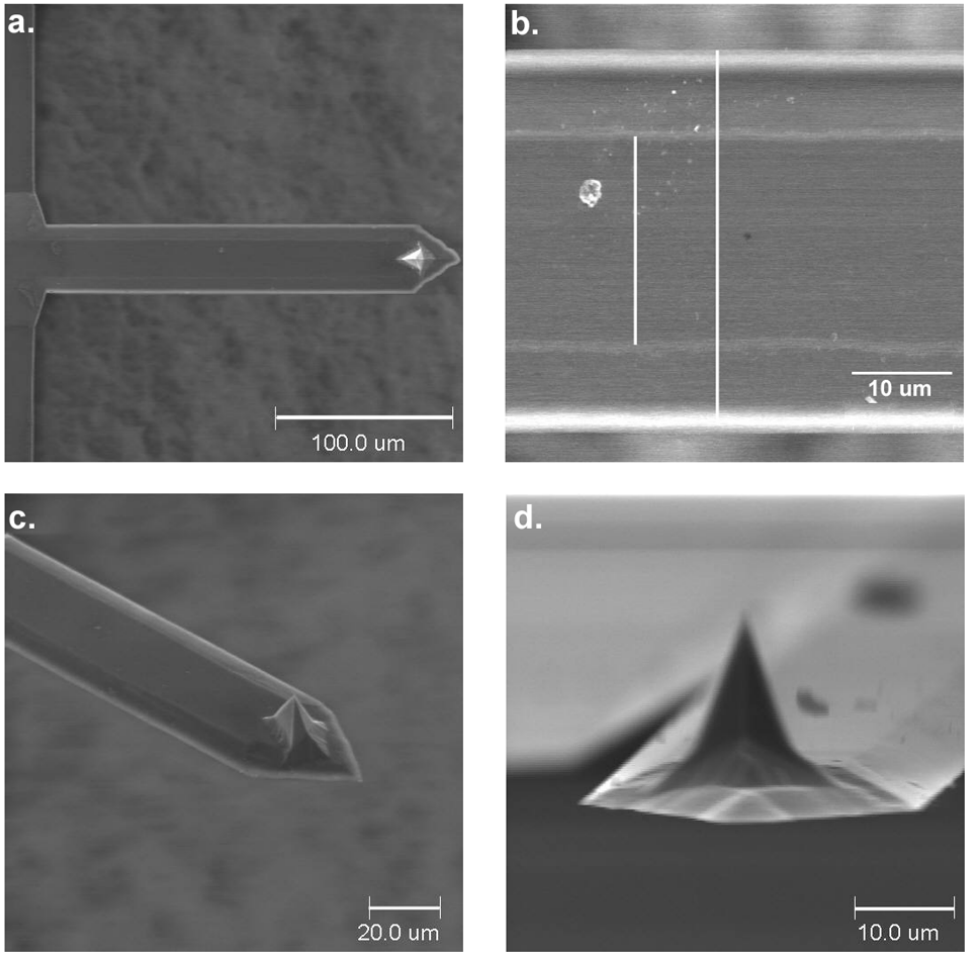

Figure 3.3. SEM images of several FESP probes fabricated by Veeco Probes. (a) Top-view of the entire cantilever beam (b) an increased magnification of the beam in (a) showing the two apparent widths of the beam (marked in white) (c) and (d) angled views of a cantilever probe showing the trapezoidal cross-sectional shape.

the top face (tip side) of the beam was 1.69 ± 0.15. The incline angle from the bottom face to the top face was on average 22.3 ± 1º.

From Euler-Bernoulli beam theory [221], the stiffness, *k*, of rectangular beams with trapezoidal cross sections is proportional to I, the second moment of its cross sectional area

$$k = \frac{3EI}{l^3} \qquad \text{Equation 3.6}$$

Where *I* for a beam with a rectangular cross-section is:

$$I = \frac{t^3 w}{12} \qquad \text{Equation 3.7}$$

Geometrically, the second moment of a beam with a trapezoidal cross section, $I_{trapezoid}$, [222] [Appendix for derivation] is:

$$I_{trapezoid} = \frac{t^3\left(a^2 + 4ab + b^2\right)}{36(a+b)} \qquad \text{Equation 3.8}$$

where *t* is the beam thickness, *a* is the width of the top face (tip side) of the beam, *b* is the width of the bottom face (see Figure 3.4). Stiffnesses for ten beams were determined based on the Euler-Bernoulli model (eqn 3.6 and 3.8) and an elastic modulus[218] of 130 GPa and are presented in Table 3.1.

The fundamental resonance mode of the beam, *fo*, is related to its stiffness by

$$f_o = \left(\frac{\alpha_i}{L}\right)^2 \sqrt{\frac{EI}{\rho A}} = \frac{1}{2\pi}\sqrt{\frac{k}{0.2427 * m}} \qquad \text{Equation 3.9}$$

where *m* is the mass of a free cantilever beam oscillating in space [7]. The effective mass of the beam is a function of the density of the silicon as well as the volume of the beam

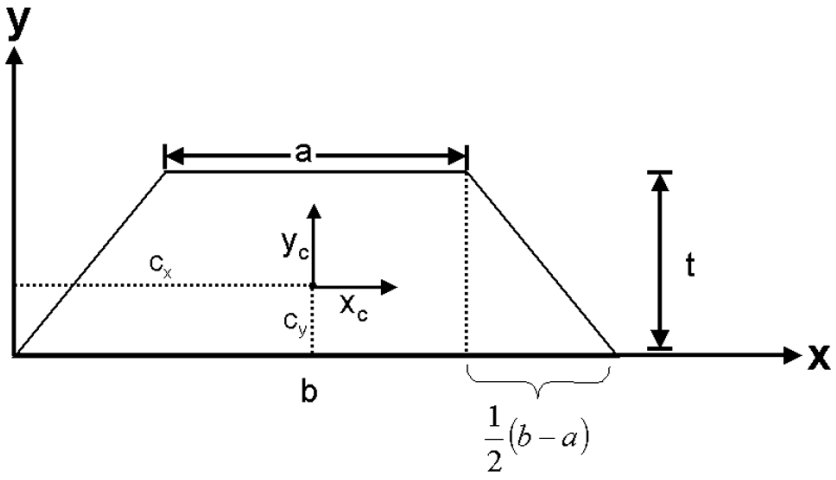

Figure 3.4. Graphical depiction of the location of the center-of-mass of a trapezoid and the corresponding measurable lengths where *a* is the width of the top portion of the beam (tip-side), *b* is the width of the bottom portion, *t* is the beam thickness, the point (c_x,c_y) represents the center-of-mass of the trapezoid.

(function of beam geometry). Calculated values of f_o (using a density[218] for silicon of 2.33 g/cm^3) also are listed in Table 3.1.

To account for dampening in air, the calculated (or modeled resonance with air dampening) was calculated using the approach reported by Chon et. al [223] is:

$$f_{air} = f_{vac} * \left[1 + \left(\frac{\pi * \rho * t}{4 * \rho_c * l} \right) \right]^{-1/2} \qquad \text{Equation 3.10}$$

where f_{air} is the primary resonant mode of the cantilever in air, f_{vac} is the primary resonant mode of the cantilever in vacuum, ρ is the density of the fluid environment that the cantilever resides (ρ_{air} = 1.18 kg/m^3) [223], t is the beam thickness, ρ_c is the density of the cantilever (ρ_c = 2330 kg/m^3) [218] and l is the length of the cantilever.

The calculated values compare favorably with measured values (~ average difference of 2%). The small difference between the computed and observed resonance frequencies is likely due to the unaccounted mass of the tip.

To estimate the impact of calculating beam stiffnesses for cantilevers with sharpened tips using the rectangular cross section model (method #3 and equations 3.6 and 3.7), the base width of the trapezoid was used as the width of the beam. Computed stiffness values ranged from 15 to 25% larger than the stiffness calculated for a trapezoidal moment (equations 3.6 and 3.8) (Table 3.2). Thus, the widespread use of method #3 for

Table 3.1. Summary of the dimension of ten different cantilever beams that were characterized from five different fabrication batches. The resulting stiffnesses for each beam as well as their measured and simulated resonant frequency.

Cantilever #	Beam Length (μm)	Beam Width *top* (μm)	Beam Width *bottom* (μm)	Beam Thickness (μm)	I (2^{nd} Moment of Inertia)	Spring Constant* (N/m)	Observed Resonant Frequency (Hz)	Calculated Resonant Frequency** (Hz)
1	249.6	23.8	41.3	3.49	1.13E-22	2.82	67,800	66,399
2	247.1	19.4	35.9	3.47	9.34E-23	2.42	67,184	67,262
3	210.2	28.7	40.5	2.56	4.79E-23	2.01	69,569	68,961
4	205.9	19.5	34.8	3.25	7.56E-23	3.38	92,700	90,854
5	206.4	21.7	36.2	2.68	4.55E-23	2.02	78,252	74,628
6	206.4	20.2	33.5	2.64	4.03E-23	1.79	75,632	73,562
7	211.2	20.8	37.4	3.67	1.17E-22	4.83	98,456	97,463
8	208.2	28.8	42.8	2.62	5.30E-23	2.29	72,456	71,867
9	210.2	21.8	38.8	3.43	9.92E-23	4.17	96,200	92,011
10	206.4	19.8	36.7	3.28	8.06E-23	3.58	92,200	91,069

* A relative uncertainty of 15% is found from a propagation of error calculation
** This reported frequency also take into account the dampening induced in air

Table 3.2. Comparing the stiffnesses of the same beam that are derived from using a trapezoidal moment, a rectangular moment, and Sader's Method (equation (3.2))

Cantilever No.	$k^*_{trapezoid}$	$k^*_{rectangle}$	k_{Sader}
1	2.82	3.66	2.34
2	2.42	3.24	3.39
3	2.01	2.38	3.39
4	3.38	4.45	5.18
5	2.02	2.58	2.79
6	1.79	2.28	2.28
7	4.83	6.37	6.38
8	2.29	2.77	4.03
9	4.17	5.48	6.05
10	3.58	4.79	5.31

* Beam stiffnesses calculated via equation (3.6) using either a trapezoid or a rectangle as the second moment of the beam's cross sectional area.

cantilevers of this type results in a substantial and systematic overestimate of the spring constant, the magnitude of which scales with cantilever thickness.

Conclusions

In light of these findings, interpretations of force-based measurements acquired with cantilevers having non-rectangular cross-sections whose spring constants were determined using method #3 should be reevaluated. In comparison with Sader's method, significantly different stiffnesses were determined. Thus, Sader's method needs to be used with caution when approximating the stiffness of AFM cantilevers. Other methods that assume a uniform width may also require the corrections delineated herein.

In summary, this new approach of carefully characterizing the cross-sectional geometry of a cantilever beam can have a large impact on calculated cantilever beam stiffnesses. The presented approach accounts for the nonrectangular cross-section of the cantilever beam that results from dynamic etch processes currently used to sharpen the probe tip. The current practice of computing beam stiffness assuming a rectangular cross section results in a gross overestimation of the actual value. Provided that the cantilever manufacturers can provide researchers in the SPM field with reliable elastic moduli for the silicon that the cantilevers are fabricated from, this geometrical method would only require that the dimensions of the cantilever be accurately determined.

CHAPTER 4

CARBON NANOTUBES

MULTIWALLED AND SINGLE WALLED CARBON NANOTUBES

Carbon nanotubes, first discovered by Sumio Iijima [224], are cylinders only composed of graphitic carbon. Single walled carbon nanotubes (SWNT) have diameters as small a 3 nm and can be several microns in length. Multiwalled carbon nanotubes (MWNT) are comprised of several concentric carbon cylinders (Figure 4.1). Their diameters are proportionate with the number of walls and can span a range from 4 to 30 nm. The lengths, like SWNTs, can be several micrometers long.

Carbon nanotubes exhibit very high thermal and electrical conductivities and have a tensile modulus outmatching steel [225]. This unique combination of properties has spawned a global research effort in nanotube applications in composites, chemical sensors, logic gates and drug delivery [226,227]. In this chapter, nanotube synthesis, characterization of properties and applications will be reviewed.

Synthesis

Several methods for creating carbon nanotubes have been developed. Arc-discharge, laser ablation and chemical vapor deposition (CVD) are the three main methods for fabricating SWNTs and MWNTs [228]. Both arc-discharge and laser ablation require solid-state carbon precursors and these processes involve the vaporization of carbon at thousands of degrees Celsius. CVD requires hydrocarbon gases as the carbon source and

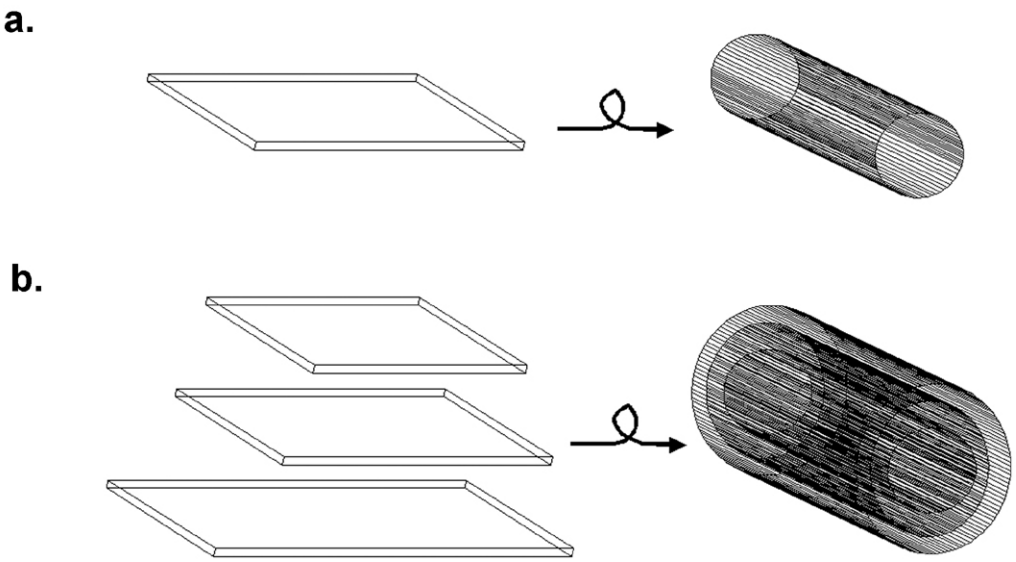

Figure 4.1. (a) Cartoon depicting the formation of a single walled carbon nanotube from a single sheet of carbon atoms rolled into a cylinder. (b) Cartoon depicting the formation of a multiwalled carbon nanotube from a multiple sheets of carbon atoms rolled on top of one another.

metal particles to act as catalysts. CVD can be carried out at significantly lower processing temperatures (500 - 1000°C) [229].

Recently Smalley and co-workers have devised a process that provides substantially higher yields and purity levels of nanotubes [230,231]. This process, coined the "HiPco Process" uses iron pentacarbonyl as the catalyst source and carbon monoxide (CO) as the carbon source. At the relatively high temperatures and pressures (~1000°C and 40 atm, respectively), $Fe(CO)_5$ decomposes and acts as nucleation sites for the growth of the carbon nanotubes. Solid carbon is produced from the CO feedstock via the Boudouard reaction:

$$CO_{(g)} + CO_{(g)} \xrightarrow{Fe(CO)_5} C_{(s)} + CO_{(2)(g)}$$

The solid carbon nucleates at the iron site and forms a uniform lattice structure. This process is capable of yielding approximately 10 grams of nanotubes per day.

It has been estimated that the global production of carbon nanotubes to date has been approximately 10 lbs. Each method for preparing carbon nanotubes can be characterized by the purity and yield of the nanotubes obtained (# of nanotubes vs. amount of catalyst vs. byproducts). The typical purity of carbon nanotube synthesis can range anywhere from 30 to 90%. Thus, improved synthetic routes must be developed if devices requiring a high purity of nanotubes are to be realistically designed and marketed.

A single nanotube's diameter, mechanical and electrical properties have been shown to be dependent on the orientation of the hexagonally packed carbon atoms relative to the longitudinal axis of the tube [[232-238]]. The orientation of the carbon atoms on the nanotube's axis is referred to as chirality and can be determined by establishing a vector on a graphene plane and wrapping the tube about this vector (see Figure 4.2). The chiral indicies (a_1, a_2) of a nanotube are determined from a vector that is drawn from a reference point (0,0) on the nanotube's backbone to another point on the nanotube's backbone. The lattice vector is established by drawing a line from the reference point (0,0) to another indicie on the graphene plane (9,$^{-}$5), (7,0) or (2,5). Then the graphene sheet is folded along one of these the lattice vectors. As a result, the carbon atoms will be arranged in either a symmetric (Figure 4.2b), positive (Figure 4.2c) or negative (Figure 4.2d) twist around the axis of the tube. A nanotube's chirality is typically determined via STM and Raman spectroscopy [239]. It has been shown that the chirality of a nanotube will influences its electronic conductivity: metallic or semiconducting [225,240].

Proposed Nanotube Uses

As alluded by de Heer [241] there has been a significant amount of "hype" involving the commercialization of nanotube-based materials and devices. To date however, there is only one known commercial product that utilizes carbon nanotubes. Hyperion Catalysis Interantional Inc. markets a composite material with, unfortunately, only marginally enhanced mechanical properties.

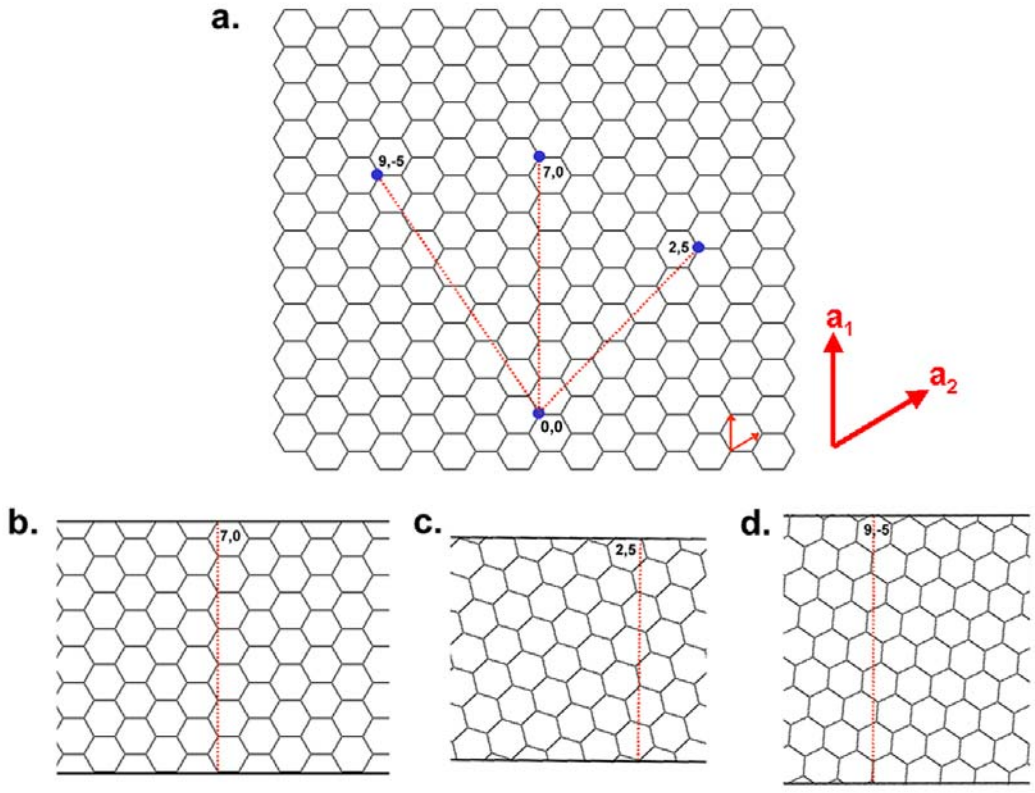

Figure 4.2. (a) Graphene sheet with three different orientation vectors drawn illustrating positive, negative and neutral chirality. Wrapping the graphene sheet around each vector individually, yields a nanotube with a specific diameter and a particular orientation of the carbon atoms about the linear axis of the nanotube (b) symmetric (c) positive and (d) negative twist.

Fundamental research is needed for development of many of the proposed applications, especially as components in devices. For example, promising nanotube applications in the semiconductor industry involve the use of carbon nanotubes in ultra-small logic gates. If possible these devices would be considerably smaller than the transistors that are created via silicon micromachining techniques[242-247]. Also, nanotubes are attractive from a packaging standpoint; since the nanotubes are extremely robust, their incorporation into packages would provide increased strength and improved thermal management. Thus, the finished products could be more robust.

Nanotubes have also been proposed as active sensing elements in chemical sensors [248-252]. For example, specific analytes in solution have been detected in solution by monitoring electron transport through the nanotube [248-250,252].

Carbon nanotubes are highly suited as fillers in composites. They are extremely strong, both thermally and electrically conductive, and coupled with their lightweight, suggest other applications of polymeric composites. A nanotube filled composite is analogous to concrete reinforced with re-bar. Re-bar acts as a structural stabilizer for the concrete so that that composite can bear larger loads and withstand larger shearing forces [253]. Typical polymeric composites utilize polymers and some type of "filler" material such as carbon black, metal particles, etc. [254].

Aerospace engineers are interested in using carbon nanotubes for space applications. It has been extremely difficult to tailor composites that can handle transport into space;

nanotube composites show promise [255]. A common problem in space is that there is no electrical "ground". Instrumentation can build up significant levels of static charge that cannot be dissipated. This leads to device failure [255]. The high electrical conductivity of nanotubes suggests their use in composites for dissipation of static charge.

Nanotube-based composites have been prepared; albeit with extensive aggregation and little control over their orientation [225,256-259]. Ideally, if the nanotubes dispersed perfectly into the polymer, there would be no mechanical defects and the bulk composite would have uniformly enhanced mechanical and electrical properties. This is illustrated in Figure 4.3.

To increase the dispersal of the nanotubes in the polymer researchers have chemically modified nanotubes in hopes of reducing aggregation. The dispersions of the tubes have been enhanced using this approach, but electron transport is significantly reduced [260-263]. Chemical modification results in a change in the hybridization of the carbon in the nanotube from sp^2 to sp^3. This modification significantly reduces the electron transport properties of the nanotube. However, composites made in this fashion would be appropriate for applications where electrical conductivity is not desired (i.e. strictly a reinforcing agent).

Research is ongoing to find ways to disperse nanotubes without covalent modification [264,265]. If polymers can be tailored to enhance the dispersal of the nanotubes and not

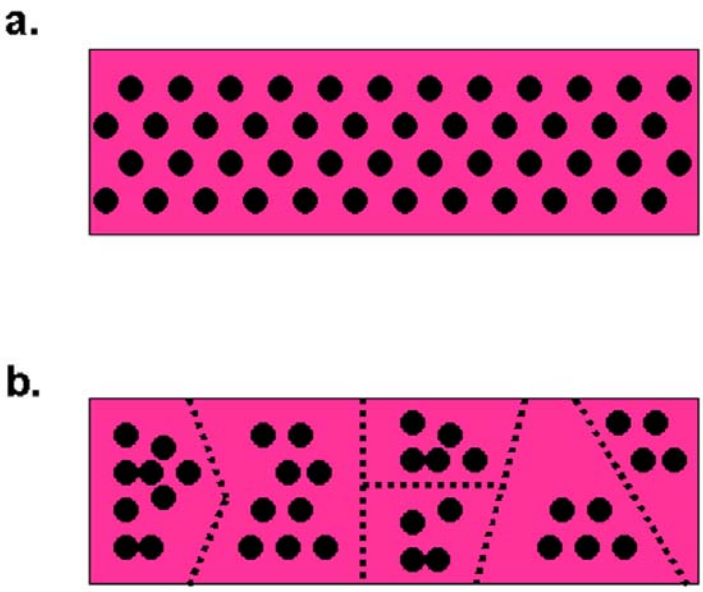

Figure 4.3. (a) Cross-sectional view of an ideal dispersal of nanotubes into a polymer. (b) typical dispersion of nanotubes into polymers which leads to defect areas (dashed lines)

sacrifice their conductive properties, viable composites for space applications will become a reality.

Characterizations of Nanotubes

Several analytical techniques have been used to probe the chemical and physical properties of carbon nanotubes. Many of these techniques and the chemical/physical they provide are summarized in Table 4.1. As noted in the table, the scanning probe microscope has proven to be the best tool in this endeavor. The remaining pages of this chapter are excerpts pertaining to the characterization of nanotubes from the reviews I have co-authored and presented. The intent is to demonstrate the power of the scanning probe microscope in characterizing the chemical, structural, and mechanical properties of SWNTs and MWNTs.

STM/STS Characterizations of Carbon Nanotubes

Odom et al. [266] and Ouyang et al. [267] performed a thorough investigation of their structural and electronic properties. This work is the basis for the advanced studies presented in the following paragraphs.

Ouyang et al. [268,269] significantly advanced the characterization of SWNT via STM and scanning tunneling spectroscopy (STS). First STM and STS were used to image and characterize junctions on individual SWNT. The atomic structures and electronic properties of metal-semiconductor and semiconductor-semiconductor junctions on individual SWNT were resolved. Spatially resolved STS spectra were obtained across a

Table 4.1 Analytical techniques that are used to characterize the various properties of carbon nanotubes

Analytical Technique(s)	Nanotube Properties	References
Temperature programmed desorption, IR spectroscopy	*bulk molecular binding*	[270-278]
Raman scattering	*degree of ordering of the nanotubes, the ratio of sp^2 to sp^3 bonding and the size of graphitic crystallites in the bulk material*	[279-281]
Electron spin resonance (ESR) and Conduction electron spin resonance (CESR)	*electronic properties*	[282,283]
scanning tunneling microscopy and spectroscopy (STM, STS)	*band gap investigation, chirality and topography*	[284-286]
contact angle measurements	*Wetting of nanotubes*	[287]
Transmission electron microscopy (TEM) and Scanning electron microscopy (SEM)	*wall structure*	[288,289]
Atomic force microscopy	*mechanical properties, electrical properties and manipulation*	[9,18,290]

metal-semiconductor junction. Second, they were able to detect energy gaps in SWNT due to the curvature of the graphene sheet and observed a pseudogap on a (8,8) SWNT bundle. This work has led to the advancement of STM and STS techniques by other researchers in the field. Their technique enables prediction of individual nanotube behavior prior to their assembly in nano-scale devices.

Lemay et al. [291] used STM and STS to map the two-dimensional structure of individual wavefunctions in a metallic SWNT. Their results verified that the dispersion relation near the Fermi level is linear. Based on the data obtained, the Fermi velocity and the p-p overlap energy was calculated to be $8.2 \pm 0.7 \times 10^5$ m/s and 2.6 ± 0.2 eV, respectively for the individual SWNT studied. Their results are comparable to those obtained with other techniques that measure bulk properties of nanotube ensembles.

The local potential barrier above a carbon nanotube connected to two metal electrodes and switched on by a backside gate was examined using a conductive tip. This tip is able to map a potential variation above the tube with a period of about 40 nm [292]. Transport current was spatially imaged for nanotubes wired between electrodes. It was found that tubes within bundles have weak electronic coupling [293].

Nanotubes filled with spherical molecules are known as “nanopeapods”. STM can be used to visualize the location of the inclusion compounds in the peapod [294]. Conductance along the backbone of the nanopeapod was measured; a drop in bandgap

energy was found at locations where fullerenes resided in the tube [295,296]. Theoretical treatment of the conduction in these nanostructures has been presented [297].

Carbon nanotubes are thermally and electrically conductive materials with high tensile strength. Their incorporation into polymer composites portends of next-generation light-weight, high-strength materials and motivates research in this area. Technical challenges that presently inhibit realization of new materials with these properties include control of the orientation and dispersion of the nanotube within the polymer matrix.

Mechanical Properties Measured with AFM (NanoSpring Introduction)

The atomic force microscope (AFM) has been used to probe many of the mechanical properties of carbon nanotubes [298] Bending properties of both SWNTs [299] and MWNTs [300-303] have been explored. It has been demonstrated that these bending properties can influence the electrical characteristics of the nanotube [304]. The radial compressibility of a MWNT has also been experimentally probed. [305] Recently Park et al. developed a model to predict the influence of nanotube bending/compression on chemical reactivity. [306]

Using the AFM as a force spectroscopic tool has enabled the measurement of the tensile strength of single walled [307] and multiwalled [308] nanotubes. More recently Chen and co-workers demonstrated the ability stretch and measure the tensile response a carbon nanocoil using a fairly elaborate experimental setup [218]. Other work has focused on the non-tensile mechanical measurements of carbon nanotubes. Radial

compression of MWNTs showed that they can be reversibly deformed up to ~40% and that compression increases nonlinearly with applied stress [305]. The elastic modulus increases with compression ranging from 9.7 to 80 GPa. The compression strength was greater than 5.3 GPa for a 10 nm diameter MWNT [309].

Collapsed MWNTs or nanotube ribbons are extremely flexible and readily conform to an underlying substrate [310]. Coiling of MWNTs was observed; the helical shape has little effect on the measured Young's modulus. Typical values for Young's modulus were 0.4 – 0.9 TPa. [311]

Rolling of carbon nanotubes while on highly ordered pyrolytic graphite (HOPG) follows a gear-like motion. This motion is governed by an overlap of the hexagonal graphite surfaces of the carbon nanotube and the HOPG. Interlocking of the atomic lattices increases the force required to move the carbon nanotube and the result is the nanotube "locks" into a gear-like motion. As a nanotube is rotated in plane the resulting "lock" into gear like motion occurs every 60 degrees, consistent with theoretical predictions [312].

The electronic properties of nanotubes, either under or after applied strain, have also been research focus. In situ measurements of the electronic properties of carbon nanotubes under stress have shown that the conductance in a SWNT drops by two orders of magnitude when deformed by an SFM tip. This is consistent with the reversible formation of sp3 bonds during the mechanical deformation [313,314]. Other studies have

measured the resistance of induced defects such as closely separated kinks in a SWNT [315]. These defects were found to have a resistance from 10 to 100 kW and even showed single electron charging behavior. The electronic behavior of carbon nanotubes has lead to their use in single electron transistors [247].

It has been demonstrated that an AFM tip can also be used to cut either multi-walled [316] or single-walled [317] nanotubes, affording a straightforward method for removing defect-laden portions or creating nanotube-fragment quantum dots. Woodside and McEuen used the AFM to study single-electron motion in nanotube quantum dots [318]. They remind us that although scanned probe techniques have great sensitivity, these techniques alter the native properties of the system under measurement.

Measurement of the impact of mechanical stress on the electrical properties of carbon nanotubes has been a research focus. Bozovic et al. [319] studied the effect of strain on the electrical properties of single walled carbon nanotubes. Using scanning gate microscopy they showed that defect sites, created by mechanical deformation, cause a significant decrease in electron transport along the tube.

Kim et al. [320] elucidated the electrical properties of a MWNT while it was being mechanically deformed using nanomanipulators, Thelander and Samuelson [321] made electrical contact to both ends of a nanotube and then used an AFM tip to manipulate the nanotube on the surface. Tip-induced bending of the nanotube caused measurable decreases in the tubes conductance. Minot and coworkers [304] have shown that the

band structure of a carbon nanotube can be dramatically altered by mechanical strain. They suspended a nanotube over a trench and clamped both ends with electrical contacts. An AFM tip was brought into contact with the tube and used to vary the strain on the nanotube. Nanotube conductance was monitored as a function of strain. Their results demonstrate that strain can open a band gap in a metallic nanotube and modify the band gap in a semiconducting nanotube.

Williams and co-workers present a unique AFM-based technique for measuring the torsional stiffness of multiwalled nanotubes [303]. They found that the torsional stiffness of a multiwalled nanotube becomes larger during repeated torsional strains.

Recently, the research groups of both Professor Hongjie Dai (Stanford University) and Professor Charles Lieber (Harvard University) have used the AFM to study the bending/buckling of nanotubes that are attached to the tip of the AFM cantilever probe [200,203]. In both research groups, they have interpreted the bending response of the tube by monitoring both the deflection of the cantilever and the oscillatory behavior of the cantilever/nanotube probe prior to and during contact with a surface (Figure 4.4, Figure 4.5). For example, Lieber and co-workers have interpreted the immediate deflection upward and subsequent static position of the beam as the nanotube making contact with the surface and then the nanotube bending out of the way. They have interpreted the corresponding drop in oscillation amplitude of the beam during the approach of the scanner towards the tip as the point at which the tube makes contact with the surface. Then (still during upward movement of the scanner) the amplitude begins to

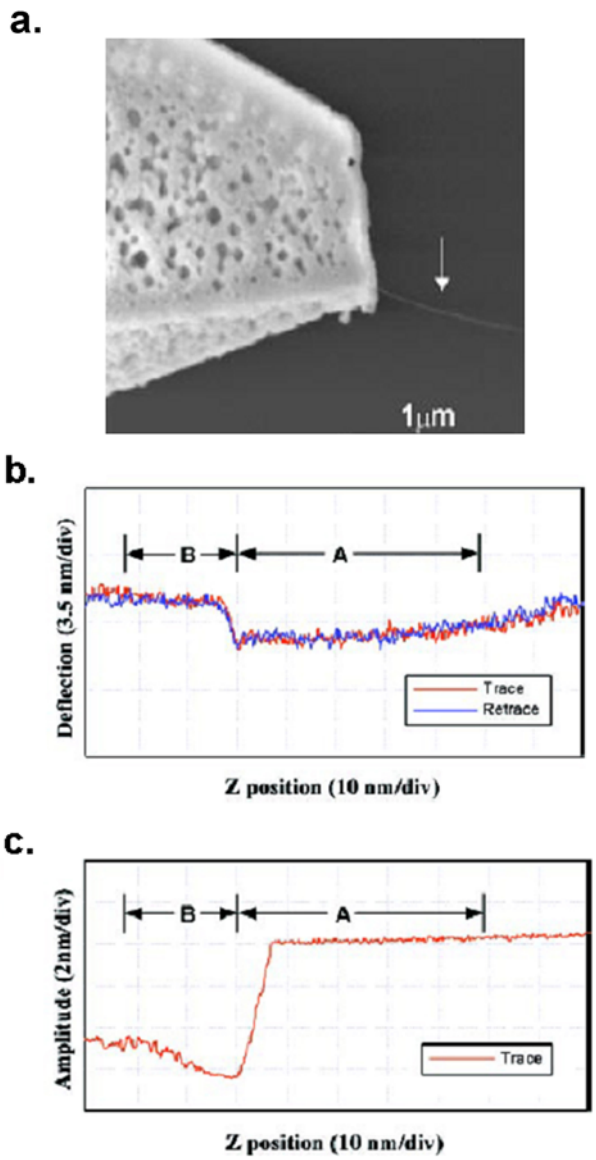

Figure 4.4. (a) SEM image of multiwalled nanotube on the end of a cantilever tip. (b) Deflection force curve of the nanotube-tipped beam when it makes contact with the substrate. (c) corresponding oscillation amplitude curve that is measured during the approach of the substrate towards the nanotube/tip. (Reproduced from Cheung, C. L.; Hafner, J. H.; Lieber, C. M. *Proceedings of the National Academy of Sciences of the United States of America* **2000**: 97; 3809-13. Permission granted from both the PNAS copyright office and from Professor Lieber).

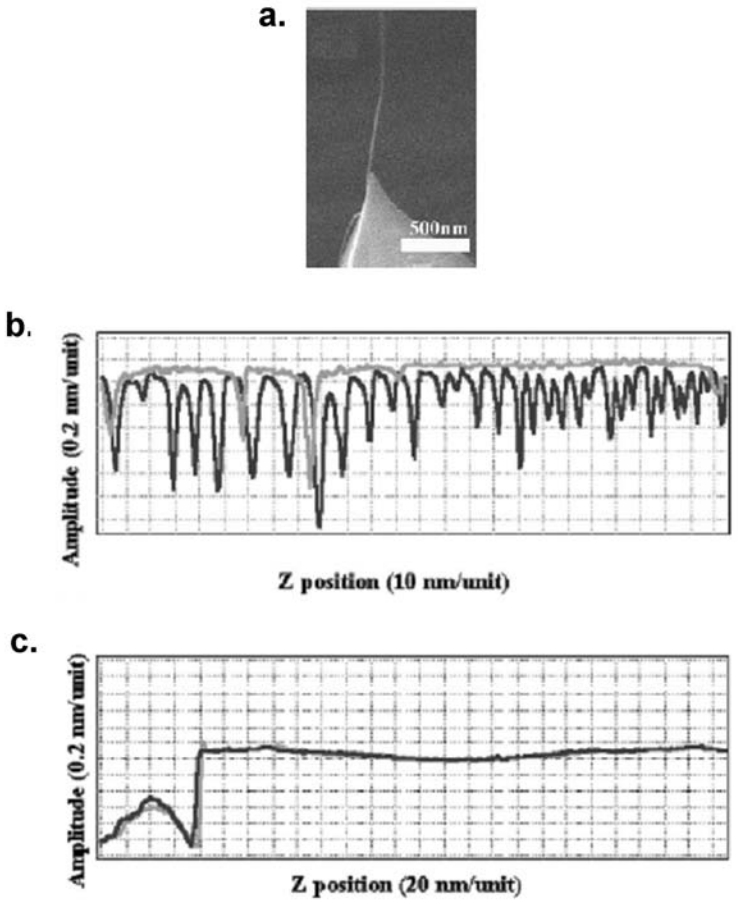

Figure 4.5. (a) SEM image of multiwalled nanotube on the end of a cantilever tip. (b) oscillation amplitude curve that is measured during the approach of the substrate towards the nanotube/tip where once the tube touches the surface the oscillation amplitude randomly drops continually during the rest of the approach and for a majority of the retract portion of the curve (approach is in grey and retract is in black). (c) oscillation amplitude curve that is measured during the approach of the substrate towards the nanotube/tip after the tube is shortened. (Yenilmez, E.; Wang, Q.; Chen, R. J.; Wang, D.; Dai, H. *Applied Physics Letters* **2002**: 80; 2225-27. Permission granted from both the AIP copyright office and from Professor Dai).

rise slightly (but never back to its free amplitude). A symmetric response for both the deflection and oscillation amplitude curves is observed during the retraction of the substrate away from the cantilever/nanotube.

Dai and co-workers have monitored the oscillation amplitude of the cantilever/nanotube to interpret the buckling characteristics of a long nanotube and then have shortened the length of the nanotube via a bias voltage between the cantilever and a conductive surface. The shortening of the nanotube is tracked following the voltage bias, by acquiring another oscillation amplitude curve where the duration of dampening is much shorter than the dampening of the long (uncut) nanotube (Figure 4.5c).

Scanning Probe Studies Aiding Nanotube Composite Research

Characterization of the defect density of nanotubes in polymer composites has been accomplished using both current sensing AFM and magnetic force microscopy [322,323]. Wagner's group has measured the force required to detach a nanotube from a polymer by laterally scratching the nanotube out of the polymer using an AFM tip [324]. More recently, they embedded a nanotube-tipped cantilever in a polymer and then measured the force required to pull the nanotube out [325]. After removal, images of the polymer surface revealed the location where the nanotube was previously embedded.

Ding et al. [326] have observed polymer sheathing in a carbon nanotube-polycarbonate composite. Contact of the polymer sheath with an AFM tip perturbs the polymer multilayer structure and the polymer sheath rolls into a ball. These observations suggest

the importance of both nanotube-polymer and polymer-polymer interactions in enhancing the performance of nanotube-polymer composites.

CHAPTER 5

ADHESION MAPPING OF CARBON NANOTUBES

Introduction

As mentioned in the previous chapter, carbon nanotubes possess high electrical conductivity and mechanical strength. This unique combination of properties has led to the investigation of using carbon nanotubes in polymeric composites. It is clear from current research, that a fundamental understanding of the interface between carbon nanotubes and polymeric materials is needed to enhance the dispersal and controlled orientation of nanotubes into polymer composites.

Thus far, only a few theoretical and experimental studies have been reported on the chemical and physical interactions at the nanotube/polymer interface. [287,324,325,327,328] One of the objectives of this research was to use chemical force microscopy to probe the nanotube/polymer interface. The aim was to measure the binding force of single molecules to the sidewalls of carbon nanotube.

Chemical Force Microscopy (CFM) [329] is an extremely versatile technique that has been used to explore the mechanical properties of single biological molecules [330-332], the adhesive forces between molecules [333-337] and adhesive mapping of polymer composites [141,338,339]. By bringing a chemically modified AFM cantilever tip into contact with the sidewall of a SWNT, the adhesion present between specific molecules and the backbone of single walled carbon nanotubes was examined.

Experimental

Materials

There were two classes of thiols used in this study; linear alkanethiols and para-substituted arylthiols. The linear alkanethiols used in this study were: 11-amino undecanethiol (Dojindo Chemicals), 1H,1H,2H, 2H perfluorodecane-1-thiol (FluroFlash^{TM}), 11-dodecane thiol, 11-mercaptoundecanoic acid, 1,6 hexanedithiol (Aldrich), bis(11-hydroxyundecyl) disulfide [340], 11-undecenethiol [341]. The para-substituted arylthiols used in this study were 4-mercaptobenzonitrile (Apin Chemicals Ltd.), 4-bromobenzenethiol, 4-methylbenzenethiol, 4-nitrobenzenethiol, benzenethiol, 4-methoxybenzenethiol, 4-fluorobenzenethiol, 4-mercaptophenol and 4-aminothiophenol were used as received (Aldrich). Stock solutions were 1mM thiol in either filtered ultrapure ethanol or hexane (Aldrich). All of these thiols are known to form well-ordered self-assembled monolayers (SAMS) [342].

Commercially available cantilevers used in these experiments were coated with gold on both sides to enable functionalization of the cantilever tip with a thiol chain (MikroMasch). The cantilevers were cleaned in 3 parts H_2SO_4/ 1 part H_2O_2 (piranha), thoroughly rinsed in EtOH and placed in 1 mM thiolic solution for 3-24 hrs. Following exposure to thiolic solutions each cantilever was thoroughly rinsed in wither filtered ethanol or hexane. Following the rinsing step, the thiolated cantilevers were placed under a backfilled dry nitrogen vacuum for 3 hrs and then placed in a dessicator before use [343].

All experiments were carried out on highly purified single walled carbon nanotube paper of predominantly (10, 10) chirality. The paper was prepared by workers in Professor Richard E. Smalley's lab at Rice University according to their previously reported method [344]. The paper consisted of single walled nanotube ropes and bundles of ropes. Figures 5.1 and 5.2 depict SEM and AFM images of the paper and verify the presence of a high number of tubes and bundles per unit area.

Instrumentation

AFM/Adhesion measurements were carried out with a Nanoscope IIIa Extended Multimode SPM (Veeco) operated in "Force Volume" mode. The piezoelectric scanner was calibrated in x, y and z with NIST certified calibration gratings (MikroMasch). Force constants for the cantilevers were acquired via the thermal resonance method [213,214] using the Signal Access Module (Veeco) and a SRS 785 Dynamic Signal Analyzer (Stanford Research Systems). Force constants ranged from 0.7 to 1.2 N/m. After the adhesion measurements were complete, each cantilever was cleaned using a UVO-Cleaner® (Jelight Company). The tip radius of each cantilever was determined using tip-deconvolution software (SPIP^{TM} by Image Metrology). All experiments were performed under a custom-built nitrogen atmosphere to reduce the relative humidity to less than 2%. [345,346]

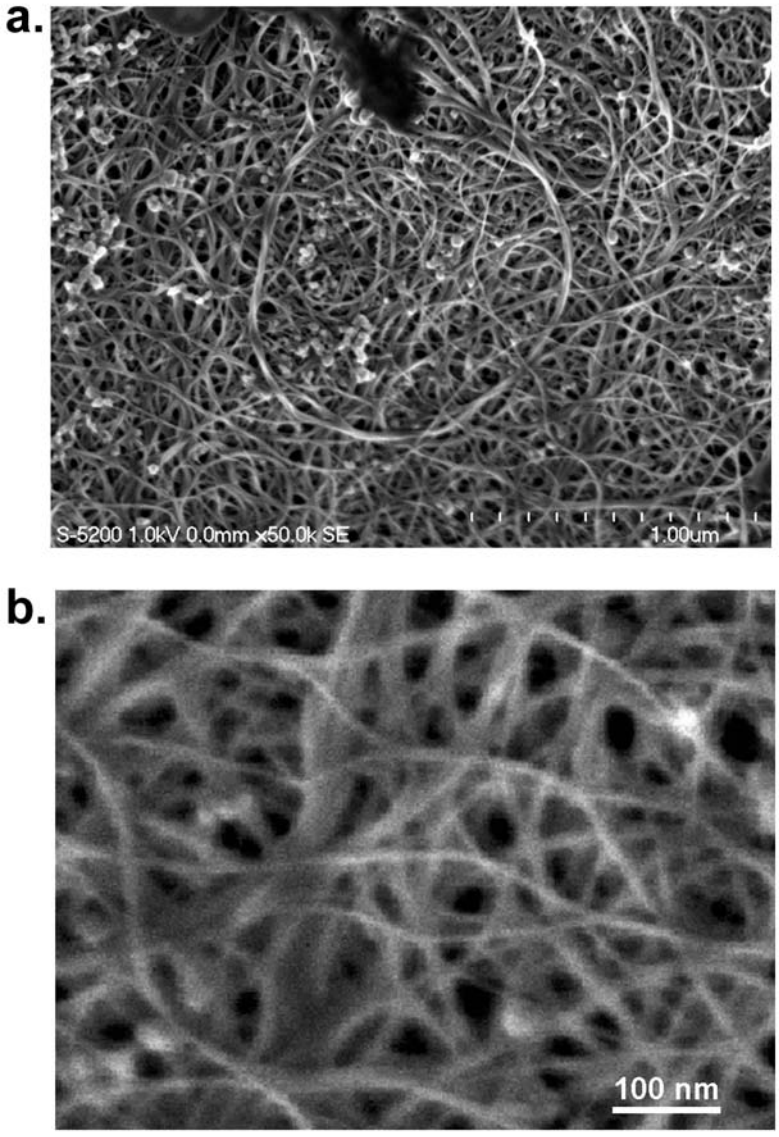

Figure 5.1. Scanning electron micrographs of SWNT paper prepared by the HiPco process. (a) low magnification. (b) high magnification.

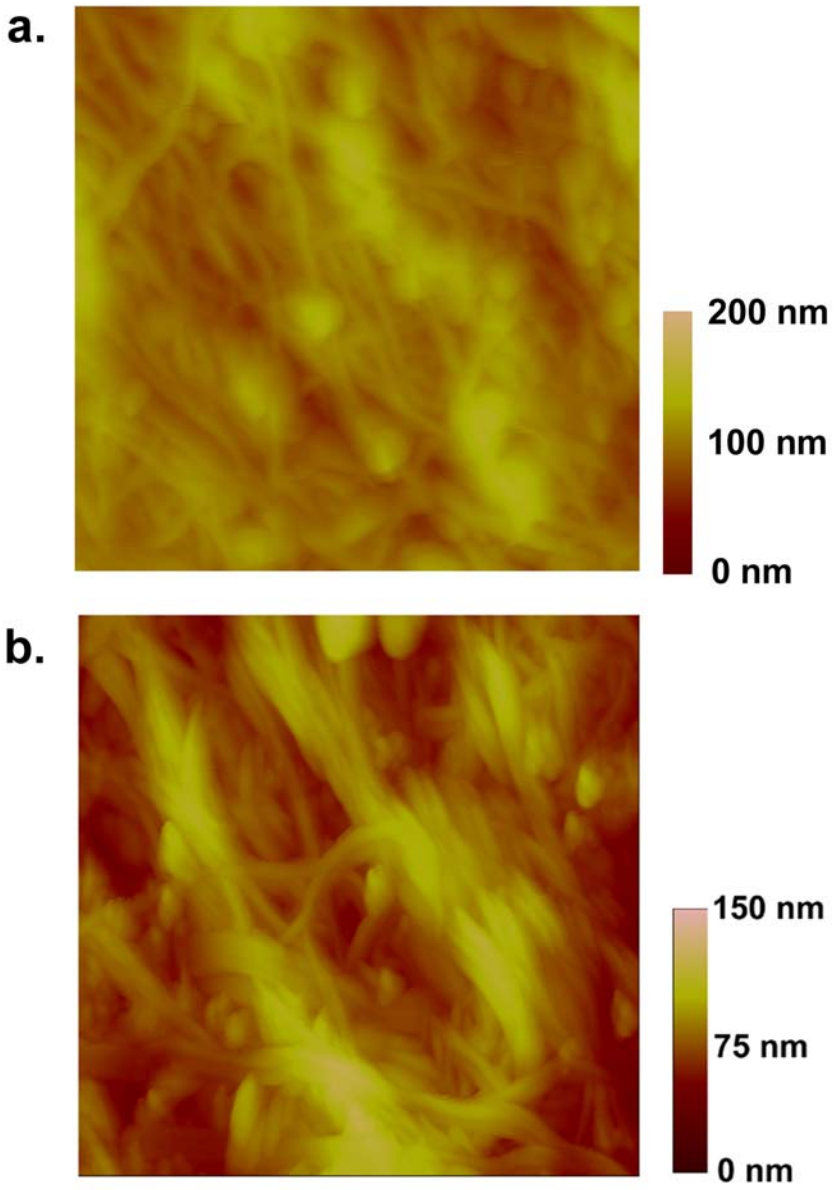

Figure 5.2 Tapping Mode™ AFM images at different locations (a) and (b) on the SWNT paper (Image sizes are 1μm x 1μm).

Force Volume Imaging and Adhesion Mapping

The force volume mode (see Chapter 1) is an extension of contact mode AFM. The sample is translated underneath the cantilever in the x,y and z direction. As the sample moves in x and y, a topographical image of the underlying sample is generated (Figure 5.3a). For every incremental movement in x and y, a corresponding z-movement is executed for each pixel in the topographical image (i.e. a force curve measurement at every pixel). All of the force measurements are summarized in a "force volume image" of the sample (Figure 5.3b). The contrast in a force volume image is related to the maximum deflection of the cantilever. Force curves that have a small pull down distance are light while force curves that have a large pull down distance are dark.

Force volume experiments in this study were acquired at 256 pixels per topographic image (i.e. 256 force measurements per image). All experiments were carried out using the same x, y scan size (50 nm X 50 nm) and the same z-loading rate (controlled via the trigger threshold). Using a method similar to the one presented by Eaton et al. [141,339] cantilever deflection (nm) vs. scanner/sample position (nm) (force curves) were extracted using a custom designed data extraction program (Visual Basic)(Appendix B.1). The program is capable of extracting 256 force measurements per image. Following the extraction of the force curves from the force volume images, the individual force curves are converted from tip deflection (nm) vs. separation (nm) to force (nN) vs. separation (nm), using the spring constants that were experimentally determined for each cantilever. Next, the force at maximum tip deflection (adhesion force) was extracted from each force curve. These forces were then used to generate 2-D adhesion maps that illustrate the

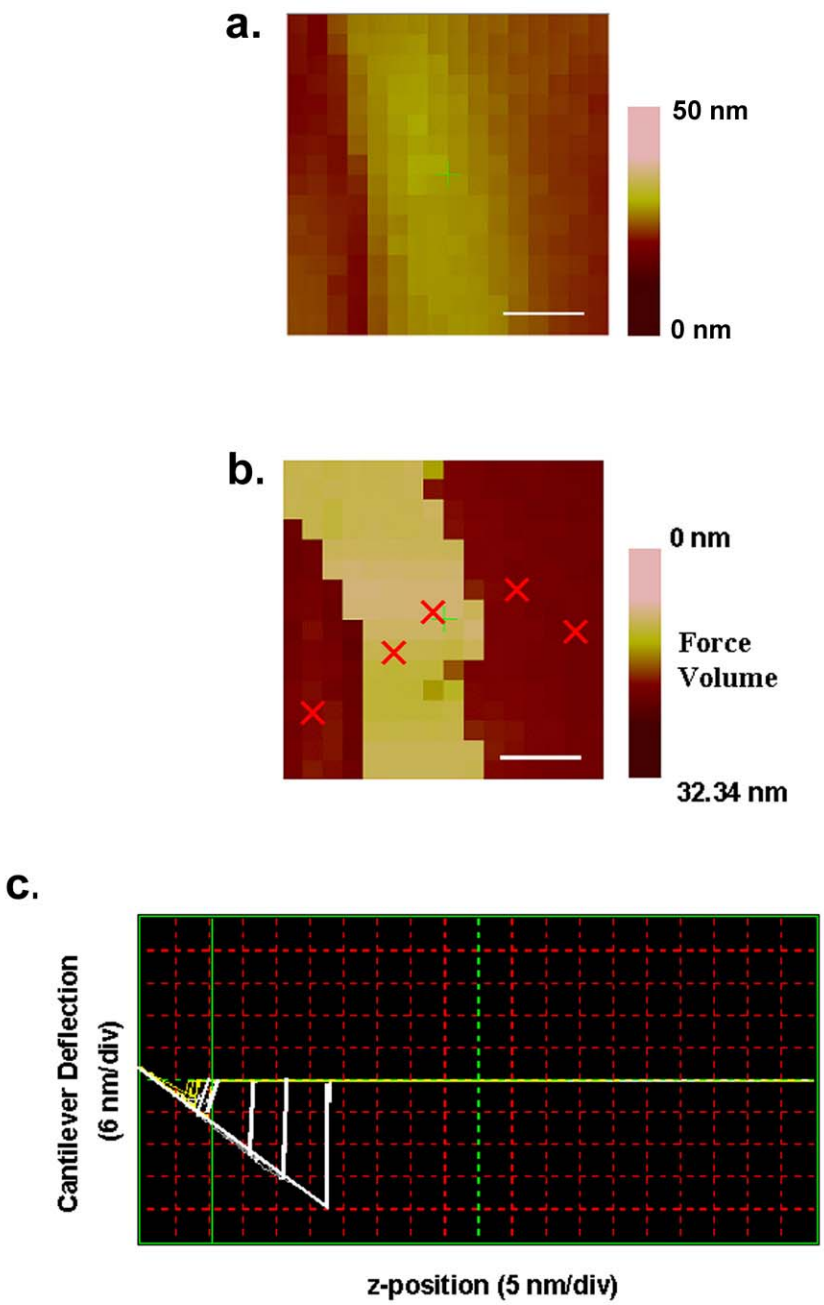

Figure 5.3. Typical force volume data acquired on the SWNT paper output from the Nanoscope IIIa software. (a) Topographical image of the SWNT paper (50 nm x 50 nm). b) Force volume image corresponding to the topographical image. c) Individual force curves taken across the sample (marked with a red "x" in the force volume image).

amount of adhesive force present between the thiol-modified cantilever and the SWNT paper. Force volume images were acquired over 10 different locations on the SWNT paper for each chemically modified tip.

Results

Adhesion Mapping of SWNT Paper

Prior to force volume imaging, the SWNT paper was imaged in Tapping Mode™ using a NSC 12 cantilever (MikroMasch) to locate areas on the paper that possessed a high density of tubes/bundles per unit area (Figure 5.2). Once these areas were located the chemically modified cantilever was mounted into the AFM to perform force volume measurements.

Figure 5.4 depicts a typical topographical image and that image's corresponding adhesion map (following data extraction) using a cantilever that had a hydroxyl-terminated thiol self assembled on its tip. After acquiring ten different adhesion maps at various locations on the SWNT paper, the frequency at which the cantilever experienced a force of a particular magnitude was investigated and plotted in a histogram.

Figure 5.5 is a histogram plot of the rupture forces that the cantilever experienced during the force volume imaging of the SWNT paper using a hydroxyl-terminated thiol. A bimodal distribution of the forces, one band centered at 5nN and the other at 12 nN is present in the data. Histograms summarizing the adhesion forces that the cantilever experienced during force volume imaging with each alkanethiol are presented in Figure

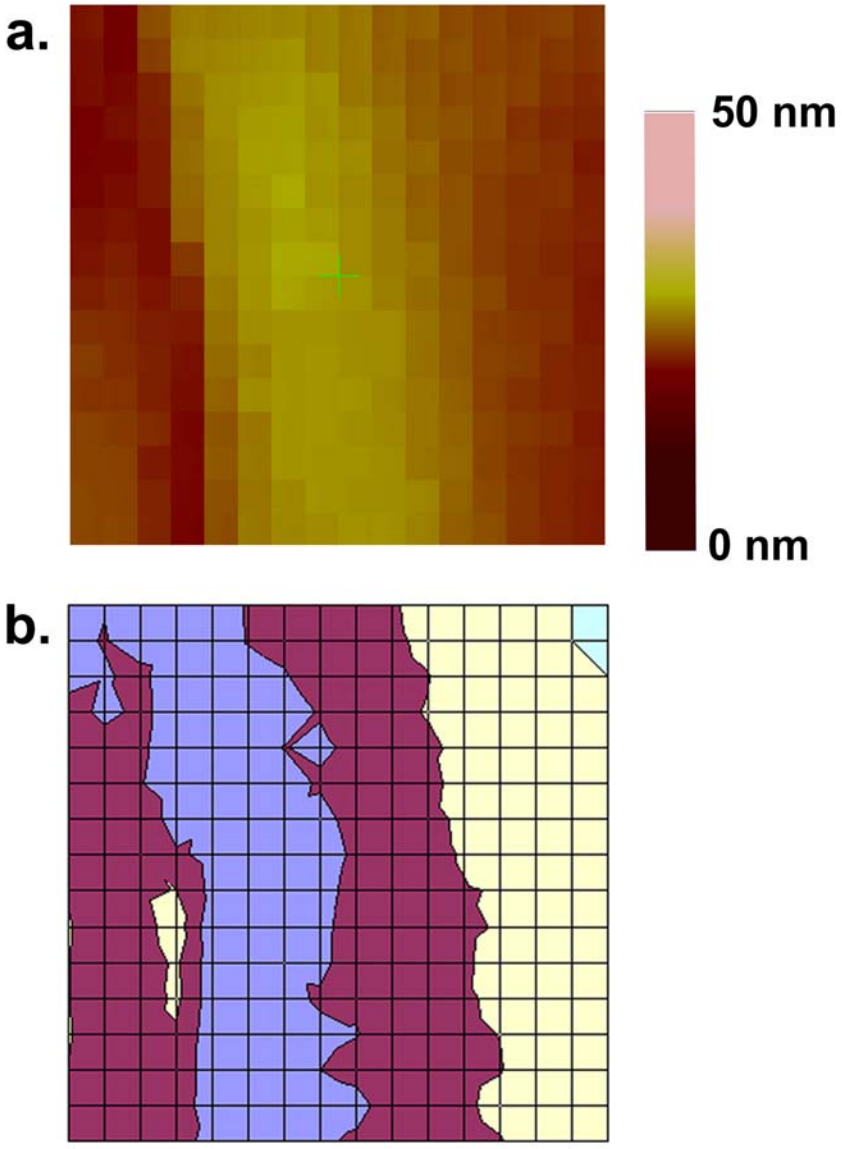

Figure 5.4. (a) Highly pixelated topographical image acquired in force volume mode using a cantilever tip that was modified with a hydroxyl-terminated alkanethiol (50 nm x 50 nm scan size). (b) Adhesion map generated from the individual force curves measured at each pixel in the image. The contrast in the adhesion map is blue represents an adhesive force from 0 to 4 nN, maroon 4-8 nN, yellow 8-12 nN, and green 12-16 nN.

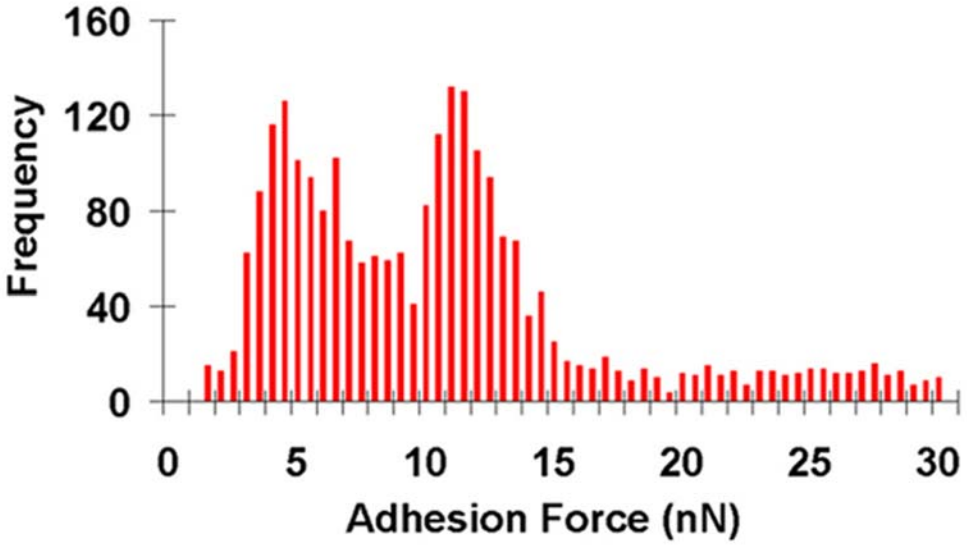

Figure 5.5. Histogram showing the distribution of forces required to detach the hydroxyl-terminated thiol modified cantilever from the SWNT paper.

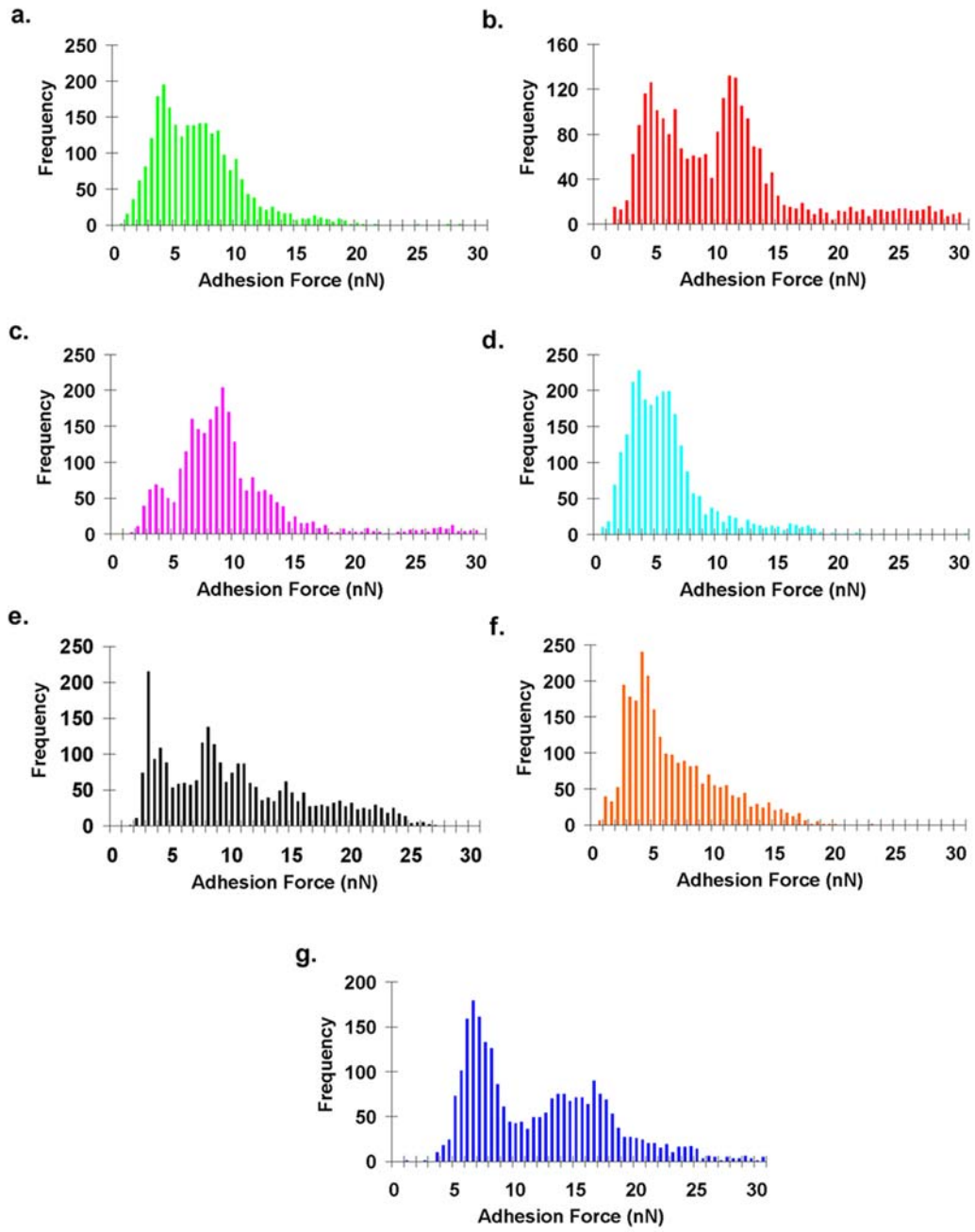

Figure 5.6. Histograms showing the distribution of forces required to detach a chemically modified cantilever tip from the SWNT paper (a) Methyl (b) Hydroxyl (c) Carboxylic Acid (d) Perfluoro (e) Undecene (f) Sulfur (g) Amine

5.6. Other thiols seem have mono-, bi-, or tri-modal distributions of forces. The average rupture force (and standard deviation) was determined for each thiol; the data is summarized in Table 5.1. From this table, no clear trend is apparent.

After further inspection of the topographic and force volume data, a direct correlation of sample topography to the adhesion forces was observed. For example, by comparing the topographical image to its adhesion map (Figure 5.7), one can see that the areas that are that are topologically "low" correspond to areas of "high" adhesion. Similarly, the areas that are topologically "high" in the image correspond to areas of "low" adhesion. This phenomena has been observed in other adhesion experiments [141,339] as well as in force modulation experiments [347]. The relationship of topography to the adhesion force is a direct function of the surface area contact that exists between the cantilever tip and the substrate during the force volume experiments.

As the cantilever travels to areas that are low ("valleys") in the topographical picture, there will be a large area of the cantilever tip/thiol touching the sample (Figure 5.8a). As the cantilever moves from the low area of the substrate to the top of a tube or bundle of tubes, there should be a decrease in the overall adhesion because there is now a lower amount of surface area contact present between the tip and the sample (Figure 5.9b). Also, notice in the adhesion map that the width of the area that has the lowest adhesive force corresponds to width of the tall feature in the topographical image (the width of the linear feature is approximately 15 nm).

Table 5.1. Summary of the total adhesive forces measured between each chemically modified cantilever and the SWNT paper.

Thiol	Average Force of Adhesion (nN)	Standard Deviation
OH	11.7	8.9
CH3	6.90	6.5
COOH	9.32	5.8
NH2	11.7	5.6
Perfluorinated	5.47	3.4
S	6.22	3.8
C=C	10.0	6.0

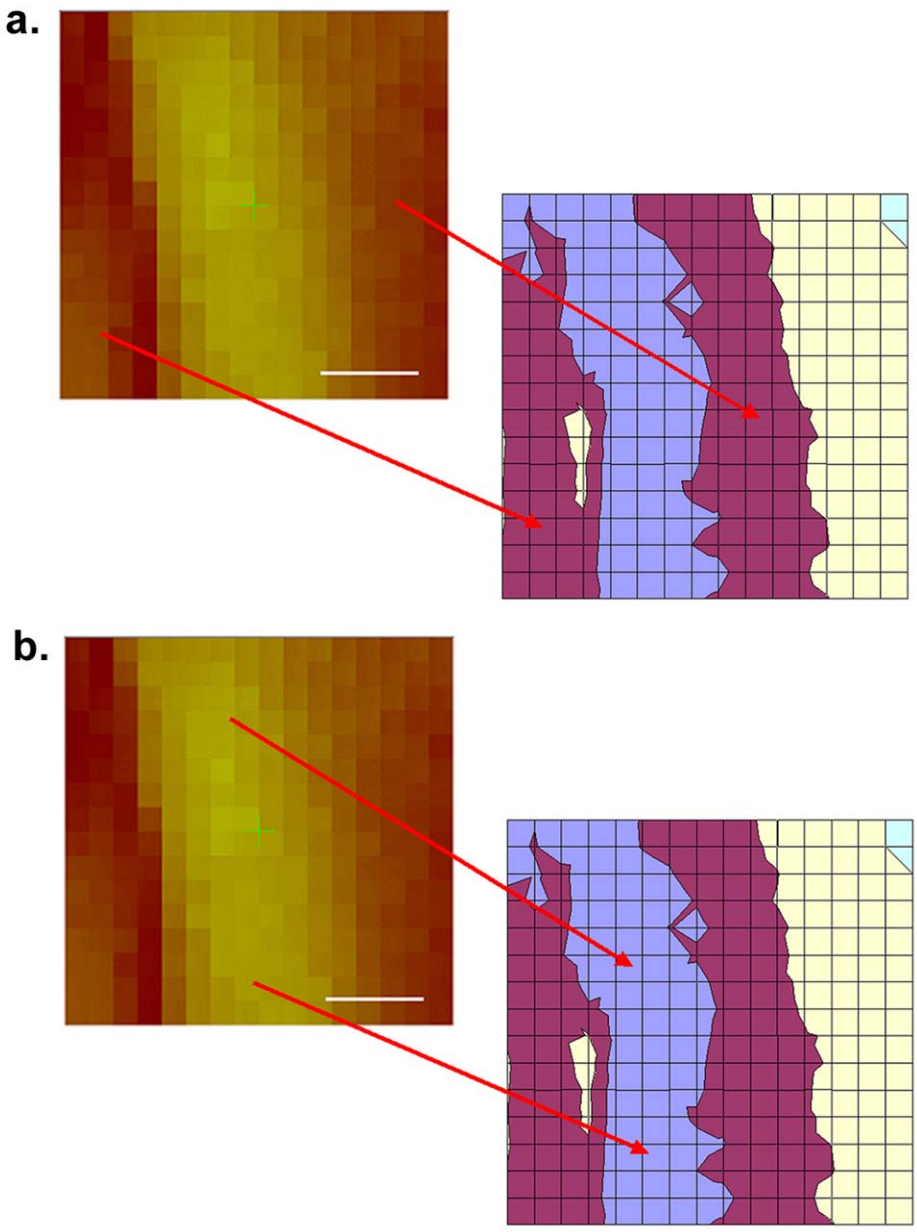

Figure 5.7. (a) Topographical image (50 nm x 50 nm) with corresponding adhesion map, red arrows denote areas of the topographical image that have a correspondingly high adhesion. (b) Topographical image (50 nm x 50 nm) with corresponding adhesion map, red arrows denote areas of the topographical image that have a correspondingly low adhesion. The contrast in the adhesion map is blue represents an adhesive force from 0 to 4 nN, maroon 4-8 nN, yellow 8-12 nN, and green 12-16 nN.

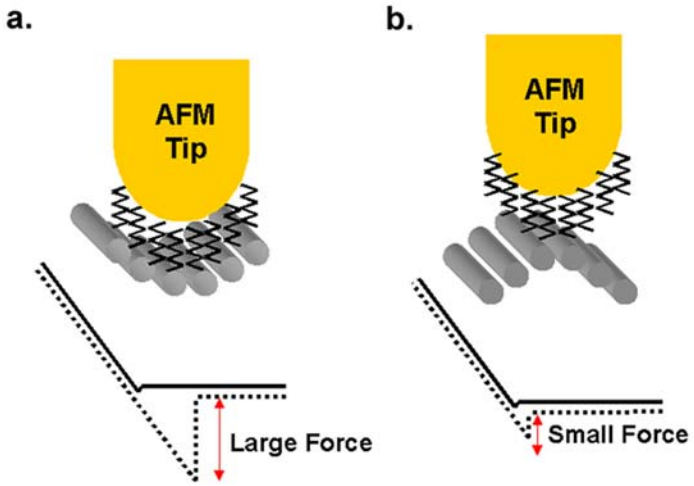

Figure 5.8. (a) Cartoon depicting the high adhesion force that the cantilever will experience as it makes contact in a topographically recessed area (i.e. between nanotubes). (b) Cartoon depicting the low adhesion force that the cantilever will experience as it makes contact in a topographically high area (i.e. along the backbone of a nanotube).

The distribution of forces observed in the histograms can be explained by the changes in sample topography as the cantilever travels from one area of the nanotube paper to the next. Since it is of interest to determine the single molecule rupture force between the thiols and the single walled nanotubes, the adhesion forces for one thiol group cannot be averaged together; it is necessary to extract the forces that only correspond to a "known" or defined contact.

Forces Corrected for Contact Area

To obtain the single molecule adhesion forces, it is necessary to correct for the surface area contact artifact that is observed when performing these force measurements. To do so, it was assumed that the rupture forces found on "high" topographical regions, are those from the smallest area of contact. The force data was parsed so that data taken from regions of "low" topography were discarded. This was accomplished by setting an upper and lower adhesion boundary that would output only the adhesion forces that were between the boundary values (Figure 5.9). These adhesion forces were then processed using the contact models proposed below.

A common approach for comparing adhesion force measurements is to divide the mean adhesive force by the radius of the cantilever tip (F/r) [329,332]. Tip radii are typically determined by either placing the cantilever probe into a high-resolution scanning electron microscope (SEM) or transmission electron microscope or by imaging a sample that possesses precisely known geometrical features (for example; gold nanoparticles dispersed onto mica) [348,349].

a.

7.55	5.95	5.52	6.33	2.29	3.29	3.12	3.77	4.25	4.19	6.09	6.56	7.75	9.62	11.18	9.81
7.67	5.61	6.11	6.86	1.12	2.34	3.16	3.21	3.40	4.90	5.16	7.22	9.39	10.00	10.28	10.46
7.91	5.98	6.34	7.26	1.38	3.11	2.89	4.00	4.50	4.61	6.01	6.75	7.74	10.33	11.16	10.02
8.24	5.90	6.17	7.55	1.42	1.90	2.85	3.60	3.93	4.70	4.95	7.16	8.06	10.54	10.93	9.72
8.08	5.25	5.38	8.89	1.57	2.68	3.35	4.27	4.23	4.92	5.85	7.19	9.10	9.47	10.50	9.47
8.16	5.96	5.86	8.66	1.76	3.16	3.54	3.52	5.10	4.80	6.64	7.08	10.57	10.37	10.15	10.21
8.26	5.18	6.14	10.19	1.36	2.28	3.13	3.51	4.85	4.51	6.46	6.74	8.57	10.29	10.66	10.34
7.72	5.26	7.20	8.10	2.85	2.74	2.65	3.24	4.70	5.10	6.41	7.66	8.36	10.36	11.27	10.51
7.80	6.16	7.76	4.86	2.59	3.88	2.87	2.48	4.51	5.12	6.52	8.47	10.62	11.14	11.18	10.04
7.17	6.28	7.89	1.51	2.79	3.55	3.35	3.14	5.01	5.35	7.17	8.62	10.17	10.60	11.42	10.37
7.09	6.74	4.24	1.26	2.62	2.74	2.82	4.32	4.69	5.91	6.88	9.65	10.20	11.73	11.30	9.46
7.65	6.84	4.81	1.34	3.22	2.55	4.05	3.62	4.41	6.05	7.37	8.85	10.17	11.00	11.19	10.88
6.84	2.39	5.39	1.36	2.82	3.07	3.13	4.12	5.17	7.23	8.20	9.47	10.81	10.96	11.86	11.33
1.90	3.59	5.12	1.20	2.79	3.37	3.84	4.91	4.93	6.90	7.85	11.14	11.67	11.55	11.85	12.87
2.88	4.23	2.07	1.69	3.02	4.09	4.45	5.02	5.59	7.27	8.88	11.16	11.66	11.87	13.11	13.69
2.59	3.84	2.12	2.70	2.91	4.18	4.61	5.14	6.01	7.54	9.61	11.13	12.97	11.64	13.29	15.00

b.

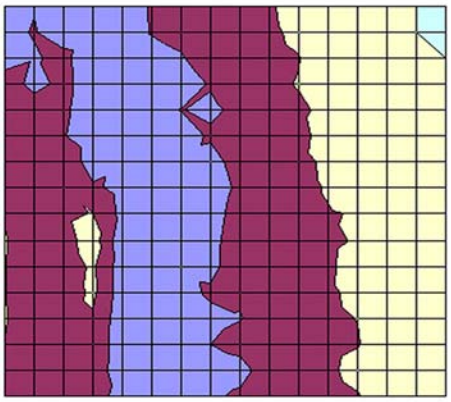

c.

0.00	0.00	0.00	0.00	1.72	2.47	2.34	2.83	3.18	3.14	0.00	0.00	0.00	0.00	0.00	0.00
0.00	0.00	0.00	0.00	0.84	1.76	2.37	2.41	2.55	3.68	3.87	0.00	0.00	0.00	0.00	0.00
0.00	0.00	0.00	0.00	1.04	2.33	2.17	3.00	3.37	3.46	0.00	0.00	0.00	0.00	0.00	0.00
0.00	0.00	0.00	0.00	1.06	1.43	2.14	2.70	2.95	3.53	3.71	0.00	0.00	0.00	0.00	0.00
0.00	3.94	0.00	0.00	1.18	2.01	2.51	3.20	3.17	3.69	0.00	0.00	0.00	0.00	0.00	0.00
0.00	0.00	0.00	0.00	1.32	2.37	2.66	2.64	3.82	3.60	0.00	0.00	0.00	0.00	0.00	0.00
0.00	3.88	0.00	0.00	1.02	1.71	2.35	2.63	3.64	3.38	0.00	0.00	0.00	0.00	0.00	0.00
0.00	3.94	0.00	0.00	2.14	2.05	1.98	2.43	3.52	3.82	0.00	0.00	0.00	0.00	0.00	0.00
0.00	0.00	0.00	3.65	1.94	2.91	2.15	1.86	3.38	3.84	0.00	0.00	0.00	0.00	0.00	0.00
0.00	0.00	0.00	1.13	2.09	2.66	2.51	2.35	3.76	0.00	0.00	0.00	0.00	0.00	0.00	0.00
0.00	0.00	3.18	0.95	1.96	2.05	2.11	3.24	3.52	0.00	0.00	0.00	0.00	0.00	0.00	0.00
0.00	0.00	3.61	1.00	2.41	1.92	3.04	2.72	3.31	0.00	0.00	0.00	0.00	0.00	0.00	0.00
0.00	1.79	0.00	1.02	2.11	2.30	2.35	3.09	3.88	0.00	0.00	0.00	0.00	0.00	0.00	0.00
1.43	2.69	3.84	0.90	2.09	2.52	2.88	3.68	3.69	0.00	0.00	0.00	0.00	0.00	0.00	0.00
2.16	3.17	1.55	1.26	2.26	3.07	3.34	3.76	0.00	0.00	0.00	0.00	0.00	0.00	0.00	0.00
1.94	2.88	1.59	2.02	2.18	3.13	3.46	3.85	0.00	0.00	0.00	0.00	0.00	0.00	0.00	0.00

Figure 5.9. (a) The measured adhesion forces from a force volume measurement carried out at a 50 nm x 50 nm scan size (b) Plot that graphically displays the numbers in (a), also referred to as an Adhesion Map. (c) Spreadsheet that is generated after using the adhesion force culling macro that only shows force that fall inside a predefined limit. All adhesion forces that fall outside the predefined limit (0 and 4 nN) are denoted as 0.00.

The tip radii of each of the cantilevers used in this study were determined after each adhesion mapping experiment. The cantilever was exposed to an oxygen plasma to remove the thiol from the cantilever tip. Then a high-resolution image of the nanotube paper was acquired with the cantilever at 8 locations on the nanotube paper (500nm scan size at 512 x 512 pixels per image). These images were then processed using commercially available tip-deconvolution software (SPIP^{TM} by Image Metrology).

The approach of normalizing the adhesion forces by F/r does not take into account the contribution of topography or compressibility of the SAM. To do so requires parsing of the adhesion data, removing adhesion data acquired at high areas of contact, measuring the tip geometry and analyzing the maximum load versus tip, monolayer and nanotube compressibility.

The AFM tip and the nanotube can be represented geometrically as a sphere pressing on a cylindrical object. If the nanotube compresses under cantilever tip (Figure 5.10), the following model is used to approximate the surface contact area:

$$ContactArea = \frac{\pi^2 \cdot r_{NT} \cdot (r_{tip} + t)}{2} \cdot Tan^{-1}\left(\frac{\sqrt{(r_{tip} + t)^2 - {r_{tip}}^2 + 4 r_{tip} r_{NT} - 4 {r_{NT}}^2}}{r_{tip} - 2 r_{NT}} \right) \qquad \text{Equation 5.1}$$

where r_{tip} = radius of the cantilever tip, r_{nt} = the radius of the nanotube and t = height of thiol. This model assumes that the nanotubes themselves are compressible under the forces exerted in these experiments and this is debatable [309,350-352]. An alternative

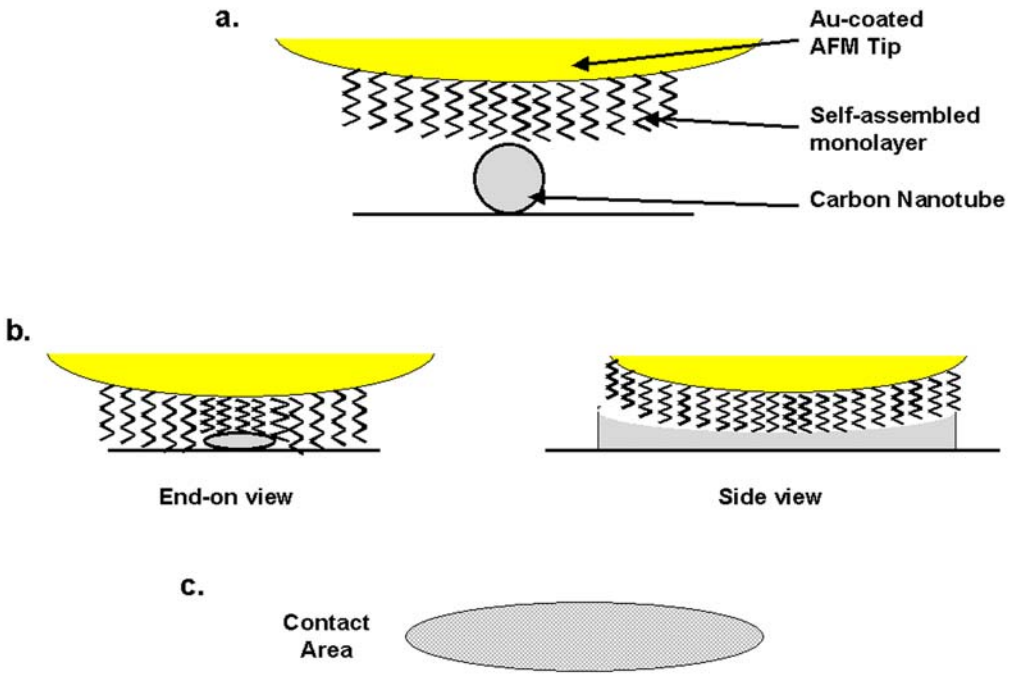

Figure 5.10. Cartoon depicting the alkane-thiol modified cantilever and the nanotube, assuming a rigid cantilever tip, pliant thiol layer and a rigid nanotube. a) prior to contact. b) thiol wraps around the tube during contact and the tube compresses radially and axially. c) the contact area between the cantilever and the tip is then numerically modeled as an elongated ellipse.

geometrical model depicts a cantilever tip (sphere), with a compressible thiol layer (second sphere coating the tip) and a nanotube (rigid cylinder) (Figure 5.11).

If the nanotube remains uncompressed under the tip, the following model is used to approximate the surface area contact. The cantilever was deflected the same amount in each experiment, so the thiols should all be deformed consistently from one experiment to the next. The same loading rate was also used from one cantilever to the next. These parameters not only influence the mechanical load on the thiol, but also influence the mechanical load on the nanotubes. The calculated pressure exerted on the nanotube surface was 66 MPa and the known bending/compression force of a single walled carbon nanotube has been reported to be around 1 GPa. Since the maximum applied pressure used in these experiments was much too small to buckle or compress the nanotubes but large enough to compress the thiol, equation 5.2 has been used to calculate the contact area:

$$ContactArea \approx \pi^2 \cdot r_{NT} \cdot \sqrt{2r_{tip} \cdot t + t^2} \qquad \text{(Equation 5.2)}$$

It is assumed that the thiols form a densely packed monolayer with a thiol packing density of 4.65 thiol molecules per square nanometer [341,353,354] with a tilt angle of 30° relative to the surface normal [355,356] . In this case it is assumed that the thiol film was totally compressible at the loads that were used in the experiments (Figure 5.11). It is understood that the thiol molecules should compress [357-360] but assessing the degree of compressibility and its endgroup dependence needs further investigation.

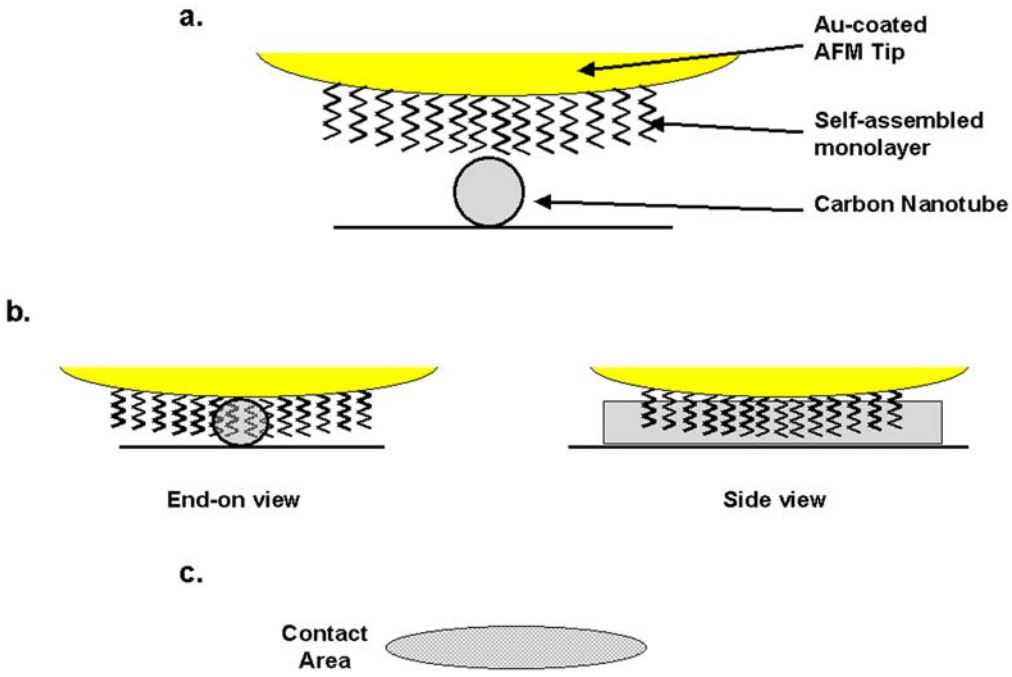

Figure 5.11. Cartoon depicting the alkane-thiol modified cantilever and the nanotube, assuming a rigid cantilever tip, pliant thiol layer and a rigid nanotube. a) prior to contact. b) thiol wraps around the tube during contact. c) the contact area between the cantilever and the tip is then numerically modeled as an ellipse.

Linear Alkanes

The adhesion forces corrected for contact area with equation (5.2) are summarized in Table 5.2. The adhesion forces for the linear alkanes are strongest for the amine-terminated alkane, which correlates with previous reports of SWNTs having a higher propensity to adhere on a surface modified with amine terminated molecules [361]. The general trend observed is that the affinity of the alkanethiol decreases in the following order: $-NH_2 > -COOH > -C=C > -OH > -F_3 \approx -SH > -CH_3$.

An attempt was made to correlate these results with MD simulations as well as temperature programmed desorption studies that have been performed in other research labs studying carbon nanotubes and graphite. A discrete correlation could not be made, however there a several plausible explanations. Many of the methods used to study molecular interactions with HOPG [362-366] and activated carbon [367,368] assess the interaction of the bulk molecule with the carbonaceous substrate (i.e. the entire molecule lying on the carbon surface [369,370]). The interest here is strictly the interaction of the endgroup molecule with the nanotube backbone and thus far only molecules such as O_2, NO_2, NH_3, and CO have been run in simulational and experimental contact with a carbon nanotube [371-375]. Comparisons were also made between the theses measured binding force and the electronegativity of the endgroup of the ω-terminated alkanethiol although no noticeable trend was observed.

Table 5.2. Measured rupture forces for the alkyl-thiols after correcting for the contact area between the cantilever tip and the SWNT paper

Thiol	Rupture Force per molecule (pN)	Standard Deviation	# of Force Curves	F / R (nN/nm)	Standard Deviation
$-CH_3$	7.55	2.03	142	0.15	0.04
-S	8.24	2.55	1185	0.11	0.04
$-CF_3$	8.74	2.64	863	0.12	0.04
-OH	9.62	2.49	696	0.09	0.02
-C=C	11.38	2.76	943	0.18	0.04
-COOH	12.2	2.65	289	0.18	0.04
$-NH_2$	23.42	4.11	1029	0.34	0.06

Para-substituted Benzenethiols

Figures 5.12 and 5.13 depict a typical topographical images with each image's corresponding adhesion map (following data extraction). It is apparent from these images that the same topologically induced adhesion artifact is present. Thus, making conclusions strictly from the adhesion histograms (Figures 5.14 and 5.15) will not yield any meaningful result.

After correcting for the contact area-induced artifact (using a tilt angle of 40°[354]), it appears that the nitrile-terminated arylthiol clearly exhibits the highest binding force whereas the methyl-terminated arylthiol adhered the least (Table 5.3). The general trend in the adhesion force per molecule in regards to the substituient located at the *para*-position is: $-C\equiv N > -H > -OCH_3 > -F > -OH > -Br > -NH_2 > -NO_2 > -CH_3$.

A majority of the measured adhesion forces for the para-substituted benzenethiols are significantly higher than the adhesion forces measured for the alkanethiols. This could be due to a contribution of the aryl group interacting with the nanotube as well as the molecule located at the para-postion. It is also important to note that several of these para-substituted arylthiols are known to have significantly different packing densities [376-378]. Benzenethiol has been reported to both self-assemble with a regular packing angle but can also lie down on the surface with an extremely small tilt angle (less than 10°) [379]. If this were taken into account, the calculated binding force for per molecule for benzenethiol would increase drastically due to the drop in packing density.

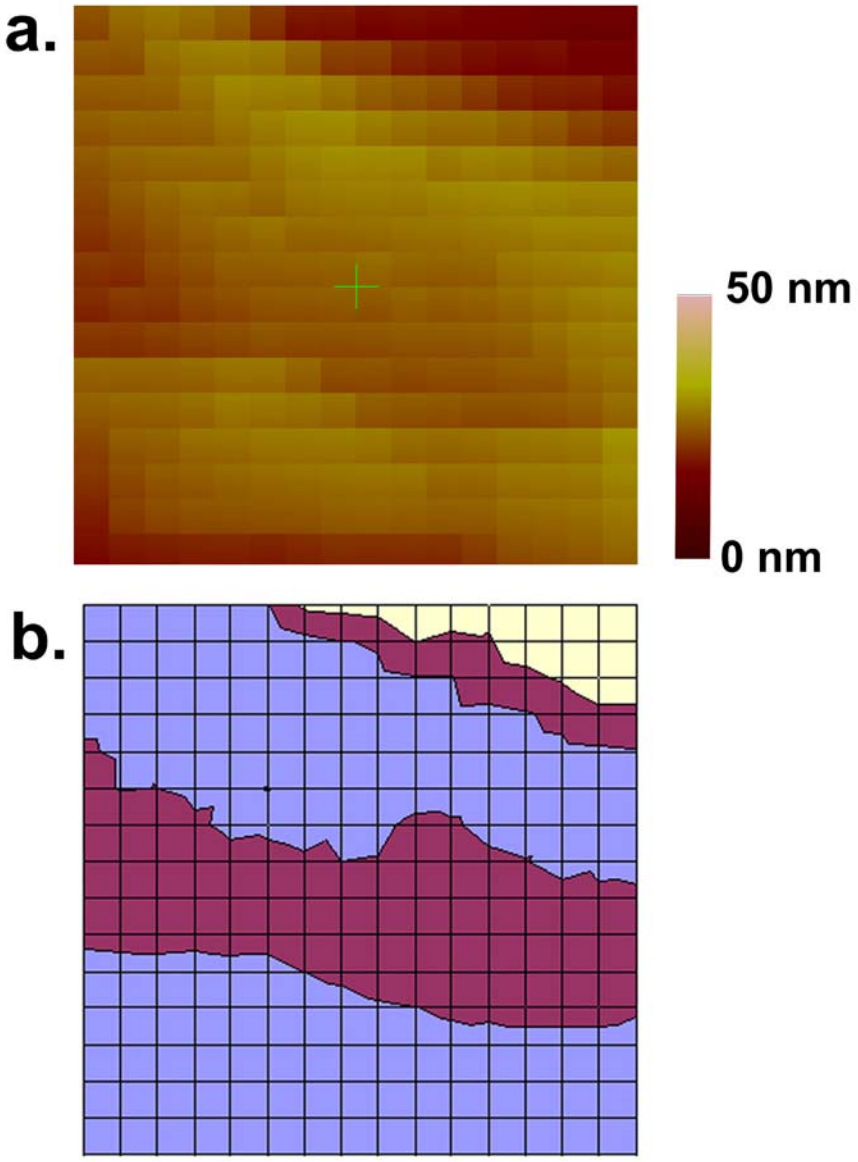

Figure 5.12. (a) Highly pixelated topographical image acquired in force volume mode using a cantilever tip that was modified with aminobenzenethiol (50 nm x 50 nm scan size). (b) Adhesion map generated from the individual force curves measured at each pixel in the image. The contrast in the adhesion map is blue represents an adhesive force from 0 to 4 nN, maroon 4-8 nN, yellow 8-12 nN, and green 12-16 nN.

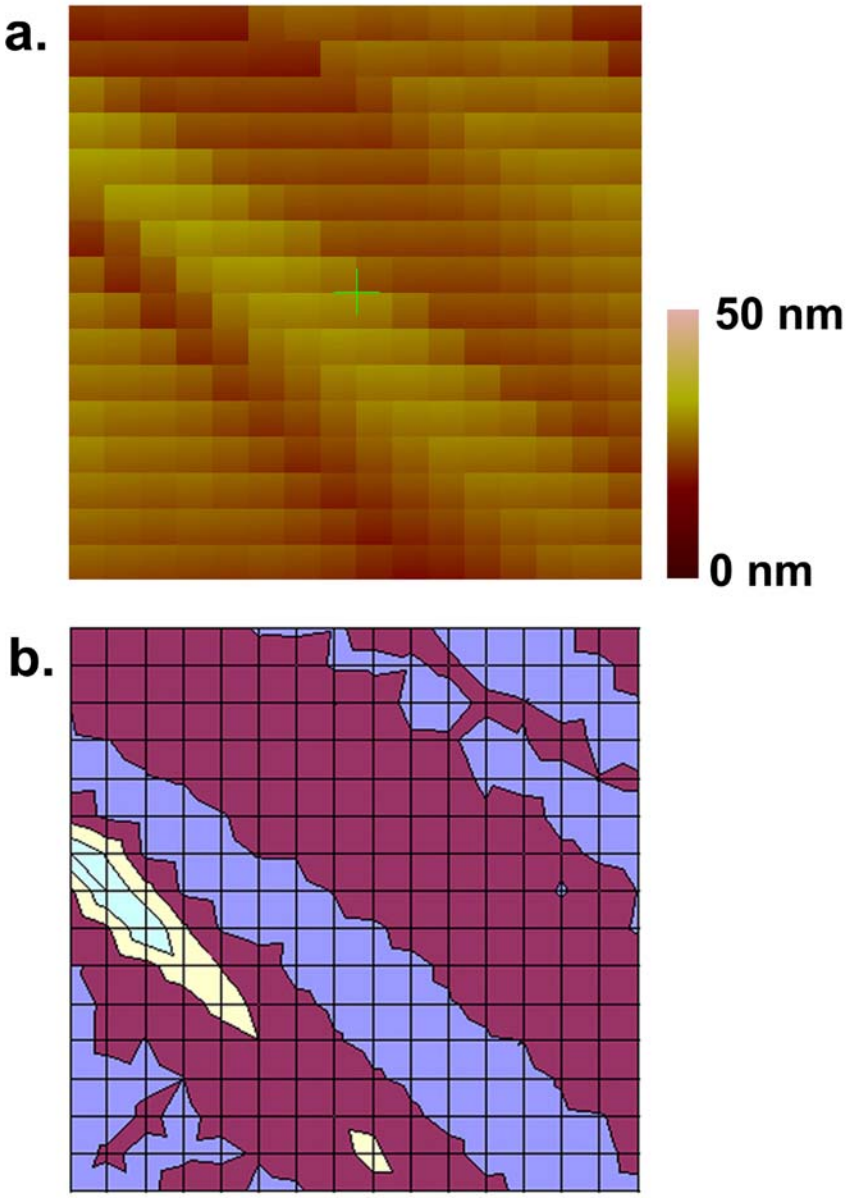

Figure 5.13. (a) Highly pixelated topographical image acquired in force volume mode using a cantilever tip that was modified with nitrobenzenethiol (50 nm x 50 nm scan size). (b) Adhesion map generated from the individual force curves measured at each pixel in the image. The contrast in the adhesion map is blue represents an adhesive force from 0 to 2 nN, maroon 2-4 nN, yellow 4-6 nN, and green 6-8 nN.

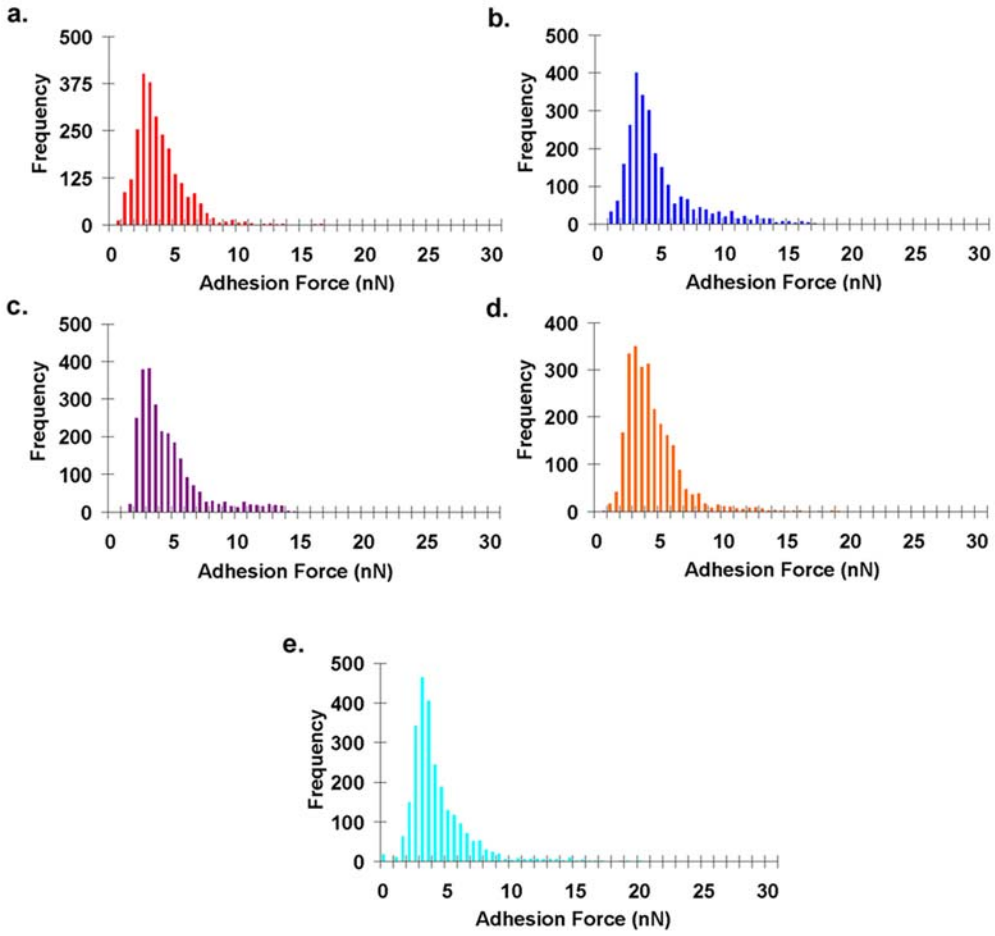

Figure 5.14. Histograms showing the distribution of forces required to detach a chemically modified cantilever tip from the SWNT paper (a) Methylbenzene (b) H-Benzene (c) Bromobenzene (d) Methoxybenzene (e) Fluorobenzene

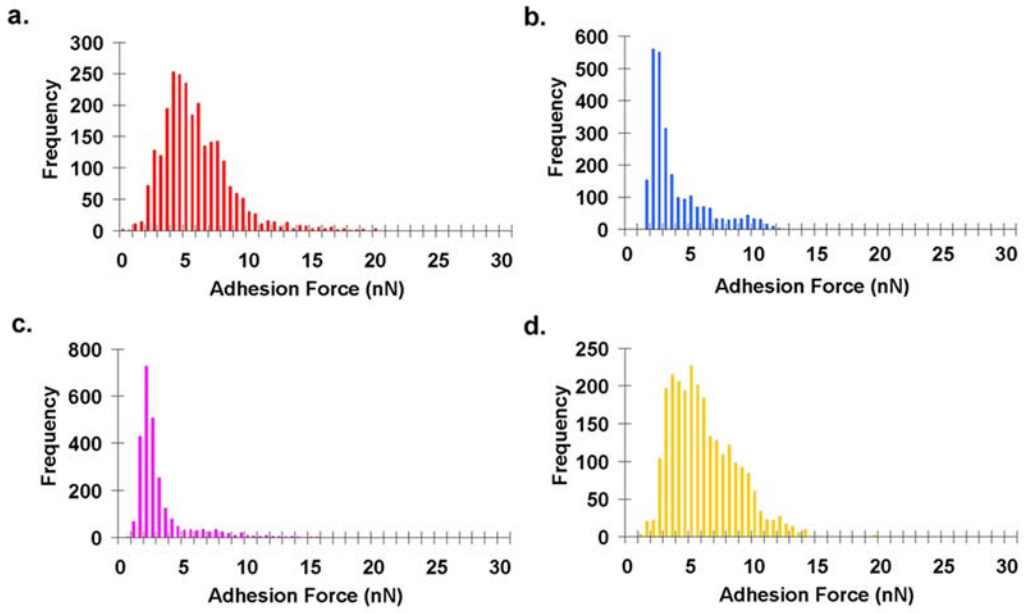

Figure 5.15. Histograms showing the distribution of forces required to detach a chemically modified cantilever tip from the SWNT paper (a) Hydroxylbenzene (b) Aminobenzene (c) Nitrobenzene (d) Cyanobenzene

Table 5.3. Measured rupture forces for the aryl-thiols after correcting for the contact area between the cantilever tip and the SWNT paper.

Thiol	Rupture Force per molecule (pN)	Standard Deviation	# of Force Curves	F / R (nN/nm)	Standard Deviation
4-Methylbenzene	18.94	5.65	873	0.22	0.06
4-Nitrobenzene	21.79	5.29	1735	0.26	0.06
4-Aminobenzene	22.64	4.66	1580	0.41	0.08
4-Bromobenzene	26.92	3.55	649	0.23	0.03
4-Hydroxybenzene	32.00	8.39	1044	0.55	0.14
4-Fluorobenzene	39.47	8.84	1436	0.39	0.09
4-Methoxybenzene	41.51	10.9	1531	0.58	0.15
H-Benzene	46.79	11.79	1256	0.52	0.13
4-Cyanobenzene	56.93	15.47	1392	0.66	0.18

An attempt has been made to correlate the experimental binding force per molecule and the ability of the substituent located at the *para* position to either accept or donate electrons with the nanotube. The parameters for used to makes these correlations are: hardness (η), ionization potential (I) [380], and each substituents sigma value (σ_p) (also called the Hammett substituent constant) [381]. Figure 5.16a depicts a somewhat linear relationship when comparing the binding force of the *para*-substituted aryl thiols to the reported sigma-value (i.e. the binding force increases as the ability of the substituent to withdraw electrons also increases). Figure 5.16b also depicts somewhat linear relationship between the measured adhesion force per molecule versus the hardness (η) and the ionization potential (I). Potential correlations with other substituent parameters for the aryl thiols were investigated but no noticeable trend was observed. [382].

Recently, scientists have demonstrated that certain molecules (when in contact with a nanotube) can modulate the band-gap of the nanotube backbone [383-385]. Star and co-workers have recently shown a strikingly similar linear relationship between the gate voltage modulation of a SWNT-based field-effect transistor (FET) and each molecules Hammett substituent constant [386] (Figure 5.17). TPD and MD studies have also shown similar trends [387-390]

One might expect that the fluorinated benzene derivative used in the adhesion mapping studies, might yield a similar response in the gate voltage modulation to that of a chlorinated aromatic compound (characterized by Star et al.), due to the similarities in the arrangements of the electrons in the outer shells of fluorine and chlorine. Deviations

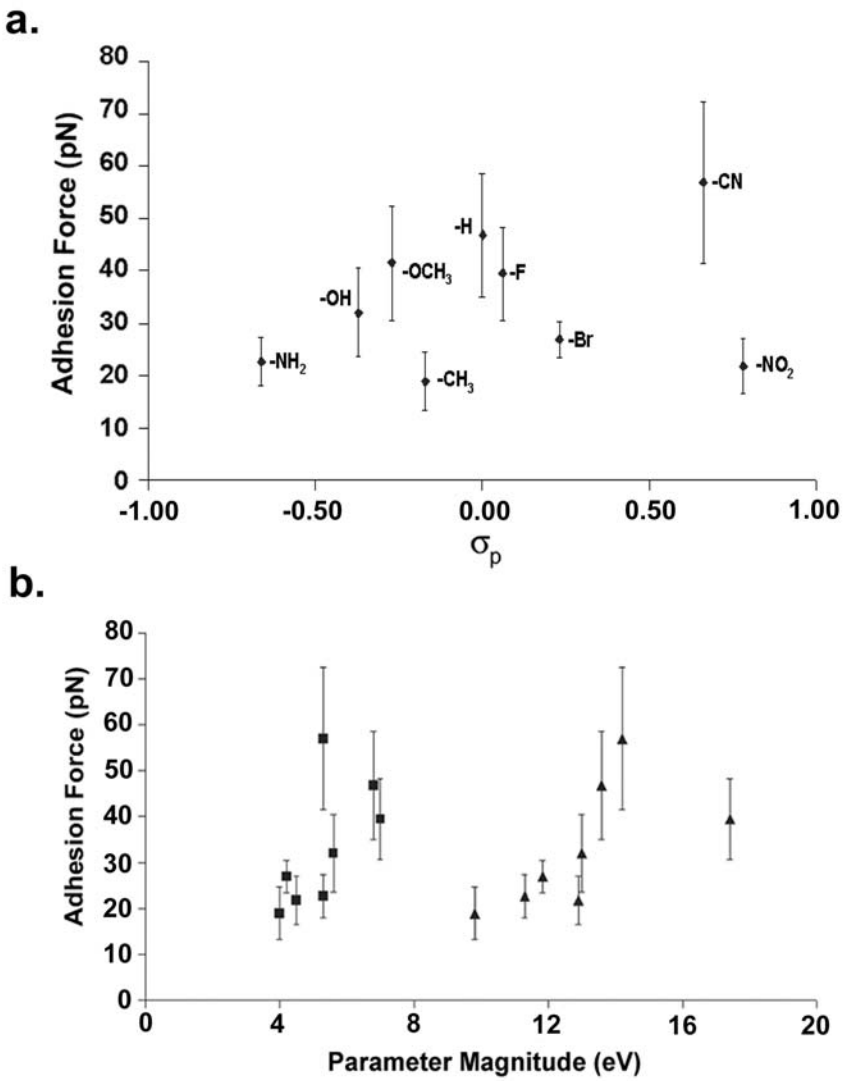

Figure 5.16. (a) Plot of the measured rupture force per molecule vs. the corresponding Hammett parameter of a *para*-substituted benzene molecule. (b) Plot of the measured rupture force per molecule vs. the magnitude of each respective hardness parameter (■- absolute hardness, ▲- basic ionization potential)

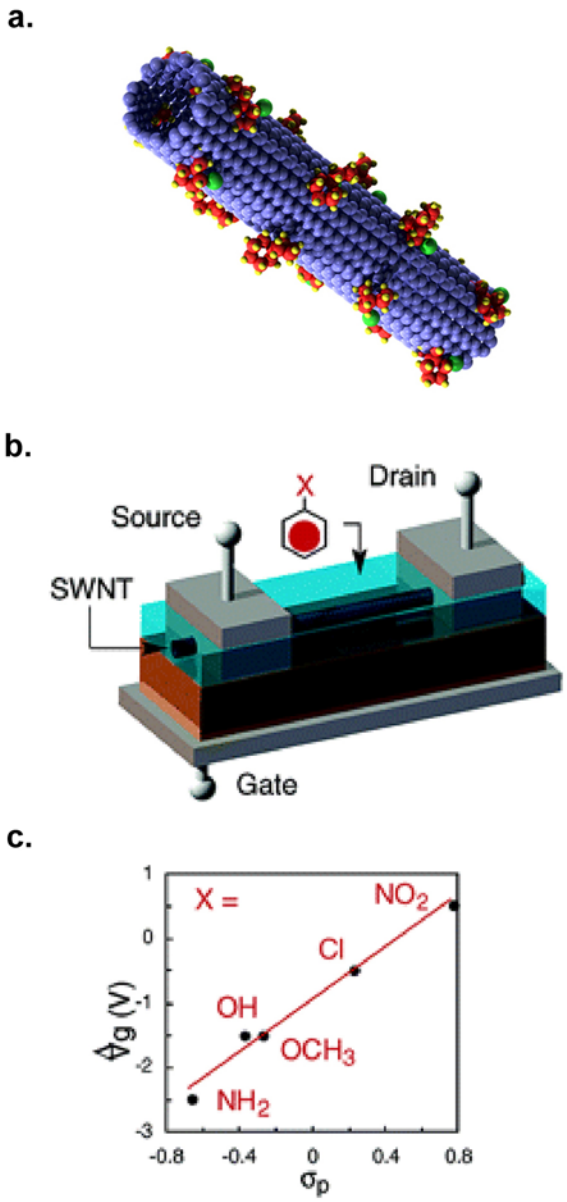

Figure 5.17. (a) Cartoon depicting the interaction of *para*-substituted benzene molecules with a SWNT (Copyright by Nanomix Inc.). (b) Cartoon depicting a SWNT-based field-effect transistor that was used to detect *para*-substituted benzene molecules. (c) Linear regression analysis of the gate voltage shift (ΔVg) of NTFET device in 0.1 M cyclohexane solutions of the selected aromatic compounds. Reproduced with permission from *Nano Letters* **2003**, 3(10), 1421-1423.Copyright 2003 American Chemical Society.

between the work done by Star et al. and the experiments presented here, could be a result of the orientation and packing of the molecules on the tip of the cantilever compared to the sterically uninhibited orientations of the para-substituted benzene molecules in solution.

Conclusions

By characterizing the local adhesion across SWNT paper, the adhesion of specific molecules and the sidewall of carbon nanotubes has been quantified. Chemical force microscopy has been used to probe the specific chemical interactions. It has demonstrated that the topography of the sample and the radius of the cantilever tip have a large impact on the adhesive forces. By accounting for the contact area between the cantilever tip and the features of the substrate, a more accurate interpretation of mechanical forces is possible [338].

The results reported herein have broad implication. Incorporating the functional groups identified herein with strong adhesive interaction with the nanotube's sidewalls into polymers could strengthen the polymer-nanotube interface. This should enable more effective dispersal of the carbon nanotubes in the polymer composite matrix. CFM can effectively be used as a tool that can further enhance our understanding of the interfaces that exists between filler and composite materials.

CHAPTER 6

MEASURING THE COMPRESSION/BENDING OF A CARBON NANOSPRING

Introduction

Creating nanometer scale devices is one of the major challenges of the new millennium. This goal cuts across many disciplines, requiring extensive collaboration between scientists and engineers. Carbon nanotubes have attracted a lot of interest for potential nanoscale applications because of their unique mechanical and electrical properties. Carbon nanotubes can be as long as hundreds of microns yet have diameters of only a few nanometers. Most single walled carbon nanotubes (SWNT) are straight, whereas the multi walled carbon nanotubes (MWNT) can have straight as well as a coiled morphology [391,392].

Knowledge of the mechanical properties of nanoscale materials is important to research that pertains to the development of functioning nanoscale devices. Several "potential" uses for many of the nanoscale materials being developed in labs across the globe have little or no evidence of the true physical characteristics of these materials. Thus, more invasive experimental techniques need to be developed that can facilitate the manipulation and interpretation of how materials on the nanoscale behave.

In an effort to achieve a more complete understanding of the mechanical response/properties of nanoscale objects, an *in situ* AFM investigation of the mechanical response of a coiled MWNT (nanospring) under compression was investigated. A

MWNT nanospring was fixed on the tip of the cantilever (Figure 6.1) and brought in contact with a surface using the precise positioning of an AFM. A multi parameter force spectroscopy (MPFS) technique has been devised that monitors several of the key output signals that are generated during a typical AFM-based force spectroscopy measurement. Vertical cantilever deflection, torsional cantilever movement, thermally-driven resonance and substrate position are all synchronously monitored during the compression and decompression of the nanospring.

Experimental Setup

The MWNT coil used herein was fabricated and mounted on a FESP silicon probe (Veeco, Santa Barbara, CA) at NASA Ames (Figure 6.1). This nanotube-mounting process has explained in detail elsewhere by Stevens and co-workers [195]. A NSC12 silicon AFM probe (NT-MDT, Zelenograd, Moscow) was used as a control cantilever since its resonance frequency was close to that of the MWNT-tipped cantilever. Cantilever spring constants were determined via the modified method presented in Chapter 3.

All mechanical tests were performed under a nitrogen atmosphere using a Nanoscope IIIa (Veeco, Santa Barbara, CA) scanning probe microscope operating in Tapping Mode™. The piezo scanner was calibrated in x, y, and z dimensions using NIST certified calibration gratings (MikroMasch). The substrate was a template stripped gold surface [393] that was pretreated with 11-dodecanethiol (Sigma-Aldrich). This surface treatment

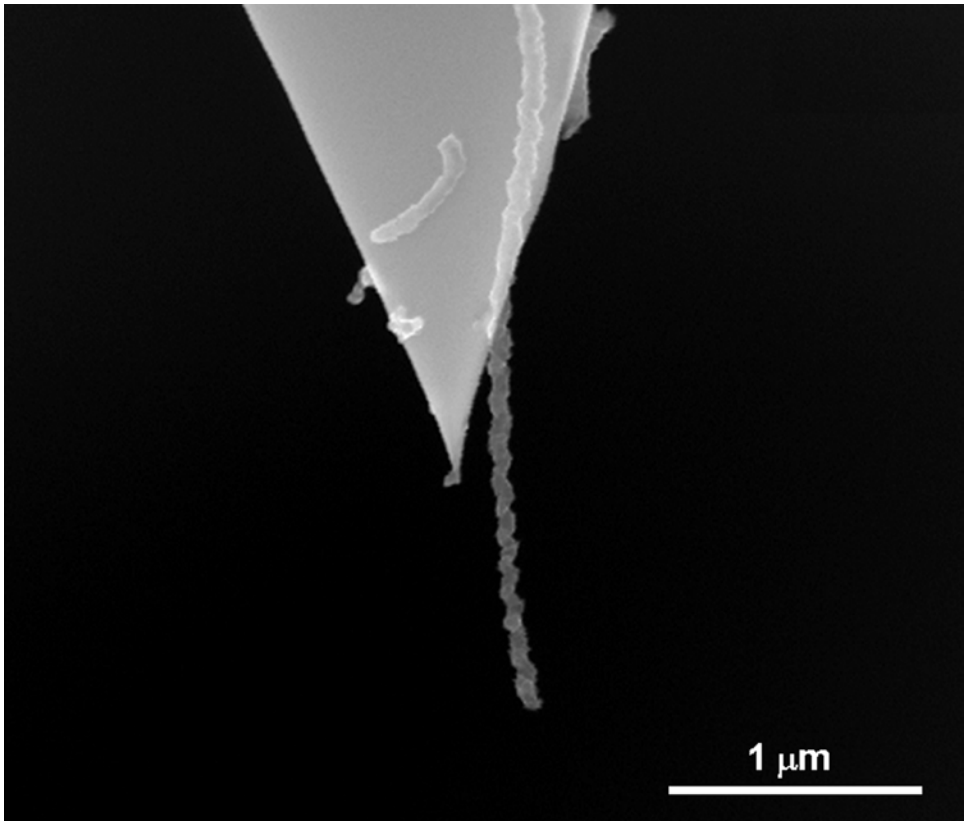

Figure 6.1. SEM image of the multiwalled nanospring mounted on the end of a cantilever tip.

was chosen to minimize adherence of the nanospring to the substrate (as was demonstrated in Chapter 5)

Each experiment commenced by cycling the scanner in the z-direction for ~2 hours to allow the scanner to reach thermal equilibrium. Then false engagement of the microscope was initiated at a point where the nanospring was not in contact with the surface of the substrate. The microscope was immediately toggled from image acquisition to force curve operation whereby cantilever deflection is monitored as a function of scanner vertical movement. Force curves were acquired at four different scanner velocities (400, 200, 100 and 50 nm/sec) with and without the cantilever being driven at its natural resonance with an oscillator on the cantilever holder. The natural resonance frequency was determined a priori using the thermal spectrum method.

To acquire cantilever resonance information simultaneously with cantilever deflection, cantilever torsion and scanner position, the cantilever deflection signal was routed from the signal access module to a SRS 785 Dynamic Signal Analyzer (DSA) (Stanford Research Systems, Sunnyvale, CA) (Figure 6.2). The DSA acquired the time-dependent deflection data, converted it into the frequency domain using a BMH window, ensemble averaged the resultant power spectral density plots (PSD), and displayed them in a "waterfall" format. The acquisition time per spectra was 7.81 ms, the number of averaged PSDs per ensemble was 25, and the number of ensembles per "waterfall" was 150. Thus, the time duration of each "waterfall" plot was 29.3 s. During this period, the number of nanospring compression/decompression cycles was proportional to the scanner

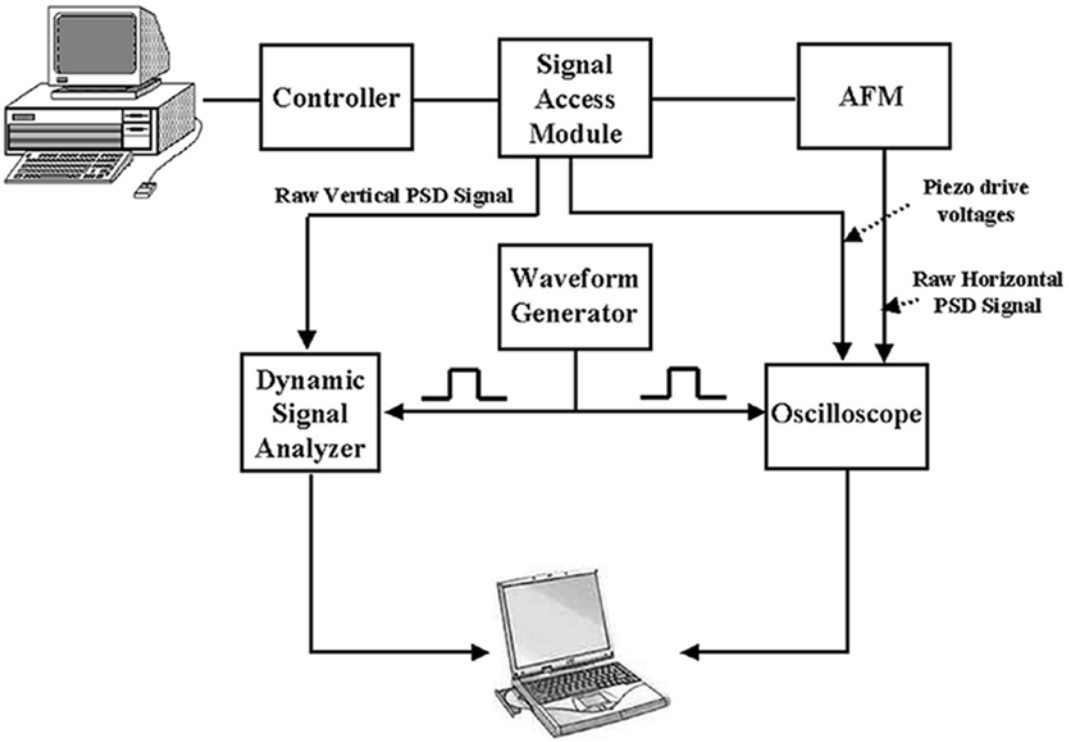

Figure 6.2. Schematic of the experimental setup used to simultaneously monitor substrate position, horizontal cantilever movement, and thermally driven resonant spectra.

velocity. A square wave pulse (2.5 V_{pp}) from a 33120A Function / Arbitrary Waveform Generator, 15 MHz (Agilent, Palo Alto, California) was used to trigger acquisition of the waterfall by the DSA. A 9304M Quad Oscilloscope (LeCroy, Chestnut Ridge, New York) was used to record the piezo drive voltage signal, the horizontal deflection signal and the triggering pulse over time. This pulse made possible time synchronization of scanner movement horizontal deflection signal and acquired thermal spectra. The horizontal cantilever deflection signal was accessed directly from the printed circuit board on the base of the microscope. All data were downloaded to a computer through a USB-B GBIB interface (National Instruments, Austin, Texas) with a data acquisition and processing program written in C++ and Visual Basic.

Results and Discussion

Standard Cantilever Contact

Figure 6.3 depicts cantilever deflection and oscillation amplitude as a function of scanner movement typical of the traces obtained when a silicon tip is brought into contact with the methyl-terminated alkanethiol modified gold substrate. On the approach of the substrate towards the tip, no cantilever deflection is observed until the tip is in contact with the substrate (Figure 6.3a). At the point of contact, the cantilever oscillation amplitude drops to a baseline value (Figure 6.3b). Further extension of the scanner results in a proportionate increase in cantilever deflection but no change in oscillation amplitude. Upon retraction, the tip remains in contact with the substrate long after the initial point of contact due to strong adhesion between the tip and the substrate. Once the restoring force of the cantilever exceeds the adhesive force, the tip releases from the

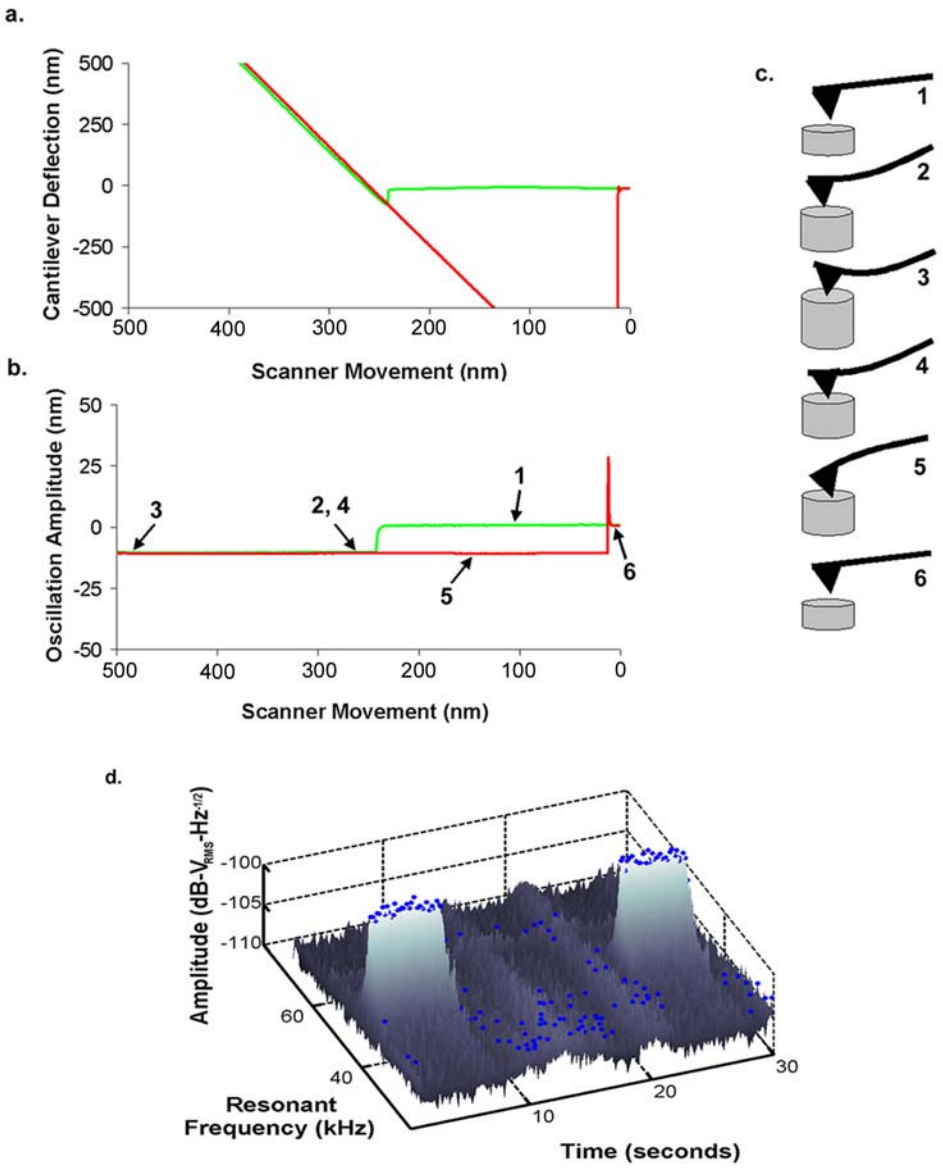

Figure 6.3. (a) Force curve and (b) cantilever oscillation amplitude curve acquired in tapping mode with a silicon cantilever. Cantilever deflection and oscillation amplitudes are displayed for both the approach (green) and retraction (red) of the scanner relative to the tip and were acquired at a z-scan size of 500 nm and a z-scan rate of 0.1 Hz. (c) Illustration of the position of the cantilever above the substrate during the movement of the scanner. (d) Cantilever thermal resonance spectra obtained during the acquisition of a single force curve (150 thermal spectra displayed). Blue markers indicate the amplitude of the highest resonance peak in each spectrum. During the initial part of the approach, the cantilever's fundamental mode of resonance is present but is subsequently damped upon the contact of the tip with the substrate. In part (a) & (b), the green trace denotes the signal acquired during scanner extension; the red trace denotes the signal acquired during scanner retraction. This color scheme is used throughout this dissertation.

surface restoring the cantilever deflection and oscillation amplitudes to the values observed initially when the cantilever tip was above the substrate surface. Release of the tip from the substrate surface produces a sharp but transient increase in amplitude due to "ringing" (high 1/f component) until its natural thermal vibration is restored. Figure 6.3c interprets the various regions of the deflection and oscillation amplitude traces by illustrating cantilever deflection and tip-substrate gap at various scanner positions.

Figure 6.3d presents the thermal resonance spectra acquired during a single force curve for the silicon tip contacting the thiolated gold substrate. For clarity, only the frequency span between 20 and 80 kHz is displayed. When the tip is above the surface of the substrate, the primary resonant mode of the cantilever is observed at 57.0 kHz. This resonant mode is eliminated upon contact and remains so until the tip is released from the surface. The 1/f noise component (not shown) is dampened as well. We postulate that when the tip is in contact with the substrate, the primary resonant mode of the cantilever beam is dampened. Varying the scanner velocity only altered the duration for which the cantilever oscillation was dampened. These observations parallel those previously reported [394].

NanoSpring Response

Deflection\Oscillation Amplitude

Figure 6.4a (upper panel) presents the cantilever deflection signal observed when a nanospring-tipped cantilever was brought into and out of contact with the methyl-terminated alkanethiol modified gold substrate. Scanner movement was large enough to

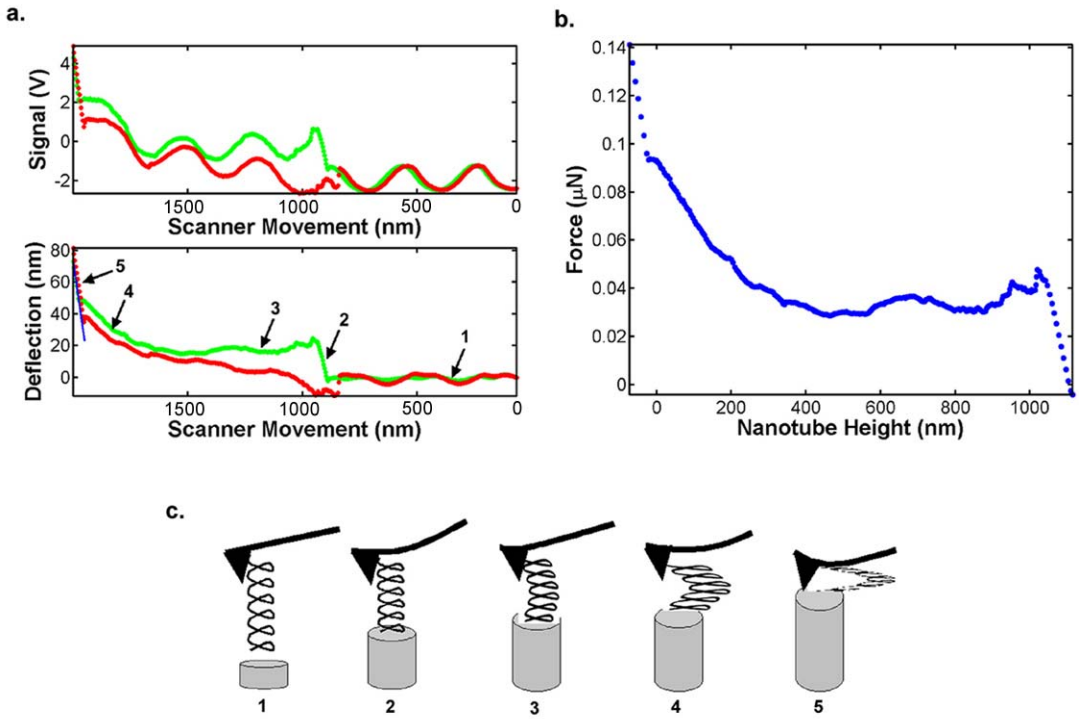

Figure 6.4. (a) Raw cantilever deflection signal (top frame) as a function of the position of the scanner (bottom frame); cantilever deflection versus scanner movement after the removal of optical interference. (b) Load exerted on the nanospring when the substrate is pushed toward the cantilever. (c) Illustration of the postulated response of the nanotube during vertical loading.

encompass both compression of the nanospring and mechanical contact between silicon cantilever tip and the substrate. The distance between point of contact of the substrate to the nanospring and to the silicon tip is ~1100 nm compares well with the length of nanospring extending above the silicon tip as measured by analysis of the SEM image (Figure 6.1). The oscillatory motion of the voltage signal, is a result of optical interference created by the laser light reflecting off of two interfaces (the top of the cantilever and the reflective substrate). Removal of the contribution of optical interference to the cantilever deflection signal was achieved by fitting a sine function to the portion of the curve in which the nanospring was not in contact with the substrate. The domain of this function was extended over the range of scanner movement and subtracted from the force curve. The result was then multiplied by the detector sensitivity. Figure 6.4a (lower panel) presents the magnitude of cantilever deflection versus scanner movement. The force applied to the nanospring was computed by multiplying cantilever deflection by the cantilever beam spring constant. Figure 6.4b depicts the force exerted on the nanospring during compression (the x-axis is a rescaling of the scanner movement axis in Figure 6.4a relative to the point of contact). From the slope of the steeply rising portion of this trace, a stiffness of 0.7 N/m for the nanospring was computed. The postulated response of the nanotube during vertical loading is illustrated in Figure 6.4c. Prior to contact of the nanospring with the substrate, no deflection is observed (item #1). During the steeply rising portion (item #2) the cantilever is deflecting rapidly with scanner movement commensurate with compressive loading of the nanospring until bending occurs. Additional movement of the scanner results in increased bending with little change in cantilever deflection (item #3). When

the nanospring is further compressed past item #3, the nanospring appears to get stiffer (plausibly a second bending moment) as the slope of the beam deflection versus scanner movement increases (item #4) until the substrate contacts the silicon tip onto which the nanospring is appended (item #5).

Repeated compression/buckling/decompression of the nanospring was very reproducible. Figure 6.5 depicts the average of five consecutive force curves acquired when scanner movement was limited to 500 nm (limiting compression of the nanospring to only 400 nm). Clearly evident in this figure is remarkable reproducibility in cantilever deflection during the bending of the buckled nanospring. Note that on the retract cycle, the nanospring remains attached to the substrate for ~60 nm indicating some adhesive interaction between the terminus of the nanospring and the chemically modified substrate. This high degree of reproducibility suggests that the placement and orientation of the nanospring is constant throughout this series of compression/decompression cycles.

It has been previously reported that monitoring shifts in oscillation amplitude can be used to interpret the mechanical response (contact and buckling) of an MWNT-tipped cantilever. Figure 6.6a presents the dependence of oscillation amplitude on scanner movement acquired during one of the force curves presented in Figure 6.5. The shape of this curve is qualitatively similar to those previously reported for MWNT-laden tips (as described in Chapter 3) A decrease in oscillation amplitude is observed when the nanospring touches the surface and it falls to the baseline upon additional loading. No

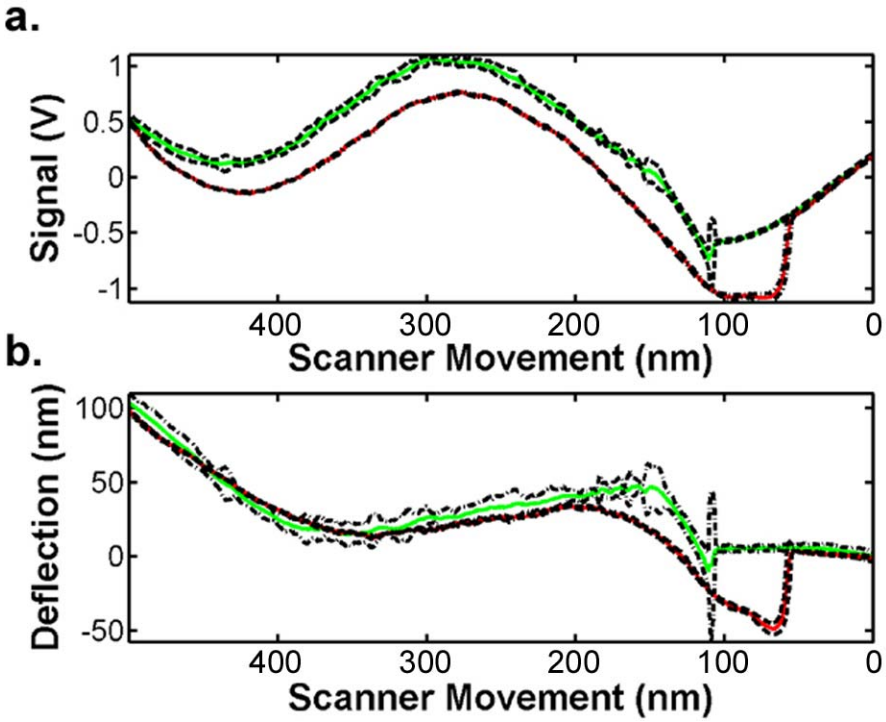

Figure 6.5. (a) Plots of the average of five force curves acquired with the nanospring tip before and (b) after correcting for optical interference. The green trace is the approach, and the red trace is the retraction of the scanner relative to the tip; black lines indicate the confidence interval about the mean ($\pm 5\sigma$).

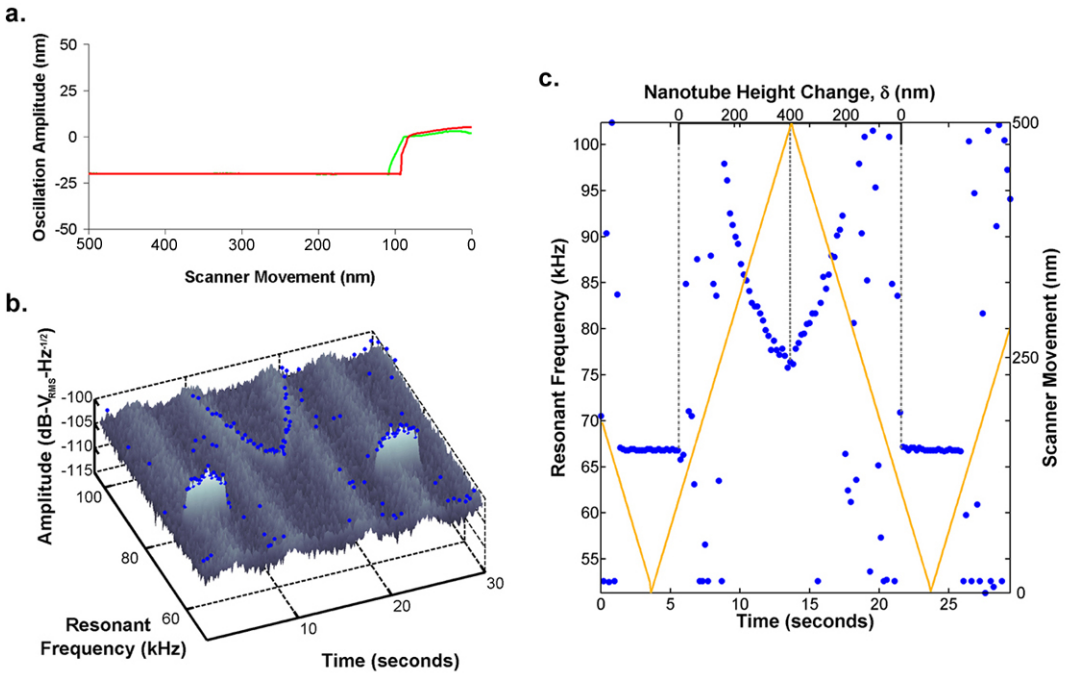

Figure 6.6. (a) Oscillation amplitude change of the nanospring-tipped cantilever as the surface is brought into intimate contact with the nanotube and then subsequently pulled away from the nanospring. (b) Time-synced cantilever thermal resonance during the acquisition of a single force curve. Blue markers indicate the peak amplitude of each FFT (150 thermal spectra displayed). (c) Nanospring-tipped cantilever peak resonance (blue) with time-correlated scanner movement (yellow). Note that a secondary x axis is provided to enable a comparison of the observed frequency shift with the extent of nanospring compression.

change in oscillation amplitude is observed until the nanospring is released from the surface on retraction of the scanner. Since the oscillation amplitude trace records the amplitude only at the drive frequency being imposed on the cantilever, a decrease in oscillation amplitude can be due to either loss of beam resonance (as observed for the silicon tip in contact with the substrate) or a shift in the resonant frequency of the cantilever. It has been widely reported that when straight SWNT and MWNT tips come in contact with a substrate, the cantilever oscillation amplitude is dampened [200,203]. Further compression results in the buckling of the nanotube; an increase in cantilever oscillation amplitude is observed at the moment of buckling. Since an increase in amplitude was not observed in this study, a shift in the resonant frequency is a likely possibility for this particular nanospring-tipped cantilever.

Resonant Response

To distinguish between dampening versus shifting of cantilever resonant frequency, we continuously acquired thermal resonance spectra during a single force curve for the nanospring-tip (Figure 6.6b). Prior to the point of contact, the cantilever resonant frequency was 67.8 kHz. At the point of contact, the fundamental vibration mode of the beam\nanospring markedly increases beyond the range of our spectral analyzer (102.4 kHz) and remains so during compression of the nanospring. After buckling of the nanospring, the resonance frequency drops to a value of 76.2 kHz at full extension of the scanner. Then, as the scanner retracts away from the nanospring, the resonance frequency increases until it again exceeds the range of the analyzer. At the point of release of the nanospring from the surface, the resonance of the free beam again returns

to its fundamental resonance. Figure 6.6c presents the time dependence of the maximum peak in the thermal spectrum as a function of time during force curve acquisition. Overlaid on the frequency-time data is the scanner movement enabling ready comparison of the frequency shifts with position. The points of contact and release of the nanospring with the substrate is identified by the zero point on the secondary x-axis labeled "nanotube height change." The time correlated horizontal photodiode signal (not shown) was unchanged during the entire extension and retraction of the scanner, indicating that the cantilever beam underwent no detectable torsional strain. Given the large torsional spring constant of this particular beam, this was the expected result.

Comparison of the oscillation amplitude (Figure 6.6a) and frequency (Figure 6.6c) versus scanner movement reveals that the point of decrease of oscillation amplitude correlates with contact of the nanospring to the substrate. For this particular coiled MWNT tip, the oscillation amplitude remains baselined through the compression and buckling regions and returns to the free oscillation value only after release of the nanotube from the substrate. This is quite different from that reported for straight nanotube-tipped cantilevers and calls into question some of the previously reported interpretations of nanotube-tipped AFM probes based exclusively on changes in the oscillation amplitude signal.

The frequency shift that was observed upon compression of the nanotube was extremely reproducible (Figure 6.7a). It is also important to note that the amplitude of the cantilever/nanospring oscillation follows a similar trend. This also brings to light a

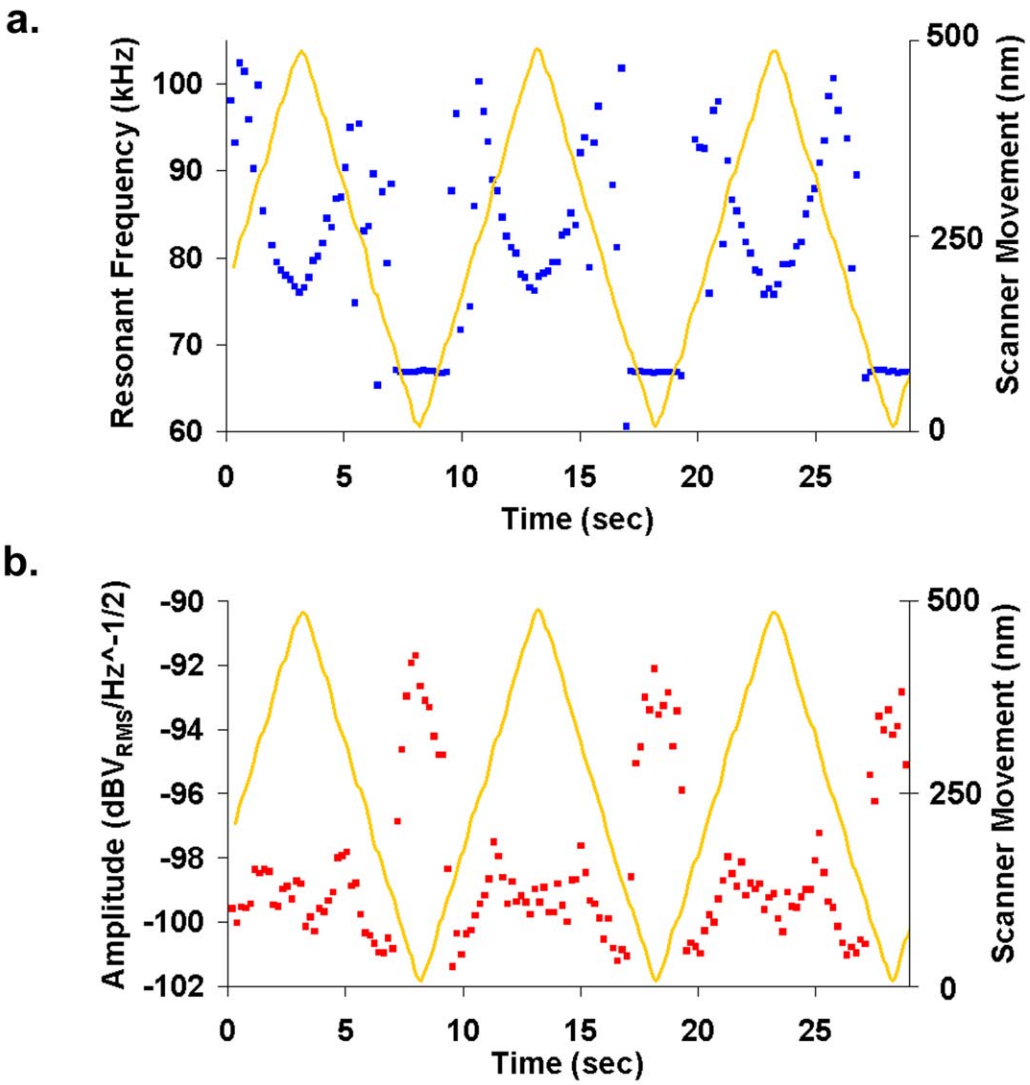

Figure 6.7. (a) Resonant frequency of the cantilever/nanospring (blue) and scanner position (yellow) upon repeated contact with the underlying substrate. (b) Corresponding resonant peak amplitude (red) of the cantilever/nanospring before and during contact with the underlying surface. Substrate was moving at 100 nm/sec.

limitation of the resonance method: if the oscillation amplitude of the cantilever/nanospring is not above the noise floor, following the resonance shifts will prove extremely difficult. This could potentially be circumvented by performing these compression studies in fluid, which inherently drops the amplitude of the noise floor but also drops the amplitude of oscillation of the cantilever beam (due to fluidic viscous dampening [223])

From high degree of reproducibility of the observed resonant shifts, it is assumed that compression and bending of the nanospring is highly reproducible and unlikely to cause defects in the nanospring. However, the location of the bending movement of the cantilever is difficult to establish. Whether this buckling phenomenon occurs randomly along the nanospring or specifically at a defect site is a point of speculation.

Modeled Response

Analytic modeling

Its proposed that the cantilever-nanospring system follows a simple two spring, two mass series model (Figure 6.8a), mathematically described by Equation 6.1

$$f_0 = \frac{1}{2\pi}\sqrt{\frac{k_{eff}}{m_{eff}}} = \frac{1}{2\pi}\sqrt{\frac{k_B + k_{NT}}{m_{eff}^B + m_{NT}}} \qquad \text{Equation 6.1}$$

where f_0 is the resonant frequency of the spring system, k_B is the cantilever beam stiffness, m_{eff} is the effective beam mass equal to 0.24 times the actual beam mass [207], and m_{NT} is the effective nanotube mass (assumed to be negligible henceforth) and the nanotube stiffness, k_{NT}, being a function of the change in nanotube height due to loading.

With a nanotube mass of zero, the system reduces to that shown in Figure 6.8a. In practice, the beam deflections measured in the experiments correspond to the variable α (defined in Figure 6a) while γ corresponds to the scanner movement after it contacts the nanotube. Note that the top plate in Figure 6.8a is the analog to the fixed end of the cantilever, and hence is fixed in space. Equation 6.1 is derived from the two-spring model by employing a conservation of power assumption (or by solving the equations of motion). Another useful relationship can be derived from the system by noting that the change in nanotube spring height, δ, is equal to $(\gamma - \alpha)$, both of which are available experimentally. An assumption here is that the scanner displacement after contact with the nanotube (i.e., γ) must always be larger than the beam deflection (i.e., α) else we would see a beam deflection larger than the amount of scanner displacement during nanotube-scanner contact. Another assumption is that the substrate mounted on the scanner is completely rigid and not deformed by the nanotube. By assuming static equilibrium we can equate the two forces acting on the effective mass, namely that due to the nanotube, ,

$$k_{NT}\delta = k_{NT}(\gamma - \alpha) \qquad \text{Equation 6.2}$$

and that due to the beam, $k_B\alpha$. This leads to Equation 6.3, an expression for nanotube stiffness under the previously discussed assumptions.

$$k_{NT} = \frac{k_B\alpha}{\delta} = \frac{k_B\alpha}{(\gamma - \alpha)} \qquad \text{Equation 6.3}$$

All of the values of the right side of the equation are experimentally determined. If the beam stiffness and the effective mass are constant then to observe a change in resonance frequency, the nanotube stiffness must vary, manifested by the change in the quantity

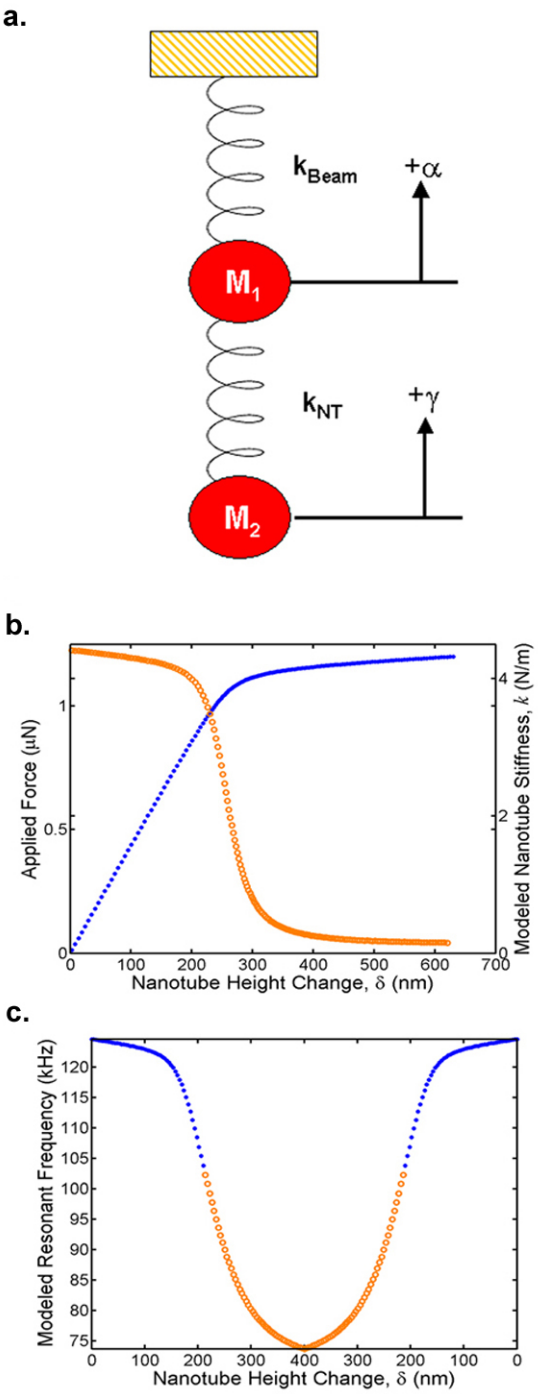

Figure 6.8. a) Model of the cantilever-nanospring system. (b) FEA simulated nanotube force versus height-change curve (blue closed circles, left-side scale) and stiffness versus height change (orange open circles, right-side scale). (c) Modeled resonance frequency versus nanotube height-change plot (orange open-circle data points fall below 102.4 kHz, to be compared with the nonzero nanotube height-change region of Figure 6.6(c).

$\alpha/(\gamma-\alpha)$ as the scanner motion proceeds. Solving Equation 6.3 for the measured beam deflection α gives the proper asymptotic behavior with respect to the nanotube stiffness (i.e., $\lim_{k_{NT}\to\infty} \alpha = \gamma$ and $\lim_{k_{NT}\to 0} \alpha = 0$).

The assumption of constant cantilever stiffness is validated in the force-distance curve (see Figure 6.4a). The linearity of cantilever deflection versus scanner movement in the contact region is indicative of constant stiffness (i.e. $k_i \equiv \partial F_i / \partial x_i$ for a single force F_i displacing a spring in the x_i coordinate). [14,395] The beam stiffness was calculated using Euler-Bernoulli beam theory [221], i.e. Equation 6.4.

$$k_B = \frac{3EI}{4L^3} \qquad \text{Equation 6.4}$$

Beam geometry was determined by using a white light interferometer (Zygo Newview 3000, Zygo Corp., Middlefield, CT) and an SEM (Hitachi S-800). The geometric values were used to calculate the second moment of the cross sectional area, I. The elastic modulus of the silicon beam was 180 Gpa [7]. When the calculated beam stiffness of 1.99 N/m and the beam mass (using a density of 2330 kg/m^3) [218] was substituted into equation 1 (with a nanotube stiffness of zero to simulate the free fundamental resonance of the cantilever), the predicted resonant frequency is 66.8 kHz, in good agreement with the value of 67.8 kHz from the thermal spectrum.

While the beam stiffness is constant, the experimental results suggest that the nanotube stiffness is not. During initial nanotube-cantilever loading, (i.e., nanotube contact with a

surface) k_{NT} is constant as the loading is mainly axial; the nanotube behaves as a simple compression spring (i.e., linear). However, upon onset of buckling, bending, and possibly other modes of deformation, the nanotube stiffness changes as the force required for a given deflection is different in this deformational mode than in the axial deformation mode. This change in nanotube stiffness produces a resonance frequency shift in accordance with Equation 6.1.

Finite Element Modeling

To validate the proposed model of the nanospring-cantilever as a two-spring system, nonlinear structural finite element analyses (FEA) were conducted to simulate the mechanical response to the applied load. The particular MWNT coil used in this study was comprised of 5-10 layers. An effective wall thickness of 0.32 nm [396] was assumed. Since the spacing and number of walls comprising the MWNT spring were not precisely known, the nanospring was geometrically modeled as a solid helical cylinder. The length and diameter of the cylinder were that of the nanospring length and coil diameter as determined by SEM (Figure 1). Previous research has shown huge ranges for the effective thickness (from 0.66 [397] to 3.4 Å [398]) and elastic modulus (from 1.0 [398] to 5.5 TPa [397]). The nanospring was given an elastic modulus of 1 TPa comparable to the literature value for a 10 wall nanotube). [399]

A computer model was generated (ProEngineer Wildfire, Parametric Technology Corp., Needham, MA) using this information and subsequently imported into the finite element analysis program (ANSYS 7.1, ANSYS Inc., Canonsburg, PA). An adaptive meshing

scheme (i.e., the p-method) was implemented with a convergence criterion of 5% on the total model strain energy. The boundary conditions fixed the displacement and rotation of all nodes at the base of the beam (effectively cantilevering the beam) and applied two force components to the nodes corresponding to the end of the modeled nanospring (to simulate the 12° angle of the cantilever relative to the thiol-treated template-stripped gold surface). It should be noted that other deformational behavior could manifest, such as a rippling mode [288,400-402] or some nanospring slippage, but our simulations did not model this, nor did it allow any collapse of the thiol-terminated gold surface. Note that this simulation assumes that the bottom of the nanotube is free to rotate and displace but does not account for any nanotube-surface interactions.

Conclusions

The results of the FEA simulation, presented in Figure 6.8b, predict nonlinearity in nanospring stiffness under applied force. Nanospring stiffness is predicted to be high during initial loading (axial) and then progresses to a lower value during secondary deformational modes. To compare the simulation to the experimental data, the nanotube stiffness values from Figure 6.4b, up through a nanospring height change of 400 nm (the amount of compression experienced by the nanotube in our experiments), were substituted into equation 1 (using the calculated beam stiffness of 1.99 N/m). The predicted resonant frequency versus nanotube height change is plotted in Figure 6.8c. Comparison of Figure 6.8c to the experimental data depicted in Figures 6.6 and 6.7 shows qualitative agreement.

The predicted nanospring stiffness (Figure 6.8b) ranges from 4 N/m down to near zero N/m. Our measured nanotube stiffness (from Figure 6.4b) varies from only 0.7 N/m in the axial regime down to roughly zero N/m after buckling. Thus, the measured value in the axial compression regime is a factor of six lower than the predicted value. However, the x-axis in Figure 3b was calculated under the assumption that scanner displacement is equal to the displacement of the bottom of the nanotube (no substrate compliance under load). If, in reality, the substrate is compliant, then the change in nanotube height during the experiment is less than the assumed value of $(\gamma - \alpha)$ and the experimentally determined stiffness would be larger than 0.7 N/m. Secondly, when the measured stiffness value is inserted into equation 1, the calculated maximum resonant frequency is only 80 kHz, in disagreement with the experimental results presented in Figure 6.7c. Thus, the discrepancy between measured and predicted nanospring stiffness values is predominantly due to errors in the measured value that result from compliance of the alkanethiol/gold/epoxy substrate and/or incomplete removal of the contribution of optical interference in cantilever deflection.

CHAPTER 7

FLY-FISHING WITH SINGLE WALLED CARBON NANOTUBES

Introduction

In Chapter 6, the mechanical response of a multiwalled carbon nanospring under compression using multi parameter force spectroscopy (MPFS) was described. Cantilever deflection, oscillation amplitude, and thermally driven resonance were simultaneously measured and synchronized with movement of the substrate. A nonlinear response of the nanospring was observed consistent with its compression, buckling and bending. In Chapter 5, chemical force microscopy was used to elucidate the adhesive interactions between an alkanethiol modified AFM cantilever and a SWNT laden surface. To reduce (and either validate or disprove) the number of assumptions needed to be made to measure the binding forces (contact area assumptions), the reverse experiment was carried out where a nanotube is mechanically peeled off of a chemically modified surface. Here, the mechanical response and interfacial adhesion of SWNTs that have several different lengths and orientations are explored. In an effort to elucidate the importance of nanotube orientation when performing adhesion measurements where the nanotube is actively peeled away from chemically modified surfaces, short, kinked, long and looped single walled nanotubes were all investigated. The work reported here may drive research avenues that have a vested interest in using the carbon nanotube as a probe in chemical force microscopy.

Experimental

Cantilevers with SWNTs attached to the probe tip were purchased from Nanodevices (now Veeco Metrology) and characterized by scanning electron microscopy prior to and following mechanical testing experiments. The probes were fabricated in a similar fashion to the process reported by Cheung et al. [200]. Each nanotube-tipped cantilever was imaged with a scanning electron microscope (Hitachi S-800). A low accelerating voltage (5kV) was used during imaging to reduce carbon deposition onto the nanotube.

All experiments were carried out by operating the microscope in Tapping Mode™ under a nitrogen atmosphere (relative humidity below 6%). All gold substrates were freshly prepared template-stripped gold [393] that was treated with 1mM thiolic solutions. Gold surfaces were modified with 11-dodecanethiol (Sigma-Aldrich), 11-amino-undecanethiol (Dojindo Chemicals), 11-mercaptoundecanol (Sigma-Aldrich) or 11-mercaptoundecanoic acid. After several hours each substrate was removed from derivatizing solution and subsequently rinsed in filtered ethanol and then stored in a dessicator prior to use. Assembly of the alkanethiol was verified via contact angle measurements. All thiolized surfaces were imaged using a native silicon cantilever probe (NSC12, MikroMasch) prior to using a nanotube-tipped cantilever. The r.m.s. roughness of each sample was below 0.5 nm. Freshly cleaved grade-1 highly oriented pyrolytic graphite (HOPG) was also used as a substrate (SPI Supplies).

Several of the mechanical tests were performed using a similar experimental setup to that previously reported in Chapter 6. A Veeco Instruments (Santa Barbara, CA) Nanoscope

IIIa scanning probe microscope with extender electronics was used for all force measurements. The piezo scanner was calibrated in x, y, and z using NIST certified calibration gratings (MikroMasch).

Each experiment commenced by cycling the scanner in the z-direction for ~2 hours to allow the scanner to reach thermal equilibrium. Then false engagement of the microscope was initiated at a point where the nanotube was not in contact with the surface of the substrate. The microscope was immediately toggled from image acquisition to force curve operation whereby cantilever deflection is monitored as a function of scanner vertical movement. Force curves were acquired at four different scanner velocities (400, 200, 100 and 50 nm/sec) with and without the cantilever being driven at its natural resonance the oscillator on the cantilever holder. The natural resonance frequency was determined a priori using the thermal spectrum method. To simultaneously acquire cantilever resonance, cantilever displacement and substrate position, the same experimental setup described in Chapter 6 was used (Figure 6.2).

Results and Discussion

A scanning electron micrograph of one of the SWNT-laden tips is shown in Figure 7.1a. To determine the mechanical response of the SWNT, cantilever beam deflection was monitored over time as the nanotube was subjected to repeated compression and decompression cycles. In other instances, MPFS was used to more completely interpret the impact of nanotube orientation as well as potentially elucidate chemical information.

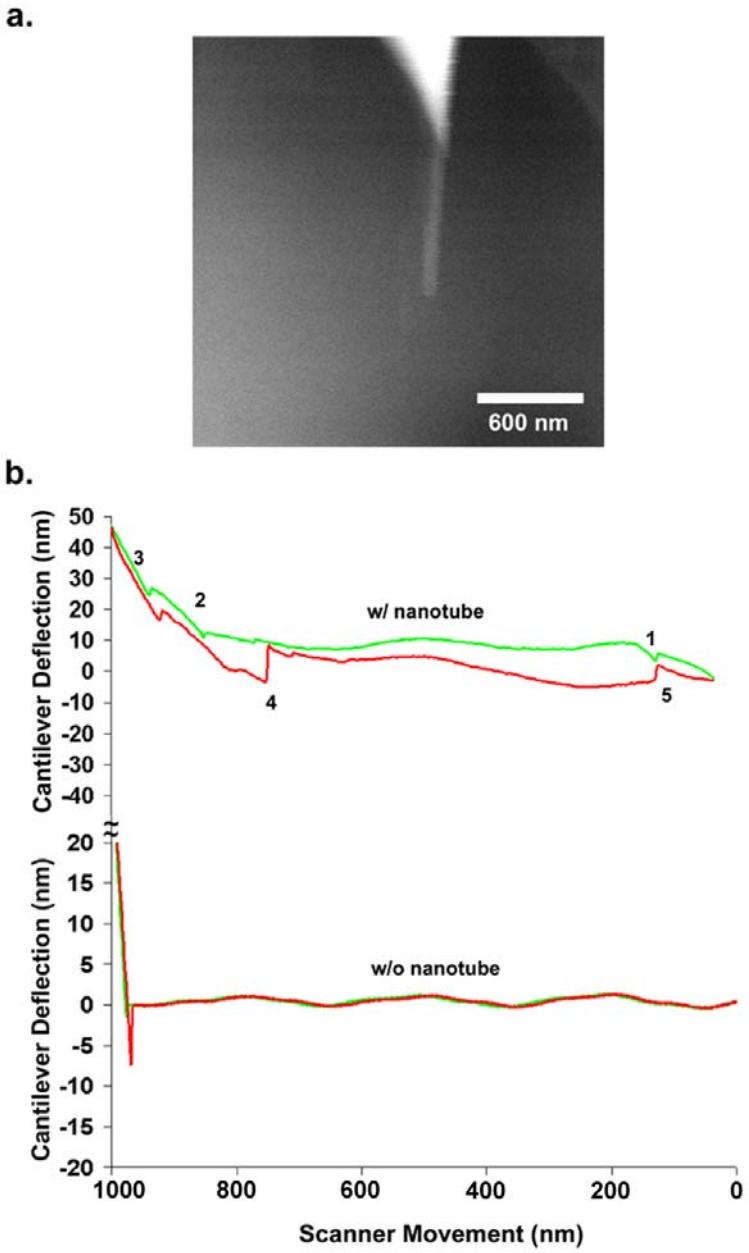

Figure 7.1. a) SEM image of a nanotube grown off of the end of an AFM tip. b) top frame: force curve acquired using the AFM tip in a) and a freshly cleaved HOPG substrate at a scanner rate of 2Hz. The green line represents the approach of the substrate towards the tip and the retraction of the scanner relative to the tip is drawn in red. b) bottom frame: force curve acquired after five repetitive up-down movements of the scanner.

Deflection-based Studies

Short Nanotube

To elucidate the adhesion between a SWNT and a substrate, a short nanotube (<600 nm long) (Figure 7.1a) was repeatedly brought into and out of contact with a freshly cleaved HOPG surface (SPI-1, 0.4° +/- 0.1° mosaic spread). Since sidewall interactions between the nanotube and the underlying substrate are what require investigation, it was thought that the tube should be pushed on by the underlying substrate and bent, so as to force the nanotube to lie on its side.

A typical force curve acquired using this probe is shown in Figure 7.1b. During the approach an initial deflection of the cantilever beam is observed roughly 700 nm away from the point of contact between the silicon tip and the surface (Figure 7.1b, point 1). As the substrate is brought closer to the silicon/nanotube junction, the tube unresistively bends or slides on the surface (no cantilever deflection). Once a large amount of stress is imposed on the tube, the tube becomes more difficult to bend thus pushing up on the cantilever (Figure 7.1b, point 2). Under even further compression, the tube is most likely force out of the way (at almost a 90^{o} angle relative to the tip) and mechanical contact is made between the silicon tip and the graphite surface (Figure 7.1b, point 3). Then, as the substrate is gradually pulled away from the silicon tip, the tube begins to "snap" back (Figure 7.1b, point 4). The substrate is eventually removed from the nanotube after a final "snap-in" of the nanotube (Figure 7.1b, point 5).

Compressing the nanotube to the point where mechanical contact is made with the silicon cantilever has an advantage in that the sensitivity parameter (as discussed in Chapter 1) could be determined, thus calibrating the movement of the cantilever beam. This facilitates the interpretation of adhesive interactions between the nanotube and the substrate (via multiplying the stiffness of the cantilever times any observed beam deflection).

Repeated cycling of the scanner gave rise to force curves which displayed the same featuresas depicted in Figure 7.1b. After five compression and decompression cycles, the force curve presented in Figure 7.1c was obtained. This curve is identical to those obtained using a naked cantilever tip indicating that the tube fractured off of the silicon tip. Further evidence of fracture was obtained by imaging the underlying surface in Tapping Mode™ and locating the tube (Figure 7.2). From cross-sectional analysis of the image feature, the nanotube is roughly 1.5 nm tall, corresponding to the diameter of a single walled carbon nanotube.

An important conclusion can be drawn from this experiment. A short nanotube on the end of a cantilever tip, although ideal for imaging purposes, is non-ideal for force spectroscopic investigations concerned with interpreting sidewall interactions between the nanotube and chemically homogenous surfaces. First, the point of contact with the substrate is the tip end, not the sidewall. Stress sufficient to bend the nanotube is required to ensure contact of the surface with the sidewall of the nanotube, this will lead to the removal of the nanotube from the silicon tip (thus terminating the spectroscopic

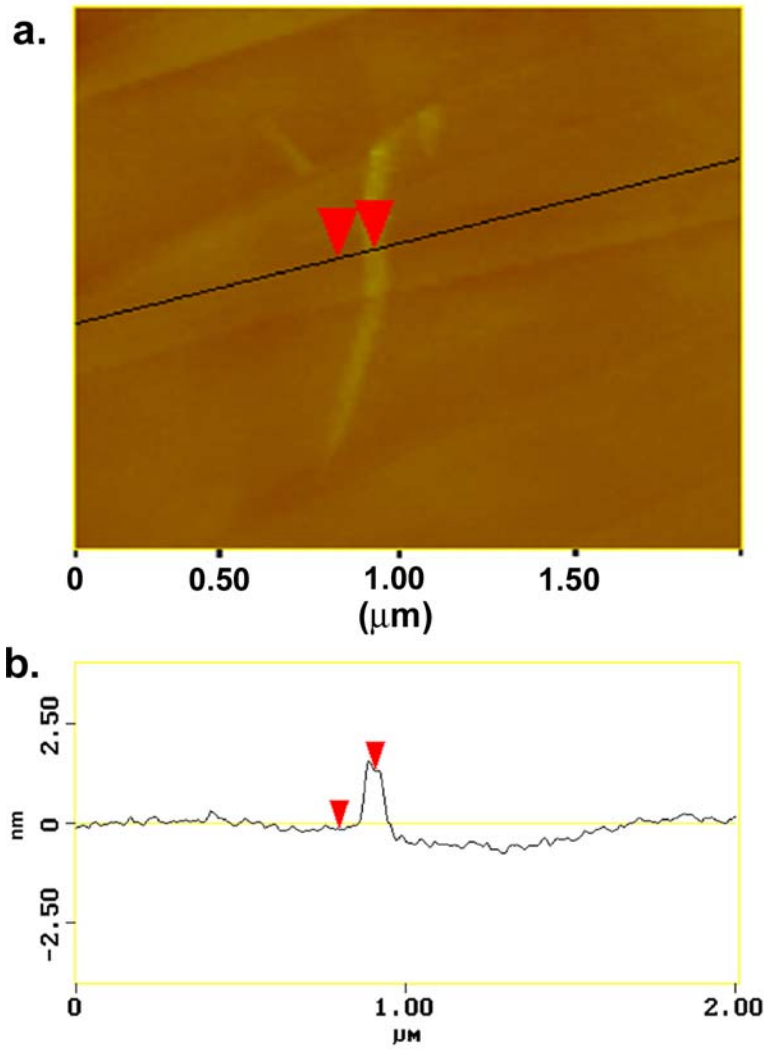

Figure 7.2. a) Cross-sectional image of the nanotube that was fractured in Figure 7.1. The vertical height of the nanotube is 1.5 nm. (b) Tapping mode™ topographical image of the fractured nanotube lying on the HOPG surface.

study). Second, since the cantilever tip/nanotube junction is a weak mechanical point, repeated compression/decompression cycles results in breakage or removal of the nanotube from the cantilever tip. Whether the mechanically weak point is the tip to catalyst or the catalyst to nanotube contact point is a matter of speculation.

Kinked Nanotube

To foster physical contact with the sidewall of a nanotube during the force measurement, a kinked or "L"–shaped nanotube was used. Figure 7.3a depicts an SEM image of the tube. The stability of the tube was significantly enhanced compared to the short nanotube.

As shown schematically in Figure 7.3b, the substrate was brought into intimate contact with then subsequently retracted away from the bent nanotube. Deflection-based adhesion measurements were performed on several different template stripped gold (TSG) surfaces that were modified using self-assembly chemistry. All substrates possessed an r.m.s. roughness less than 0.5 nm thereby minimizing topologically induced artifacts in the adhesion data. All of experiments were carried out using the same scanner z-velocity.

Force curves acquired on chemically modified TSG substrates are presented in Figure 7.4. Note that the final pull-off event on the retract portion of each curve approximates the length of the lower "L" portion of the nanotube (as shown in the SEM image).

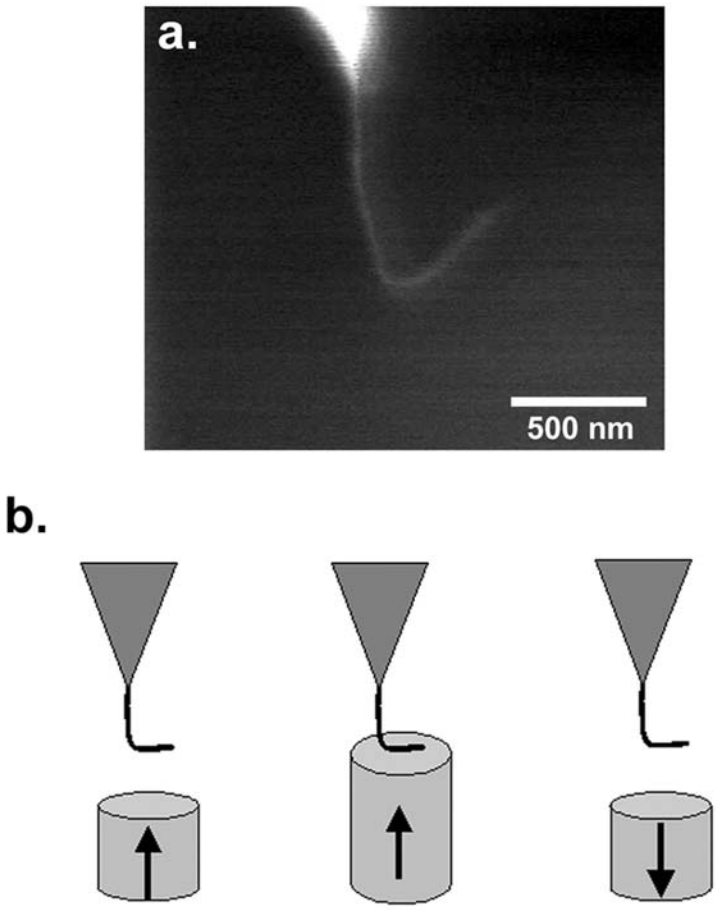

Figure 7.3. (a) SEM image of a kinked SWNT grown off of the tip of an AFM cantilever. (b) Cartoon depicting the adhesion experiment facilitating contact between the sidewall of the nanotube and the substrate.

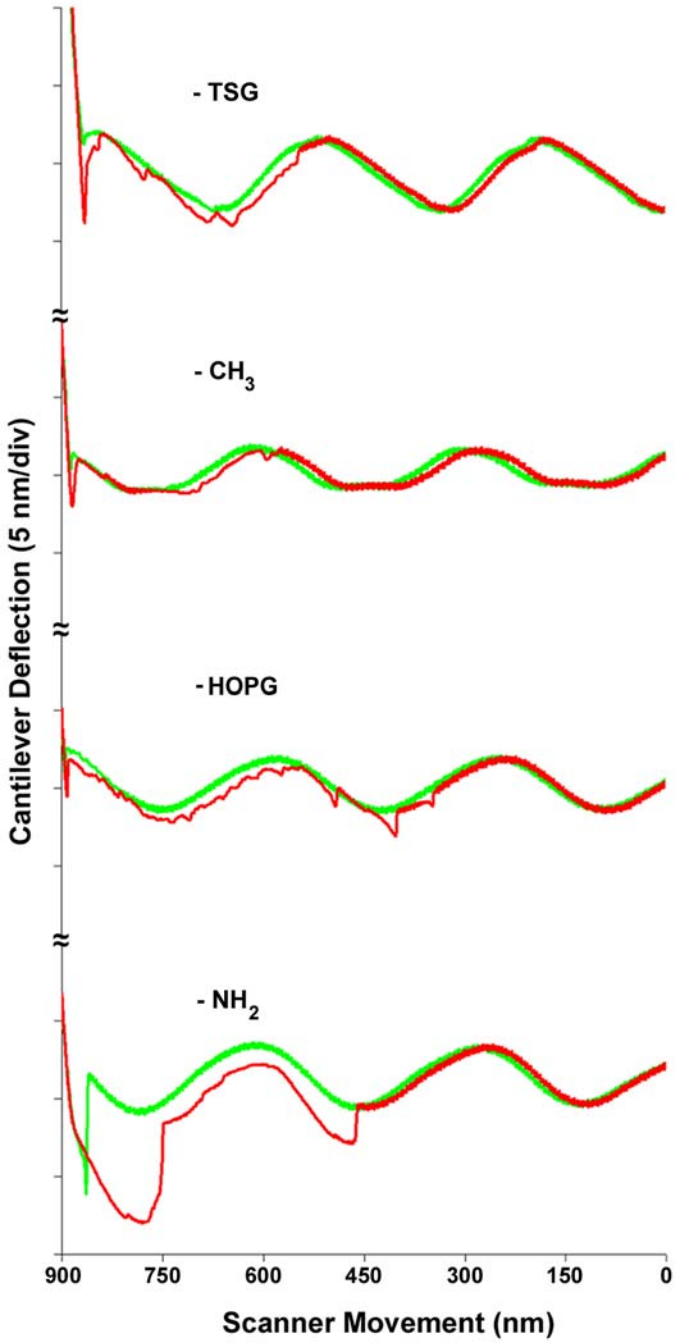

Figure 7.4. Force curves acquired using the kinked SWNT-tipped cantilever shown in Figure 7.3 (a). Notice the increase in deflection of the cantilever beam follows a similar trend to what was observed using the adhesion mapping studies presented in Chapter 4. The periodic motion of the extension and retraction curves is an artifact of the optical interference of light bouncing off of the cantilever and light also bouncing off of the reflective substrate.

Variability in the contact length results from buckling and slip stick motion of the nanotube. A general trend was observed in the deflection data. The amine-terminated SAM generated the largest adhesive interaction (2.5 nm pull-down), whereas the methyl-terminated SAM caused the lowest beam deflection (0.75 nm). It is also worth drawing attention to the pull-off events. It appears that the tube is being "peeled" off of the surface similar to the separation of Velcro. This trend mirrors what was observed using the adhesion mapping approach presented in Chapter 5.

The idea of using a nanotube to control the length of contact between the outer surface of the nanotube and a chemically modified has merit in the present context. To our knowledge, there has yet to be reported a controlled synthetic route for creating these "kinked" nanotubes [391,392] . The "L"–shaped nanotube used herein was an accidental by-product of the synthesis of straight nanotubes. However, as was the case in the study presented in Chapter 6, the optical inference that is observed due to the use of such large scan sizes, makes elucidating and quantifying the chemically-significant rupture forces a very difficult task.

Long and Looped Nanotubes

Long nanotubes and looped nanotubes mounted on the tip of an AFM cantilever could prove advantageous for adhesion studies (Figure 7.5). Since both the long and looped nanotubes are very large (over 2 μm in length), the probability of removing the nanotube from the tip of the cantilever is reduced. It could be possible to make contact with the nanotube without coming close to making mechanical contact between the silicon tip and

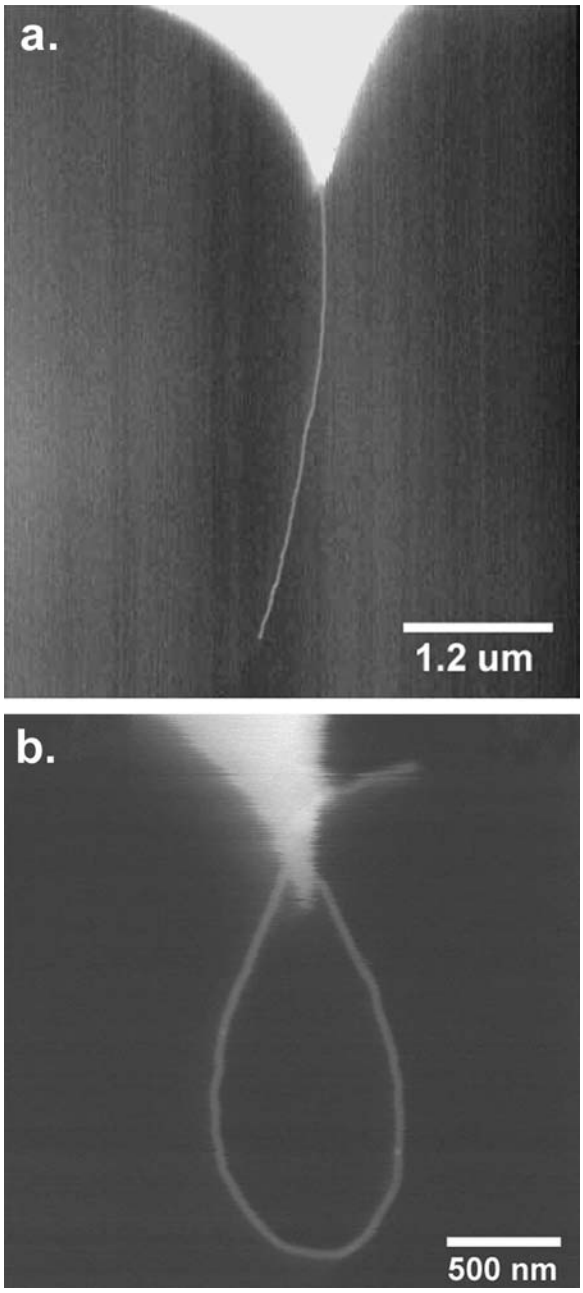

Figure 7.5. SEM images of SWNT-tipped cantilevers fabricated by NanoDevices (now Veeco Metrology). (a) long straight SWNT. (b) long looped SWNT. Images were obtained with a Hitachi model S-800 scanning electron microscope operating under a low accelerating voltage (5kV).

the substrate, thus avoiding potential defects located at the tip-nanotube interface. Due to the excessive lengths of these nanotubes, the Euler buckling force should be so small that the nanotube buckles immediately forcing the tube to lie on the surface. Also, a tube such as the looped nanotube could provide both a controlled orientation and defined contact length during the adhesion studies.

First the long straight nanotube was brought into contact with the substrate. The position of the nanotube relative to the surface was controlled by periodically turning on the piezoelectric drive in the cantilever holder and monitoring changes in the oscillation amplitude of the cantilever. Approximately 1.25 μm of the nanotube was laid down on the surface prior to peeling (scanner movement direction reversal). Force curves are depicted in Figure 7.6. The severe impact of the optical interference masks the adhesive interaction. However, differences in the amount that the cantilever bends, seems to depend upon the chemical identity of the surface. The magnitude of the interference compared to the adhesion-induced deflection made removal of the optical interference difficult. Detector sensitivity cannot be measured without making mechanical contact with the silicon tip; this was not attempted for fear that mechanical damage or removal of the nanotube would occur. Thus, the deflection of the cantilever beam relative to the chemical identity of the substrate is strictly interpreted from the change in voltage on the PSD.

A similar set of experiments were performed with the SWNT loop. The force curves obtained are depicted in Figure 7.7. Note that compared to the long , straight nanotube,

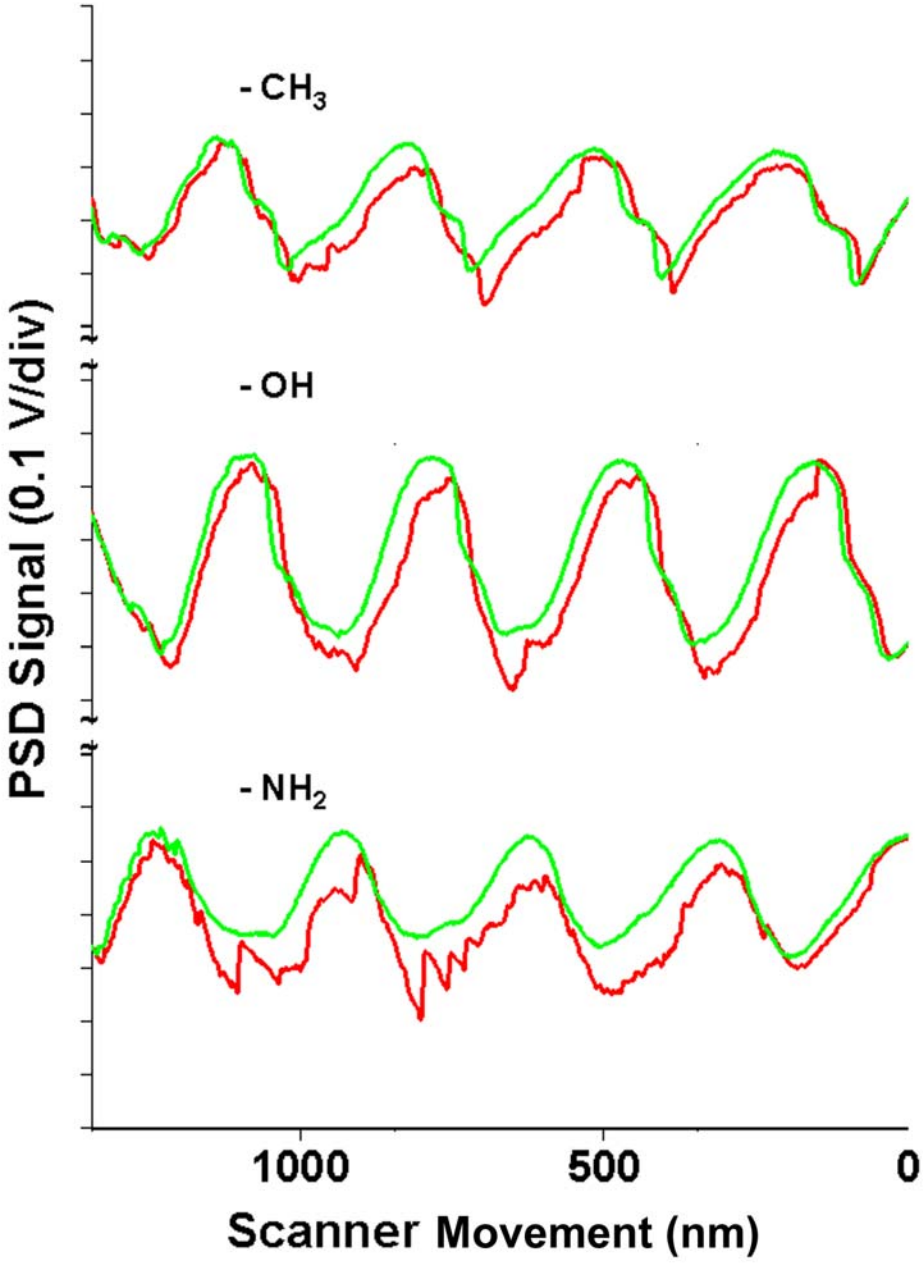

Figure 7.6. Force curves acquired between the long SWNT-tipped cantilever in Figure 7.6.(a) on TSG substrates modified with C_{11} alkanethiols with different terminal groups. Alternate terminal groups are noted above each force curve. All of the above force curves were obtained at a velocity of 100 nm/sec in the z-direction. Using a z-scan size of 1350 nm.

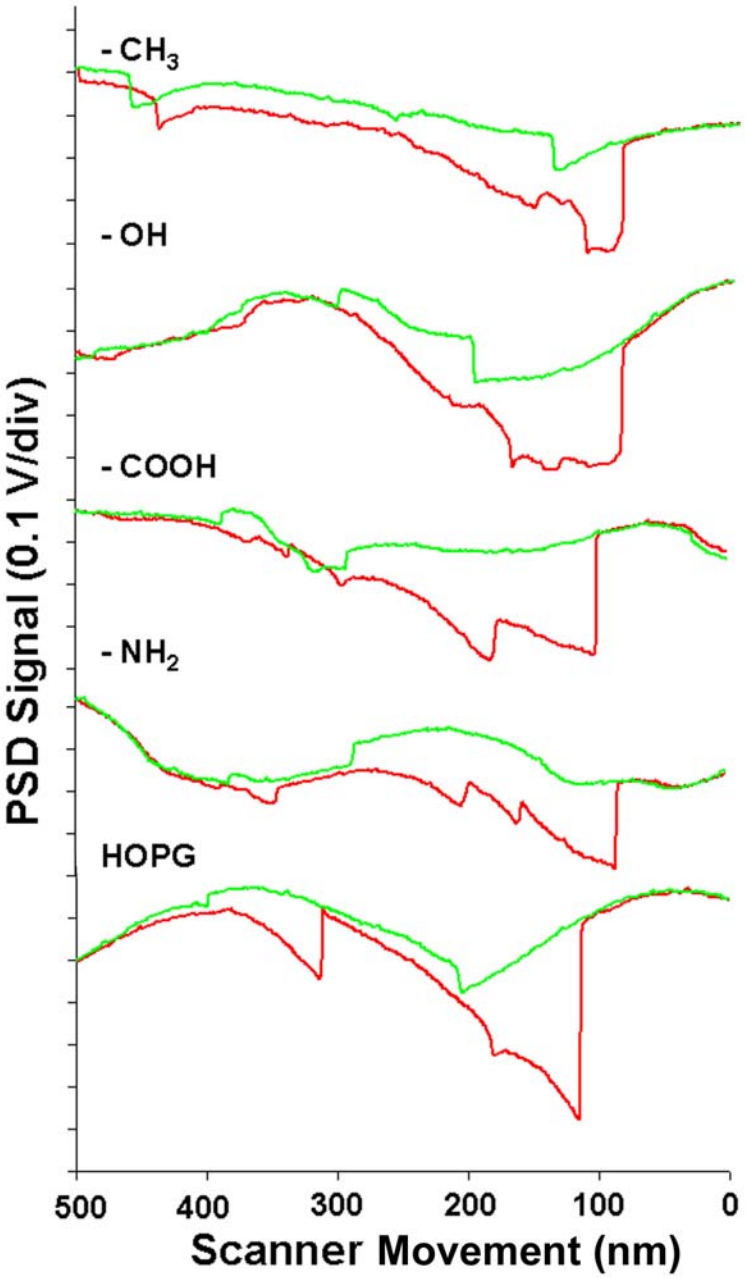

Figure 7.7. Force curves acquired between the looped SWNT-tipped cantilever in Figure 7.6.(b) on TSG substrates modified with C_{11} alkanethiols with different terminal groups as well as a freshly cleaved graphite surface. All of the above force curves were obtained at a velocity of 100 nm/sec in the z-direction.

the cantilever deflection for the looped tube is substantial. Even though the optical interference isn't as bad, the ignorance of the sensitivity factor precludes quantization of the rupture forces.

Multi Parameter Force Spectroscopy Studies

Cantilever deflection can result from adhesion between the nanotube and the surface or from the nanotube's response to the applied load (buckling). Thus, multi parameter force spectroscopy was used to discriminate between these two scenarios.

Short Nanotube

In this section, experiments taken with the same nanotube-tipped cantilever will be presented. An SEM micrograph of the nanotube-tipped cantilever is depicted in Figure 7.8a. Following interchanging of the sample, the laser position was never moved on the backside of the cantilever until a different cantilever/nanotube probe was used. When a substrate was brought into intimate contact with the end of the short tube, the scanner movement after contact was maintained at 50 nm (i.e. the piezo-scanner was retracted from the substrate once the substrate had been "pushed" 50 nm into the nanotube. This scanner displacement after substrate/tube contact should be enough to "force" interaction between the end of the nanotube and the substrate (Figure 7.8b). At all scanner z-velocities, the cantilever deflection and amplitude curves were consistently similar.

The cantilever deflection of the nanotube-tipped probe when brought into mechanical contact with the methyl-terminated SAM is linear in the approach and retract curve

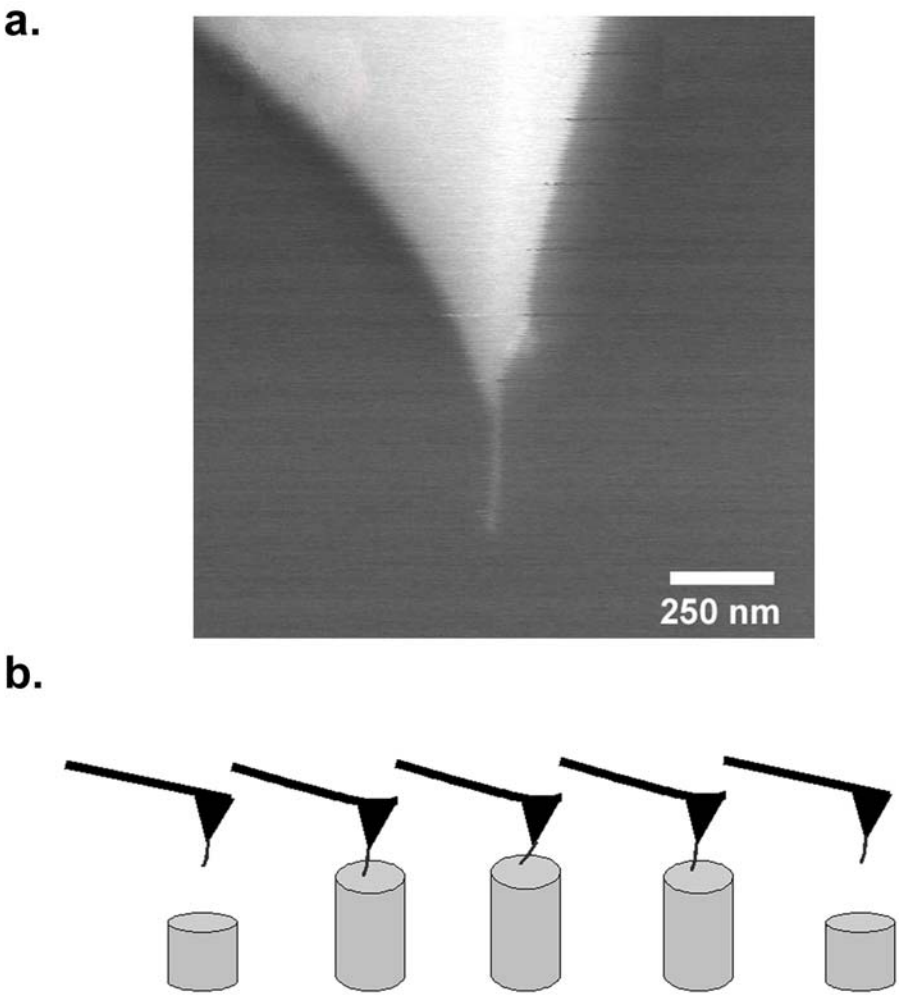

Figure 7.8. (a) SEM image of a short SWNT grown off of a cantilever tip. (b) cartoon depicting a force spectroscopic study that will test end-on interactions of the nanotube with the substrate.

(Figure 7.9). The corresponding cantilever oscillation amplitude drops to a baseline value as soon as the tube touches the surface. The time-correlated beam resonance and scanner movement (Figure 7.9c and 7.9d) are consistent with previous experiments for a native silicon cantilever touching a surface. That is, the beam motion goes to a much higher frequency as soon as mechanical contact is made between the end of the nanotube and the substrate as demonstrated previously in Chapter 5 and by Roters et al [394]. The beam does not have a restored thermal motion until the substrate is fully removed from the end of the nanotube.

When the short nanotube is brought into contact with the hydroxyl-terminated SAM a highly nonlinear beam deflection is present (see Figure 7.10) when the nanotube is loaded and unloaded. This nonlinearity in the contact region could be induced by the nanotube's ability to slide on the surface. Note that the corresponding cantilever oscillation amplitude curve begins to show "fine structure" during the retract portion of the plot. The observed movement could be due to either a loss of mechanical motion at the point of resonance or could be due to the movement of the resonant mode. Since the AFM software monitors the cantilever's amplitude at a single frequency, shifts in the cantilever/nanotube resonance will drop the amplitude of oscillation. The amplitude of oscillation at that singular frequency does indeed drop, but a more accurate description would be that the mechanical resonance of the system might change. In the case of the short nanotube and the hydroxyl-SAM, during the retraction of the substrate from the nanotube the tube seems to reproducibly "snap" back into its natural position, which will cause a noticeable increase in total "system" resonance until the substrate is fully

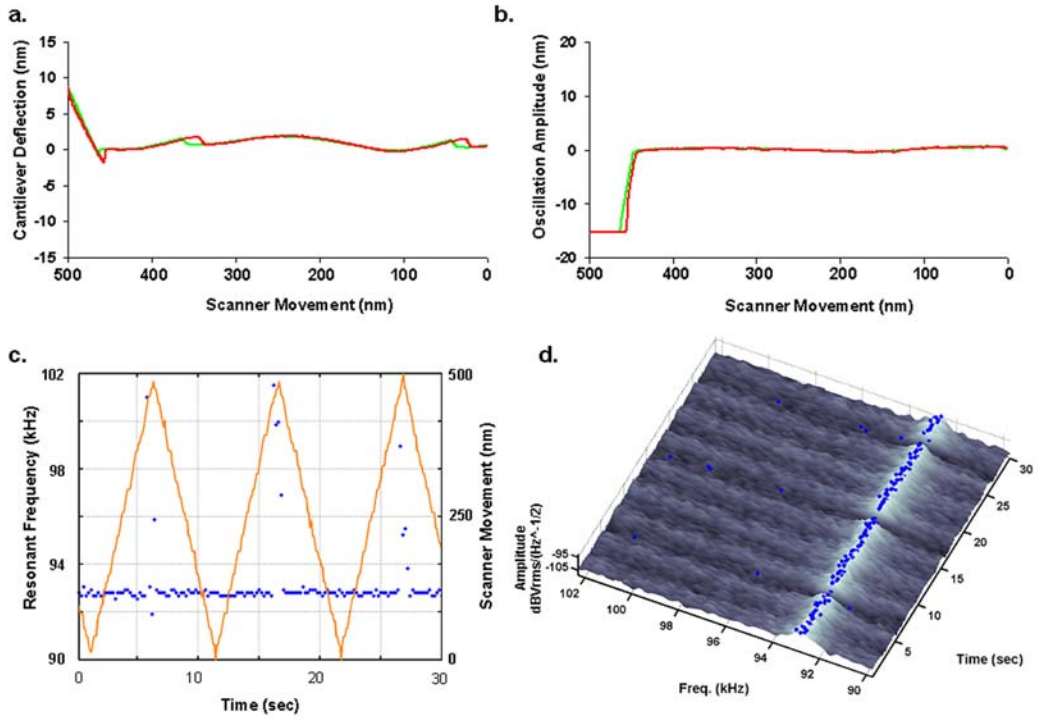

Figure 7.9. Force measurements made between a methyl-terminated alkanethiol-modified TSG substrate. (a) Force curve. (b) Oscillation amplitude. (c) Substrate position (orange) and cantilever/nanotube peak resonance (blue). (d) Waterfall of the thermally-driven resonance of the cantilever/nanotube during the force measurement.

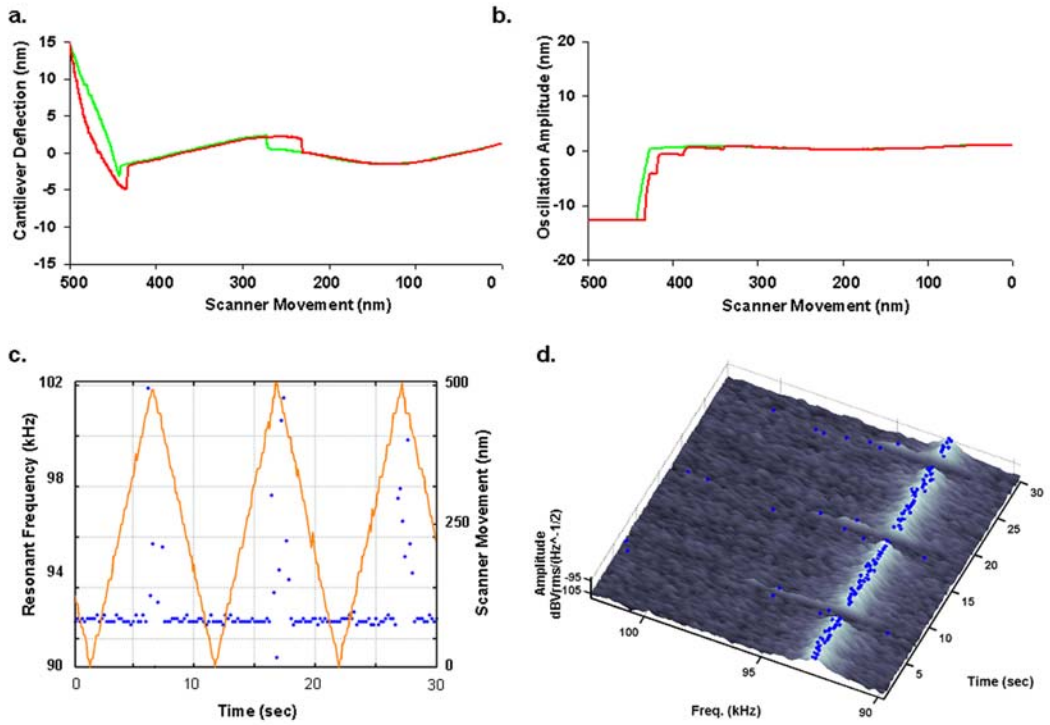

Figure 7.10. Force measurements made between a hydroxyl-terminated alkanethiol-modified TSG substrate. (a) Force curve. (b) Oscillation amplitude. (c) Substrate position (orange) and cantilever/nanotube peak resonance (blue). (d) Waterfall of the thermally-driven resonance during force measurements using the cantilever/short nanotube.

removed from the nanotube. Similar responses are seen for not only the hydroxyl-terminated SAM but also for the amine- and carboxylic acid-terminated SAMs (Figures 7.11, 7.12 respectively).

It is interesting to note that when HOPG is brought into contact and released from the tube, the contact area of the deflection curve (both the approach and retract) are almost linear and superimpose able (Figure 7.13). At the same time when the cantilever beam's resonance is monitored as a function of scanner displacement, a "roll-down" is observed in the peak resonance when the graphite is being pulled away or "unbending" the nanotube. This could be due to either some type of adhesive interaction between the nanotube and the graphite, or due to the tube being more readily able to restore its orientation on a surface that has such a low coefficient of friction [403,404]. Graphite has a frictional coefficient that is 100 orders of magnitude smaller than many of the thiols used to create the self-assembled monolayers [148,405-410]

.

The low frictional coefficient could explain why there is no noticeable cantilever deflection hysteresis when the graphite contacts the tube; the tube is simply sliding out from under the vertical load. Thus, these experiments may help in interpreting previous rheological studies of carbon nanotubes [312,411,412]. The only noticeable change in these experiments when using different piezo-scanner z-velocities was that at the lower scanner rate (lower velocity) we were able to elucidate more of the fine features in the cantilevers resonant response. This is most likely the result of two scenarios; 1. The

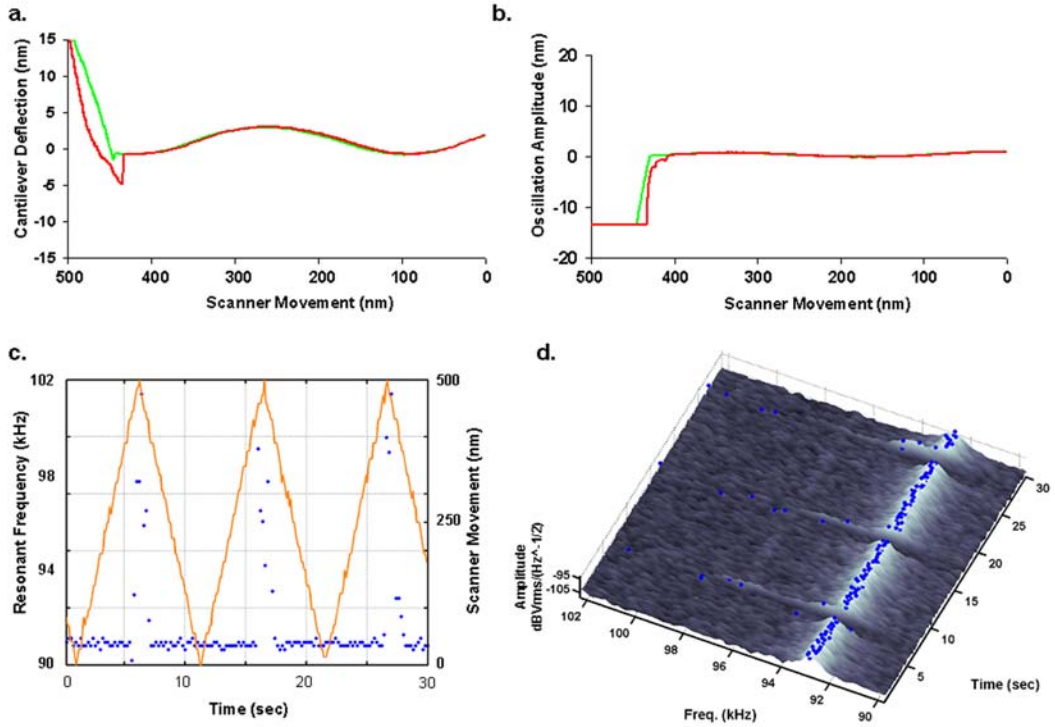

Figure 7.11. Force measurements made between a carboxylic acid-terminated alkanethiol-modified TSG substrate. (a) Force curve. (b) Oscillation amplitude. (c) Substrate position (orange) and cantilever/nanotube peak resonance (blue). (d) Waterfall of the thermally-driven resonance during force measurements using the cantilever/short nanotube.

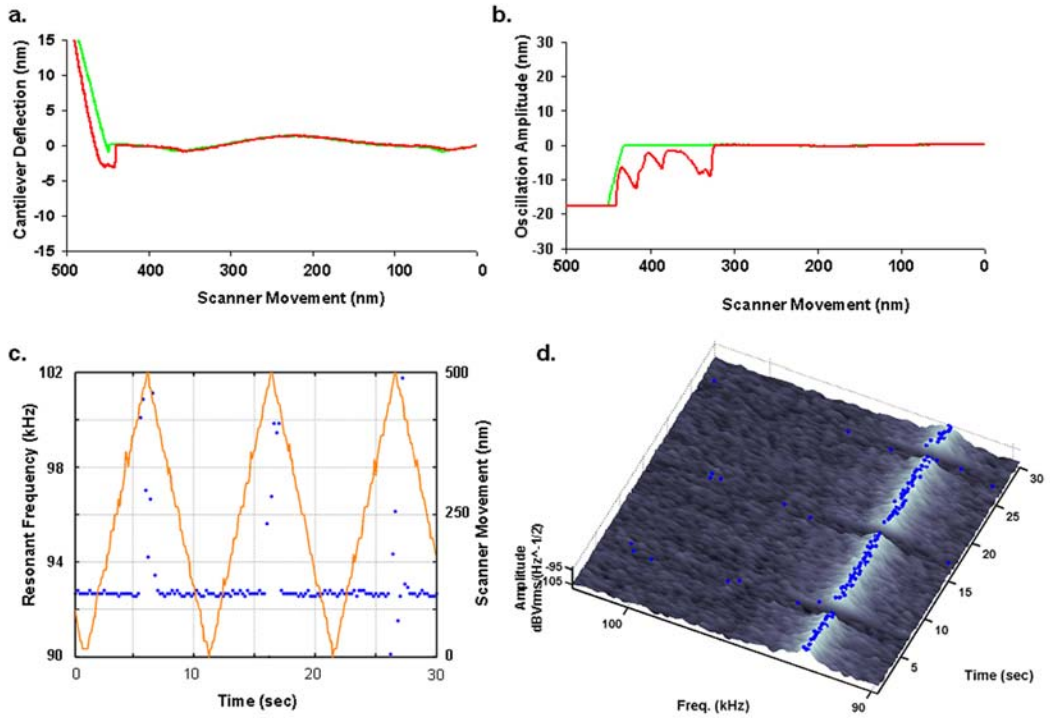

Figure 7.12. Force measurements made between a amine-terminated alkanethiol-modified TSG substrate. (a) Force curve. (b) Oscillation amplitude. (c) Substrate position (orange) and cantilever/nanotube peak resonance (blue). (d) Waterfall of the thermally-driven resonance of during force measurements using the cantilever/short nanotube.

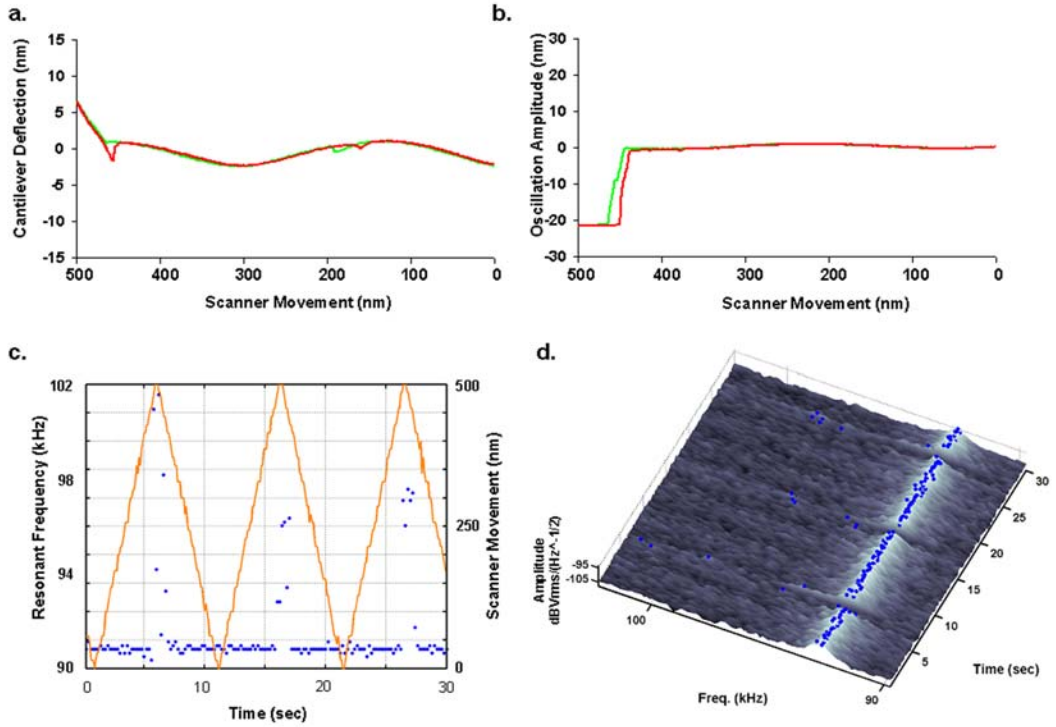

Figure 7.13. Force measurements made between a freshly cleaved HOPG substrate. (a) Force curve. (b) Oscillation amplitude. (c) Substrate position and cantilever/nanotube resonance. (d) Waterfall of the thermally-driven resonance of the during force measurements using the cantilever/short nanotube.

lower velocity gives the nanotube more time to reach a mechanically stable configuration 2. The sampling rate of the DSA is optimized relative to the number of scanner cycles during the entire measurement (i.e. at the slowest velocity the scanner has moved only slightly more than one full cycle, thus more thermal spectra are acquired during the approach and retract cycle.

Long Nanotube

Figure 7.14 presents force curve information acquired when a SWNT approximately 3.5 μm long was brought in and out of contact with a methyl-terminated alkanethiol modified gold substrate. This surface is known to have a low affinity for nanotubes (as previously demonstrated in Chapter 5). Scanner extension in this run was limited to 1.35 μm, thereby avoiding mechanically induced damage (and possible fracture!) of the SWNT. Figure 7.14c depicts a plot of the cantilever oscillation amplitude as a function of scanner extension acquired while the cantilever was mechanically driven at a frequency of 69.5 kHz. During the approach, no change in oscillation amplitude is observed until the scanner has extended ~800 nm. At this point, the oscillation amplitude drops possibly indicating contact and/or bending of the SWNT against the opposing surface. As the scanner continues to extend, the magnitude of oscillation dampening is intermittent. When the scanner is retracted from the cantilever, the oscillation amplitude remains negative of its value in free space well past the initial point of dampening. Only after the scanner has retracted ~1100 nm from its maximal extension is the oscillation amplitude restored to zero dampening. This point marks the release of the substrate from the nanotube.

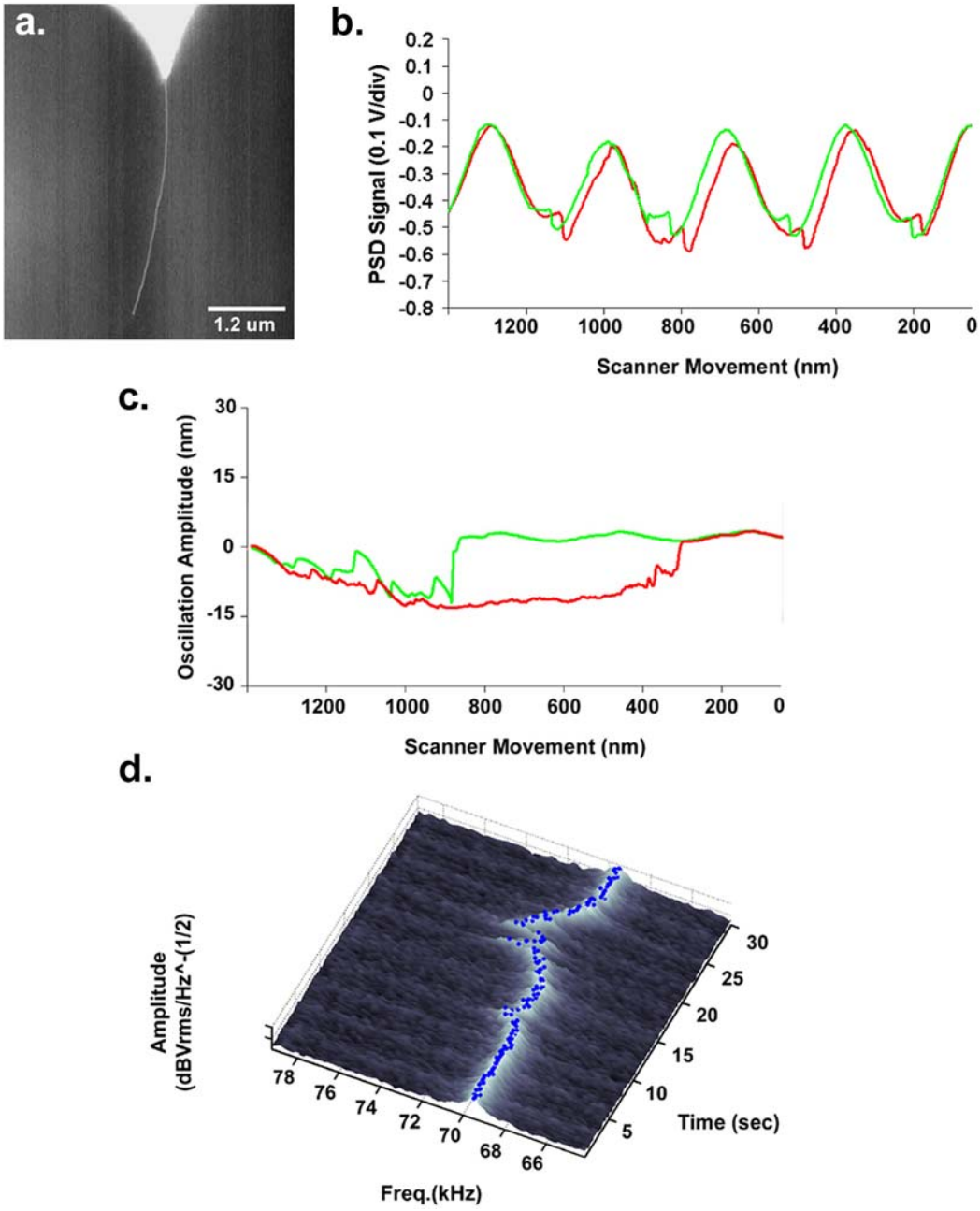

Figure 7.14. (a) The same SEM image presented in Figure 7.5(a). (b) Force curve plot acquired on using the nanotube-tipped cantilever shown in Figure 7.14. (a) and a 12-dodecanethiol-functionalized gold substrate (without mechanical oscillation of the cantilever). (c) Cantilever oscillation amplitude plot acquired as the long SWNT is brought into and out of contact with same surface while the cantilever is driven at a frequency of 69.5 kHz. (d) Thermal spectra acquired simultaneously with the force curve and presented in a waterfall format.

Following completion of this cycle, the piezoelectric device mechanically driving cantilever oscillation was turned off. A force curve was acquired simultaneously recording both cantilever deflection and thermal resonance. Figure 7.14b depicts a plot of cantilever deflection versus scanner movement over the identical range presented in Figure 7.14c. Interestingly, no discernable deflection of the cantilever commensurate with point of contact is evident in this curve. Substantial optical interference, due to the magnitude of scanner extension and to the highly reflective gold coatings on both the substrate and cantilever, masks the contact event.

To gain insight into the mechanical response of the SWNT under the applied load, the thermal resonance and oscillation amplitude of the cantilever was time correlated with scanner movement (see Figure 7.15). As the scanner extends toward the tube, no shift in resonance (or dampening in oscillation) is observed until the scanner has extended ~800 nm. At this point, the resonance frequency increases by ~1 kHz. Continued upward extension of the scanner produces a decrease in resonance frequency to a plateau ~250 Hz higher than the fundamental resonance of the beam prior to contact of the nanotube with the substrate. Upon retraction of the scanner, the frequency increases to 72 kHz. With continued retraction, the SWNT is eventually released from contact with the substrate and resonance returns to its original value (69.5 kHz). Note that the release event occurs after the scanner has retracted ~1100 nm. When referenced to the starting position of the scanner, there exists a 600 nm difference in the apparent points of contact and release.

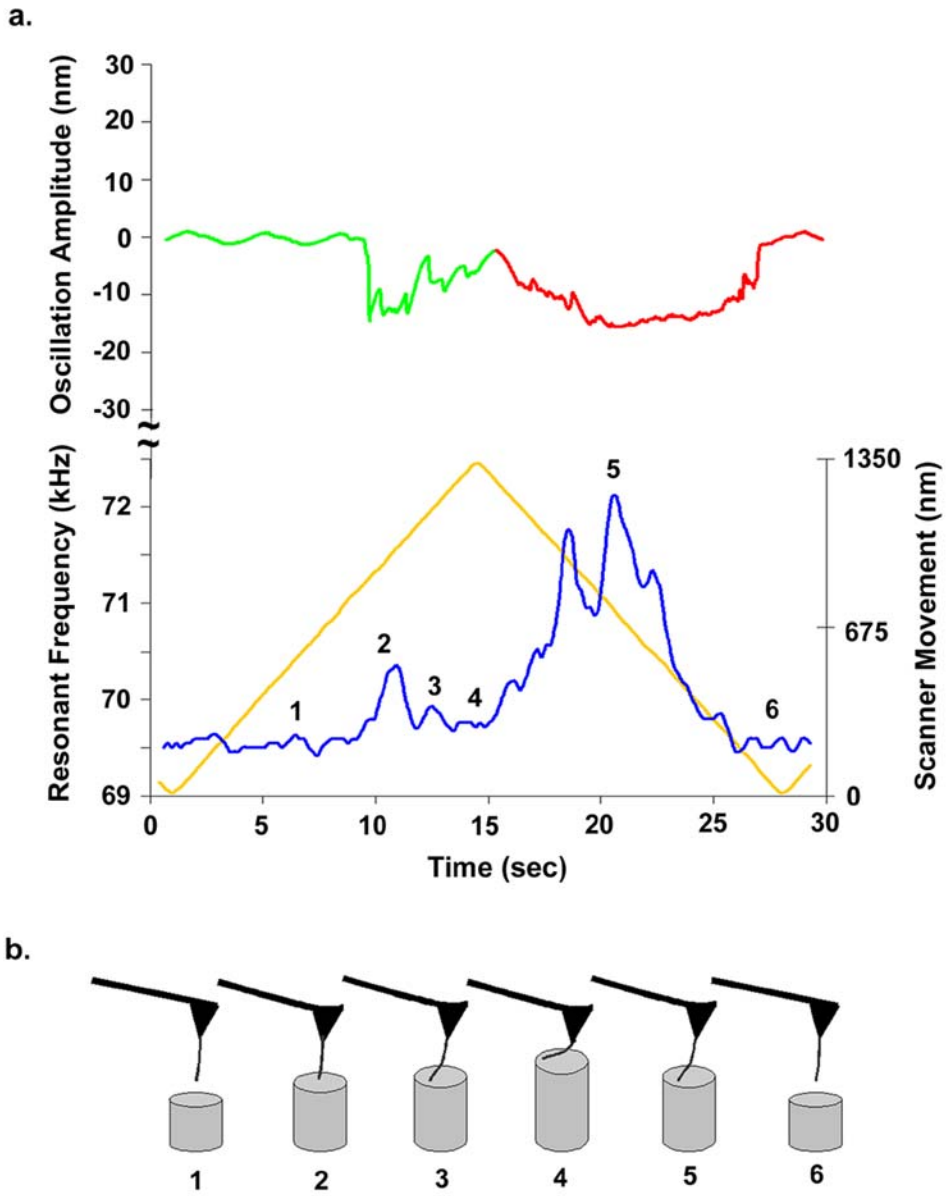

Figure 7.15. (a) Plot of the scanner movement (gold), thermal resonance (blue) and oscillation amplitude (green and red) of the cantilever versus time during the compressive loading of a SWNT in contact with a 12-dodecanethiol-functionalized gold substrate. To facilitate comparison, only the frequency of maximum amplitude is depicted here. The complete set of thermal spectra is presented in Figure 3(c). Note that the scanner was retracted after 1.35 μm of the nanotube was in contact with the substrate. (b) Schematic of the orientation of the nanotube during compression and pull-off.

As was previously shown in Chapter 6, the compression-induced buckling or bending of a carbon nanospring is a highly repeatable and reversible process, giving rise to symmetrical resonance frequency shifts during the compression/decompression cycle. In contrast, compression/decompression of long SWNTs exhibit asymmetric resonance frequency shifts. Figure 7.16 presents the frequency shifts as a function of scanner movement observed when the nanotube was repeatedly brought into and out of contact with the methyl-terminated alkanethiol-modified gold surface. This data attests to the repeatability in nanotube response to compressive loading.

It is postulated that contact and release of the nanotube occurs at the same vertical position of the scanner (~250 nm). A pictorial representation of SWNT contact, compression, bending and release from the substrate is provided in Figure 7.15b. No detectable deflection, frequency shift or change in oscillation amplitude is observed upon contact due to slip-stick motion of the nanotube on the substrate surface and to the stiffness of the cantilever to which the nanotube is attached (2.0 N/m). The observed change in oscillation amplitude and frequency shift after an 800 nm extension of the scanner is due to bending of the nanotube as a consequence of axial compression.

To test this hypothesis, the SWNT-tipped cantilever is modeled as two springs in series. The following equation can be used to approximate the experimental compression stiffness:

$$f_0 = \frac{1}{2\pi}\sqrt{\frac{k_B + k_{NT}}{m_{eff}^B + m_{NT}}} \qquad \text{Equation 7.1}$$

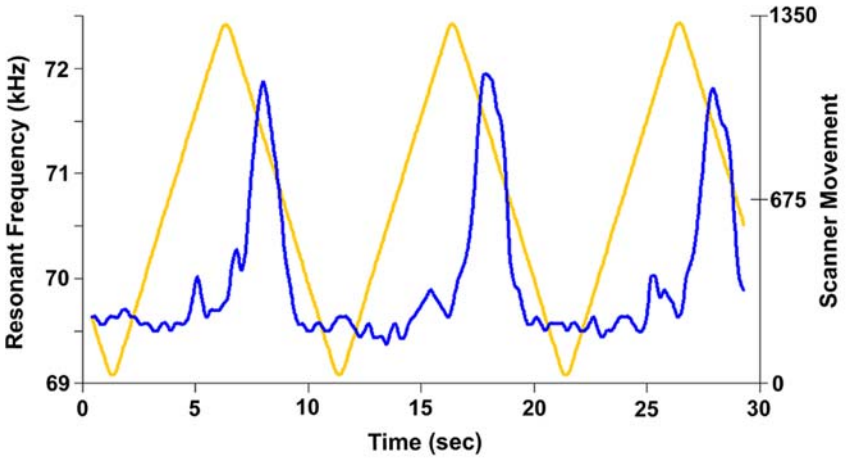

Figure 7.16. Plot of resonance frequency shifts (blue) and scanner movement (gold) versus time for sequential engagements of a SWNT with a 12-dodecanethiol-functionalized gold substrate. Note that the scanner was retracted after 1.25 μm of the nanotube was in contact with the substrate.

where f_0 is the resonant frequency of the spring system, k_B is the cantilever beam stiffness, m^B_{eff} is the effective beam mass equal to 0.24 times the actual beam mass, [207] m_{NT} is the mass of the nanotube, and k_{NT} is the nanotube stiffness. From the experimentally measured resonance shift of 964 Hz, the calculated compression stiffness is 0.035 N/m assuming $m_{NT} << m^B_{eff}$.

The theoretical axial compression stiffness of this particular nanotube can be calculated from the following equation:

$$k_{axial} = \frac{E \cdot A}{L} \qquad \text{Equation 7.2}$$

where E is the elastic modulus of the tube in the axial direction, A is the cross-sectional area of the nanotube, and L is the total length of the nanotube. We compute a cross-sectional area for the cylindrical SWNT of 0.65 nm^2 (assuming an outer diameter of 1.50 nm and an inner diameter of 1.19 nm). The length of the nanotube is equal to its nominal length (3.59 μm) minus scanner movement following contact (600 nm). Assuming a bending modulus of 153 GPa, [352] the calculated compression stiffness on this particular tube using equation 2 is 0.033 N/m. The remarkably good agreement between the experimentally measured and theoretical values for axial compression stiffness must be viewed with caution since both the reported axial compression moduli and cantilever calibration methods can have relatively large degrees of uncertainty. [206,299,352,413]

As a second test of the hypothesis, the distance between the substrate and the cantilever was increased and the force curve was reacquired under the same conditions used in acquiring the data presented in Figure 7.17 (scanner velocity of 100 nm/s and extension

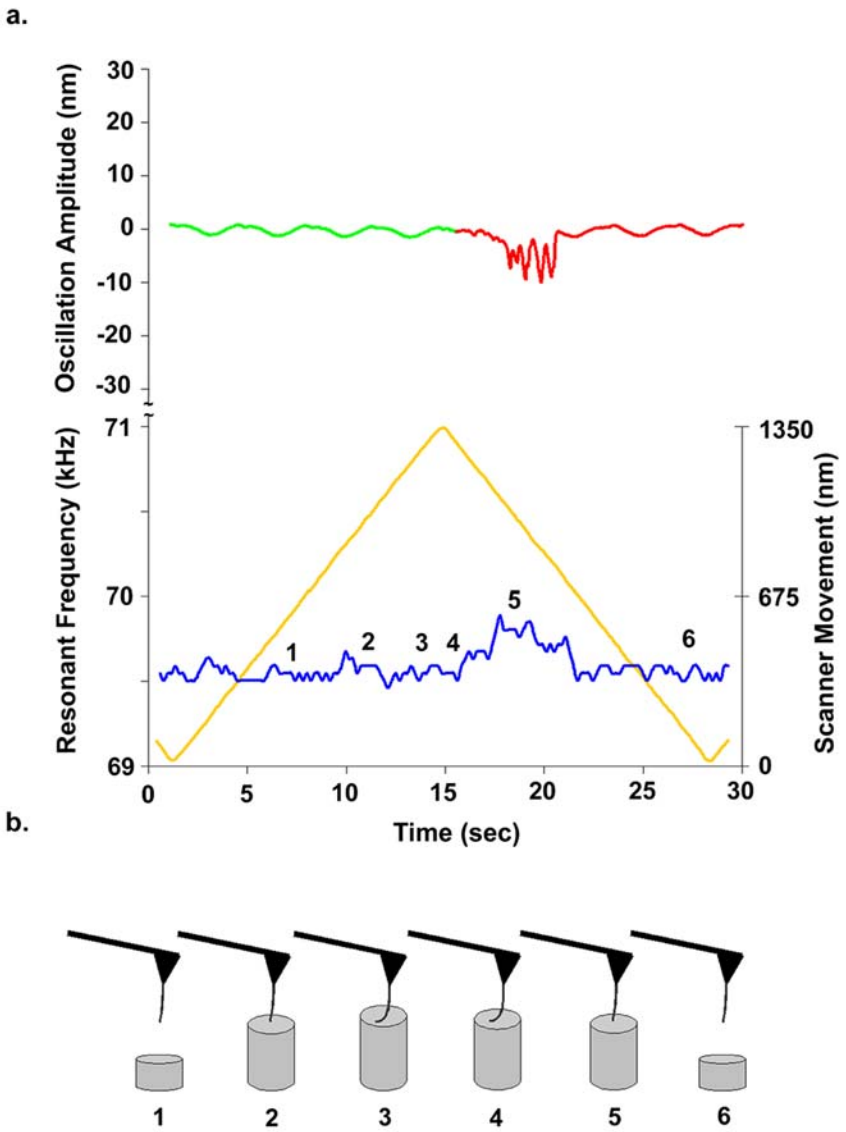

Figure 7.17. (a) Plot of the scanner movement (gold), thermal resonance (blue) and oscillation amplitude (green and red) of the cantilever versus time during the compressive loading of a SWNT in contact with a 12-dodecanethiol-functionalized gold substrate. Note that the scanner was retracted after only 500 nm of the nanotube came in contact with the substrate. (b) Schematic of the orientation of the nanotube during compression and pull-off.

of 1350 nm). This substantially reduces the compressive loading of the nanotube by reducing time the tube is in contact with the substrate. Figure 7.17 depicts the data acquired under these conditions. Note that there is no change in oscillation amplitude or frequency on the approach. Shifts in oscillation amplitude and frequency occur only during retraction of the scanner. The magnitude and duration of the frequency shift is reduced compared to that observed under higher axial compression (Figure 7.15). No deflection event was seen in the force curve (data not shown). This result supports the hypothesis that the point of contact is undetectable for long SWNTs in the presence of slip-stick phenomena and that the frequency shift observed on the approach of the scanner in Figures 7.15 and 7.17 are due to nanotube bending.

The asymmetry in resonance shifts during a compression/decompression cycle could potentially be the result of adhesive interactions between the tube and the substrate. As a test of this hypothesis, compressive loading of the long SWNT was performed on three surfaces with differing chemical functionality. All substrates were template-stripped gold that were modified with 1 mM ethanolic solutions [393]. Figure 7.18 presents a comparison of the oscillation amplitude curves obtained on an undecylmercaptan-modified surface with methyl, hydroxyl, and amino termini acquired under conditions identical to the data presented in Figure 7.15. Little difference is observed in these curves. Figure 7.19 presents the corresponding resonance of the cantilever time correlated with scanner movement. All three substrates give rise to asymmetry in the frequency response. In contrast to the oscillation amplitude curves (Figure 7.18), large differences in resonance frequency shifts are observed during scanner retraction

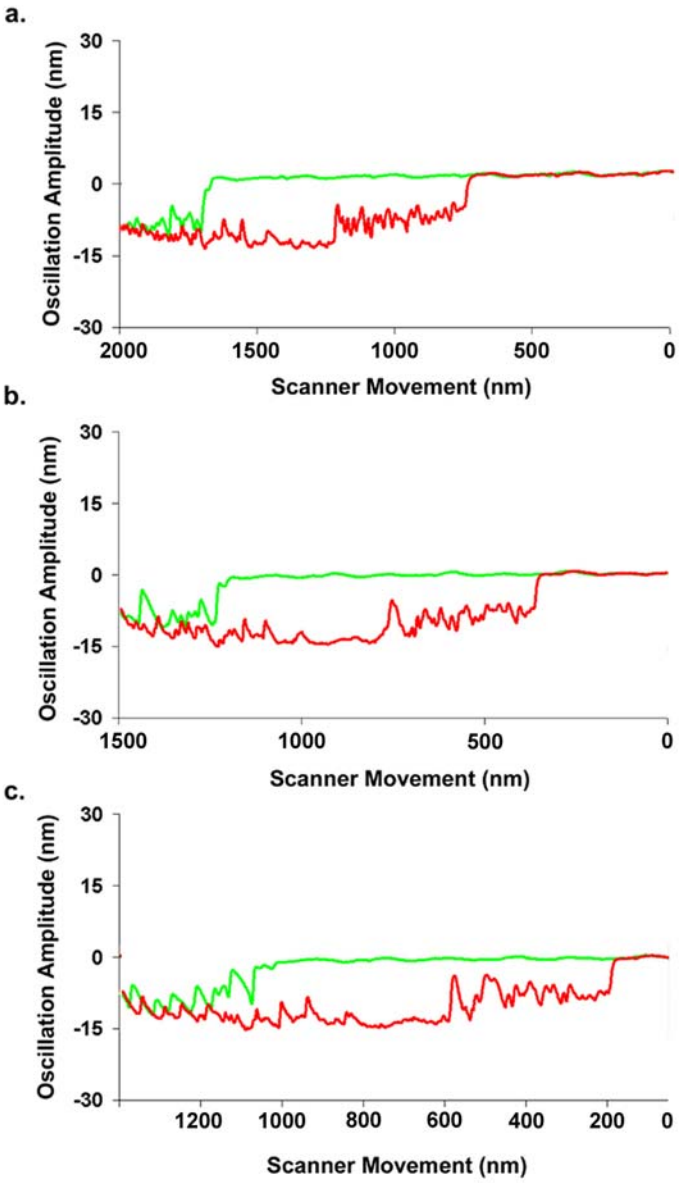

Figure 7.18. Cantilever oscillation amplitude plots acquired as a long SWNT is brought into and out of contact with a (a) 12-dodecanethiol (b) 11-hydroxy-undecanethiol, and (c) 11-amino-undecanethiol functionalized gold substrate while the cantilever was driven at a frequency of 69.5 kHz.

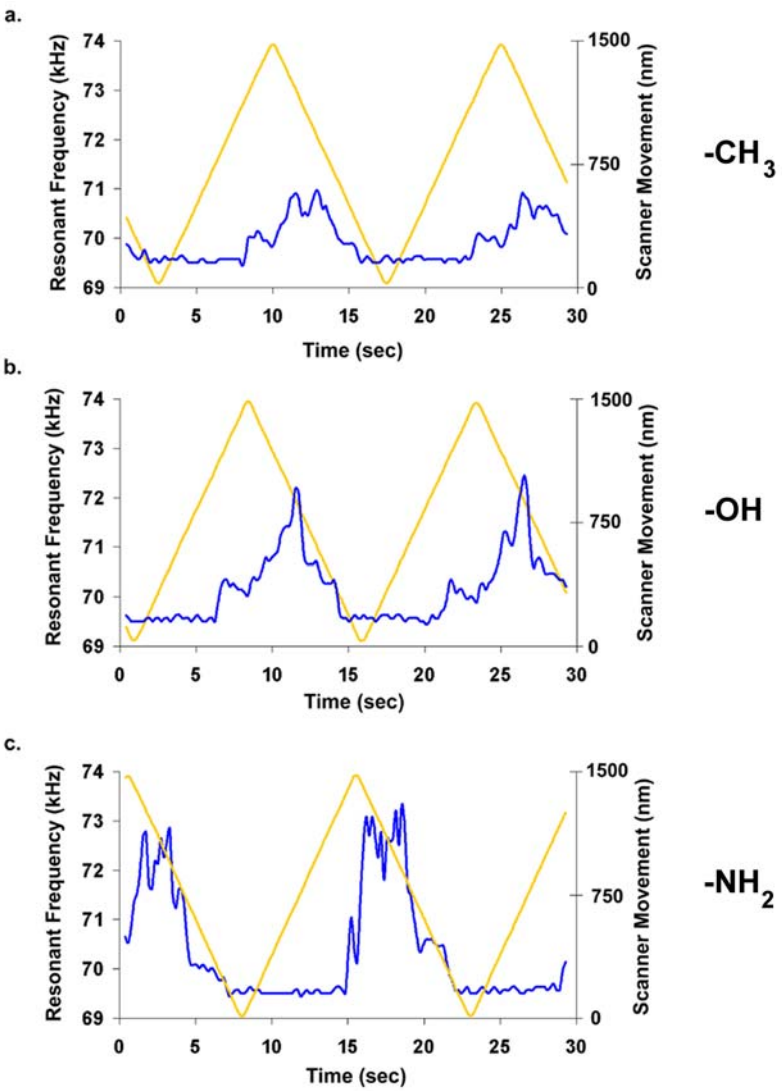

Figure 7.19. Plots of scanner movement (gold) and thermal resonance (blue) of the cantilever versus time for a long SWNT brought into and out of contact with (a) 12-dodecanethiol (b) 11-hydroxy-undecanethiol, and c) 11-amino-undecanethiol functionalized gold substrates. (all at 200 nm/sec)

commensurate with differing degrees of adhesion between the sidewall of the nanotube and the terminus of the alkanethiol monolayer on the substrate. It is interesting to note that the trend in frequency shift (CH_3 < OH < NH_2) mirrors that observed in the previously reported assessment of the affinity of alkanethiol-modified gold-coated AFM probe tips to the surface of SWNT paper (Chapter 5). The observed trend supports the hypothesis that adhesion of the nanotube to the substrate gives rise to asymmetry in the frequency response curves. In addition, since the same length of nanotube is in contact with each substrate, frequency shift data may serve as an alternate means for assessing the strength of adhesion.

In an attempt to elucidate the rupture force per molecule in this peeling study, a model is proposed that is somewhat similar to the two springs in series model used in the previous chapter. Here, the nanotube and the cantilever are modeled in a the same way as before but now another spring (or springs) need to be added which represent the molecular interactions that exist between the sidewall of the nanotube and the chemically homogeneous surface (Figure 7.20). If one models the cantilever/nanotube/surface in this way, the following numerical model can be results:

$$f_0 = \frac{1}{2\pi}\sqrt{\frac{k_B + k_{NT} + \sum k_{NT/Mol}}{m_{eff}^B + m_{NT} + \sum m_{Mol}}} \qquad \text{Equation 7.3}$$

where k_B is the cantilever beam stiffness, k_{NT} is the bending stiffness of the nanotube, Σ $k_{NT/mol}$ is the sum of the stiffnesses of each molecule interacting with the sidewall of the nanotube, m^B_{eff} is the effective mass of the cantilever, m_{NT} is the mass of the nanotube and Σ m_{mol} is the sum of the mass of each molecule interacting with the sidewall of the

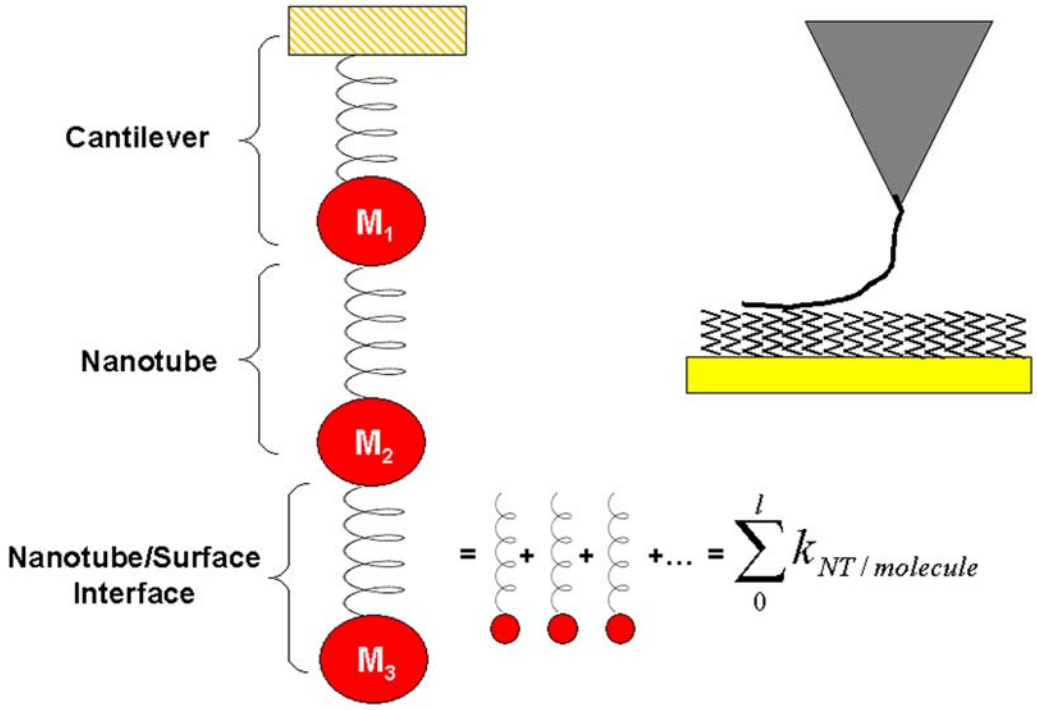

Figure 7.20. A plausible model for the cantilever/nanotube/surface interaction. Schematic on the right is of a nanotube-tipped cantilever interacting with a chemically homogenous surface. This model is similar to the two-springs in series model used to model the mechanical response of the carbon nanospring studied in Chapter 6. M_1, M_2, and M_3 are the mass of the cantilever, nanotube and the molecules on the surface respectively. The stiffness of the interaction between the nanotube and the molecules on the surface is the sum of the forces of each individual NT/molecule along the contact length of the nanotube.

nanotube. It was assumed that Σm_{mol} and m_{NT} were negligible relative to the mass of the cantilever beam.

The results from the experimental data are shown in Table 7.1. It is very interesting to note that the adhesion force per molecule follows a trend that mirrors the adhesion forces observed via the adhesion mapping studies. Although the values are slightly different than the forces elucidated via adhesion mapping, taking into account that a fairly general mechanical model was used to asses the interfacial adhesion the results are nonetheless impressive. It should be mentioned that this model is not refined by any means and that there more than likely are other elements that are not considered in this model but are definitely present. For example, Rabe and co-workers have studied the mechanical contact of a naked cantilever tip with a substrate. They have brought to light that there is likely a dashpot element that would need to be characterized and could be a factor in these experiments [414] (this is further addressed Chapter 8).

Looped Nanotube

For the following experiments, the same nanotube-tipped cantilever was used in each trial (SEM image inset in Figure 7.21). As determined using the SEM, the nanotube loop was approximately 3 μm in total length. For all experiments the after the point of contact between the nanotube and the substrate was established (as was determined via changes in the oscillation amplitude of the cantilever) a final pull-off event that was 400 nm away from the initial retraction point was maintained from substrate to substrate (Figure 7.21 a and b). Near the end of the approach curve in the cantilever oscillation plot, it was

Table 7.1 Summary of the experimental rupture forces measured via the peeling study involving the long nanotube. The reported rupture forces are based upon a three springs in series model where the average resonance at pull off was determined from the data presented in Figure 7.19.

Thiol Terminal Group	Average Pull-off Resonance (Hz)	Change in Resonance (Hz)	Rupture force per molecule (pN)
- CH_3	70349	849	7.79
- OH	70869	1369	13.05
- NH_2	72058	2558	34.50

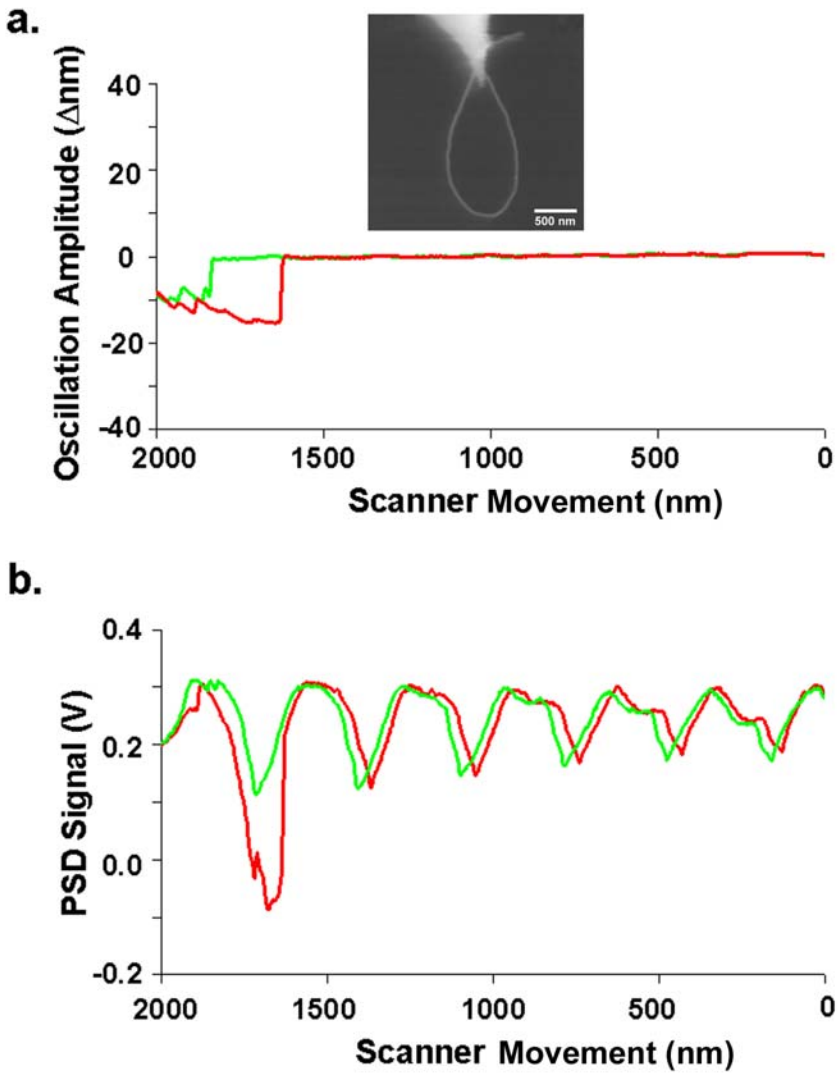

Figure 7.21. (a) SEM image (inset) of the looped SWNT and the oscillation amplitude curve obtained between the tube and a 11-mercaptoundecanoic self-assembled monolayer. (b) the corresponding force curve that possess a large amount of optical interference which inhibits determining the rupture force between the nanotube and the substrate.

typical that an amplitude drop would occur roughly 200 nm before the scanner was fully extended. Then, during retraction the cantilever would not reach a restored oscillation until the substrate had moved almost exactly 200 nm past that point of the initial dampening (thus, the tube remained in contact with the substrate during the first 400 nm of travel of the retraction of the scanner from the surface, i.e. total compression of 400 nm) (Figure 7.22). This could plausibly be explained by more of the nanotube being in contact from relaxation of the tube onto the surface during the approach.

When the nanotube loop is brought into and out of contact with a SAM composed of 11-dodecanethiol at a velocity of 100 nm/sec the resonant response appears to look strikingly similar to the resonant response for a long straight nanotube. When the substrate initially touches the loop the resonant frequency jumps up but then starts to drop down roughly 1 kHz. Then as the substrate is removed from the nano-loop the frequency of the cantilever\loop increase until the sample is no longer in contact. The loop gives the same resonance signature with repetitive measurements (possibly indicating that the tube is undergoing the same mechanical and chemical strains during each extension and retraction).

It is postulated that the looped nanotube is pulled in tension as the surface is initially brought into contact with the underlying surface (Figure 7.23 c. point #1 to point #2). Then as the scanner continues to push up on the loop, the loop may slide on the methylated surface (Figure 7.23 c. point #3 to point #4). Then as the sample is removed from the nano-loop, the loop is pulled in tension due to possible stiction with the

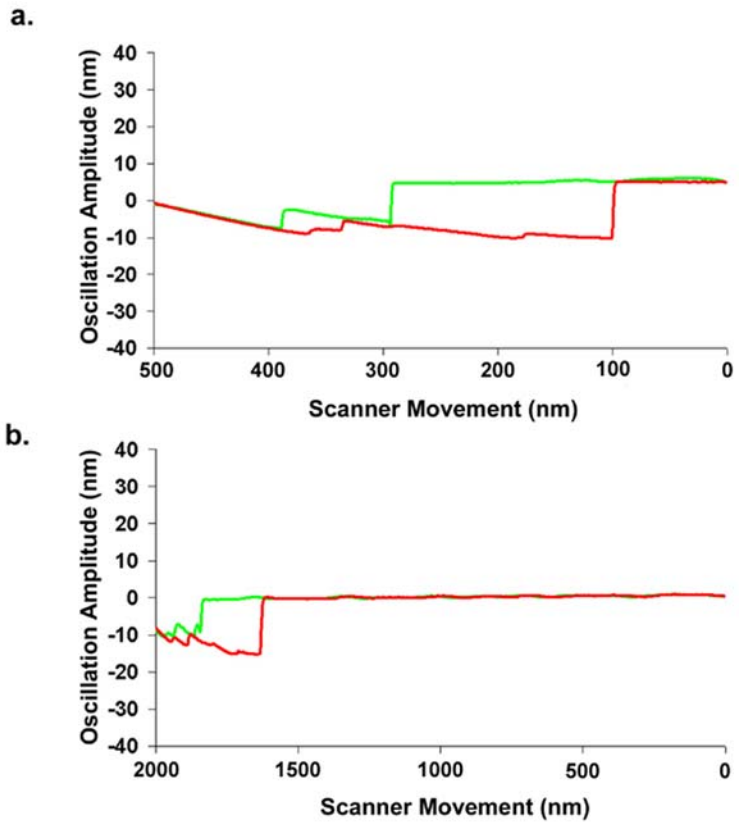

Figure 7.22. Oscillation amplitude curves acquired when the looped SWNT is brought into and out of contact with a TSG substrate that has a carboxylic acid terminated thiol. The same oscillation amplitude dampening during the approach was investigated at two different scanner velocities (a) 400 nm/sec. (b) 100 nm/sec.

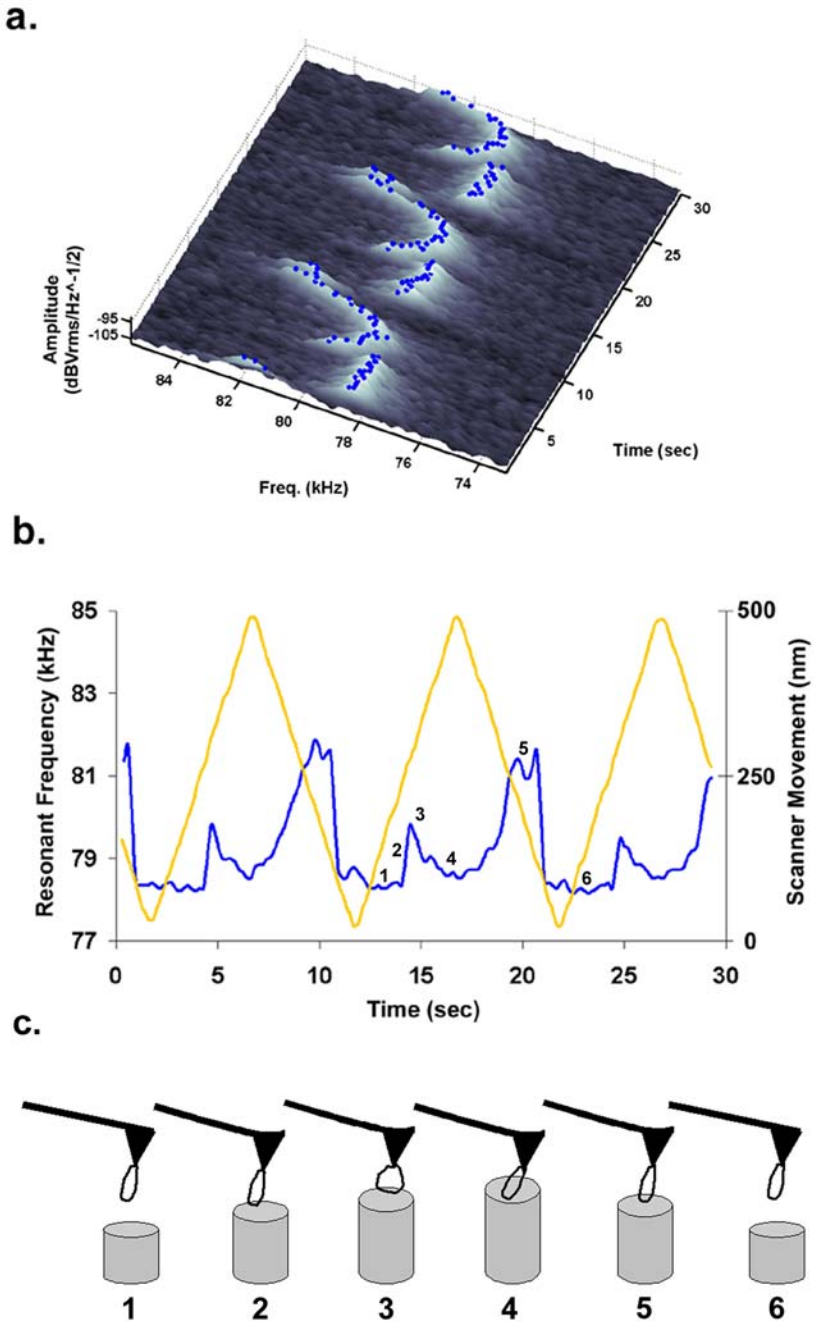

Figure 7.23. (a) Thermally-driven resonance of the looped nanotube/cantilever as it is repetitively brought into and out of contact with a methyl-terminated alkanethiol-modified TSG substrate at 100 nm/sec. (b) peak resonance of the nanotube/cantilever with corresponding substrate position. (c) schematic of the possible orientation of the looped tube during compression.

underlying surface (as was the case with the long nanotube) (Figure 7.23 c. point #5 to point #6)

When the looped nanotube is brought into and out of contact with a SAM composed of 11-mercaptoundecanol the resonant response looks qualitatively different than the resonant response of the methyl-terminated SAM (Figure 7.24). During the approach cycle the resonance jumps up roughly 1.5 kHz and stays at that level (plateaus) and stays at a plateau during a portion of the retraction and them gradually increases until the substrate is fully removed from the nano-loop. This could be explained in the following manner: the loop once touched by the surface begins to "bow" and continues to do so until the substrate is remove from the nanotube. The observed shifts in the cantilever/nanotube's resonance are extremely reproducible regardless of the velocity of the scanner.

When the nanotube loop is brought into and out of contact with a SAM composed of 11-mercaptoundecanoic acid the resonant response looks qualitatively similar to that of the hydroxyl terminated alkanethiol SAM. Again in this case the loop demonstrates a very reproducible resonance response (Figure 7.25a). One interesting item to note is that during the retraction of the sample, there appears to be a resonant plateau followed by a final increase in frequency before the tube is fully removed from the surface. These resonant plateaus could potentially indicate that the looped nanotube is reversibly being uncompressed until an adhesive force dominates the sidewall of the tube.

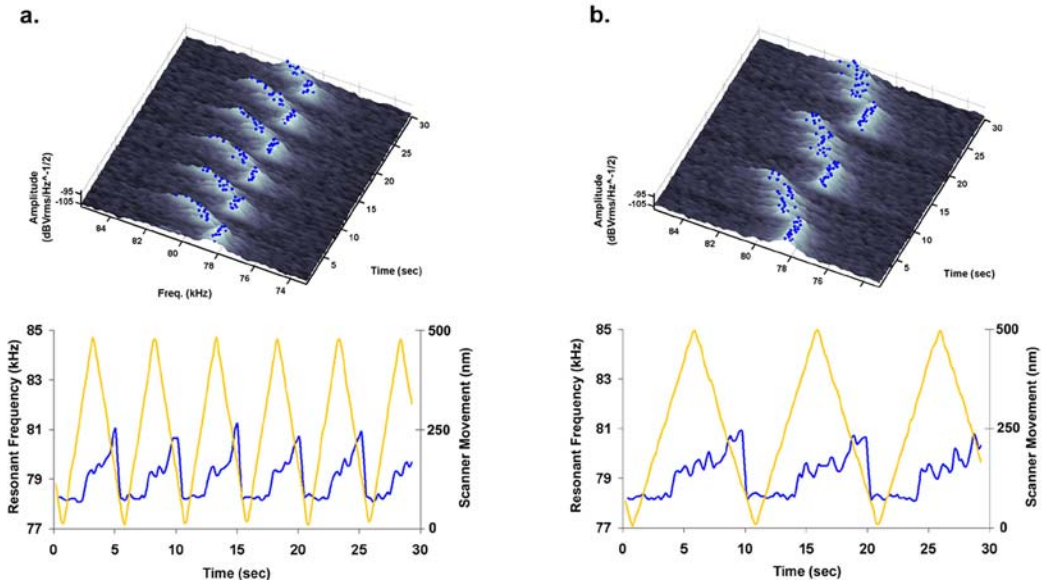

Figure 7.24. Repetitive compression/decompression cycles of the SWNT loop on a hydroxyl-terminated alkanethiol-modified TSG substrate. (a) 200 nm/sec. (b) 100 nm/sec respectively.

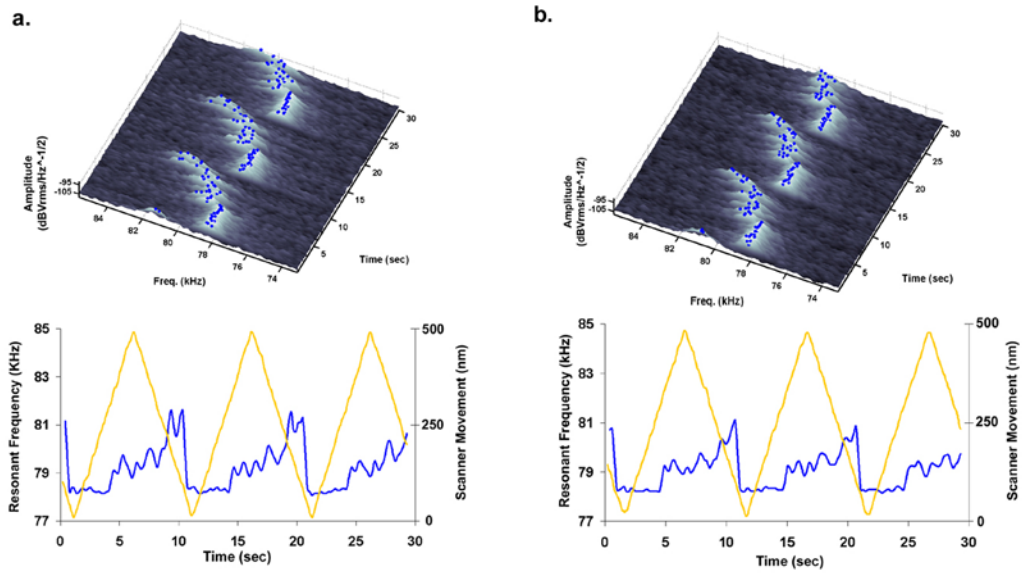

Figure 7.25. Repetitive compression/decompression cycles at 100 nm/sec of the SWNT loop on alternate surfaces (a) carboxylic acid-terminated alkanethiol (b) amine-terminated alkanethiol.

When the nanotube loop is brought into and out of contact with a SAM composed of 11-amino-undecanethiol the resonant response looks qualitatively similar to that of the carboxylic acid-terminated alkanethiol SAM. Although in this case, the stepwise progression of the resonance during retraction is much less pronounced (Figure 7.25b). The release frequency is also about 0.5 kHz less than the carboxylic acid.

When the nanotube loop is brought into and out of contact with freshly cleaved SPI-1 (ultra flat) HOPG the resonant response looks qualitatively similar to that of the carboxylic acid and amine-terminated alkanethiol SAMs. One interesting difference is that during the approach, the resonant frequency of the beam/nano-loop increases only 0.5 kHz, and remains flat (Figure 7.26). This could be indicative of the loop being able to slide on the surface of the graphite (as was the case with the short nanotube). Then during the retraction of the graphite from the loop, the resonance jumps about 1 kHz and then drops. Then there is a final increase in resonance prior to removal from the graphite (beam's resonance is restored). A similar motion is also observed in the deflection curve that is presented in Figure 7.7 (bottom curve). During retraction of the sample the cantilever beam gets pulled downward, begins to bend up, and then gets pulled down again one last time before the tube is fully removed from the substrate.

It is interesting that the methyl-terminated SAM and the graphite surface yielded somewhat similar responses to each and that the other substrates (amine, hydroxyl and carboxylic acid terminated) all exhibited a "plateau" upon contact and compression. Recent rheological studies of self-assembled monolayers on gold have been studied and

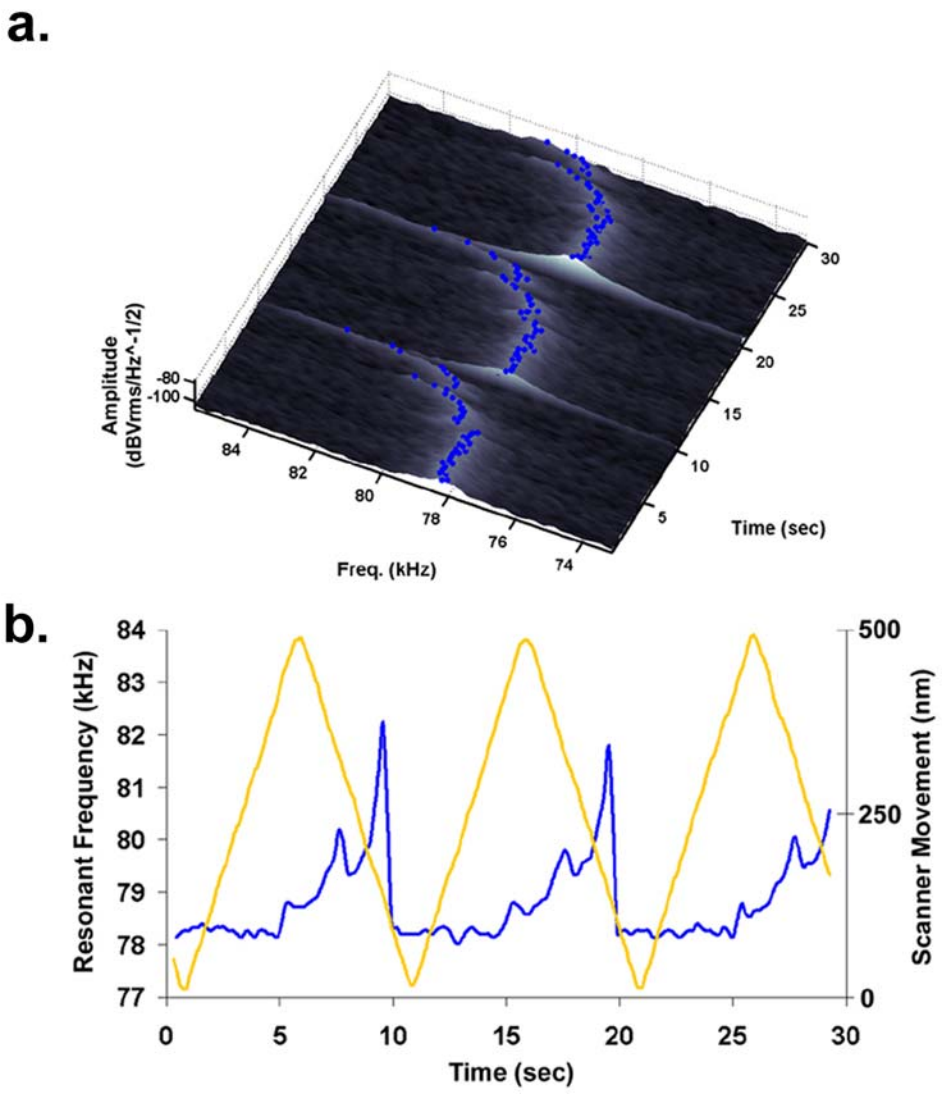

Figure 7.26. Repetitive compression/decompression cycles of the SWNT loop on HOPG at 100 nm/sec. (a) thermally-driven resonance waterfall of the cantilever/nanotube during the compression. (b) Substrate position (yellow) and peak resonance of the cantilever/nanotube during the compression event.

coefficients of friction have been reported. Graphite (as mentioned earlier) has extremely low coefficients of friction [404], while hydroxyl and carboxylic acid terminated alkanethiols have much larger coefficients of friction [406,407,410]. These frictional properties correlate fairly well with the nanotube\substrates investigated here and are most likely the driving force for the looped nanotube's inability to slide on these surfaces.

Conclusions

In a broader context, the results presented herein have important consequences for imaging and force spectroscopy studies involving carbon nanotube tips. The commonly used method of monitoring oscillation amplitude as a function of scanner position has limited applicability. Depending upon the mechanical properties of the tip, this plot may not be a reliable indicator of the point of contact and release from the opposing substrate. Secondly, since amplitude is measured at a specific frequency, decreased amplitude may be observed when resonance amplitude is diminished or shifted in frequency. Diminished amplitudes do not provide a reliable indicator of the state of the nanotube [200,203]. Thus, multi parameter force spectroscopy (MPFS) can provide a more accurate interpretation of nanoscale adhesion phenomena and can provide information that was previously unattainable.

CHAPTER 8

FUTURE DIRECTIONS OF RESEARCH

Adhesion Mapping

In Chapter 5 several thiols molecules were evaluated using adhesion mapping. However, there are several other chemical moieties found in the polymers commonly used in composites. Adhesion mapping studies could also be carried out by coating the entire cantilever tip with polymers that could potentially be used in nanotube-based composites. Poly aromatic molecules would be interesting candidates for study via the adhesion mapping approach (Figure 8.1)[415]. It would be expected that these molecules should pose very large binding forces per molecule due to the potential for a high number of π-π overlaps to occur between the aromatic end group and the sidewall of the nanotube. There are several other candidates for these studies which include DNA [416,417] and porphyrins [418] (which have both been shown to interact with the back bone of a carbon nanotube.

It has been reported that if a SWNT is sufficiently loaded that the carbon atoms that are being mechanically loaded have been shown to undergo a sp^2 to sp^3 transition [419] (this would inherently alter the reactivity of the nanotube backbone [306]). Dynamic tests where the mechanical load is gradually increased on the backbone of the carbon nanotube while the adhesion mapping is being performed.

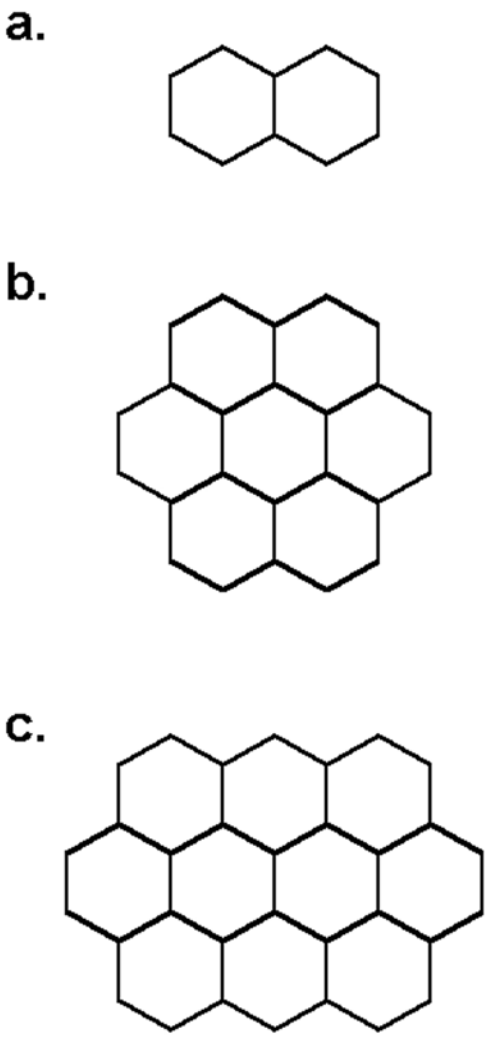

Figure 8.1. Potentially interesting molecules that could be of interest in using for the adhesion mapping studies. (a) naphthalene. (b) coronene. (c) ovalene.

Based on the results presented for characterizing adhesion between chemically modified cantilevers and SWNT paper, one of the questions remaining unanswered is the role of hydration layers in the adhesion of nanotubes with the SAMs. A proposed study of adhesion in fluid would provide an answer to this question. This study is nontrivial and will require careful selection of a solvent that will stabilize the monolayer and effectively wet both the monolayer and the nanotube [329].

Nanostructure Mechanics

The development and utilization of multi parameter force spectroscopy as introduced in Chapters 6 and 7, should create an entirely new way to probe materials on the nanoscale. Additional experiments regarding the peeling of the nanotubes off of the chemically modified surfaces could be performed to investigate the possibility of a time dependence of these interactions. For example, the AFM used herein was limited in that the velocity used during the approach was also that for retraction of the scanner. Newer models of commercial AFMs enable force curve acquisition at variable velocities (i.e. one velocity for the approach and another velocity for the retraction of the scanner.

Another potentially fruitful endeavor would be to extend MPFS to measuring the shearing response between that nanotube and a substrate. This can be accomplished by bringing the nanotube into physical contact with the surface and then translate the surface in the x and y plane. Nanoscale shearing could be measured by monitoring cantilever deflection, torsion and resonant frequency.

One of the current challenges in nanotube research is the acquisition of information regarding defect identity and location on individual nanotubes. TEM can and has been used to study the wall structure of both the SWNT and MWNT structures [288]. In this work it was not possible to locate defect areas in the nanotubes sidewalls without detachment of the nanotube from the tip. The design of a cantilever chip holder that can be mounted in s TEM would enable characterization of the nanotube without sacrificing the nanotube. This would provide a means to correlate the location of a defect with the measured resonance response during the mechanical peeling tests. With the MWNTs, knowing the exact number of walls in each coil would allow further refinement of the models used to predict the mechanical response of the nanospring.

The study presented in Chapter 6 where a MWNT spring was repetitively compressed and decompressed should open up other areas of nanostructure research. One could study the mechanical response of coils that have different tighter or wider helical rises, different numbers of walls and varying numbers of coils per unit length. This will help scientists understand the physical limitations of devices that could potentially be made using nano-scale springs.

In Chapter 6 the carbon nanospring was only compressed a small amount, it should be of interest to monitoring the frequency response of the nanosprings under even larger compression lengths. This could provide insight into the plausible orientation, shape and size of the spring while its being mechanically loaded (Figure 8.2). The higher vibration modes of the cantilever could also be studied during the compression of the nanosprings

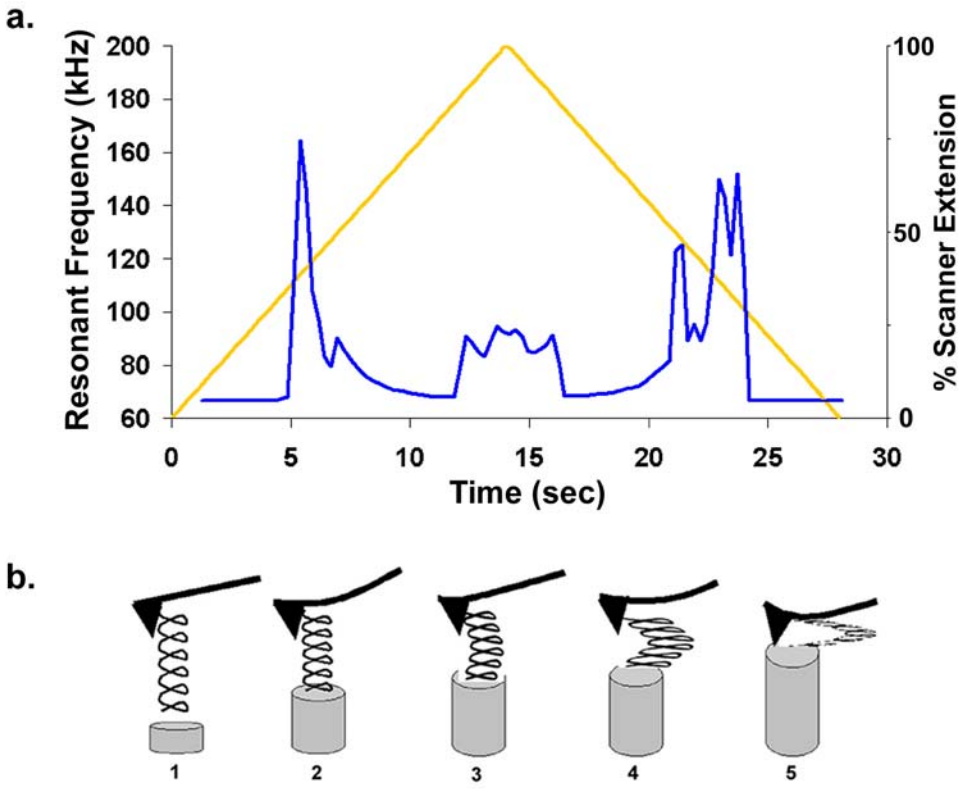

Figure 8.2. (a) Nanospring-tipped cantilever peak resonance (blue) with time-correlated scanner movement (yellow). Scanner velocity during compression was 100 nm/sec. The nanospring was compressed 1000 nm. (b) Illustration of the postulated response of the nanotube during vertical loading.

and nanotubes. This should provide more information regarding the orientation of the tube coming off of the surface as well as enhance the understanding of the dynamic nature of these nanoscale springs. This could be accomplished by utilizing a data acquisition card that has a higher acquisition rate than the analyzer used in the experiments presented here. Then, one could monitor more than one cantilever vibration mode during a single compression\decompression cycle. The multi parameter force spectroscopy (MPFS) approach should be applicable to a myriad of nanostructures [252,420,421] and help researchers determine the feasibility and tolerances of proposed nanoscale devices.

Biomolecules

MPFS provided a straightforward means for determining the stiffness of nanoscale materials. An obvious extension of this approach is the determination of the stiffness of biopolymers under mechanical load. Force spectroscopic investigations of biomolecules such as DNA that are performed using the AFM, typically rely solely on knowledge of the stiffness of the cantilever beam and the deflection of the cantilever during unwinding of the molecule. MPFS will provide more information regarding the mechanical response of biological molecules and could be used to reduce the vertical load applied to biopolymers.

Currently, force spectroscopic investigations involve strictly monitoring the vertical movement of the cantilever during biopolymer unwinding. These deflection-based experiments require making mechanical contact between a chemically modified

cantilever tip and a molecule tethered to a substrate. This mechanical contact (vertical load) can damage or alter the natural state of the biopolymer, MPFS could eliminate the need to make mechanical contact between the underlying surface and the tip (which in some instances can destroy molecular recognition elements on the surface). Force example, if one were to track the thermal motion of the cantilever during the extension of the scanner towards the cantilever, as soon as dampening is observed, the scanner could be turned around (retracted) thus easing (or eliminating) the forces exerted on the molecules to be strictly those induced by van der Waals interactions (Figure 8.3).

Nanotube-tipped Plastic Cantilevers

The work presented in this dissertation is, in fact, only a portion of the research I conducted during my tenure at Georgia Tech. In a project that has been jointly worked on in collaboration with Professor Jonathan Colton and Andrew McFarland, we have created injection-molded cantilevers that could potentially have nanotubes embedded at the end of the beam (simply by pushing the polymeric beam into a low-density field of vertically aligned nanotubes). If this nanotube tethering mechanism can be achieved, not only would SPM be revolutionized, but also the experiments that were just presented could truly be in their infancy.

Also, cantilever-based sensing that currently utilizes cantilevers that are produced via silicon micromachining could also be severely impacted by the implementation of these plastic cantilevers. The implementation of plastic cantilevers into disposable sensing

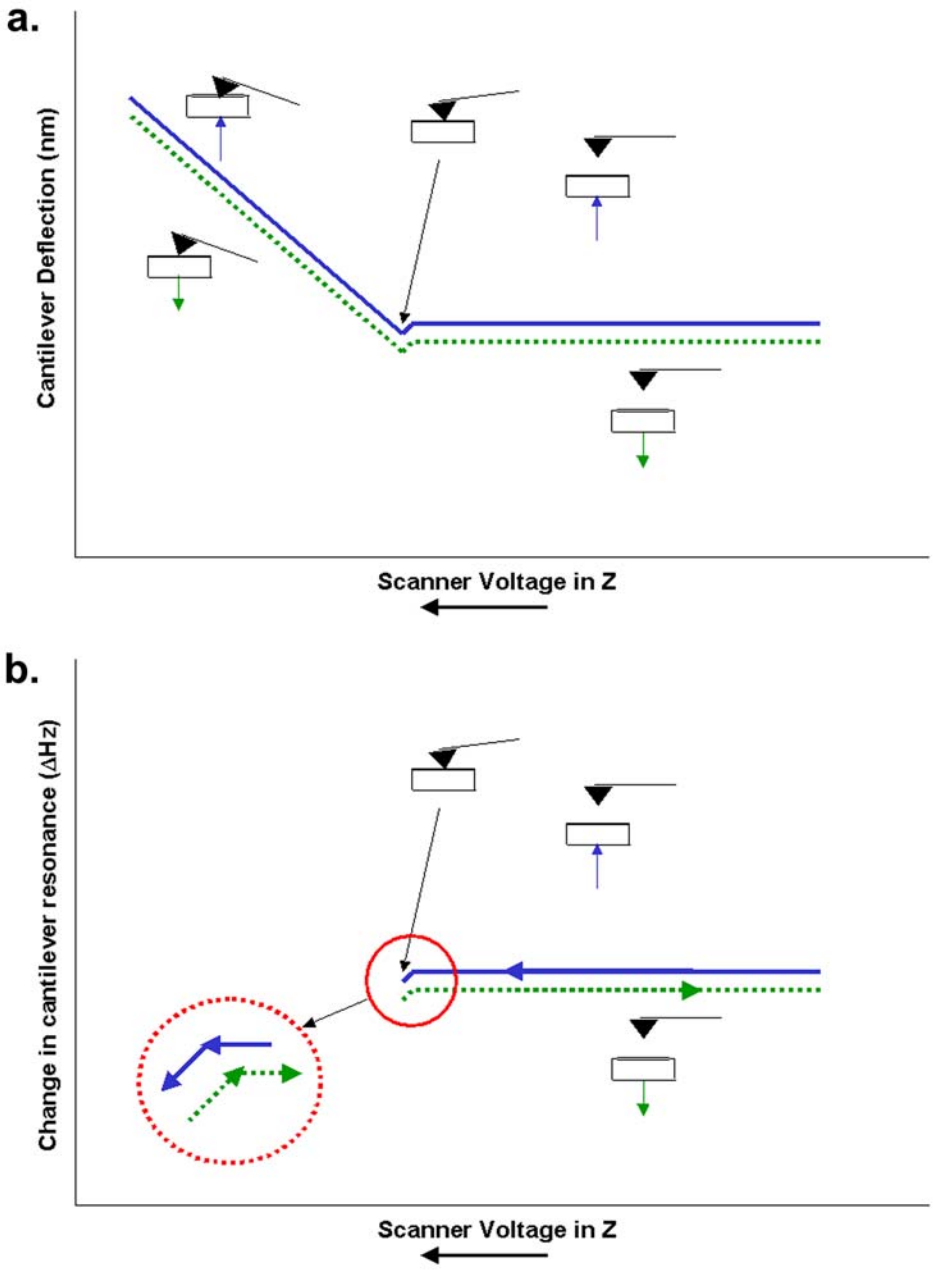

Figure 8.3. (a) Ideal force curve where mechanical contact is made between the cantilever tip and the substrate and where no interfacial adhesion is present between the cantilever tip and the underlying surface. (b) Theoretical curve obtained using MPFS where the scanner is retracted after the detection of a certain amount of change in the cantilever beam's resonance (zoomed-in portion of the plot).

units could propel cantilever-based sensing from the lab into more dynamic environments.

APPENDIX A:

DERIVATION OF THE SECOND MOMENT OF INERTIA OF A TRAPEZOID

Defining the moment of inertia of a trapezoid is done first by locating the center of mass (y_c) in the cross-section of the beam.

$$y_c \equiv \frac{1}{A}\int y dA$$

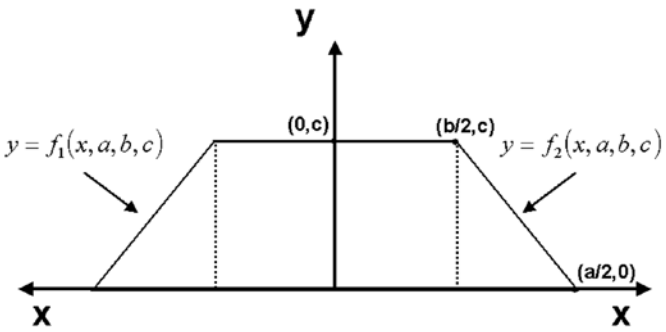

This integration can be achieved by breaking up the trapezoid into two triangles and a rectangle.

$$y_c \equiv \frac{1}{A}\left\{\int_{-a/2}^{-b/2}\left[\int_0^{f_1} y dy\right]dx + \int_{-b/2}^{b/2}\left[\int_0^{c} y dy\right]dx + \int_{b/2}^{a/2}\left[\int_0^{f_2} y dy\right]dx\right\}$$

This integration can also be evaluated by re-establishing the faces of the trapezoid in terms of y (i.e. reverse order).

Where:

$$y = f_1(x,a,b,c),\ \ or\ \ x = g_1(y,a,b,c)$$

and

$$y = f_2(x,a,b,c),\ \ or\ \ x = g_2(y,a,b,c)$$

By utilizing Fubini's Theorem the complicated integral becomes less difficult to solve:

$$y_c \equiv \frac{1}{A}\left\{\int_0^c \left[\int_{g_1}^{g_2} dx\right] y dy\right\}$$

This integration yields the centroid of the trapezoid:

$$c_y = \frac{h}{3}\left(\frac{2a+b}{a+b}\right)$$

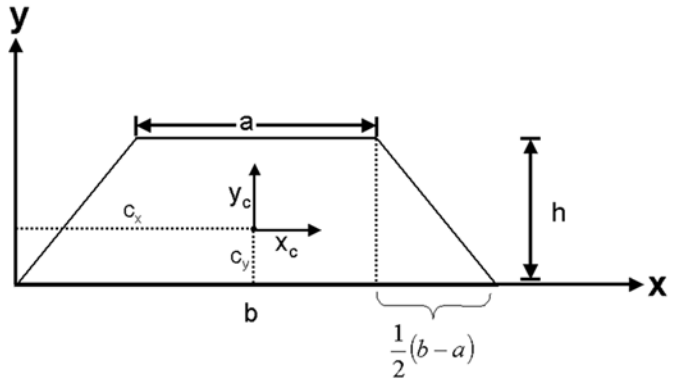

With the center of mass of the trapezoid defined, the second moment of the trapezoid can be derived by translating the center of mass of the trapezoid's location to the origin.

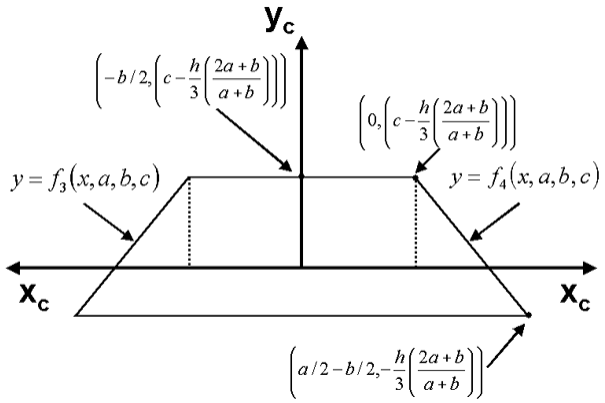

Now, one decomposes the trapezoid into two triangles and a rectangle; and integrates.

Where:

$$I_{xc} = \int y^2 dA$$

$$y = f_3(x,a,b,c), or: x = g_3(y,a,b,c)$$

and

$$y = f_4(x,a,b,c), or: x = g_4(y,a,b,c)$$

The moment is now expressed as:

$$I_{xc} = \int_{-\frac{h}{3}\left(\frac{2a+b}{a+b}\right)}^{c-\frac{h}{3}\left(\frac{2a+b}{a+b}\right)} \left[\int_{g_3}^{g_4} dx \right] y^2 dy$$

From this, the 2nd moment of the trapezoid is defined:

$$I_{xc} = \frac{h^3\left(a^2 + 4ab + b^2\right)}{36(a+b)}$$

APPENDIX B:

LIST OF PUBLISHED WORK

McFarland, Andrew W.; Poggi, Mark A.; Bottomley, Lawrence A.; Colton, Jonathan S.; "Entirely Injection Molded Polymeric Scanning Probe Microscopy Probes". *Nano Letters*, in prep.

Poggi, Mark A.; Bottomley, Lawrence A.; Lillehei, Peter T. "Chemical Force Microscopy of Single Walled Carbon Nanotube Paper". *Chemistry of Materials*, submitted.

McFarland, Andrew W.; Poggi, Mark A.; Bottomley, Lawrence A.; Colton, Jonathan S.; "Characterization of Microcantilevers Solely by Frequency Response Acquisition". submitted.

Poggi, Mark A.; Bottomley, Lawrence A.; Lillehei, Peter T. "A Force Spectroscopic Investigation of Single Walled Carbon Nanotube Tipped Cantilevers: Nanoscale Fly-Fishing". *Nano Letters*, submitted.

Poggi, Mark A.; McFarland, Andrew W.; Colton, Jonathan S.; Bottomley, Lawrence A. "An Improved Method for Determining the Spring Constant of AFM Cantilevers with a Nonrectangular Cross-section". *Analytical Chemistry*, in review **(2004)**.

Poggi, Mark A.; Bottomley, Lawrence A.; Shen, Shanxiang "The Impact Of Nano- And Meso-Scale Particles On The Performance Of Microcantilever-Based Sensors". *Analytical Chemistry*, in press **(2004)**.

McFarland, Andrew W.; Poggi, Mark A.; Bottomley, Lawrence A.; Colton, Jonathan S. "Injection Molding of High Aspect Ratio Micron-Scale Thickness Polymer Microcantilevers". *Nanotechnology*, in press (**2004**)

Gadsby, Elizabeth, Poggi, Mark A.; Bottomley, Lawrence A.; "Microscopy: Atomic Force and Scanning Tunneling Microscopy", *Encyclopedia of Analytical Chemistry*, in press (**2004**).

Roberson, Luke B.; Poggi, Mark A.; Kowalik, Janusz.; Smested, Greg P.; Bottomley, Lawrence A.; Tolbert, Laren M.; "Correlation of Morphology and Performance in Inorganic-Organic TiO2-Polythiophene Hybrid Solid-State Solar Cells". *Coordination Chemistry Reviews*, in press (**2004**).

McFarland, Andrew W.; Poggi, Mark A.; Bottomley, Lawrence A.; Colton, Jonathan S. "Production and Characterization of Polymer Microcantilevers". *Review of Scientific Instruments*, (**2004**), 75(8), 2756-2758.

Bottomley, Lawrence A.; Poggi, Mark A.; Lillehei, Peter T.; "Molecular Design of Next-Generation Single walled Carbon Nanotubes-Polymer Composites". *Proceedings Microscopy and Microanalysis*, (**2004**), 10(2), 134-135

Bottomley, Lawrence A.; Lillehei, Peter T.; Poggi, Mark A.; Eric Horowitz.; Jaimie Anderson.; Vincent Conticello.; "Force Spectroscopy of Biopolymers: Correlating Molecular Structure and Single Molecule Elasticity". *Proceedings Microscopy and Microanalysis*, (**2004**), 10(2), 204-205.

Lillehei, Peter T.; Poggi, Mark A.; Polk, Brian J.; Smith, J. Anthony.; Bottomley, Lawrence A. "Plastic tip arrays for force spectroscopy". *Analytical Chemistry*, (**2004**), 76(13), 3861-3863.

Poggi, Mark A.; Gadsby, Elizabeth D.; Bottomley, Lawrence A.; King, William P.; Oroudjev, Emin.; Hansma, Helen G.; "Scanning Probe Microscopy". *Analytical Chemistry*, (**2004**), 76(12), 3432-3446.

Poggi, Mark A.; Boyles, Jeffrey S.; Bottomley, Lawrence A.; McFarland, Andrew W.; Colton, Jonathan S.; Nguyen, Cattien V.; Stevens, Ramsey M.; Lillehei, Peter T.; "Measuring the Compression of a Carbon Nanospring". *Nano Letters*, (**2004**), 4(6), 1009-1016.

McFarland, Andrew W.; Colton, Jonathan S.; Poggi, Mark A.; Bottomley, Lawrence A.; "Plastic Bio-MEMS Sensors". *ANTEC Proceedings*, Chicago, IL, **2004**, pp 3717-3721.

Bottomley, Lawrence A.; McFarland, Andrew W.; Poggi, Mark A.; Colton, Jonathan S. "Polymeric microcantilevers for sensing applications". *Polymeric Materials Science and Engineering*, **2004**, (90) 164-165.

Bottomley, Lawrence A.; Poggi, Mark A.; McFarland, Andrew W.; Colton, Jonathan S.; Lillehei, Peter T.; "Force spectroscopy of single walled carbon nanotubes for improved polymer composites". *Polymeric Materials Science and Engineering*, **2004**, (90) 149-151.

Poggi, Mark A.; Bottomley, Lawrence A.; Lillehei, Peter T. "Measuring The Adhesion Forces Between Thiol-Modified AFM Cantilevers and Single Walled Carbon Nanotubes". *Nano Letters*, (**2004)**, 4(1), 61-64.

Poggi, Mark A.; Bottomley, Lawrence A.; Lillehei, Peter T. "Chemical Force Microscopy of Single Walled Carbon Nanotubes". *Proceedings - Electrochemical Society*, **2003**; (2003-15), pp 297-304.

Nelson, Brent A.; Poggi, Mark A.; Bottomley, Lawrence A.; King, William P. "Temperature-dependence of Water Bridge Formation in Atomic Force Microscopy". *Proceedings of the IMECE*, **2003**, (2), MEMS, pp 1-8.

Poggi, Mark A.; Bottomley, Lawrence A.; Lillehei, Peter T. “Scanning Probe Microscopy”. *Analytical Chemistry* 2002, 74(12), 2851-2862.

REFERENCES

[1] G Binnig, H Rohrer, C Gerber, E Weibel: Tunneling through a controllable vacuum gap. Applied Physics Letters 1982: 40; 178-80.

[2] G Binnig, H Rohrer: In Touch with Atoms. Review of Modern Physics 1999: 71; 324-30.

[3] G Binnig, CF Quate, C Gerber: Atomic Force Microscope. Physical Review Letters 1986: 56; 930-34.

[4] Chemical-Abstracts-Service(CAS): Maintained by The American Chemical Society 2004.

[5] E Meyer, R Overney, K Dransfeld, T Gyalog: Nanoscience: Friction and Rheology on the Nanometer Scale, World Scientific Publishing, River Ridge, NJ, 1998.

[6] R Wiesendanger: Scanning Probe Microscopy and Spectroscopy: Methods and Applications, Cambridge University Press, Cambridge, Great Britain, 1994.

[7] D Sarid: Oxford Series on Optical Sciences, Vol. 2: Scanning Force Microscopy with Applications to Electric, Magnetic, and Atomic Forces, 1991.

[8] M Madou: Fundamentals of Micromachining, CRC Press, Boca Raton, FL, 1997.

[9] MA Poggi, ED Gadsby, LA Bottomley, WP King, E Oroudjev, H Hansma: Scanning Probe Microscopy. Analytical Chemistry 2004: 76; 3432-46.

[10] FJ Giessibl: Advances in atomic force microscopy. Reviews of Modern Physics 2003: 75; 949-83.

[11] LA Bottomley: Scanning probe microscopy. Analytical Chemistry 1998: 70; 425R-75R.

[12] LA Bottomley, JE Coury, PN First: Scanning Probe Microscopy. Analytical Chemistry 1996: 68; 185-230.

[13] NA Burnham, RJ Colton, HM Pollock: Interpretation issues in force microscopy. J. Vac. Sci. Technol. A 1991: 9; 2548-56.

[14] NA Burnham, RJ Colton, HM Pollock: Interpretation of force curves in force microscopy. Nanotechnology 1993: 4; 64-80.

[15] LB Roberson, MA Poggi, J Kowalik, GP Smestad, LA Bottomley, LM Tolbert: Correlation of morphology and device performance in inorganic–organic TiO2–polythiophene hybrid solid-state solar cells. Coordination Chemistry Reviews 2004.

[16] SI Lee, SW Howell, A Raman, R Reifenberger: Nonlinear dynamic perspectives on dynamic force microscopy. Ultramicroscopy 2003: 97; 185-98.

[17] H Holscher, SM Langkat, A Schwarz, R Wiesendanger: Measurement of three-dimensional force fields with atomic resolution using dynamic force spectroscopy. Applied Physics Letters 2002: 81; 4428-30.

[18] MA Poggi, LA Bottomley, PT Lillehei: Scanning Probe Microscopy. Analytical Chemistry 2002: 74; 2851-62.

[19] WA Hofer, AS Foster, AL Shluger: Theories of scanning probe microscopes at the atomic scale. Reviews of Modern Physics 2003: 75; 1287-331.

[20] M Balantekin, A Atalar: Power dissipation analysis in tapping-mode atomic force microscopy. Physical Review B: Condensed Matter and Materials Physics 2003: 67; 193404/1-04/4.

[21] R Boisgard, JP Aime, G Couturier: Analysis of mechanisms inducing damping in dynamic force microscopy: surface viscoelastic behavior and stochastic resonance process. Applied Surface Science 2002: 188; 363-71.

[22] TR Rodriguez, R Garcia: Theory of Q control in atomic force microscopy. Applied Physics Letters 2003: 82; 4821-23.

[23] C Su, L Huang, K Kjoller, K Babcock: Studies of tip wear processes in tapping mode atomic force microscopy. Ultramicroscopy 2003: 97; 135-44.

[24] M Stark, RW Stark, WM Heckl, R Guckenberger: Inverting dynamic force microscopy: from signals to time-resolved interaction forces. Proceedings of the National Academy of Sciences of the United States of America 2002: 99; 8473-78.

[25] PM Hoffmann: Dynamics of small amplitude, off-resonance AFM. Applied Surface Science 2003: 210; 140-45.

[26] G Couturier, R Boisgard, L Nony, JP Aime: Noncontact atomic force microscopy: Stability criterion and dynamical responses of the shift of frequency and damping signal. Review of Scientific Instruments 2003: 74; 2726-34.

[27] W-J Chang, S-S Chu: Analytical solution of flexural vibration responses on taped atomic force microscope cantilevers. Physics Letters A 2003: 309; 133-37.

[28] TE Schaffer, M Richter, MB Viani: Array detector for the atomic force microscope. Applied Physics Letters 2000: 76; 3644-46.

[29] TE Schaffer: Force spectroscopy with a large dynamic range using small cantilevers and an array detector. Journal of Applied Physics 2002: 91; 4739-46.

[30] AG Onaran, FL Degertekin, B Hadimioglu: Tapping mode and elasticity imaging in liquids using an atomic force microscope actuated by acoustic radiation pressure. Applied Physics Letters 2002: 80; 4063-65.

[31] WP King, TW Kenny, KE Goodson, G Cross, M Despont, U Durig, H Rothuizen, GK Binnig, P Vettiger: Atomic force microscope cantilevers for combined thermomechanical data writing and reading. Applied Physics Letters 2001: 78; 1300-02.

[32] EM Chow, HT Soh, HC Lee, JD Adams, SC Minne, G Yaralioglu, A Atalar, CF Quate, TW Kenny: Integration of through-wafer interconnects with a two-dimensional cantilever array. Sensors and Actuators, A: Physical 2000: A83; 118-23.

[33] M Despont, J Brugger, U Drechsler, U Durig, W Haberle, M Lutwyche, H Rothuizen, R Stutz, R Widmer, G Binnig, H Rohrer, P Vettiger: VLSI-NEMS chip for parallel AFM data storage. Sensors and Actuators, A: Physical 2000: A80; 100-07.

[34] GLW Cross, M Despont, U Drechsler, UT Durig, H Rothuizen, GK Binnig, P Vettiger, WP King, KE Goodson: Thermomechanical formation and thermal sensing of nanometer-scale indentations in PMMA thin films for parallel and dense AFM data storage. Mater. Res. Soc. Symp. Proc. 2001: 649; Q2.3.1-Q2.3.6.

[35] T Sulchek, RJ Grow, GG Yaralioglu, SC Minne, CF Quate, SR Manalis, A Kiraz, A Aydine, A Atalar: Parallel atomic force microscopy with optical interferometric detection. Applied Physics Letters 2001: 78; 1787-89.

[36] T Akiyama, U Staufer, NF de Rooij, D Lange, C Hagleitner, O Brand, H Baltes, A Tonin, HR Hidber: Integrated atomic force microscopy array probe with metal-oxide-semiconductor field effect transistor stress sensor, thermal bimorph actuator, and on-chip complementary metal-oxide-semiconductor electronics. Journal of Vacuum Science & Technology, B: Microelectronics and Nanometer Structures 2000: 18; 2669-75.

[37] T Sulchek, R Hsieh, JD Adams, SC Minne, CF Quate, DM Adderton: High-speed atomic force microscopy in liquid. Review of Scientific Instruments 2000: 71; 2097-99.

[38] T Ando, N Kodera, E Takai, D Maruyama, K Saito, A Toda: A high-speed atomic force microscope for studying biological macromolecules. Proceedings of the National Academy of Sciences of the United States of America 2001: 98; 12468-72.

[39] ADL Humphris, J Tamayo, MJ Miles: Active Quality Factor Control in Liquids for Force Spectroscopy. Langmuir 2000: 16; 7891-94.

[40] K Yamanaka, Y Maruyama, T Tsuji, K Nakamoto: Resonance frequency and Q factor mapping by ultrasonic atomic force microscopy. Applied Physics Letters 2001: 78; 1939-41.

[41] FL Degertekin, B Hadimioglu, T Sulchek, CF Quate: Actuation and characterization of atomic force microscope cantilevers in fluids by acoustic radiation pressure. Applied Physics Letters 2001: 78; 1628-30.

[42] J Tamayo, ADL Humphris, MJ Miles: Piconewton regime dynamic force microscopy in liquid. Applied Physics Letters 2000: 77; 582-84.

[43] J Tamayo, AD Humphris, RJ Owen, MJ Miles: High-Q dynamic force microscopy in liquid and its application to living cells. Biophysical journal 2001: 81; 526-37.

[44] T Sulchek, GG Yaralioglu, CF Quate, SC Minne: Characterization and optimization of scan speed for tapping-mode atomic force microscopy. Review of Scientific Instruments 2002: 73; 2928-36.

[45] T Akiyama, U Staufer, NF de Rooij: Fast driving technique for integrated thermal bimorph actuator toward high-throughput atomic-force microscopy. Review of Scientific Instruments 2002: 73; 2643-46.

[46] RW Stark, WM Heckl: Higher harmonics imaging in tapping-mode atomic-force microscopy. Review of Scientific Instruments 2003: 74; 5111-14.

[47] P Zahl, M Bierkandt, S Schroder, A Klust: The flexible and modern open source scanning probe microscopy software package GXSM. Review of Scientific Instruments 2003: 74; 1222-27.

[48] ML Trawick, M Megens, C Harrison, DE Angelescu, DA Vega, PM Chaikin, RA Register, DH Adamson: Correction for piezoelectric creep in scanning probe microscopy images using polynomial mapping. Scanning 2003: 25; 25-33.

[49] JH Kindt, JB Thompson, MB Viani, PK Hansma: Atomic force microscope detector drift compensation by correlation of similar traces acquired at different setpoints. Review of Scientific Instruments 2002: 73; 2305-07.

[50] W Arnold, S Hirsekorn, M Kopycinska, U Rabe, M Reinstaedtler, V Scherer: Atomic force acoustic microscopy at ultrasonic frequencies. Proceedings of SPIE-The International Society for Optical Engineering 2002: 4703; 53-64.

[51] O Pfeiffer, R Bennewitz, A Baratoff, E Meyer, P Grutter: Lateral-force measurements in dynamic force microscopy. Physical Review B: Condensed Matter and Materials Physics 2002: 65; 161403/1-03/4.

[52] J Alcaraz, L Buscemi, M Puig-de-Morales, J Colchero, A Baro, D Navajas: Correction of Microrheological Measurements of Soft Samples with Atomic Force Microscopy for the Hydrodynamic Drag on the Cantilever. Langmuir 2002: 18; 716-21.

[53] S Fujisawa, H Ogiso: Compensation of cross talk in the optical lever deflection method used in atomic force microscopy. Review of Scientific Instruments 2003: 74; 5115-17.

[54] R Piner, RS Ruoff: Crosstalk between friction and height signals in atomic force microscopy. Review of Scientific Instruments 2002: 73; 3392-94.

[55] T Nishino, A Nozawa, M Kotera, K Nakamae: In situ observation of surface deformation of polymer films by atomic force microscopy. Review of Scientific Instruments 2000: 71; 2094-96.

[56] GH Buh, JJ Kopanski: Atomic force microscope laser illumination effects on a sample and its application for transient spectroscopy. Applied Physics Letters 2003: 83; 2486-88.

[57] T Akiyama, S Gautsch, NF de Rooij, U Staufer, P Niedermann, L Howald, D Muller, A Tonin, HR Hidber, WT Pike, MH Hecht: Atomic force microscope for planetary applications. Sensors and Actuators, A: Physical 2001: A91; 321-25.

[58] W Barth, T Debski, N Abedinov, T Ivanov, H Heerlein, B Volland, T Gotszalk, IW Rangelow, K Torkar, K Fritzenwallner, P Grabiec, K Studzinska, I Kostic, P Hudek: Evaluation and fabrication of AFM array for ESA-Midas/Rosetta space mission. Microelectronic Engineering 2001: 57-58; 825-31.

[59] HU Krotil, T Stifter, O Marti: Combined dynamic adhesion and friction measurement with the scanning force microscope. Applied Physics Letters 2000: 77; 3857-59.

[60] HU Krotil, T Stifter, O Marti: Lock-in technique for concurrent measurement of adhesion and friction with the scanning force microscope. Review of Scientific Instruments 2001: 72; 150-56.

[61] SA Syed Asif, KJ Wahl, RJ Colton, OL Warren: Quantitative imaging of nanoscale mechanical properties using hybrid nanoindentation and force modulation. J. Appl. Phys. 2001: 90; 1192-200.

[62] H Takano, S-S Wong, JA Harnisch, MD Porter: Mapping the Subsurface Composition of Organic Films by Electric Force Microscopy. Langmuir 2000: 16; 5231-33.

[63] MS Anderson: Locally enhanced Raman spectroscopy with an atomic force microscope. Applied Physics Letters 2000: 76; 3130-32.

[64] MS Anderson: Infrared spectroscopy with an atomic force microscope. Applied Spectroscopy 2000: 54; 349-52.

[65] T Trenkler, T Hantschel, R Stephenson, P De Wolf, W Vandervorst, L Hellemans, A Malave, D Buchel, E Oesterschulze, W Kulisch, P Niedermann, T Sulzbach, O Ohlsson: Evaluating probes for \"electrical\" atomic force microscopy. Journal of

Vacuum Science & Technology, B: Microelectronics and Nanometer Structures 2000: 18; 418-27.

[66] T Hantschel, P Niedermann, T Trenkler, W Vandervorst: Highly conductive diamond probes for scanning spreading resistance microscopy. Applied Physics Letters 2000: 76; 1603-05.

[67] P Boggild, TM Hansen, O Kuhn, F Grey, T Junno, L Montelius: Scanning nanoscale multiprobes for conductivity measurements. Review of Scientific Instruments 2000: 71; 2781-83.

[68] L Shi, O Kwon, AC Miner, A Majumdar: Design and batch fabrication of probes for sub-100 nm scanning thermal microscopy. Journal of Microelectromechanical Systems 2001: 10; 370-78.

[69] IW Rangelow, T Gotszalk, N Abedinov, P Grabiec, K Edinger: Thermal nano-probe. Microelectronic Engineering 2001: 57-58; 737-48.

[70] K Edinger, T Gotszalk, IW Rangelow: Novel high resolution scanning thermal probe. Journal of Vacuum Science & Technology, B: Microelectronics and Nanometer Structures 2001: 19; 2856-60.

[71] MH Li, JJ Wu, YB Gianchandani: High performance scanning thermal probe using a low temperature polyimide-based micromachining process. Annual International Conference on Micro Electro Mechanical Systems, Proceedings, 13th, Miyazaki, Japan, Jan. 23-27, 2000 2000: 763-68.

[72] DJ Wold, CD Frisbie: Formation of metal-molecule-metal tunnel junctions. Microcontacts to alkanethiol monolayers with a conducting AFM tip. Journal of the American Chemical Society 2000: 122; 2970-71.

[73] XD Cui, A Primak, X Zarate, J Tomfohr, OF Sankey, AL Moore, TA Moore, D Gust, G Harris, SM Lindsay: Reproducible measurement of single-molecule conductivity. Science 2001: 294; 571-4.

[74] MA Topinka, BJ LeRoy, SE Shaw, EJ Heller, RM Westervelt, KD Maranowski, AC Gossard: Imaging coherent electron flow from a quantum point contact. Science 2000: 289; 2323-26.

[75] AR Burns: Domain structure in model membrane bilayers investigated by simultaneous atomic force microscopy and fluorescence imaging. Langmuir 2003: 19; 8358-63.

[76] D Hu, M Micic, N Klymyshyn, YD Suh, HP Lu: Correlated topographic and spectroscopic imaging beyond diffraction limit by atomic force microscopy metallic tip-enhanced near-field fluorescence lifetime microscopy. Review of Scientific Instruments 2003: 74; 3347-55.

[77] A Noy, TR Huser: Combined force and photonic probe microscope with single molecule sensitivity. Review of Scientific Instruments 2003: 74; 1217-21.

[78] K Fukushima, S Kawai, D Saya, H Kawakatsu: Measurement of mechanical properties of three-dimensional nanometric objects by an atomic force microscope incorporated in a scanning electron microscope. Review of Scientific Instruments 2002: 73; 2647-50.

[79] MT Browne, P Charalambous, RE Burge, XC Yuan: Combined microscope for scanning X-ray transmission and surface topography. Ultramicroscopy 2002: 92; 221-32.

[80] SI Bondarenko, N Nakagawa, AA Shablo, PP Pavlov: Three channel non-force magnetic SQUID microscope. Physica B: Condensed Matter (Amsterdam, Netherlands) 2003: 329-333; 1512-13.

[81] F Dubreuil, J Daillant, P Guenoun: Direct Topographic Measurement of Multilayers on Water by Atomic Force Microscopy. Langmuir 2003: 19; 8409-15.

[82] KH Choi, JM Friedt, F Frederix, A Campitelli, G Borghs: Simultaneous atomic force microscope and quartz crystal microbalance measurements: Investigation of human plasma fibrinogen adsorption. Applied Physics Letters 2002: 81; 1335-37.

[83] O Hayden, R Bindeus, FL Dickert: Combining atomic force microscope and quartz crystal microbalance studies for cell detection. Measurement Science and Technology 2003: 14; 1876-81.

[84] JM Friedt, L Francis, KH Choi, F Frederix, A Campitelli: Combined atomic force microscope and acoustic wave devices: Application to electrodeposition. Journal of Vacuum Science & Technology, A: Vacuum, Surfaces, and Films 2003: 21; 1500-05.

[85] HJ Mamin, D Rugar: Sub-attonewton force detection at millikelvin temperatures. Applied Physics Letters 2001: 79; 3358-60.

[86] T Hugel, M Seitz: The study of molecular interactions by AFM force spectroscopy. Macromolecular Rapid Communications 2001: 22; 989-1016.

[87] J Zlatanova, SM Lindsay, SH Leuba: Single molecule force spectroscopy in biology using the atomic force microscope. Progress in Biophysics & Molecular Biology 2000: 74; 37-61.

[88] C Bustamante, SB Smith, J Liphardt, D Smith: Single-molecule studies of DNA mechanics. Current Opinion in Structural Biology 2000: 10; 279-85.

[89] M Carrion-Vazquez, AF Oberhauser, TE Fisher, PE Marszalek, H Li, JM Fernandez: Mechanical design of proteins studied by single-molecule force spectroscopy and protein engineering. Progress in Biophysics & Molecular Biology 2000: 74; 63-91.

[90] H Clausen-Schaumann, M Seitz, R Krautbauer, HE Gaub: Force spectroscopy with single bio-molecules. Current Opinion in Chemical Biology 2000: 4; 524-30.

[91] W Baumgartner, P Hinterdorfer, H Schindler: Data analysis of interaction forces measured with the atomic force microscope. Ultramicroscopy 2000: 82; 85-95.

[92] C Gergely, B Senger, JC Voegel, JKH Horber, P Schaaf, J Hemmerle: Semi-automatized processing of AFM force-spectroscopy data. Ultramicroscopy 2001: 87; 67-78.

[93] BA Todd, SJ Eppell, FR Zypman: Improved analysis of the time domain response of scanning force microscope cantilevers. Journal of Applied Physics 2000: 88; 7321-27.

[94] BA Todd, SJ Eppell, FR Zypman: Squeezing out hidden force information from scanning force microscopes. Applied Physics Letters 2001: 79; 1888-90.

[95] OI Vinogradova, H-J Butt, GE Yakubov, F Feuillebois: Dynamic effects on force measurements. I. Viscous drag on the atomic force microscope cantilever. Review of Scientific Instruments 2001: 72; 2330-39.

[96] JB Thompson, JH Kindt, B Drake, HG Hansma, DE Morse, PK Hansma: Bone indentation recovery time correlates with bond reforming time. Nature 2001: 414; 773-6.

[97] F Oesterhelt, D Oesterhelt, M Pfeiffer, A Engel, HE Gaub, DJ Muller: Unfolding pathways of individual bacteriorhodopsins. Science 2000: 288; 143-6.

[98] AF Oberhauser, PK Hansma, M Carrion-Vazquez, JM Fernandez: Stepwise unfolding of titin under force-clamp atomic force microscopy. Proceedings of the National Academy of Sciences of the United States of America 2001: 98; 468-72.

[99] K Mitsui, K Nakajima, H Arakawa, M Hara, A Ikai: Dynamic measurement of single protein's mechanical properties. Biochemical and Biophysical Research Communications 2000: 272; 55-63.

[100] H Li, AF Oberhauser, SB Fowler, J Clarke, JM Fernandez: Atomic force microscopy reveals the mechanical design of a modular protein. Proceedings of the National Academy of Sciences of the United States of America 2000: 97; 6527-31.

[101] H Li, M Carrion-Vazquez, AF Oberhauser, PE Marszalek, JM Fernandez: Point mutations alter the mechanical stability of immunoglobulin modules. Nature Structural Biology 2000: 7; 1117-20.

[102] H Li, AF Oberhauser, SD Redick, M Carrion-Vazquez, HP Erickson, JM Fernandez: Multiple conformations of PEVK proteins detected by single-molecule techniques. Proceedings of the National Academy of Sciences of the United States of America 2001: 98; 10682-86.

[103] PF Lenne, AJ Raae, SM Altmann, M Saraste, JKH Horber: States and transitions during forced unfolding of a single spectrin repeat. FEBS Letters 2000: 476; 124-28.

[104] H Clausen-Schaumann, M Rief, C Tolksdorf, HE Gaub: Mechanical stability of single DNA molecules. Biophysical Journal 2000: 78; 1997-2007.

[105] J-BD Green, GU Lee: Atomic Force Microscopy with Patterned Cantilevers and Tip Arrays: Force Measurements with Chemical Arrays. Langmuir 2000: 16; 4009-15.

[106] Y-S Lo, Y-J Zhu, TP Beebe, Jr.: Loading-Rate Dependence of Individual Ligand-Receptor Bond-Rupture Forces Studied by Atomic Force Microscopy. Langmuir 2001: 17; 3741-48.

[107] C Yuan, A Chen, P Kolb, VT Moy: Energy Landscape of Streptavidin-Biotin Complexes Measured by Atomic Force Microscopy. Biochemistry 2000: 39; 10219-23.

[108] T Hugel, M Grosholz, H Clausen-Schaumann, A Pfau, H Gaub, M Seitz: Elasticity of Single Polyelectrolyte Chains and Their Desorption from Solid Supports Studied by AFM Based Single Molecule Force Spectroscopy. Macromolecules 2001: 34; 1039-47.

[109] R Krautbauer, H Clausen-Schaumann, HE Gaub: Cisplatin changes the mechanics of single DNA molecules. Angewandte Chemie, International Edition 2000: 39; 3912-15.

[110] O Lioubashevski, F Patolsky, I Willner: Probing of DNA and single-base mismatches by chemical force microscopy using peptide nucleic acid-modified sensing tips and functionalized surfaces. Langmuir 2001: 17; 5134-36.

[111] S Cocco, R Monasson, JF Marko: Force and kinetic barriers to unzipping of the DNA double helix. Proceedings of the National Academy of Sciences of the United States of America 2001: 98; 8608-13.

[112] L Schmitt, M Ludwig, HE Gaub, R Tampe: A metal-chelating microscopy tip as a new toolbox for single-molecule experiments by atomic force microscopy. Biophysical Journal 2000: 78; 3275-85.

[113] PE Marszalek, H Li, JM Fernandez: Fingerprinting polysaccharides with single-molecule atomic force microscopy. Nature biotechnology 2001: 19; 258-62.

[114] R Matzke, K Jacobson, M Radmacher: Direct, high-resolution measurement of furrow stiffening during division of adherent cells. Nature Cell Biology 2001: 3; 607-10.

[115] S Oyama, K Miyake, S Yasuda, O Takeuchi, J Sumaoka, M Komiyama, DN Futaba, R Morita, M Yamashita, H Shigekawa: Interactive force between cyclodextrin inclusion complexes studied by atomic force microscopy. Japanese Journal of Applied Physics, Part 1: Regular Papers, Short Notes & Review Papers 2001: 40; 4419-22.

[116] WR Bowen, RW Lovitt, CJ Wright: Direct Quantification of Aspergillus niger Spore Adhesion in Liquid Using an Atomic Force Microscope. Journal of Colloid and Interface Science 2000: 228; 428-33.

[117] WR Bowen, RW Lovitt, CJ Wright: Atomic force microscopy study of the adhesion of Saccharomyces cerevisiae. Journal of Colloid and Interface Science 2001: 237; 54-61.

[118] YF Dufrene: Direct characterization of the physicochemical properties of fungal spores using functionalized AFM probes. Biophysical Journal 2000: 78; 3286-91.

[119] BC van der Aa, RM Michel, M Asther, MT Zamora, PG Rouxhet, YF Dufrene: Stretching cell surface macromolecules by atomic force microscopy. Langmuir 2001: 17; 3116-19.

[120] YF Dufrene, CJP Boonaert, HC Van der Mei, HJ Busscher, PG Rouxhet: Probing molecular interactions and mechanical properties of microbial cell surfaces by atomic force microscopy. Ultramicroscopy 2001: 86; 113-20.

[121] A Chen, VT Moy: Cross-linking of cell surface receptors enhances cooperativity of molecular adhesion. Biophysical Journal 2000: 78; 2814-20.

[122] I Lee, RE Marchant: Force measurements on platelet surfaces with high spatial resolution under physiological conditions. Colloids and Surfaces, B: Biointerfaces 2000: 19; 357-65.

[123] M Grandbois, W Dettmann, M Benoit, HE Gaub: Affinity imaging of red blood cells using an atomic force microscope. Journal of Histochemistry and Cytochemistry 2000: 48; 719-24.

[124] M Fiorini, R McKendry, MA Cooper, T Rayment, C Abell: Chemical force microscopy with active enzymes. Biophysical Journal 2001: 80; 2471-76.

[125] G Kada, L Blayney, LH Jeyakumar, F Kienberger, VP Pastushenko, S Fleischer, H Schindler, FA Lai, P Hinterdorfer: Recognition force microscopy/spectroscopy of ion channels: applications to the skeletal muscle Ca2+ release channel (RYR1). Ultramicroscopy 2001: 86; 129-37.

[126] Y Harada, M Kuroda, A Ishida: Specific and Quantized Antigen-Antibody Interaction Measured by Atomic Force Microscopy. Langmuir 2000: 16; 708-15.

[127] JD Adams, G Parrott, C Bauer, T Sant, L Manning, M Jones, B Rogers, D McCorkle, TL Ferrell: Nanowatt chemical vapor detection with a self-sensing, piezoelectric microcantilever array. Applied Physics Letters 2003: 83; 3428-30.

[128] ADL Humphris, M Antognozzi, TJ McMaster, MJ Miles: Transverse Dynamic Force Spectroscopy: A Novel Approach to Determining the Complex Stiffness of a Single Molecule. Langmuir 2002: 18; 1729-33.

[129] M Kappl, H-J Butt: The colloidal probe technique and its application to adhesion force measurements. Particle & Particle Systems Characterization 2002: 19; 129-43.

[130] W Zhang, X Zhang: Single molecule mechanochemistry of macromolecules. Progress in Polymer Science 2003: 28; 1271-95.

[131] BB Akhremitchev, JE Bemis, S Al-Maawali, Y Sun, L Stebounova, GC Walker: Application of scanning force and near field microscopies to the characterization of minimally adhesive polymer surfaces. Biofouling 2003: 19; 99-104.

[132] F Chen, U Mohideen, GL Klimchitskaya, VM Mostepanenko: Demonstration of the Lateral Casimir Force. Physical Review Letters 2002: 88; 101801/1-01/4.

[133] M Kudera, C Eschbaumer, HE Gaub, US Schubert: Analysis of metallo-supramolecular systems using single-molecule force spectroscopy. Advanced Functional Materials 2003: 13; 615-20.

[134] S Zapotoczny, T Auletta, MR de Jong, H Schoenherr, J Huskens, FCJM van Veggel, DN Reinhoudt, GJ Vancso: Chain Length and Concentration Dependence of b-Cyclodextrin-Ferrocene Host-Guest Complex Rupture Forces Probed by Dynamic Force Spectroscopy. Langmuir 2002: 18; 6988-94.

[135] AV Tivanski, JE Bemis, BB Akhremitchev, H Liu, GC Walker: Adhesion Forces in Conducting Probe Atomic Force Microscopy. Langmuir 2003: 19; 1929-34.

[136] C Dicke, G Haehner: pH-Dependent Force Spectroscopy of Tri(ethylene Glycol)- and Methyl-Terminated Self-Assembled Monolayers Adsorbed on Gold. Journal of the American Chemical Society 2002: 124; 12619-25.

[137] S Zepeda, Y Yeh, A Noy: Determination of Energy Barriers for Intermolecular Interactions by Variable Temperature Dynamic Force Spectroscopy. Langmuir 2003: 19; 1457-61.

[138] JC Mabry, T Yau, H-W Yap, J-BD Green: Developments for inverted atomic force microscopy. Ultramicroscopy 2002: 91; 73-82.

[139] J-BD Green: Analytical instrumentation based on force measurements: combinatorial atomic force microscopy. Analytica Chimica Acta 2003: 496; 267-77.

[140] SDA Connell, S Allen, CJ Roberts, J Davies, MC Davies, SJB Tendler, PM Williams: Investigating the Interfacial Properties of Single-Liquid Nanodroplets by Atomic Force Microscopy. Langmuir 2002: 18; 1719-28.

[141] P Eaton, JR Smith, P Graham, JD Smart, TG Nevell, J Tsibouklis: Adhesion Force Mapping of Polymer Surfaces: Factors Influencing Force of Adhesion. Langmuir 2002: 18; 3387-89.

[142] F Sato, H Okui, U Akiba, K Suga, M Fujihira: A study of topographic effects on chemical force microscopy using adhesive force mapping. Ultramicroscopy 2003: 97; 303-14.

[143] K-i Akabori, K Tanaka, T Kajiyama, A Takahara: Anomalous Surface Relaxation Process in Polystyrene Ultrathin Films. Macromolecules 2003: 36; 4937-43.

[144] VN Bliznyuk, HE Assender, GAD Briggs: Surface Glass Transition Temperature of Amorphous Polymers. A New Insight with SFM. Macromolecules 2002: 35; 6613-22.

[145] ME Harmon, D Kuckling, CW Frank: Photo-Cross-Linkable PNIPAAm Copolymers. 5. Mechanical Properties of Hydrogel Layers. Langmuir 2003: 19; 10660-65.

[146] CS Hodges: Measuring forces with the AFM: polymeric surfaces in liquids. Advances in Colloid and Interface Science 2002: 99; 13-75.

[147] BC Bunker, BI Kim, JE Houston, R Rosario, AA Garcia, M Hayes, D Gust, ST Picraux: Direct Observation of Photoswitching in Tethered Spiropyrans Using the Interfacial Force Microscope. Nano Letters 2003: 3; 1723-27.

[148] JE Houston, HI Kim: Adhesion, Friction, and Mechanical Properties of Functionalized Alkanethiol Self-Assembled Monolayers. Accounts of Chemical Research 2002: 35; 547-53.

[149] T Hugel, B Holland Nolan, A Cattani, L Moroder, M Seitz, E Gaub Hermann: Single-molecule optomechanical cycle. Science 2002: 296; 1103-6.

[150] U Rabe, S Amelio, M Kopycinska, S Hirsekorn, M Kempf, M Goken, W Arnold: Imaging and measurement of local mechanical material properties by atomic force acoustic microscopy. Surface and Interface Analysis 2002: 33; 65-70.

[151] F Benmouna, TD Dimitrova, D Johannsmann: Nanoscale Mapping of the Mechanical Properties of Polymer Surfaces by Means of AFM Noise Analysis: Spatially Resolved Fibrillation of Latex Films. Langmuir 2003: 19; 10247-53.

[152] TD Dimitrova, D Johannsmann, N Willenbacher, A Pfau: Mesoscopic fibrillation properties of pressure sensitive adhesives based on latex films. Langmuir 2003: 19; 5748-55.

[153] DC Bardos: Contact angle dependence of solid probe-liquid drop forces in AFM measurements at. charges. Surface Science 2002: 517; 157-76.

[154] D Bedrov, GD Smith: The role of local conformations in the stretching of a poly(ethylene oxide) chain in solution. Journal of Chemical Physics 2003: 118; 6656-63.

[155] PM Biesheuvel: Dynamic Charge Regulation Model for the Electrostatic Forces between Ionizable Materials. Langmuir 2002: 18; 5566-71.

[156] H-J Butt, V Franz: Rupture of molecular thin films observed in atomic force microscopy. I. Theory. Physical Review E: Statistical, Nonlinear, and Soft Matter Physics 2002: 66; 031601/1-01/9.

[157] J Fraxedas, S Garcia-Manyes, P Gorostiza, F Sanz: Nanoindentation: toward the sensing of atomic interactions. Proceedings of the National Academy of Sciences of the United States of America 2002: 99; 5228-32.

[158] DL Patrick, JF Flanagan, P Kohl, RM Lynden-Bell: Atomistic Molecular Dynamics Simulations of Chemical Force Microscopy. Journal of the American Chemical Society 2003: 125; 6762-73.

[159] D Dean, J Seog, C Ortiz, AJ Grodzinsky: Molecular-Level Theoretical Model for Electrostatic Interactions within Polyelectrolyte Brushes: Applications to Charged Glycosaminoglycans. Langmuir 2003: 19; 5526-39.

[160] OK Dudko, AE Filippov, J Klafter, M Urbakh: Beyond the conventional description of dynamic force spectroscopy of adhesion bonds. Proceedings of the National Academy of Sciences of the United States of America 2003: 100; 11378-81.

[161] Y Leng, S Jiang: Dynamic Simulations of Adhesion and Friction in Chemical Force Microscopy. Journal of the American Chemical Society 2002: 124; 11764-70.

[162] C Friedsam, AK Wehle, F Kuehner, HE Gaub: Dynamic single-molecule force spectroscopy: Bond rupture analysis with variable spacer length. Journal of Physics: Condensed Matter 2003: 15; S1709-S23.

[163] MikroMasch AFM Probe Guide. 2004.

[164] Veeco Metrology SPM Probe Guide. 2004.

[165] A Chand, MB Viani, TE Schaffer, PK Hansma: Microfabricated small metal cantilevers with silicon tip for atomic force microscopy. Journal of Microelectromechanical Systems 2000: 9; 112-16.

[166] S Hosaka, K Etoh, A Kikukawa, H Koyanagi: Megahertz silicon atomic force microscopy (AFM) cantilever and high-speed readout in AFM-based recording. Journal of Vacuum Science & Technology, B: Microelectronics and Nanometer Structures 2000: 18; 94-99.

[167] J Yang, T Ono, M Esashi: Mechanical behavior of ultrathin microcantilever. Sensors and Actuators, A: Physical 2000: A82; 102-07.

[168] J McCarthy, Z Pei, M Becker, D Atteridge: FIB micromachined submicron thickness cantilevers for the study of thin film properties. Thin Solid Films 2000: 358; 146-51.

[169] S Heisig, O Rudow, E Oesterschulze: Optical active gallium arsenide cantilever probes for combined scanning near-field optical microscopy and scanning force microscopy. Journal of Vacuum Science & Technology, B: Microelectronics and Nanometer Structures 2000: 18; 1134-37.

[170] DW Lee, T Ono, M Esashi: Cantilever with integrated resonator for application of scanning probe microscope. Sensors and Actuators, A: Physical 2000: A83; 11-16.

[171] H Kawakatsu, H Toshiyoshi, D Saya, K Fukushima, H Fujita: Strength measurement and calculations on silicon-based nanometric oscillators for scanning force microcopy operating in the gigahertz range. Applied Surface Science 2000: 157; 320-25.

[172] PN Minh, T Ono, M Esashi: Microfabrication of miniature aperture at the apex of SiO2 tip on silicon cantilever for near-field scanning optical microscopy. Sensors and Actuators, A: Physical 2000: A80; 163-69.

[173] M Stopka, D Drews, K Mayr, M Lacher, W Ehrfeld, T Kalkbrenner, M Graf, V Sandoghdar, J Mlynek: Multifunctional AFM/SNOM cantilever probes: fabrication and measurements. Microelectronic Engineering 2000: 53; 183-86.

[174] C Lehrer, L Frey, S Petersen, T Sulzbach, O Ohlsson, T Dziomba, HU Danzebrink, H Ryssel: Fabrication of silicon aperture probes for scanning near-field optical microscopy by focused ion beam nano machining. Microelectronic Engineering 2001: 57-58; 721-28.

[175] L Manning, B Rogers, M Jones, JD Adams, JL Fuste, SC Minne: Self-oscillating tapping mode atomic force microscopy. Review of Scientific Instruments 2003: 74; 4220-22.

[176] Y Miyahara, M Deschler, T Fujii, S Watanabe, H Bleuler: Non-contact atomic force microscope with a PZT cantilever used for deflection sensing, direct oscillation and feedback actuation. Applied Surface Science 2002: 188; 450-55.

[177] B Rogers, D York, N Whisman, M Jones, K Murray, JD Adams, T Sulchek, SC Minne: Tapping mode atomic force microscopy in liquid with an insulated piezoelectric microactuator. Review of Scientific Instruments 2002: 73; 3242-44.

[178] AJ Brook, SJ Bending, J Pinto, A Oral, D Ritchie, H Beere, M Henini, A Springthorpe: Integrated piezoresistive sensors for atomic force-guided scanning Hall probe microscopy. Applied Physics Letters 2003: 82; 3538-40.

[179] RJ Grow, SC Minne, SR Manalis, CF Quate: Silicon nitride cantilevers with oxidation-sharpened silicon tips for atomic force microscopy. Journal of Microelectromechanical Systems 2002: 11; 317-21.

[180] M Bale, RE Palmer: Microfabrication of silicon tip structures for multiple-probe scanning tunneling microscopy. Journal of Vacuum Science & Technology, B: Microelectronics and Nanometer Structures 2002: 20; 364-69.

[181] EM Chow, GG Yaralioglu, CF Quate, TW Kenny: Characterization of a two-dimensional cantilever array with through-wafer electrical interconnects. Applied Physics Letters 2002: 80; 664-66.

[182] L Aigouy, Y De Wilde, M Mortier: Local optical imaging of nanoholes using a single fluorescent rare-earth-doped glass particle as a probe. Applied Physics Letters 2003: 83; 147-49.

[183] KB Crozier, DA Fletcher, GS Kino, CF Quate: Micromachined silicon nitride solid immersion lens. Journal of Microelectromechanical Systems 2002: 11; 470-78.

[184] Y Lee, AJ Bard: Fabrication and Characterization of Probes for Combined Scanning Electrochemical/Optical Microscopy Experiments. Analytical Chemistry 2002: 74; 3626-33.

[185] Y Lee, Z Ding, AJ Bard: Combined scanning electrochemical/optical microscopy with shear force and current feedback. Analytical Chemistry 2002: 74; 3634-43.

[186] WL Hughes, ZL Wang: Nanobelts as nanocantilevers. Applied Physics Letters 2003: 82; 2886-88.

[187] SG Nilsson, EL Sarwe, L Montelius: Fabrication and mechanical characterization of ultrashort nanocantilevers. Applied Physics Letters 2003: 83; 990-92.

[188] DW Lee, M Despont, U Drechsler, C Gerber, P Vettiger, A Wetzel, R Bennewitz, E Meyer: Switchable cantilever fabrication for a novel time-of-flight scanning force microscope. Microelectronic Engineering 2003: 67-68; 635-43.

[189] G Genolet, M Despont, P Vettiger, D Anselmetti, NF de Rooij: All-photoplastic, soft cantilever cassette probe for scanning force microscopy. Journal of Vacuum Science & Technology, B: Microelectronics and Nanometer Structures 2000: 18; 617-20.

[190] G Genolet, M Despont, P Vettiger, U Staufer, W Noell, NF de Rooij, T Cueni, MP Bernal, F Marquis-Weible: Micromachined photoplastic probe for scanning near-field optical microscopy. Review of Scientific Instruments 2001: 72; 3877-79.

[191] AW McFarland, MA Poggi, LA Bottomley, JS Colton: Production and characterization of polymer microcantilvers. Review of Scientific Instruments 2004: 75; 2756-58.

[192] JH Hafner, CL Cheung, AT Woolley, CM Lieber: Structural and functional imaging with carbon nanotube AFM probes. Progress in Biophysics & Molecular Biology 2001: 77; 73-110.

[193] CL Cheung, JH Hafner, TW Odom, K Kim, CM Lieber: Growth and fabrication with single-walled carbon nanotube probe microscopy tips. Applied Physics Letters 2000: 76; 3136-38.

[194] JH Hafner, C-L Cheung, TH Oosterkamp, CM Lieber: High-Yield Assembly of Individual Single-Walled Carbon Nanotube Tips for Scanning Probe Microscopies. Journal of Physical Chemistry B 2001: 105; 743-46.

[195] RMD Stevens, NA Frederick, BL Smith, DE Morse, GD Stucky, PK Hansma: Carbon nanotubes as probes for atomic force microscopy. Nanotechnology 2000: 11; 1-5.

[196] AT Woolley, C Li Cheung, JH Hafner, CM Lieber: Structural biology with carbon nanotube AFM probes. Chemistry & Biology 2000: 7; R193-R204.

[197] CV Nguyen, K-J Chao, RMD Stevens, L Delzeit, A Cassell, J Han, M Meyyappan: Carbon nanotube tip probes: Stability and lateral resolution in scanning probe microscopy and application to surface science in semiconductors. Nanotechnology 2001: 12; 363-67.

[198] S Akita, Y Nakayama, S Mizooka, Y Takano, T Okawa, Y Miyatake, S Yamanaka, M Tsuji, T Nosaka: Nanotweezers consisting of carbon nanotubes operating in an atomic force microscope. Applied Physics Letters 2001: 79; 1691-93.

[199] K Umemura, J Komatsu, T Uchihashi, N Choi, S Ikawa, T Nishinaka, T Shibata, Y Nakayama, S Katsura, A Mizuno, H Tokumoto, M Ishikawa, R Kuroda: Atomic Force Microscopy of RecA-DNA Complexes Using a Carbon Nanotube Tip. Biochemical and Biophysical Research Communications 2001: 281; 390-95.

[200] CL Cheung, JH Hafner, CM Lieber: Carbon nanotube atomic force microscopy tips: direct growth by chemical vapor deposition and application to high-resolution imaging. Proceedings of the National Academy of Sciences of the United States of America 2000: 97; 3809-13.

[201] L Delzeit, CV Nguyen, RM Stevens, J Han, M Meyyappan: Growth of carbon nanotubes by thermal and plasma chemical vapour deposition processes and applications in microscopy. Nanotechnology 2002: 13; 280-84.

[202] Y Yang, J Zhang, X Nan, Z Liu: Toward the Chemistry of Carboxylic Single-Walled Carbon Nanotubes by Chemical Force Microscopy. Journal of Physical Chemistry B 2002: 106; 4139-44.

[203] E Yenilmez, Q Wang, RJ Chen, D Wang, H Dai: Wafer scale production of carbon nanotube scanning probe tips for atomic force microscopy. Applied Physics Letters 2002: 80; 2225-27.

[204] T Nishino, T Ito, Y Umezawa: Carbon Nanotube Scanning Tunneling Microscopy Tips for Chemically Selective Imaging. Analytical Chemistry 2002: 74; 4275-78.

[205] ES Snow, PM Campbell, JP Novak: Atomic force microscopy using single-wall C nanotube probes. Journal of Vacuum Science & Technology, B: Microelectronics and Nanometer Structures 2002: 20; 822-27.

[206] NA Burnham, X Chen, CS Hodges, GA Matei, EJ Thoreson, CJ Roberts, MC Davies, SJB Tendler: Comparison of calibration methods for atomic-force microscopy cantilevers. Nanotechnology 2003: 14; 1-6.

[207] JP Cleveland, S Manne, D Bocek, PK Hansma: A nondestructive method for determining the spring constant of cantilevers for scanning force microscopy. Review of Scientific Instruments 1993: 64; 403-5.

[208] M Tortonese, M Kirk: Characterization of application specific probes for SPMs. Proceedings of SPIE-The International Society for Optical Engineering 1997: 3009; 53-60.

[209] CT Gibson, BL Weeks, C Abell, T Rayment, S Myhra: Calibration of AFM cantilever spring constants. Ultramicroscopy 2003: 97; 113-18.

[210] JE Sader, I Larson, P Mulvaney, LR White: Method for the calibration of atomic force microscope cantilevers. Review of Scientific Instruments 1995: 66; 3789-98.

[211] JE Sader: Frequency response of cantilever beams immersed in viscous fluids with applications to the atomic force microscope. Journal of Applied Physics 1998: 84; 64-76.

[212] JE Sader, JWM Chon, P Mulvaney: Calibration of rectangular atomic force microscope cantilevers. Review of Scientific Instruments 1999: 70; 3967-69.

[213] JL Hutter, J Bechhoefer: Calibration of atomic-force microscope tips. Review of Scientific Instruments 1993: 64; 1868-73.

[214] H-J Butt, M Jaschke: Calculation of thermal noise in atomic force microscopy. Nanotechnology 1995: 6; 1-7.

[215] N Maeda, TJ Senden: A Method for the Calibration of Force Microscopy Cantilevers via Hydrodynamic Drag. Langmuir 2000: 16; 9282-86.

[216] VSJ Craig, C Neto: In Situ Calibration of Colloid Probe Cantilevers in Force Microscopy: Hydrodynamic Drag on a Sphere Approaching a Wall. Langmuir 2001: 17; 6018-22.

[217] RG Cain, S Biggs, NW Page: Force Calibration in Lateral Force Microscopy. Journal of Colloid and Interface Science 2000: 227; 55-65.

[218] X Chen, S Zhang, DA Dikin, W Ding, RS Ruoff, L Pan, Y Nakayama: Mechanics of a Carbon Nanocoil. Nano Letters 2003: 3; 1299-304.

[219] UJK Rabe, W Arnold: Vibrations of free and surface-coupled atomic force microscope cantilevers: theory and experiment. Review of Scientific Instruments 1996: 67; 3281-93.

[220] NT-MDT SPM Probe Division:*www.nt-mdt.com*. 2004.

[221] S Timoshenko: Theory of Elasticity, McGraw-Hill, New York, 1970.

[222] E Oberg, FD Jones, HL Horton, HH Ryffel, RE Grenn: Machinery's Handbook, Industrial Press, New York, 1996.

[223] JWM Chon, P Mulvaney, JE Sader: Experimental validation of theoretical models for the frequency response of atomic force microscope cantilever beams immersed in fluids. Journal of Applied Physics 2000: 87; 3978-88.

[224] S Iijima: Helical microtubules of graphitic carbon. Nature (London, United Kingdom) 1991: 354; 56-8.

[225] MS Dresselhaus, G Dresselhaus, P Avouris: Carbon Nanotubes: *Synthesis, Structure, Properties, and Applications*, Springer-Verlag, Berlin, 2001.

[226] R Saito, G Dresselhaus, MS Dresselhaus: Phyisical Properties of Carbon Nanotubes, Imperial College Press, London, England, 1998.

[227] RH Baughman, AA Zakhidov, WA de Heer: Carbon nanotubes-the route toward applications. Science (Washington, DC, United States) 2002: 297; 787-92.

[228] H Dai: Carbon Nanotubes: Synthesis, Integration, and Properties. Accounts of Chemical Research 2002.

[229] W Ebbesen Thomas (Ed.)^(Eds.), Carbon Nanotubes: Preparation and Properties. CRC Press, Boca Raton, FL, 1997.

[230] MJ Bronikowski, PA Willis, DT Colbert, KA Smith, RE Smalley: Gas-phase production of carbon single-walled nanotubes from carbon monoxide via the HiPco process: A parametric study. Journal of Vacuum Science & Technology, B: Microelectronics and Nanometer Structures 2001: 19; 1800-05.

[231] P Nikolaev, MJ Bronikowski, RK Bradley, F Rohmund, DT Colbert, KA Smith, RE Smalley: Gas-phase catalytic growth of single-walled carbon nanotubes from carbon monoxide. Chemical Physics Letters 1999: 313; 91-97.

[232] EL Ivchenko, B Spivak: Chirality effects in carbon nanotubes. Physical Review B: Condensed Matter and Materials Physics 2002: 66; 155404/1-04/9.

[233] J Jiang, J Dong, DY Xing: Size and helical symmetry effects on the nonlinear optical properties of chiral carbon nanotubes. Physical Review B: Condensed Matter and Materials Physics 1999: 59; 9838-41.

[234] C Dekker, SJ Tans, MH Devoret, LJ Geerligs, RJA Groeneveld, LC Venema, JWG Wildoer, ARM Verschueren, A Bezryadin: Electronic properties of individual single-wall carbon nanotubes: transport and STM results. Molecular Nanostructures, Proceedings of the International Winterschool on Electronic

Properties of Novel Materials, 11th, Kirchberg, Austria, Mar. 1-8, 1997 1998: 467-71.

[235] P Bernier, C Journet, WK Maser, A Loiseau, M Lamy de la Chapelle, S Lefrant, P Deniard, R Lee, JE Fischer: Carbon single wall nanotubes. Elaboration and physical properties. Condensed Matter News 1998: 6; 51-56.

[236] JC Charlier, TW Ebbesen, P Lambin: Structural and electronic properties of pentagon-heptagon pair defects in carbon nanotubes. Physical Review B: Condensed Matter 1996: 53; 11108-13.

[237] MF Lin, KWK Shung: Plasmons and optical properties of carbon nanotubes. Physical Review B: Condensed Matter 1994: 50; 17744-7.

[238] RA Jishi, MS Dresselhaus, G Dresselhaus: Symmetry properties of chiral carbon nanotubes. Physical Review B: Condensed Matter and Materials Physics 1993: 47; 16671-4.

[239] C Kramberger, R Pfeiffer, H Kuzmany, V Zolyomi, J Kurti: Assignment of chiral vectors in carbon nanotubes. Physical Review B: Condensed Matter and Materials Physics 2003: 68; 235404/1-04/4.

[240] K Tanaka, T Yamabe, K Fukui (Ed.)^(Eds.), The Science andTechnology of Carbon Nanotubes. Elsevier, Kidlington, Oxford, 1999.

[241] WA de Heer: Nanotubes and the pursuit of applications. MRS Bulletin 2004: 29; 281-85.

[242] SJ Tans, RM Verschueren, C Dekker: Nature 1998: 393; 49.

[243] K Keren, RS Berman, E Buchstab, U Sivan, E Braun: DNA-templated carbon nanotube field-effect transistor. Science 2003: 302; 1380-2.

[244] A Javey, J Guo, Q Wang, M Lundstrom, H Dai: Ballistic carbon nanotube field-effect transistors. Nature (London, United Kingdom) 2003: 424; 654-57.

[245] R Martel: Nanotube electronics. High-performance transistors. Nature Materials 2002: 1; 203-04.

[246] A Javey, H Kim, M Brink, Q Wang, A Ural, J Guo, P McIntyre, P McEuen, M Lundstrom, H Dai: High-k dielectrics for advanced carbon-nanotube transistors and logic gates. Nature Materials 2002: 1; 241-46.

[247] HW Postma, T Teepen, Z Yao, M Grifoni, C Dekker: Carbon nanotube single-electron transistors at room temperature. Science 2001: 293; 76-9.

[248] J Li, Y Lu, Q Ye, M Cinke, J Han, M Meyyappan: Carbon Nanotube Sensors for Gas and Organic Vapor Detection. Nano Letters 2003: 3; 929-33.

[249] J Li, HT Ng: Carbon nanotube sensors. Encyclopedia of Nanoscience and Nanotechnology 2004: 1; 591-601.

[250] A Modi, N Koratkar, E Lass, B Wei, PM Ajayan: Miniaturized gas ionization sensors using carbon nanotubes. Nature (London, United Kingdom) 2003: 424; 171-74.

[251] S Ghosh, AK Sood, N Kumar: Carbon Nanotube Flow Sensors. Science (Washington, DC, United States) 2003: 299; 1042-44.

[252] J Kong, NR Franklin, C Zhou, MG Chapline, S Peng, K Cho, H Dailt: Nanotube molecular wires as chemical sensors. Science (Washington, D. C.) 2000: 287; 622-25.

[253] D Trejo, P Monteiro, G Thomas: Mechanical properties and corrosion susceptibility of dual-phase steel in concrete. Cement and Concrete Research 1994: 24; 1245-54.

[254] JI Kroschwitz, Editor: Polymers: High Performance Polymers and Composites, 1991.

[255] PJ Glatkowski, JW Connell, DH Landis, Jr., JG Smith, Jr., JW Piche, Electrostatic dissipative coatings for use with spacecraft, PCT Int. Appl. (Eikos, Inc., USA). Wo, 2003, p. 48 pp.

[256] RE Gorga, RE Cohen: Toughness enhancements in poly(methyl methacrylate) by addition of oriented multiwall carbon nanotubes. Journal of Polymer Science, Part B: Polymer Physics 2004: 42; 2690-702.

[257] DA Heller, PW Barone, JP Swanson, RM Mayrhofer, MS Strano: Using Raman Spectroscopy to Elucidate the Aggregation State of Single-Walled Carbon Nanotubes. Journal of Physical Chemistry B 2004: 108; 6905-09.

[258] JB Bai, A Allaoui: Effect of the length and the aggregate size of MWNTs on the improvement efficiency of the mechanical and electrical properties of nanocomposites - experimental investigation. Composites, Part A: Applied Science and Manufacturing 2003: 34A; 689-94.

[259] DW Schaefer, J Zhao, JM Brown, DP Anderson, DW Tomlin: Morphology of dispersed carbon single-walled nanotubes. Chemical Physics Letters 2003: 375; 369-75.

[260] PJ Boul, J Liu, ET Mickelson, CB Huffman, LM Ericson, IW Chiang, KA Smith, DT Colbert, RH Hauge, JL Margrave, RE Smalley: Reversible sidewall functionalization of buckytubes. Chemical Physics Letters 1999: 310; 367-72.

[261] J Chen, MA Hamon, H Hu, Y Chen, AM Rao, PC Eklund, RC Haddon: Solution properties of single-walled carbon nanotubes. Science (Washington, D. C.) 1998: 282; 95-98.

[262] K Kamaras, ME Itkis, H Hu, B Zhao, RC Haddon: Covalent bond formation to a carbon nanotube metal. Science (Washington, DC, United States) 2003: 301; 1501.

[263] MS Strano, CA Dyke, ML Usrey, PW Barone, MJ Allen, H Shan, C Kittrell, RH Hauge, JM Tour, RE Smalley: Electronic structure control of single-walled carbon nanotube functionalization. Science (Washington, DC, United States) 2003: 301; 1519-22.

[264] C Park, Z Ounaies, KA Watson, RE Crooks, J Smith, Joseph, SE Lowther, JW Connell, EJ Siochi, JS Harrison, TLS Clair: Dispersion of single wall carbon nanotubes by in situ polymerization under sonication. Chemical Physics Letters 2002: 364; 303-08.

[265] Z Ounaies, C Park, KE Wise, EJ Siochi, JS Harrison: Electrical properties of single wall carbon nanotube reinforced polyimide composites. Composites Science and Technology 2003: 63; 1637-46.

[266] TW Odom, J-L Huang, P Kim, CM Lieber: Structure and Electronic Properties of Carbon Nanotubes. Journal of Physical Chemistry B 2000: 104; 2794-809.

[267] M Ouyang, J-L Huang, CM Lieber: Scanning tunneling microscopy studies of the one-dimensional electronic properties of single-walled carbon nanotubes. Annual Review of Physical Chemistry 2002: 53; 201-20.

[268] M Ouyang, JL Huang, CL Cheung, CM Lieber: Energy gaps in "metallic" single-walled carbon nanotubes. Science 2001: 292; 702-5.

[269] M Ouyang, JL Huang, CL Cheung, CM Lieber: Atomically resolved single-walled carbon nanotube intramolecular junctions. Science 2001: 291; 97-100.

[270] AD Migone, S Talapatra: Gas adsorption on carbon nanotubes. Encyclopedia of Nanoscience and Nanotechnology 2004: 3; 749-67.

[271] BY Wei, HM Lin, HJ Lai, YS Yang, SH Chien: Desorption behavior of gaseous molecules on single-walled carbon nanotube bundles. Reviews on Advanced Materials Science 2003: 5; 306-10.

[272] C Branca, C Corsaro, F Frusteri, V Magazu, A Mangione, F Migliardo, U Wanderlingh: Structural and vibrational properties of carbon nanotubes by TEM and infrared spectroscopy. Diamond and Related Materials 2004: 13; 1249-53.

[273] MD Ellison, MJ Crotty, D Koh, RL Spray, KE Tate: Adsorption of NH3 and NO2 on single-walled carbon nanotubes. Journal of Physical Chemistry B 2004: 108; 7938-43.

[274] SM Keogh, TG Hedderman, E Gregan, G Farrell, G Chambers, HJ Byrne: Spectroscopic Analysis of Single-Walled Carbon Nanotubes and Semiconjugated Polymer Composites. Journal of Physical Chemistry B 2004: 108; 6233-41.

[275] Z Yao, N Braidy, GA Botton, A Adronov: Polymerization from the Surface of Single-Walled Carbon Nanotubes - Preparation and Characterization of Nanocomposites. Journal of the American Chemical Society 2003: 125; 16015-24.

[276] EV Basiuk, VA Basiuk, J-G Banuelos, J-M Saniger-Blesa, VA Pokrovskiy, TY Gromovoy, AV Mischanchuk, BG Mischanchuk: Interaction of Oxidized Single-Walled Carbon Nanotubes with Vaporous Aliphatic Amines. Journal of Physical Chemistry B 2002: 106; 1588-97.

[277] MA Hamon, H Hu, P Bhowmik, S Niyogi, B Zhao, ME Itkis, RC Haddon: End-group and defect analysis of soluble single-walled carbon nanotubes. Chemical Physics Letters 2001: 347; 8-12.

[278] M Namkung, JS Namkung, B Wincheski, J Seo, C Park, Spectroscopy-Based Characterization of Single Wall Carcon Nanotubes, Proceedings of the International Symposium on Clusters and Nano-Assemblies (ISCANA'03), 2003.

[279] VG Hadjiev, S Arepalli, P Nikolaev, S Jandl, L Yowell: Enhanced raman microprobe imaging of single-wall carbon nanotubes. Nanotechnology 2004: 15; 562-67.

[280] MA Lopez-Manchado, J Biagiotti, L Valentini, JM Kenny: Dynamic mechanical and raman spectroscopy studies on interaction between single-walled carbon nanotubes and natural rubber. Journal of Applied Polymer Science 2004: 92; 3394-400.

[281] A Jorio, MA Pimenta, AG Souza Filho, R Saito, G Dresselhaus, MS Dresselhaus: Characterizing carbon nanotube samples with resonance Raman scattering. New Journal of Physics 2003: 5; 1-17, Paper No. 139.

[282] H Zhang, S Liu, A Wei, Y He, X Tang, X Xue, L Liang, C Wu: Electron spin resonance of carbon nanotubes prepared under two kinds of inert gas ambient. Journal of Physics and Chemistry of Solids 2000: 61; 1123-25.

[283] M Kosaka, TW Ebbesen, H Hiura, K Tanigaki: Electron spin resonance of carbon nanotubes. Chemical Physics Letters 1994: 225; 161-4.

[284] TW Odom, J-L Huang, CM Lieber: STM studies of single-walled carbon nanotubes. Journal of Physics: Condensed Matter 2002: 14; R145-R67.

[285] TW Odom, J-L Huang, P Kim, CM Lieber: Atomic structure and electronic properties of single-walled carbon nanotubes. Nature (London) 1998: 391; 62-64.

[286] JWG Wildoer, LC Venema, AG Rinzier, RE Smalley, C Dekker: Electronic structure of atomically resolved carbon nanotubes. Nature (London) 1998: 391; 59-62.

[287] AH Barber, SR Cohen, HD Wagner: Static and Dynamic Wetting Measurements of Single Carbon Nanotubes. Physical Review Letters 2004: 92; 186103/1-03/4.

[288] P Poncharal, L Wang, D Ugarte, WA de Heer: Electrostatic deflections and electromechanical resonances of carbon nanotubes. Science 1999: 283; 1513-16.

[289] C Richard, F Balavoine, P Schultz, W Ebbesen Thomas, C Mioskowski: Supramolecular self-assembly of lipid derivatives on carbon nanotubes. Science 2003: 300; 775-8.

[290] H Dai, JH Hafner, AG Rinzler, DT Colbert, RE Smalley: Nanotubes as nanoprobes in scanning probe microscopy. Nature (London) 1996: 384; 147-50.

[291] SG Lemay, JW Janssen, M van den Hout, M Mooij, MJ Bronikowski, PA Willis, RE Smalley, LP Kouwenhoven, C Dekker: Two-dimensional imaging of electronic wavefunctions in carbon nanotubes. Nature 2001: 412; 617-20.

[292] SJ Tans, C Dekker: Molecular transistors: potential modulations along carbon nanotubes. Nature (London) 2000: 404; 834-35.

[293] M Freitag, M Radosavljevic, W Clauss, AT Johnson: Local electronic properties of single-wall nanotube circuits measured by conducting-tip AFM. Physical Review B: Condensed Matter and Materials Physics 2000: 62; R2307-R10.

[294] J Lee, H Kim, SJ Kahng, G Kim, YW Son, J Ihm, H Kato, ZW Wang, T Okazaki, H Shinohara, Y Kuk: Bandgap modulation of carbon nanotubes by encapsulated metallofullerenes. Nature (London, United Kingdom) 2002: 415; 1005-08.

[295] Y Cho, S Han, G Kim, H Lee, J Ihm: Orbital Hybridization and Charge Transfer in Carbon Nanopeapods. Physical Review Letters 2003: 90; 106402/1-02/4.

[296] DJ Hornbaker, SJ Kahng, S Misra, BW Smith, AT Johnson, EJ Mele, DE Luzzi, A Yazdani: Mapping the one-dimensional electronic states of nanotube peapod structures. Science (Washington, DC, United States) 2002: 295; 828-31.

[297] CL Kane, EJ Mele, AT Johnson, DE Luzzi, BW Smith, DJ Hornbaker, A Yazdani: Theory of scanning tunneling spectroscopy of fullerene peapods. Physical Review B: Condensed Matter and Materials Physics 2002: 66; 235423/1-23/15.

[298] D Qian, GJ Wagner, WK Liu, M-F Yu, RS Ruoff: Mechanics of carbon nanotubes. Appl. Mech. Rev. 2002: 55; 495-533.

[299] J-P Salvetat, GAD Briggs, J-M Bonard, RR Bacsa, AJ Kulik, T Stockli, NA Burnham, L Forro: Elastic and Shear Moduli of Single-Walled Carbon Nanotube Ropes. Physical Review Letters 1999: 82; 944-47.

[300] JP Salvetat, JM Bonard, NH Thomson, AJ Kulik, L Forro, W Benoit, L Zuppiroli: Mechanical properties of carbon nanotubes. Applied Physics A 1999: 69; 255-60.

[301] MR Falvo, GJ Clary, RM Taylor, 2nd, V Chi, FP Brooks, Jr., S Washburn, R Superfine: Bending and buckling of carbon nanotubes under large strain. Nature (London) 1997: 389; 582-84.

[302] SS Wong, JD Harper, PT Lansbury, Jr., CM Lieber: Carbon Nanotube Tips: High-Resolution Probes for Imaging Biological Systems. Journal of the American Chemical Society 1998: 120; 603-04.

[303] PA Williams, SJ Papadakis, AM Patel, MR Falvo, S Washburn, R Superfine: Torsional Response and Stiffening of Individual Multiwalled Carbon Nanotubes. Physical Review Letters 2002: 89; 255502/1-02/4.

[304] ED Minot, Y Yaish, V Sazonova, J-Y Park, M Brink, PL McEuen: Tuning Carbon Nanotube Band Gaps with Strain. Physical Review Letters 2003: 90; 156401/1-01/4.

[305] M-F Yu, T Kowalewski, RS Ruoff: Investigation of the Radial Deformability of Individual Carbon Nanotubes under Controlled Indentation Force. Physical Review Letters 2000: 85; 1456-59.

[306] S Park, D Srivastava, K Cho: Generalized Chemical Reactivity of Curved Surfaces: Carbon Nanotubes. Nano Letters 2003: 3; 1273-77.

[307] M-F Yu, BS Files, S Arepalli, RS Ruoff: Tensile loading of ropes of single wall carbon nanotubes and their mechanical properties. Physical Review Letters 2000: 84; 5552-55.

[308] M-F Yu, O Lourie, MJ Dyer, K Moloni, TF Kelly, RS Ruoff: Strength and breaking mechanism of multiwalled carbon nanotubes under tensile load. Science (Washington, D. C.) 2000: 287; 637-40.

[309] W Shen, B Jiang, BS Han, S-s Xie: Investigation of the Radial Compression of Carbon Nanotubes with a Scanning Probe Microscope. Physical Review Letters 2000: 84; 3634-37.

[310] M-F Yu, MJ Dyer, RS Ruoff: Structure and mechanical flexibility of carbon nanotube ribbons: An atomic-force microscopy study. Journal of Applied Physics 2001: 89; 4554-57.

[311] A Volodin, M Ahlskog, E Seynaeve, C Van Haesendonck, A Fonseca, JB Nagy: Imaging the Elastic Properties of Coiled Carbon Nanotubes with Atomic Force Microscopy. Physical Review Letters 2000: 84; 3342-45.

[312] MR Falvo, J Steele, RM Taylor, II, R Superfine: Gearlike rolling motion mediated by commensurate contact: Carbon nanotubes on HOPG. Physical Review B: Condensed Matter and Materials Physics 2000: 62; R10665-R67.

[313] TW Tombler, C Zhou, J Kong, H Dai: Gating individual nanotubes and crosses with scanning probes. Applied Physics Letters 2000: 76; 2412-14.

[314] TW Tombler, C Zhou, L Alexseyev, J Kong, H Dai, CS Jayanthi, M Tang, S-Y Wu: Reversible electromechanical characteristics of carbon nanotubes under local-probe manipulation. Nature (London) 2000: 405; 769-72.

[315] D Bozovic, M Bockrath, JH Hafner, CM Lieber, H Park, M Tinkham: Electronic properties of mechanically induced kinks in single-walled carbon nanotubes. Applied Physics Letters 2001: 78; 3693-95.

[316] D-H Kim, J-Y Koo, J-J Kim: Cutting of multiwalled carbon nanotubes by a negative voltage tip of an atomic force microscope: a possible mechanism. Physical Review B: Condensed Matter and Materials Physics 2003: 68; 113406/1-06/4.

[317] J-Y Park, Y Yaish, M Brink, S Rosenblatt, PL McEuen: Electrical cutting and nicking of carbon nanotubes using an atomic force microscope. Applied Physics Letters 2002: 80; 4446-48.

[318] MT Woodside, PL McEuen: Scanned probe imaging of single-electron charge states in nanotube quantum dots. Science (Washington, DC, United States) 2002: 296; 1098-101.

[319] D Bozovic, M Bockrath, JH Hafner, CM Lieber, H Park, M Tinkham: Plastic deformations in mechanically strained single-walled carbon nanotubes. Physical Review B: Condensed Matter and Materials Physics 2003: 67; 033407/1-07/4.

[320] KS Kim, SC Lim, IB Lee, KH An, DJ Bae, S Choi, J-E Yoo, YH Lee: In situ manipulation and characterizations using nanomanipulators inside a field emission-scanning electron microscope. Review of Scientific Instruments 2003: 74; 4021-25.

[321] C Thelander, L Samuelson: AFM manipulation of carbon nanotubes: Realization of ultra-fine nanoelectrodes. Nanotechnology 2002: 13; 108-13.

[322] J Li, R Stevens, L Delzeit, HT Ng, A Cassell, J Han, M Meyyappan: Electronic properties of multiwalled carbon nanotubes in an embedded vertical array. Applied Physics Letters 2002: 81; 910-12.

[323] PT Lillehei, C Park, JH Rouse, EJ Siochi: Imaging Carbon Nanotubes in High Performance Polymer Composites via Magnetic Force Microscopy. Nano Letters 2002: 2; 827-29.

[324] CA Cooper, SR Cohen, AH Barber, HD Wagner: Detachment of nanotubes from a polymer matrix. Applied Physics Letters 2002: 81; 3873-75.

[325] AH Barber, SR Cohen, HD Wagner: Measurement of carbon nanotube-polymer interfacial strength. Applied Physics Letters 2003: 82; 4140-42.

[326] W Ding, A Eitan, FT Fisher, X Chen, DA Dikin, R Andrews, LC Brinson, LS Schadler, RS Ruoff: Direct Observation of Polymer Sheathing in Carbon Nanotube-Polycarbonate Composites. Nano Letters 2003: 3; 1593-97.

[327] K Liao, S Li: Interfacial characteristics of a carbon nanotube–polystyrene composite system. Applied Physics Letters 2001: 79; 4225-27.

[328] HD Wagner: Nanotube-polymer Adhesion:a mechanics approach. Chemical Physics Letters 2002: 361; 57-61.

[329] A Noy, DV Vezenov, CM Lieber: Chemical Force Microscopy. Annu. Rev. Mater. Sci. 1997: 27; 381-421.

[330] X Jiang, C Ortiz, PT Hammond: Exploring the Rules for Selective Deposition: Interactions of Model Polyamines on Acid and Oligoethylene Oxide Surfaces. Langmuir 2002: 18; 1131-43.

[331] MP Schotanus, KS Aumann, K Sinniah: Using Force Spectroscopy To Investigate the Binding of Complementary DNA in the Presence of Intercalating Agents. Langmuir 2002: 18; 5333-36.

[332] J Seog, D Dean, AHK Plaas, S Wong-Palms, AJ Grodzinsky, C Ortiz: Direct Measurement of Glycosaminoglycan Intermolecular Interactions via High-Resolution Force Spectroscopy. Macromolecules 2002: 35; 5601-15.

[333] VV Tsukruk, VN Bliznyuk: Adhesive and Friction Forces between Chemically Modified Silicon and Silicon Nitride Surfaces. Langmuir 1998: 14; 446-55.

[334] J Zhang, J Kirkham, C Robinson, ML Wallwork, DA Smith, A Marsh, M Wong: Determination of the Ionization State of 11-Thioundecyl-1-phosphonic Acid in Self-Assembled Monolayers by Chemical Force Microscopy. Analytical Chemistry 2000: 72; 1973-78.

[335] ML Wallwork, DA Smith, J Zhang, J Kirkham, C Robinson: Complex Chemical Force Titration Behavior of

Amine-Terminated Self-Assembled Monolayers. Langmuir 2001: 17; 1126-31.

[336] DA Smith, ML Wallwork, J Zhang, J Kirkham, C Robinson, A Marsh, M Wong: The Effect of Electrolyte Concentration on the Chemical Force Titration Behavior of w-Functionalized SAMs: Evidence for the Formation of Strong Ionic Hydrogen Bonds. Journal of Physical Chemistry B 2000: 104; 8862-70.

[337] GY Choi, JF Kang, A Ulman, W Zurawsky, C Fleischer: Acid-Base Interaction in the Adhesion between Two Solid Surfaces. Langmuir 1999: 15; 8783-86.

[338] AS Duwez, B Nysten: Mapping Aging Effects on Polymer Surfaces: Specific Detection of Additives by Chemical Force Microscopy. Langmuir 2001: 17; 8287-92.

[339] P Eaton, F Fernandez Estarlich, RJ Ewen, TG Nevell, JR Smith, J Tsibouklis: Combined Nanoindentation and Adhesion Force Mapping Using the Atomic Force Microscope: Investigations of a Filled Polysiloxane Coating. Langmuir 2002: 18; 10011-15.

[340] LA Bottomley, JA Jones, Y Ding, DP Allison, T Thundat, RJ Warmack: Scanning Tunneling Microscopic Imaging of Electrostatically Immobilized Nucleic Acids. The Influence of Self-assembled Monolayer Structure on the Binding of Plasmid DNA to Gold Surfaces. S.P.I.E. Proc. Biomed. Optics Soc. 1993: 1891; 48-55.

[341] CD Bain, EB Troughton, YT Tao, J Evall, GM Whitesides, RG Nuzzo: Formation of monolayer films by the spontaneous assembly of organic thiols from solution onto gold. Journal of the American Chemical Society 1989: 111; 321-35.

[342] MD Porter, TB Bright, DL Allara, CED Chidsey: Spontaneously organized molecular assemblies. 4. Structural characterization of n-alkyl thiol monolayers on gold by optical ellipsometry, infrared spectroscopy, and electrochemistry. Journal of the American Chemical Society 1987: 109; 3559-68.

[343] X Nan, Z Gu, Z Liu: Immobilizing Shortened Single-Walled Carbon Nanotubes (SWNTs) on Gold Using a Surface Condensation Method. Journal of Colloid and Interface Science 2002: 245; 311-18.

[344] J Liu, AG Rinzler, H Dai, JH Hafner, RK Bradley, PJ Boul, A Lu, T Iverson, K Shelimov, CB Huffman, F Rodriguez-Macias, Y-S Shon, TR Lee, DT Colbert, RE Smalley: Fullerene pipes. Science (Washington, D. C.) 1998: 280; 1253-56.

[345] ST Patton, KC Eapen, JS Zabinski: Effects of adsorbed water and sample aging in air on the .mu.N level adhesion force between Si(100) and silicon nitride. Tribology International 2001: 34; 481-91.

[346] GA Willing, RD Neuman: Analysis of Asperity-Asperity Adhesion Forces Utilizing Statistical Analysis Techniques and the Force Selectivity of the Scanning Probe Microscope. Langmuir 2002.

[347] G Bar, S Rubin, AN Parikh, BI Swanson, TA Zawodzinski, Jr., MH Whangbo: Scanning Force Microscopy Study of Patterned Monolayers of Alkanethiols on Gold. Importance of Tip-Sample Contact Area in Interpreting Force Modulation and Friction Force Microscopy Images. Langmuir 1997: 13; 373-77.

[348] JA DeRose, JP Revel: Examination of atomic (scanning) force microscopy probe tips with the transmission electron microscope. Microscopy and Microanalysis 1997: 3; 203-13.

[349] J Vesenka, R Miller, E Henderson: Three-dimensional probe reconstruction for atomic force microscopy. Review of Scientific Instruments 1994: 65; 2249-51.

[350] V Lordi, N Yao: Radial compression and controlled cutting of carbon nanotubes. Journal of Chemical Physics 1998: 109; 2509-12.

[351] CF Cornwell, LT Wille: Elastic properties of single-walled carbon nanotubes in compression. Solid State Communications 1997: 101; 555-58.

[352] D Srivastava, M Menon, K Cho: Nanoplasticity of Single-Wall Carbon Nanotubes under Uniaxial Compression. Phys. Rev. Lett. 1999: 83; 2973-76.

[353] CED Chidsey, DN Loiacono: Chemical Functionality in Self -Assembled Monolayers: Structural and Electrochemical Properties. Langmuir 1990: 6; 682-91.

[354] A Ulman: Formation and Structure of Self-Assembled Monolayers. Chemical Reviews (Washington, D. C.) 1996: 96; 1533-54.

[355] RG Nuzzo, LH Dubois, DL Allara: Fundamental studies of microscopic wetting on organic surfaces. 1. Formation and structural characterization of a self-consistent series of polyfunctional organic monolayers. Journal of the American Chemical Society 1990: 112; 558-69.

[356] LH Dubois, RG Nuzzo: Synthesis, structure, and properties of model organic surfaces. Annual Review of Physical Chemistry 1992: 43; 437-63.

[357] M Salmeron, A Folch, G Neubauer, M Tomitori, DF Ogletree: Nanometer Scale Mechanical Properties of Au(111) thin Films. Langmuir 1992: 8; 2832-42.

[358] M Salmeron, G Neubauer, A Folch, M Tomitori, DF Ogletree, P Sautet: Viscoelastic and Electrical Poperties of Self-Assembled Monolayers on Au(111) Films. Langmuir 1993: 9; 3600-11.

[359] RC Thomas, JE Houston, TA Michalske, CR Crooks: The Mechanical Response of Gold Substrates Passivated by Self-Assembling Monolayer Films. Science 1993: 259; 1883-85.

[360] SA Joyce, RC Thomson, JE Houston, TA Michalske, CR Crooks: Mechanical Relaxation of Organic Monolayer Films Measured by Force Microscopy. Phys. Rev. Lett. 1992: 68; 2790-93.

[361] J Liu, MJ Casavant, M Cox, DA Walters, P Boul, W Lu, AJ Rimberg, KA Smith, DT Colbert, RE Smalley: Controlled deposition of individual single-walled carbon nanotubes on chemically functionalized templates. Chemical Physics Letters 1999: 303; 125-29.

[362] TL Sordo, JA Sordo, R Florez: Theoretical study of adsorption of hydrocarbons on graphite. Journal of Computational Chemistry 1990: 11; 291-6.

[363] FJ Lopez-Garzon, I Fernandez-Morales, M Domingo-Garcia: A gas-solid chromatographic study of the adsorption of hydrocarbons and alcohols on graphite. Chromatographia 1987: 23; 97-101.

[364] S Kwon, J Russell, X Zhao, RD Vidic, JK Johnson, E Borguet: Combined Experimental and Theoretical Investigation of Polar Organic Adsorption/Desorption from Model Carbonaceous Surfaces: Acetone on Graphite. Langmuir 2002: 18; 2595-600.

[365] S Kwon, R Vidic, E Borguet: The effect of surface chemical functional groups on the adsorption and desorption of a polar molecule, acetone, from a model carbonaceous surface, graphite. Surface Science 2003: 522; 17-26.

[366] JK Oman, SJ Garrett: Adsorption and laser-induced thermal desorption of 1,3-butadiene on HOPG(0001). Journal of Physical Chemistry B 2002: 106; 10417-23.

[367] K Dettmer, T Knobloch, W Engewald: Stability of reactive low boiling hydrocarbons on carbon based adsorbents typically used for adsorptive enrichment and thermal desorption. Fresenius' Journal of Analytical Chemistry 2000: 366; 70-78.

[368] K Wang, DD Do: Multicomponent adsorption, desorption and displacement kinetics of hydrocarbons on activated carbon - dual diffusion and finite kinetics model. Separation and Purification Technology 1999: 17; 131-46.

[369] KR Paserba, N Vaidyanathan, AJ Gellman: Conformational Entropy Effects on the Desorption Kinetics of Polyethers from Graphite. Langmuir 2002: 18; 9799-809.

[370] AJ Gellman, KR Paserba: Kinetics and Mechnism of Oligomer Desorption from Surfaces: n-Alkanes on Graphite. Journal of Physical Chemistry B 2002: 106; 13231-41.

[371] DC Sorescu, KD Jordan, P Avouris: Theoretical study of oxygen adsorption on graphite and the (8,0) single-walled carbon nanotube. Journal of Physical Chemistry B 2001: 105; 11227-32.

[372] S Santucci, S Picozzi, F Di Gregorio, L Lozzi, C Cantalini, L Valentini, JM Kenny, B Delley: NO2 and CO gas adsorption on carbon nanotubes: Experiment and theory. Journal of Chemical Physics 2003: 119; 10904-10.

[373] S Peng, K Cho: Chemical Control of Nanotube Electronics. Nanotechnology 2000: 11; 57-60.

[374] H Chang, JD Lee, SM Lee, YH Lee: Adsorption of NH3 and NO2 molecules on carbon nanotubes. Applied Physics Letters 2001: 79; 3863-65.

[375] A Goldoni, R Larciprete, L Petaccia, S Lizzit: Single-Wall Carbon Nanotube Interaction with Gases: Sample Contaminants and Environmental Monitoring. Journal of the American Chemical Society 2003: 125; 11329-33.

[376] M Ruths: Boundary Friction of Aromatic Self-Assembled Monolayers: Comparison of Systems with One or Both Sliding Surfaces Covered with a Thiol Monolayer. Langmuir 2003: 19; 6788-95.

[377] Y-T Tao, C-C Wu, J-Y Eu, W-L Lin, K-C Wu, C-h Chen: Structure Evolution of Aromatic-Derivatized Thiol Monolayers on Evaporated Gold. Langmuir 1997: 13; 4018-23.

[378] DL Pugmire, MJ Tarlov, RD Van Zee, J Naciri: Structure of 1,4-Benzenedimethanethiol Self-Assembled Monolayers on Gold Grown by Solution and Vapor Techniques. Langmuir 2003: 19; 3720-26.

[379] CM Whelan, CJ Barnes, CGH Walker, NMD Brown: Benzenethiol adsorption on Au(111) studied by synchrotron ARUPS, HREELS and XPS. Surface Science 1999: 425; 195-211.

[380] RG Parr, RG Pearson: Absolute hardness: companion parameter to absolute electronegativity. Journal of the American Chemical Society 1983: 105; 7512-16.

[381] C Hansch, A Leo, RW Taft: A survey of Hammett substituent constants and resonance and field parameters. Chemical Reviews (Washington, DC, United States) 1991: 91; 165-95.

[382] F De Proft, W Langenaeker, P Geerlings: Ab initio determination of substituent constants in a density functional theory formalism: calculation of intrinsic group electronegativity, hardness, and softness. Journal of Physical Chemistry 1993: 97; 1826-31.

[383] P Qi, O Vermesh, M Grecu, A Javey, Q Wang, H Dai, S Peng, KJ Cho: Toward Large Arrays of Multiplex Functionalized Carbon Nanotube Sensors for Highly Sensitive and Selective Molecular Detection. Nano Letters 2003: 3; 347-51.

[384] K Bradley, J-CP Gabriel, M Briman, A Star, G Gruner: Charge transfer from ammonia physisorbed on nanotubes. Physical Review Letters 2003: 91; 218301/1-01/4.

[385] KAS Fernando, Y Lin, W Wang, S Kumar, B Zhou, S-Y Xie, LT Cureton, Y-P Sun: Diminished Band-Gap Transitions of Single-Walled Carbon Nanotubes in Complexation with Aromatic Molecules. Journal of the American Chemical Society 2004: 126; 10234-35.

[386] A Star, T-R Han, J-CP Gabriel, K Bradley, G Gruener: Interaction of aromatic compounds with carbon nanotubes: correlation to the Hammett parameter of the substituent and measured carbon nanotube FET response. Nano Letters 2003: 3; 1421-23.

[387] C Vidal-Madjar, E Bekassy-Molnar: Molecular statistical theory of adsorption for hydrocarbons on graphite. Effect of polarizability anisotropy in adsorption potential. Journal of Physical Chemistry 1984: 88; 232-8.

[388] L Senf, H Frank: Thermal desorption of organic pollutants enriched on activated carbon. V. Desorption behavior and temperature profile. Journal of Chromatography 1990: 520; 131-5.

[389] A Torrents, R Damera, OJ Hao: Low-temperature thermal desorption of aromatic compounds from activated carbon. Journal of Hazardous Materials 1997: 54; 141-54.

[390] PKT Liu, SM Feltch, NJ Wagner: Thermal desorption behavior of aliphatic and aromatic hydrocarbons loaded on activated carbon. Industrial & Engineering Chemistry Research 1987: 26; 1540-5.

[391] AA Koos, R Ehlich, ZE Horvath, Z Osvath, J Gyulai, JB Nagy, LP Biro: STM and AFM investigation of coiled carbon nanotubes produced by laser evaporation of fullerene. Materials Science & Engineering, C: Biomimetic and Supramolecular Systems 2003: C23; 275-78.

[392] P Lambin, GI Mark, LP Biro: Structural and electronic properties of coiled and curled carbon nanotubes having a large number of pentagon-heptagon pairs. Physical Review B: Condensed Matter and Materials Physics 2003: 67; 205413/1-13/9.

[393] M Hegner, P Wagner, G Semenza: Ultralarge atomically flat template-stripped Au surfaces for scanning probe microscopy. Surface Science 1993: 291; 39-46.

[394] A Roters, D Johannsmann: Distance-dependent noise measurements in scanning force microscopy. Journal of Physics: Condensed Matter 1996: 8; 7561-77.

[395] B Cappella, G Dietler: Force-distance curves by atomic force microscopy. Surface Science Reports 1999: 34; 1-104.

[396] T Vodenitcharova, LC Zhang: Effective wall thickness of a single-walled carbon nanotube. Physical Review B: Condensed Matter and Materials Physics 2003: 68; 165401/1-01/4.

[397] BI Yakobson, CJ Brabec, J Bernholc: Nanomechanics of carbon tubes: instabilities beyond linear response. Physical Review Letters 1996: 76; 2511-14.

[398] JP Lu: Elastic Properties of Carbon Nanotubes and Nanoropes. Physical Review Letters 1997: 79; 1297-300.

[399] J-P Salvetat, AJ Kulik, J-M Bonard, GAD Briggs, T Stoeckli, K Metenier, S Bonnamy, F Beguin, NA Burnham, L Forro: Elastic modulus of ordered and disordered multiwalled carbon nanotubes. Advanced Materials (Weinheim, Germany) 1999: 11; 161-65.

[400] RS Ruoff, DC Lorents: Mechanical and thermal properties of carbon nanotubes. Carbon 1995: 33; 925-30.

[401] T Kuzumaki, T Hayashi, H Ichinose, K Miyazawa, K Ito, Y Ishida: In-situ observed deformation of carbon nanotubes. Philosophical Magazine A: Physics of Condensed Matter: Structure, Defects and Mechanical Properties 1998: 77; 1461-69.

[402] JZ Liu, Q Zheng, Q Jiang: Effect of a Rippling Mode on Resonances of Carbon Nanotubes. Physical Review Letters 2001: 86; 4843-46.

[403] S Lee, A Puck, M Graupe, R Colorado, Jr., Y-S Shon, TR Lee, SS Perry: Structure, Wettability, and Frictional Properties of Phenyl-Terminated Self-Assembled Monolayers on Gold. Langmuir 2001: 17; 7364-70.

[404] J-A Ruan, B Bhushan: Frictional behavior of highly oriented pyrolytic graphite. Journal of Applied Physics 1994: 76; 8117-20.

[405] B Bhushan, H Liu: Nanotribological properties and mechanisms of alkylthiol and biphenyl thiol self-assembled monolayers studied by AFM. Physical Review B: Condensed Matter and Materials Physics 2001: 63; 245412/1-12/11.

[406] NJ Brewer, BD Beake, GJ Leggett: Friction force microscopy of self-assembled monolayers: Influence of adsorbate alkyl chain length, terminal group chemistry, and scan velocity. Langmuir 2001: 17; 1970-74.

[407] NJ Brewer, GJ Leggett: Chemical Force Microscopy of Mixed Self-Assembled Monolayers of Alkanethiols on Gold: Evidence for Phase Separation. Langmuir 2004: 20; 4109-15.

[408] JD Kiely, JE Houston: Contact Hysteresis and Friction of Alkanethiol Self-Assembled Monolayers on Gold. Langmuir 1999: 15; 4513-19.

[409] HI Kim, JE Houston: Separating Mechanical and Chemical Contributions to Molecular-Level Friction. Journal of the American Chemical Society 2000: 122; 12045-46.

[410] L Zhang, L Li, S Chen, S Jiang: Measurements of Friction and Adhesion for Alkyl Monolayers on Si(111) by Scanning Force Microscopy. Langmuir 2002: 18; 5448-56.

[411] K Miura, M Ishikawa, R Kitanishi, M Yoshimura, K Ueda, Y Tatsumi, N Minami: Bundle structure and sliding of single-walled carbon nanotubes observed by frictional-force microscopy. Applied Physics Letters 2001: 78; 832-34.

[412] K Miura, T Takagi, S Kamiya, T Sahashi, M Yamauchi: Natural Rolling of Zigzag Multiwalled Carbon Nanotubes on Graphite. Nano Letters 2001: 1; 161-63.

[413] O Lourie, DM Cox, HD Wagner: Buckling and Collapse of Embedded Carbon Nanotubes. Physical Review Letters 1998: 81; 1638-41.

[414] U Rabe, M Kopycinska, S Hirsekorn, W Arnold: Evaluation of the contact resonance frequencies in atomic force microscopy as a method for surface characterisation. Ultrasonics 2002: 40; 49-54.

[415] R Zacharia, H Ulbricht, T Hertel: Interlayer cohesive energy of graphite from thermal desorption of polyaromatic hydrocarbons. Physical Review B: Condensed Matter and Materials Physics 2004: 69; 155406/1-06/7.

[416] M Zheng, A Jagota, MS Strano, AP Santos, P Barone, SG Chou, BA Diner, MS Dresselhaus, RS McLean, GB Onoa, GG Samsonidze, ED Semke, M Usrey, DJ Walls: Structure-Based Carbon Nanotube Sorting by Sequence-Dependent DNA Assembly. Science (Washington, DC, United States) 2003: 302; 1545-48.

[417] GI Dovbeshko, OP Repnytska, ED Obraztsova, YV Shtogun: DNA interaction with single-walled carbon nanotubes: a SEIRA study. Chemical Physics Letters 2003: 372; 432-37.

[418] H Li, B Zhou, Y Lin, L Gu, W Wang, KAS Fernando, S Kumar, LF Allard, Y-P Sun: Selective Interactions of Porphyrins with Semiconducting Single-Walled Carbon Nanotubes. Journal of the American Chemical Society 2004: 126; 1014-15.

[419] L Liu, CS Jayanthi, M Tang, SY Wu, TW Tombler, C Zhou, L Alexseyev, J Kong, H Dai: Controllable Reversibility of an sp2 to sp3 Transition of a Single Wall Nanotube under the Manipulation of an AFM Tip: A Nanoscale Electromechanical Switch? Physical Review Letters 2000: 84; 4950-53.

[420] ZL Wang, RP Gao, P Poncharal, WA de Heer, ZR Da, ZW Pan: Mechanical and electrostatic properties of carbon nanotubes and nanowires. Materials Science and Engineering C 2001: 16; 3-10.

[421] J Kong, H Dai: Full and Modulated Chemical Gating of Individual Carbon Nanotubes by Organic Amine Compounds. Journal of Physical Chemistry B 2001: 105; 2890-93.

VITA

Mark Andrew Poggi was born and raised in the polar environment of Marquette, Michigan. At a very young age he was inspired by his mother and father to pursue life to the fullest extent. Mr. Poggi earned his bachelors degree in Chemistry at Michigan State University. While at MSU he developed a large interest in mathematics. This led him to elect numerous courses in the Department of Mathematics.

These dual interests led Mr. Poggi to pursue graduate studies in the field of Analytical Chemistry. His strong appreciation for the vast span of the scientific field led him to elect taking courses not only in the School of Chemistry and Biochemistry but also in Chemical Engineering, Electrical Engineering and Materials Science Engineering.

His research experience under the guidance of Professor Lawrence A. Bottomley exposed him to numerous research projects in analytical chemistry as well as mechanical engineering. During his tenure at Georgia Tech he was nominated as a Georgia Tech Presidential Fellow, a recipient of the Analytical Chemistry Graduate Student Fellowship sponsored by the American Chemical Society, a three-year recipient of a NASA Graduate Student research fellowship and a recipient of many other awards. Mr. Poggi published over twenty scientific manuscripts pertaining to his work at Georgia Tech.

Mr. Poggi has been happily married to his wife Meredith for almost three years. He's repeatedly said that she's the "glue" that keeps him together.